DOCTOR OF PHILOSOPHY

Propagation of High Intensity Focused Ultrasound through a Patient-specific Ribcage Model

Cao, Rui

Award date:
2014

Propagation of High Intensity Focused Ultrasound through a Patient-specific Ribcage Model

by

RUI CAO

A Thesis Submitted in Fulfilment of the Requirements of the University of Dundee for the Degree for Doctor of Philosophy (Ph.D.) in Mechanical Engineering

School of Engineering, Physics and Mathematics,

College of Art, Science and Engineering, University of Dundee,

Dundee, UK

November 2014

Table of Contents

Dedication

I hereby declare that this thesis is my own work and effort and that it has not been submitted anywhere for any award. Where other sources of information have been used, they have been acknowledged.

……..

Rui Cao

Certificate

This is to certify that Rui Cao has done this research under my supervision and that she has fulfilled the conditions of Ordinance 39 of the University of Dundee, so that she is qualified to submit for the Degree of Doctor of Philosophy.

……..……

Dr. Zhihong Huang

Copyright

Acknowledgements

I would like to express my deepest gratitude to my supervisor, Dr. Zhihong Huang for her guidance, caring, patience on my PhD project and providing me with an excellent atmosphere for the research. I would like to thank Dr. Ghulam Nabi for kindly providing the clinical data for research and for guidance on my project. My sincere thanks also goes to, Prof. Sandy Cochran and Prof. Andreas Melzer for their kindly guidance in regular group meeting and providing me with excellent experimental facilities. I would express my heartfelt thanks to Prof. George Corner for his suggestions on my thesis even after his retirement.

I would like to thank Dr. Jing Gao and Dr. Xu Xiao, who have helped me and provided valuable suggestions on my research. I would like to thank all the members and former members in ultrasound group and friends in Dundee: Benjamin Cox, Christine Démodé, Cheng Wei, Chenghuo Shang, Chunhui Li, Efstratios Kokkalis, Guangying Shangguan, Han Wang, Yunwei Xu, Ioannis Karakitsios, Joyce Joy, Muhammad Sadiq, Nhan Le, Qinqin Gui, Robert Ssekitoleko, Shaozhen Song, Srikanta Sundaresh, Tingyi Jiang, Xiaochun Liao, Xiaowei Zhou, Yang Kuang, Yuting Ling, Yongqiang Qiu, Zhen Qiu and Zhengtian Song, for working and discussing together, and for all the fun we have had in the past four years.

I would give my special thanks to my parents, who gave my birth, raised me and are always supporting and encouraging me with their best wishes. I would like to thank my grandmother on my mother's side, who passed away in 2011 when I was in the UK, for years of her care. Last but not least, I would say thank you to my girlfriend, who has accompanied me on my entire PhD life for four years, even if we lived in different countries with time difference of seven or eight hours. Her support inspired me from the deep of my heart.

The research presented in this thesis was funded by China Scholarship Council (CSC) and University of Dundee.

Abstract

A method of 3D modelling of high intensity focused ultrasound (HIFU) treatment through ribcage using patient data is described. This is further tested experimentally to derive at various parameters which could be indirectly useful in defining amount of energy and alteration needed in treatment protocols for the upper abdominal pathologies covered under ribcage.

In the last ten years, feasibility and safety of HIFU treatment have been tested in a growing number of clinical studies. However, there are still challenges, such as the treatment through the ribcage. HIFU propagates through the ribs could lead to insufficient energy delivery to the focal target and heat deposition at the ribs may lead to surrounding soft tissue damage due to the bones properties of absorption and reflection to the ultrasound wave. Current research has not involved the physical human anatomical structures into the experimental study of the HIFU treatment through the ribcage. Therefore, our aim was to build a patient-specific physical ribcage model that possesses human anatomical structures to investigate its effect on HIFU treatment.

Ribcage model was reconstructed based on patient data. This prototyping model possessed human anatomical structures and provided useful information in the treatment planning by applying HIFU sonication on tissue mimicking phantoms. In order to determine the optimal phantoms for medical imaging and HIFU application, the properties of tissue mimicking materials (TMMs) were characterised, including acoustic, thermal and elastic properties. Acoustic pressure distribution, acoustic power delivery and focus splitting were investigated with and without the presence of ribcage model in the focused ultrasound field.

Multi-channel phased array transducer was applied to investigate the changes in temperature at focus and temperature was monitored by magnetic resonance imaging (MRI) thermometry. Sonications on phantom with varied focal lengths and ribcage locations using robotic arm were performed. Thermometry revealed that heating at focus can be controlled either by changing power or duration of application in order to achieve optimal results. Focal temperature change related to the shadow area on the transducer elements caused by the ribcage model in HIFU beam path. The experimental data based

on the patient-specific ribcage model may contribute to design and optimise the sonication protocol in pre-clinical planning stage. It is believed that the HIFU sonication experiments using realistic phantoms based on patient data would be a step towards translation of this technology into more widespread clinical practice.

List of Abbreviations and Symbols

ABS	Acrylonitrile Butadiene Styrene
ARFI	Acoustic radiation force impulse
BPH	Benign prostatic hyperplasia
BSA	Bovine serum albumin
COSHH	Control of Substances Hazardous to Health
CT	Computed tomography
DICOM	Digital Imaging and Communications in Medicine
DQA	Daily Quality Assurance
FDA	Food and Drug Administration
FIESTA	Fast imaging employing steady state acquisition
HCC	Hepatocellular carcinoma
HIFU	High intensity focused ultrasound
IR	Infrared
IRB	Institutional review board
MRgFUS	Magnetic resonance-guided focused ultrasound surgery
MRI	Magnetic resonance imaging
PAA	Polyacrylamide
PCa	Prostate cancer
PRF	Proton resonance frequency
PVA	Polyvinyl alcohol
PZT	Lead zirconate titanate
RFB	Radiation force balance
ROT	Region of Treatment
RP	Rapid prototyping
SD	Standard deviation
SWE	Shear wave elastography
tcMRgFUS	Transcranial magnetic resonance-guided focused ultrasound

TMMs	Tissue mimicking materials
TPS	Transient plane source
TURP	Trans-urethral resection of the prostate

A	Area of heat source
A_0	Force area
A_s	Amplitude of the received ultrasound pulse through sample
A_w	Amplitude of the received ultrasound pulse through water
c	Specific heat capacity
D	Distance of ultrasound transmission path
E	Young's modulus
F	Force
F_a	Calibration factor for absorbing target
g	Gravitational acceleration
h	Thickness of sample
I	Electric current
I_{sal}	Spatial average linear intensity
k	Thermal conductivity
L_0	Original length of sample
ΔL	Changes in length
q	Heat flux
R	Resistance of heat source
t	Duration time
t_0	Ultrasound propagation time in free field
T	Temperature response
T_r	Transmission coefficient
Δt	Time difference in ultrasound transmission with and without sample

V_{pp}	Peak to peak voltage
v_{sw}	Speed of shear wave
v_s	Speed of sound in sample
v_w	Speed of sound in water
x	Distance between heat source to thermocouple
Z	Acoustic impedance

α	Thermal diffusivity
α_s	Acoustic attenuation coefficient of sample
α_w	Acoustic attenuation coefficient of water
ε	Strain
μ	Shear modulus
ρ	Density
σ	Stress
υ	Poisson's ratio

List of Figures

List of Tables

Chapter 1 Introduction

1.1. Background

High intensity focused ultrasound (HIFU, also referred as focused ultrasound surgery or FUS) applies high intensity focused ultrasound energy to locally heat and destroy diseased or damaged tissue through ablation. Ultrasound beam can be focused geometrically through lens or a spherically curved transducer, or electronically by adjusting the relative phases of elements in an array of transducer. Since HIFU penetrates the overlaying tissue safely and only destroys the tissue at focal region deep in the body, it is considered as a non-invasive modality of treatment. Compared with traditional surgical resection and chemotherapy, HIFU provides remarkable advantages. Working with medical imaging technology, HIFU can perform precise tissue ablation with image guidance. The procedure of treatment can be monitored in real time and its result can be evaluated by medical imaging. Nowadays, HIFU has been an important component in cancer therapy and has been applied to treatment such as uterine fibroids, cancers of liver, kidney prostate and breast (Madersbacher *et al.* 2000; Poissonnier *et al.* 2003; Wu *et al.* 2003a; Wu *et al.* 2004a; Wu *et al.* 2004b; Wu *et al.* 2004c; Azzouz & de la Rosette 2006).

However, there are a number of challenges to overcome which obstruct the widespread development of HIFU applications. In abdominal HIFU applications, when the tumours are behind the ribcage, the presence of ribs in focused ultrasound beam path has become a main issue and received considerable critical attention. When applying extracorporeal HIFU through ribs, high acoustic absorption and reflection coefficient of ribs (Goss *et al.* 1978) may lead to tissue damage surrounding the ribs and insufficient energy delivered to target (Kennedy *et al.* 2003; Kennedy *et al.* 2004; Li *et al.* 2006; Cao *et al.* 2012). This not only reduces the efficacy of the treatment but also produce side effects such as the overheating of healthy tissues.

A lot of work has been done to address the ribs issue, especially numerical computing of the focused ultrasound wave propagation in tissues through the ribcage. Some studies applied animal ribs or several pieces of human ribs attaching to a frame, which can partially mimic human anatomical structures. Nevertheless, no research can

provide full effect of the practical ribcage with human anatomical structures on HIFU therapy so far, because to apply human ribs in the HIFU experiment is difficult to achieve due to the restriction of approval by local institutional review board (IRB) (Association 2008). Even it is possible to implement human experiment, the power used on the patient for pre-treatment planning stage must stay lower than that used in the treatment stage for safety reason. Results from this power level, therefore, cannot provide enough information for the treatment planning. The complex structures of the human body and variety of acoustic and thermal properties of bio-tissues result in a challenge in the control and evaluation of HIFU ablation. A prediction of HIFU treatment process through ribcage was required for every individual patient. The determination of patient-specific treatment plan called for investigation using patient's own anatomical structures.

Therefore, for a customized treatment planning, a physical patient-specific ribcage model, which possessed human anatomical structures, was needed to investigate the effect of the presence of ribs on HIFU treatment. For this purpose, a 3D modelling technology was required to convert the image data of the patient to a physical 3D model. With the patient-specific model, full effect of ribcage on HIFU treatment can be investigated before the treatment. Therapeutic parameters of HIFU treatment through ribcage can be determined according to the prediction and optimisation based on the characterisation results.

1.2. Project aims and objectives

The primary aim of this research is to bridge the gap from HIFU technology to clinical applications. This calls for overcoming the challenge of the presence of ribcage located in the focused ultrasound beam in HIFU treatment. In order to investigate the ribcage effect on HIFU application, a physical ribcage model, which possesses human anatomical structures, is needed to implement the HIFU sonication test through the ribcage.

There is a list of objectives to be achieved:

- To develop a rapid image-based modelling technique, which can translate medical image data into 3D models that possess human anatomical structures and can be used as human tissue substitutes

- To determine best materials with similar properties to human tissues for HIFU experiment
- To provide image guidance to determine the focal region, image monitoring to verify the HIFU beam path, and temperature measurement to evaluate the lesion caused by HIFU
- To electrically and mechanically steer the focus or move the HIFU transducer to achieve multi-focus in the experiment
- Finally, to verify the results of phantom study on a cadaver model, which should have human anatomical features and tissue properties

The technical obstacles include reconstruction of the ribcage model with patient anatomical structures, determination of tissue substitutes used in HIFU experiments, image guidance to locate the focus and determine the beam path of HIFU, measures of temperature monitor during HIFU application, and accurate movement of the focal target or ribcage model position using mechanical device.

1.3. Contents of thesis

This thesis consists of six chapters: Chapter 1 and Chapter 2 is on background and literature review; Chapter 3, Chapter 4 and Chapter 5 present the experimental techniques; Chapter 6 concludes the current work and provides the suggestions for future work.

Chapter 1 introduces the background and aim of the study.

Chapter 2, the literature review, starts with development and current status of HIFU technology, and followed by the challenges of the HIFU treatment and current research to overcome the challenges. The HIFU system and technology of tissue mimicking material phantoms are also presented in this chapter.

Chapter 3 focuses on the development of 3D modelling reconstruction of patient-specific ribcage models. Fabrication and characterisation of tissue mimicking materials were conducted and suitable materials were determined according to their acoustic, thermal and elastic properties.

Chapter 4 presents the investigation of the effect of ribcage on focused ultrasound field. Measurements were arranged to determine the acoustic pressure distribution,

acoustic power delivery, and focal temperature elevation with the presence of ribcage models. The setup included different locations to cover both transcostal (with the focused ultrasound beam axis on a rib) and intercostal (with the beam axis between the ribs) position. Results were analysed according to the anatomical structures of the ribcage and verified using the projection of the ribcage on the HIFU transducer.

Chapter 5 depicts HIFU experiment on a cadaver model, which has life-like flexibility and tissue quality. Before applying experiment on cadaver, flow effect on focal temperature change was evaluated on phantom and *ex-vivo* tissues.

Chapter 6 provides the conclusions of the current work and suggestions for future work.

1.4. List of publications

Peer-reviewed Journal Articals:

Cao R., Huang Z., Varghese T., & Nabi G. (2013). Tissue mimicking materials for the detection of prostate cancer using shear wave elastography: A validation study. Medical physics, 40(2), 022903.

Ahmad S., Cao R., Varghese T., Bidaut L., & Nabi G. (2013). Transrectal quantitative shear wave elastography in the detection and characterisation of prostate cancer. Surgical endoscopy, 27(9), 3280-3287.

Cao R., Melzer A., Hoskins P., Nabi G., Huang Z. (2014). Patient-specific 3D Modelling of Focused Ultrasound Surgery (FUS) with Ribcage. Ultrasonics, submitted.

Proceedings:

Cao R., Gao J., Melzer A., Nabi G., & Huang Z. (2012, November). Rapid 3D human ribcage and kidney modeling for transcostal HIFU surgery. In 12th International Symposium on Therapeutic Ultrasound (Vol. 1503, No. 1, pp. 95-100). AIP Publishing.

Gao J., Volovick A., Cao R., Nabi G., Cochran S., Melzer A., & Huang Z. (2012, November). Optimizing sonication protocols for transthoracic focused ultrasound surgery.

In 12th International Symposium on Therapeutic Ultrasound (Vol. 1503, No. 1, pp. 146-151). AIP Publishing.

Cao R., Le N., Nabi G., & Huang Z. Full acoustic and thermal characterization of HIFU field in the presence of a ribcage model. In 13th International Symposium on Therapeutic Ultrasound. AIP Publishing. In Press.

Chapter 2 Literature Review

This chapter reviews the history, development and clinical applications of HIFU in section 2.1. Limitations and challenges of HIFU treatment is discussed together with the current research development to overcome these limitations and challenges in section 2.2. Section 2.3 describes the HIFU system and section 2.4 reviews the tissue mimicking materials used as tissue substitutes in the study of HIFU performance.

2.1. Development and current status of HIFU

2.1.1. Development and clinical experiences of HIFU

HIFU is a modality of therapeutic ultrasound, involving non-invasive methods to direct acoustic energy into the body. By applying high intensity focused ultrasound energy at a selected target, heat deposited within the tight focal volume induces high temperature at focus, which destroys tissues within the body without damaging surrounding tissues. It has been widely used from the 1990s because of the development of imaging techniques for targeting and monitoring. Resent research and development have explored the applications of HIFU, including application in neurosurgery, ophthalmology, gynaecology, urology and oncology.

The first work to investigate the bio-effect of focused ultrasound was reported in 1942 (Lynn *et al.* 1942). A focused ultrasound generator was designed, built, and operated by Lynn et al. and local brain effect in animals produced by focused ultrasound of high intensity was demonstrated. In the 1950s and 1960s, HIFU was used to produce lesions (the damaged tissue volume is commonly known as a 'lesion') in brain (Fry *et al.* 1954; Fry 1955; Fry 1958; Fry & Fry 1960). The first application of HIFU in human was the treatment of Parkinson's disease and painful neuromata reported in 1960 (Ballantine *et al.* 1960; Fry & Fry 1960). However, this treatment was not taken further probably because of the development of the drug L-dopa. What is more, the early studies were limited because technology for precise image guidance and damage monitoring was not available. With the development of image guidance and phased array technology, ultrasound phased array transducer and computed tomography (CT) scans have been used

to achieve a non-invasive adaptive focusing in the transcranial surgery in the early 21st century (Clement & Hynynen 2002; Aubry *et al.* 2003). In 2009, the first report on successful clinical application of transcranial magnetic resonance-guided focused ultrasound (tcMRgFUS) in functional brain disorders shows all treatments were well tolerated, without side effects or neurological deficits (Martin *et al.* 2009).

In 1950s, HIFU was applied in the treatment of ophthalmology (Lavine O 1952). HIFU has been demonstrated to produce lesions in the vitreous, lens, retina and choroid (Purnell *et al.* 1964; Lizzi *et al.* 1978; Coleman *et al.* 1985a; Coleman *et al.* 1985b) in the following years. The laser surgery limited the progress of the research development of HIFU on ophthalmology because of the simplification of the newer technology. Ultrasonic lesions were performed on animal liver and kidney to study the properties of focused ultrasound in tissues by applying HIFU during the 1970s and 1980s (Linke *et al.* 1973; Frizzell *et al.* 1977; Frizzell 1988).

In the late 1990s and the beginning of the 21st century, focused ultrasound was evaluated and clinical used for the treatment of prostate cancer, benign prostatic hyperplasia (BPH) and cancer tumours of the kidney and liver (Mulligan *et al.* 1997; Nakamura *et al.* 1997; Visioli *et al.* 1999; Paterson *et al.* 2003).

Successful clinical trial results were reported on treatment of prostatic diseases in the 1990s (Foster *et al.* 1993; Gelet *et al.* 1993). However, the long-term results were disappointing because 43.8% of patients required a salvage trans-urethral resection of the prostate (TURP) within 4 years (Madersbacher *et al.* 2000). HIFU seems unlikely to be accepted as an alternative in the treatment of prostate cancer, but more studies are under way (Poissonnier *et al.* 2003; Azzouz & de la Rosette 2006). The first experimental study of focused extracorporeal pyrotherapy on treatment of bladder tumours was reported in 1996 and showed 67% of 20 patients with primary tumour had not recurrent tumours (Vallancien *et al.* 1996). Up to 2012, over 15,000 patients with prostate cancer have been treated worldwide (Al-Bataineh *et al.* 2012).

Also in the 1990s, HIFU inducing coagulative necrosis in renal parenchyma and renal tumours has been demonstrated in animal experiments (Chapelon *et al.* 1992; Adams *et al.* 1996; Watkin *et al.* 1997). More clinical data of treatment of abdominal tumours was reported in the 2000s (Wu *et al.* 2001a; Wu *et al.* 2001b; Kennedy *et al.*

2004; Wu *et al.* 2004c). From these trials, extracorporeal treatment of hepatocellular carcinoma (HCC) with HIFU proved to be safe, effective, and feasible. Kidney tumours were not ablated as reliably as liver tumours, but encouraging results were reported in China (Wu *et al.* 2003a) and in a Western population (Illing *et al.* 2005). Flank pain disappeared in 9 of 10 patients with advanced stage renal cell carcinoma after HIFU treatment (Wu *et al.* 2003a).

The first clinical trial of magnetic resonance-guided focused ultrasound surgery (MRgFUS) for uterine leiomyomas was performed with a clinical MR imaging–compatible focused ultrasound system ExAblate 2000 (Tempany *et al.* 2003). Patients' response to MRgFUS was assessed and results showed MR imaging–guided focused ultrasound led to surgery symptomatic improvement, sustained to 12 months after treatment in the following research (Fennessy *et al.* 2007). 119 consecutive patients with 187 uterine fibroids were treated with HIFU using imaging and histopathologic examination in China from May 2004 to June 2005 (Ren *et al.* 2007). Imaging and histopathologic evidence directly validate HIFU ablation as an effective treatment of uterine fibroids.

HIFU applications were also investigated in the treatment of bone tumours (Wu 2006; Gianfelice *et al.* 2008; Liberman *et al.* 2009) and breast cancer (Wu *et al.* 2003b; Wu *et al.* 2004a). In the 2000s, a group in Chongqing, China, led by Dr. Feng Wu et al., has demonstrated the focused ultrasound surgery to be safe, effective and feasible in over one thousand patients with liver cancer, breast cancer, malignant bone tumour, soft tissue sarcoma and other malignant tumours (Wu *et al.* 2001a; Wu *et al.* 2004a; Wu *et al.* 2004c). In the study of pain palliation in patients with bone metastases treated using ExAblate system, 72% of the patients reported a significant pain reduction (Liberman *et al.* 2009). In early Chinese clinical experience (Wu *et al.* 2004c), breast cancer patients who received breast conservation treatment with FUS were alive in the follow-up time (range 10 to 36 months) and all but one was disease-free.

Other studies with very small numbers of patients include pancreatic (Wu 2006), testicular cancer (Kratzik *et al.* 2006) and thyroid nodules (Esnault *et al.* 2011). HIFU has been used in lipolysis recent years (Shalom *et al.* 2013) and proved to be well tolerated and safe by evaluating the complications, blood tests, and urine analysis of the patients.

2.1.2. Safety issues of clinical applications of HIFU

The risk factors in HIFU treatment which may contribute to post-ablation complications must be taken into account and optimised. Local pain, postoperative fever, pelvic hematoma and skin burns have been reported as the complications of HIFU treatment (Stewart *et al.* 2003; Kennedy *et al.* 2004; Wu *et al.* 2004c; Li *et al.* 2007). The most severe treatment-related adverse events have been transient pain (7 in 11) and superficial skin burns (3 in 11) in the clinical trial using JC HIFU system (Chongqing Haifu Medical Technology Co. Ltd., Chongqing, China) in Oxford, UK (Kennedy *et al.* 2004). Based on the results of clinical applications of HIFU in cancer, complications were summarised in a cancer treatment review paper (Al-Bataineh *et al.* 2012) from a clinical point of view, as shown in Table 2.1.

Table 2.1 Complications of HIFU therapy in different applications (Al-Bataineh *et al.* 2012)

Object of HIFU therapy	Complications
Prostate cancer	Urinary retention, urinary infection, urethral stenosis, dysuria, recto-urethral fistula
Liver tumours	Skin redness and burns, biliary obstruction, symptomatic pleural effusions , fistula formation
Pancreas tumours	Tumour-duodenal fistulas, duodenal stent, a third-degree burn of the anterior abdominal wall
Bone malignancies	Third-degree skin burn, peripheral nerve damage, bone fracture, ligamentous laxity, epiphysiolyses, secondary infections

Two severe complications were reported including superior mesentery arterial infarction (patient with the superior mesentery artery running out from the centre of tumour) and perforation of the terminal ileum (patient with metastatic tumours close to the terminal ileum) (Li *et al.* 2007).

Tolerance of HIFU ablation in patients with HCC was investigated (Cheung *et al.* 2012). To identify factors that affect the tolerance, the risk factors for patients developing

serious complications were examined using univariate analysis. Parameters included patient age, preprocedure levels of serum bilirubin, albumin, alanine transaminase and aspartate transaminase, platelet count, international normalised ratio, total diameter of HCC, ablation time, ablation energy, presence of cirrhosis on imaging, and comorbid illness. Results showed that HIFU ablation is a generally well-tolerated treatment modality. Patient age is the only factor that was found to be significant in HIFU intolerance in Cheung et al.'s study.

In terms of HIFU device technology, the potential risks resulting from the high power levels required for effective therapy, should be considered. The safety issues for HIFU transducer design was reported by Fleury et al. (Fleury *et al.* 2005). They listed the failure modes that may present risk to the patient, including over- (or under-) estimation of acoustic power, lack of control of the acoustic beam, lack of localization of the targets to be treated, transducer damage or failure, and error in operation. Meanwhile, suggestions were given to ensure safe use.

2.2. Challenges in HIFU treatment of abdominal tumours

Despite HIFU has a lot of advantages, the application of HIFU has challenges which have to be taken into consideration. In general, structures filled with air and bones in the pathway of the ultrasound wave, blood flow, and organ motion are the main challenges, which are described in section 2.2.1. The development of current research in HIFU treatment through ribs will be illustrated in section 2.2.2.

2.2.1. Challenges

In the treatment of abdominal organs, ribs as obstruction in the pathway of focused ultrasound may affect the efficacy of the treatment and lead to undesired interference in healthy tissues (Kohrmann *et al.* 2002; Kennedy *et al.* 2003; Wu *et al.* 2004b; Li *et al.* 2006). The effect of a ribcage on focused ultrasound field has been investigated and results show 50% acoustic pressure reduced using ribcage model and 73% decreased using porcine ribs at transcostal propagation (Cao *et al.* 2012). Because of the absorption of the acoustic energy by the interposed ribs, it was not successful to apply HIFU on the upper pole of the kidney (Kohrmann *et al.* 2002). High absorption coefficient of the bones

(Goss *et al.* 1978) can also lead to overheating on the ribs and surrounding tissues (muscle, fat and etc.) during the treatment. There is an unacceptable temperature rise on the rib surface if the rib position approaches the focal plane (Kennedy *et al.* 2003). Experiments on goats indicate that obvious damage resulted from ribcage was found on the skin surface, ribs and corresponding liver surface (Li *et al.* 2006). Clinical results of skin damage during liver HIFU treatment also have been reported (Kennedy *et al.* 2004; Wu *et al.* 2004a; Li *et al.* 2007). The rate of skin burn has decreased (less than 5%) compared with that at the beginning of the clinical trial (10 - 20%), because of the improvement of performing HIFU ablation and evaluating damaged-skin changes on real-time ultrasound imaging (Wu *et al.* 2004a). Apart from the effect of the ribcage, ultrasound cannot propagate through air filled structures. HIFU therefore is not suitable for damaging the tumours located in lung or bowel.

The effect of blood perfusion on the ablation of abdominal organs using HIFU has been considered as another challenge in HIFU application, because the heat transfer from warmer regions to cooler regions affects the heat deposition to the focus. Animal experiments have been applied to investigate the effect of blood perfusion on lesion size (Chen *et al.* 1993a) and the effect of flow rate on total energy consumption of the target tissues (Bu *et al.* 2013). The lesion size obtained with normal blood flow on the livers of anaesthetized rats was significantly smaller than that with reduced blood flow by ligating hepatic artery and portal vein (Chen *et al.* 1993a) (hepatic blood flow was reduced by 98% due to the ligating), when the exposure time was longer than 3 s. The energy consumption reduced with the decrease in perfusion rate of dual-vessel perfusion, of portal vein perfusion alone, and of hepatic artery perfusion in an isolated porcine liver perfusion model (Bu *et al.* 2013). Phantom experiment also confirmed that the blood flow near HIFU beam significantly reduced the HIFU efficacy (Hariharan *et al.* 2007; Dasgupta *et al.* 2009).

Organ motion due to respiration during the treatment is another limitation and could compromise treatment efficacy. When significant movements occur, the ultrasound beam could focus on surrounding tissues and lead to overheating on healthy tissues and insufficient energy delivery to the target. The quantity of organ motion has been reported in several studies. For pancreas, the average respiratory excursion was 1.8 cm in the supine position, 1.9 cm when prone, and 2.2 cm in the lateral decubitus position (Bryan

et al. 1984). Abdominal organs can move up to 20 mm during a respiratory cycle, reaching speed up to 15 mm/s (Ross *et al.* 1990; Davies *et al.* 1994).

2.2.2. Current research in HIFU treatment through ribcage

Several techniques have been developed to investigate the effect of the ribs, to enhance the efficacy of HIFU and to avoid or minimize overheating of the ribs and surrounding tissues. To minimize the overheating on ribs and surrounding tissues from clinical point of view, partial rib resection has been used to create a better acoustic window for therapy when no other treatment options are available (Wu *et al.* 2004b; Zhu *et al.* 2009). There was no significant difference in liver and renal function of the patients before and one week after partial rib removal and no severe skin burn occurred in this HIFU treatment. However, this approach has potential morbidity and diminishes the attributed advantages of HIFU as a non-invasive therapy.

More numerical studies were presented to study the ultrasound filed and address this issue (Liu *et al.* 2007; Khokhlova *et al.* 2010; Liu *et al.* 2010; Gelat *et al.* 2012b; Gao *et al.* 2014). The ultrasound focus could be split by the ribs as obstacle in the pathway of the ultrasound beam. Focus splitting associated with the propagation of focused ultrasound through the ribcage has been investigated theoretically (Khokhlova *et al.* 2010). Khokhlova et al. have shown that the variation in the intensity at focus in the presence/absence of the ribcage depends on three parameters: the position of the radiator axis relative to the middle of the intercostal space, the ratio of the width of the intercostal space to the period of the spatial structure of ribs, and the number of ribs within the beam aperture. They are for models of an idealized ribcage consisting of a regular array of reflectors. The maximum intensity at the focus is reached when the beam area is obscured by ribs is minimal.

In order to reduce the deposition energy at the ribs, medical images were applied to compute the deactivated elements of the transducer in the HIFU focusing through ribcage (Liu *et al.* 2007; Liu *et al.* 2010; Quesson *et al.* 2010). Based on the relative position of the focus and the ribs, as identified from anatomical image data, elements that covered by the shadow of the ribs were deactivated. Compared with all elements active, benefit of deactivating selected elements for avoiding overheating at ribs and ensuring enough temperature for ablation at focus was demonstrated.

In recent years, the CT scan data of a human ribcage was used instead of the regular strips as the topology in the computational simulation (Gelat *et al.* 2011, 2012a; Gelat *et al.* 2012b). This was a step forward to mimic the realistic human structures in the HIFU field. However, the practical experiment was still required to validate the computational simulation.

Gao et al. (Gao *et al.* 2014) investigated the factors affecting the acoustic beam patterns with propagation of focused ultrasound through the ribcage by experimental exploration using regular sectional absorbers (Aptflex F28, Precision Acoustics, Dorchester, Dorset, UK) instead of the ribcage and by numerical study using a 2D model based on the absorbers used in experimental setup. The rib substitute with rectangular cross section was also used in computational study (Lin *et al.* 2013) and experimental study (Qiao *et al.* 2013). Lin et al. calculated the propagation of focused ultrasound in tissue with rib-like structures. Qiao et al. applied the acoustic absorber strips to validate their simulation results of turning off the elements blocked by the ribs. The acoustic absorber material possessed similar acoustic properties to the ribs and the structures as strips were close to the ribcage.

Some researches applied animal ribs in the focusing experiment using a therapeutic phased array combined with simulation (Aubry *et al.* 2008; Bobkova *et al.* 2010). Two approaches were proposed by Bobkova et al. (Bobkova *et al.* 2010), one based on geometric acoustics and the other accounting for diffraction effects associated with propagation through the ribcage were tested theoretically and experimentally. The ability to produce thermal lesions with a split focal pattern in *ex-vivo* porcine tissue placed beyond the rib phantom was also demonstrated. Time reversal method (Aubry *et al.* 2008) was utilised to decrease the effect of the ribs and a fresh porcine ribcage was used in the experiment. However, as time reversal required an acoustic source at the target location, which made this technique invasive, it can hardly be used in HIFU treatment through the ribs. Pigs under anesthesia were selected as the target in the transcostal (Marquet *et al.* 2011) and intercostal (Quesson *et al.* 2010) HIFU ablation in the liver.

To address the numerical predictions applying no experimental practice with the structure of human anatomy, human ribs were also used by attaching three human ribs to a frame in the experiment (Cochard *et al.* 2009; Marquet *et al.* 2011). However, it is difficult to fully establish the human ribcage structures with separated human ribs. Other

experimental data reporting on the ribs and surrounding soft tissues so far has been limited to animal ribs or tissue mimicking phantoms fabricated for this purpose. The reported data may not be applicable to humans, as anatomy and structure of ribs and surrounding structures have little or no resemblance to real patients.

A wide variation exists in anatomical features of ribs in clinical practice (Sedlin *et al.* 1963; Dansereau & Stokes 1988; Abrams *et al.* 2003; Bellemare *et al.* 2003). The geometric structure of the ribcage varies within each rib and between ribs and is affected by factors such as age, sex and disease (Sedlin *et al.* 1963; Bellemare *et al.* 2003). For the cross section area of rib cortex (Sedlin *et al.* 1963), it increased until skeletal maturity. The area then decreased sharply until 35 years old and this decline in area became less dramatically after age 35. These values reached minimum in the eighth decade, which was approximately 25% less than those of the early twenties. In the sex differences study (Bellemare *et al.* 2003), the mean ribcage size was smaller in females than males in total 40 subjects (21 normal male and 19 normal female). The cross sectional geometry of five non-embalmed human cadavers (59 ± 13 years, 71 ± 30 kg, 3 male, 2 female) was measured (Abrams *et al.* 2003). Results show that the standard deviation of the cross section area is approximate half of the mean value (no specific SD was given). This indicates the data points could be spread out over a large range of values. Overall, there are significant differences in rib cross section area among humans. The data from phantoms and animals may not be sufficient to plan HIFU therapy. A patient-specific reconstructed model that fully possesses human anatomical structures is required to investigate the ribcage effect on each individual patient and determine the customized treatment plan.

2.3. HIFU system

HIFU system provides focused ultrasound therapy transducer and solutions of locating the target and monitoring the process of the treatment. During procedure of HIFU application, anatomical feature is acquired via medical imaging modality such as MRI and ultrasound imaging. The imaging modalities are also used for monitoring the process of the treatment. Characterisation of the HIFU system plays an important role in the development of the pre-surgical planning. To ensure the safety and efficacy of HIFU treatment, a fundamental knowledge of the acoustic field and energy output of HIFU

system is required to predict and control the size and the location of the focal lesions. This section reports the physical principles of HIFU and the characterisation of HIFU system.

2.3.1. Physical principles of HIFU

The piezoelectric effect was first demonstrated in 1880 (Curie & Curie 1880). The piezoelectric material will produce an internal mechanical strain when an electrical field is applied, which can lead to generating ultrasound wave towards the axis of the ultrasound transducer. For HIFU transducer, to generate a tight ellipsoid lesion at focus curved bowl or multi-element phased array are needed to produce ultrasound beams, as shown in Figure 2.1.

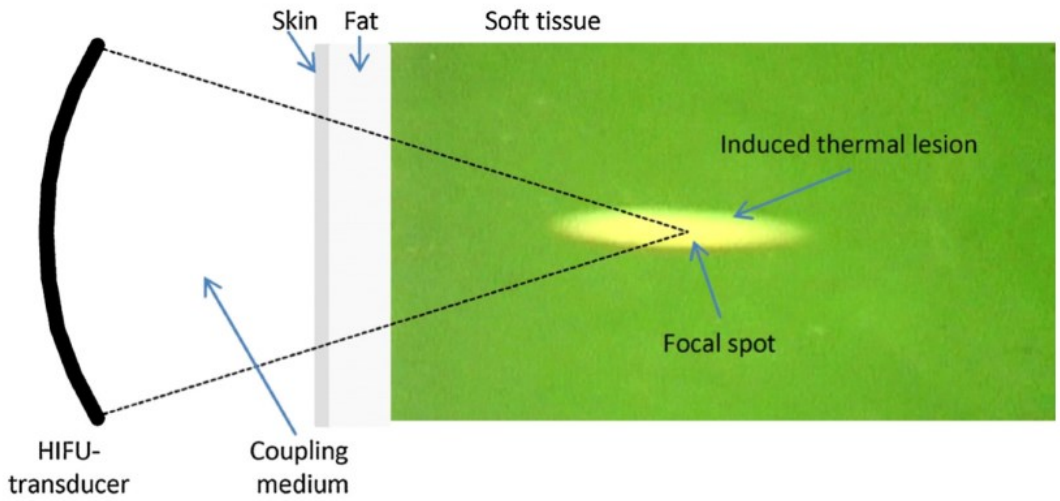

Figure 2.1 Principle of HIFU ablation (Jenne *et al.* 2012)

The ultrasound wave propagates through coupling medium and multi-layer tissues before reaching the focal spot (Figure 2.1). At each tissue interface, part of the ultrasound wave will be reflected with the rest of them transmitting. If the acoustic properties are similar at interfaces, the transmission coefficient is close to unity. On the other hand, the regions with different acoustic properties from tissues (e.g. between transducer and skin) reflect, absorb and scatter the incident wave, resulting in a reduction of acoustic intensity in the direction of ultrasound propagation. For an extracorporeal HIFU treatment,

therefore, coupling the ultrasound energy to the skin surface is required. The coupling medium could be a water balloon, coupling gel, or other suitable liquid path, because most soft tissues in the human body have acoustic properties similar to those of water or water based gel.

For most tissues, the attenuation coefficient, used to describe the loss in incident acoustic energy in a medium, is related to the ultrasound frequency (Hill *et al.* 2004). According to the research at the beginning of 21st century, the attenuation coefficient of most tissues increases with heating and HIFU ablation (Clarke *et al.* 2003; Zderic *et al.* 2004). There is little absorption of ultrasound during the propagation in the pathway by the homogeneous tissue with a proper coupling medium. This causes the heating rate of the normal tissue less than the cooling rate in the beam propagation path. Therefore, HIFU does not heat the tissue out of the focal region, which avoids intervening normal tissues. The acoustic energy deposition occurs only at the focus and results in local temperature rise to cause tissue necrosis. As a result, by using HIFU system, the focal region obtains the most energy deposition to kill the cells whereas in the sharply demarcated surrounding tissue there is no evidence of cell damage (Chen *et al.* 1993b).

2.3.2. HIFU devices

In the early years, focused ultrasound was generated from quartz crystals which were either concave in shape (Lynn *et al.* 1942) or were planar with polystyrene lens placed in front of the vibrating crystal for focusing (Fry *et al.* 1954). Quartz has been replaced by the low loss forms of lead zirconate titanate (PZT). This material may be used in the form of a concave bowl shape (Warwick & Pond 1968) or as a plane disk/plastic lens combination (Terhaar *et al.* 1989). A single element HIFU transducer (transducing electrical to mechanical energy) normally contains a piezoelectric element in bowl shape, backing layer, casing and electrical connection. In Figure 2.2, an electric field from electrical connection of high-frequency alternating current can be applied to the piezoelectric element through its front and back faces. The piezoelectric material in spherical shape vibrates and generates a focus proximal to its centre of curvature. The backing layer is located behind the piezoelectric element to prevent excessive vibration.

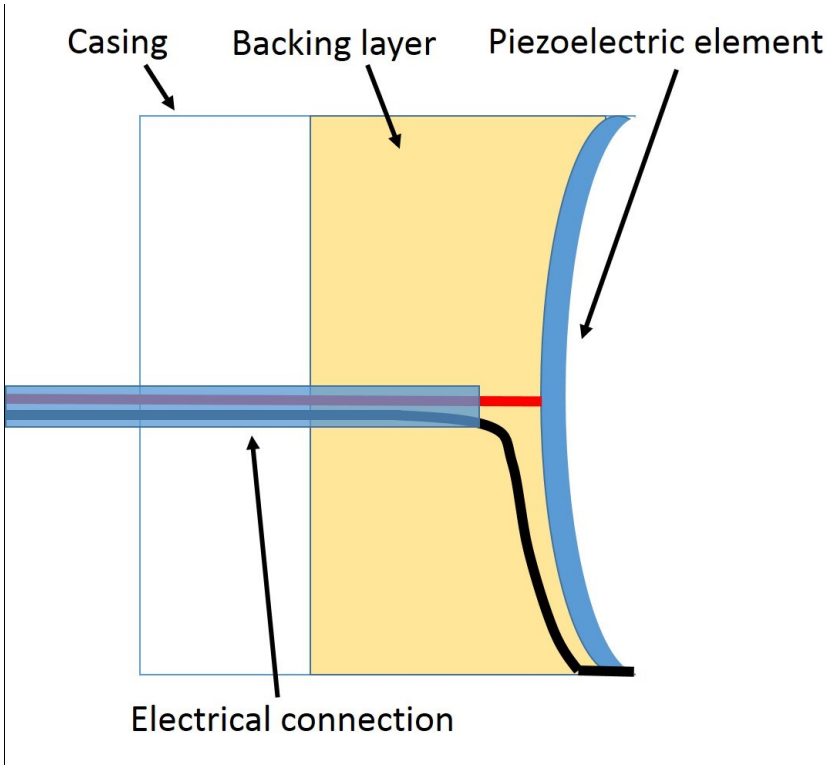

Figure 2.2 Cross-sectional view of the schematic of a HIFU transducer showing its components

In the 1990s, phased array technology for HIFU applications has led to the design of transducer that allows electronic ultrasound beam steering and controlling the focal size without physically moving the transducer (Hynynen *et al.* 1996; Wan *et al.* 1996). Because the phased array transducer is made of multiple small elements, each of which can be pulsed independently, the ultrasound beam can be steered electronically by shifting the phases of the ultrasound waves radiated by each element (Figure 2.3).

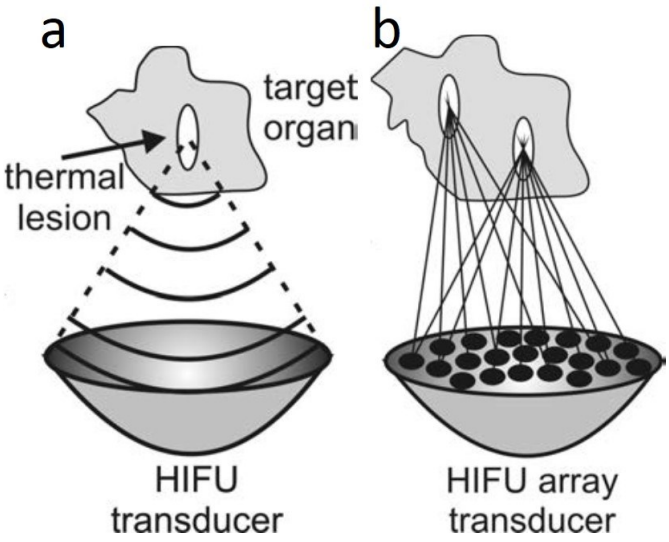

Figure 2.3 Comparison of (a) single element and (b) phased array transducer (Khokhlova & Hwang 2011)

In HIFU treatment, the focused ultrasound wave penetrates a coupling medium (e.g. a water balloon) and overlaying tissue to focus in the targeted area. A small volume of focal tissue is then heated rapidly and protein is denatured due to the high local concentration of acoustic energy. The skin and overlaying tissues are unaffected or show only a negligible temperature rise.

For the treatment of a larger tumour, single lesions have to be repeated without gaps to cover the entire tumour tissue. According to the principle in conventional surgery, the extent of HIFU should include the tumour lesion and its marginal tissue about 1.5 - 2.0 cm around the tumour (Wu *et al.* 2003b; Wu *et al.* 2004c). This is to ensure the ablation of any adjacent microsatellites and to obtain a sufficient tumour-free margin. The focus of HIFU system is usually 1 to 3 mm in width and about 10 mm in length according to the -6 dB ultrasonic beam size (Zhou 2011). The HIFU therapy is a time consuming procedure, because a lot of single sonications are required to allow the ablation of a large tumour and a defined cooling time is necessary to prevent adjacent healthy tissue from heat deposition and overheating between two single sonications. This geometrical size of focal region requires the movement of the focus to completely cover the larger treatment target. For scanning the target with focus, HIFU system should be able to physically move or rotate the transducer with a fixed focus, or use phased array technology to electrically steer the focus of a multi-element HIFU transducer.

To allow accurately locating the target tissue, focused ultrasound devices require imaging guidance to implement the ablation within the body. MRI is capable of providing images with high resolution as well as temperature measurement. However, MRI guidance is expensive and not suitable for all patients, such as patients who have pacemaker, artificial joints, or metal artery stent. Moreover, the HIFU device must be specially designed for compatibility and cannot contain ferromagnetic metals for usage with MRI. In comparison, ultrasound guidance is more convenient than MRI guidance and compatible with the HIFU device. It allows real time imaging during the treatment, but the image quality of ultrasound imaging is not as good as MRI. Another drawback of ultrasound guided HIFU is the lack of monitoring of the temperature. Both MRI and ultrasound imaging guidance possess advantages and disadvantages, therefore, patient-specific circumstances should be taken into consideration to determine a suitable treatment plan.

With the capability of damaging a selected region of tissue with minimal effects to surrounding tissues, HIFU has been applied to treat target tissues located within the body and used to manufacture medical devices for the treatment of those diseases. Modern HIFU devices operate at focal intensity levels from 1000 W/cm^2 to greater than 25000W/cm^2 *in situ* (Canney *et al.* 2008). The focused ultrasound tumour therapeutic system Model-JC and Model-JC 200 (Chongqing Haifu Medical Technology Co. Ltd., Chongqing, China) have been developed in China and are widely used for liver tumour and uterine fibroids treatment (Wu *et al.* 2004b). Another focused ultrasound system guided by diagnostic ultrasonography is HIFUNIT 9000 tumour therapy system (Shanghai Aishen Technology, Shanghai, China). An MRI guided system, ExAblate 2000 (InSightec, Tirat Carmel, Haifa, Israel), has been approved by Food and Drug Administration (FDA) for treatment of uterine fibroids in October 2004. This system performed with MRI for HIFU sonication, image guidance and temperature monitoring. A clinical trial of uterine surgery using ExAblate 2000 was reported in 2003 (Tempany *et al.* 2003). ExAblate 2100 for bone treatment and ExAblate 4000 for transcranial surgery have been undergoing the evaluation of safety and effectiveness. Sonablate (SonaCare Medical, NC, USA) and Ablatherm (EDAP-TMS, Lyon, France) are transrectal devices for the treatment of benign prostatic hyperplasia and prostate cancer (Madersbacher *et al.* 1994; Chaussy & Thüroff 2000).

2.3.3. Characterisation of HIFU field

HIFU system has the ability to generate high temperatures within tissue guided by medical imaging modality. However, different route of the ultrasound wave and varied tissue properties require different levels of the acoustic power utilised for diseased tissue ablation. To ensure the energy delivering to correct location using accurate energy level, it is necessary to evaluate the acoustic power carried by the ultrasound wave and monitor the procedure of wave propagation before and during the treatment. Therefore, accurate measurement and characterisation methods of the HIFU system are required. The most commonly used measurement methods of HIFU fields are the hydrophone to determine focal acoustic pressure distribution and the radiation force balance (RFB) to determine total output acoustic power.

2.3.3.1. Ultrasound beam profile characterisation

The acoustic intensity distribution as a function of position within planes of interest can provide a visualised profile of the ultrasound beam. Ultrasonic needle hydrophone and polyvinylidene fluoride (PVdF) membrane are widely used to characterise ultrasound fields. However, hydrophone techniques are limited to relatively low intensities to avoid sensor damage. Measurements were thus carried out at low output level and the pressure distribution at high output levels could be extrapolated based on linear propagation model (Hill *et al.* 1994). Stepper motors scanned the hydrophone across a plane in the focal region of the transducer (perpendicular to the direction of the ultrasound beam). The focal region was defined as the volume enclosing the full width half maximum dimensions (Hill *et al.* 1994; Kun & Wan 2004). Hill et al. proposed that spatial average linear intensity (I_{sal}) was determined by the intensity spatially averaged over the area enclosed by the half-pressure-maximum contour in the focal plane under linear conditions.

Fibre optic hydrophone is another tool to measure acoustic pressure. It was originally developed for measurement of shock waves of high pressure amplitude in lithotripter acoustic output field (Staudenraus & Eisenmenger 1993; Wurster *et al.* 1994). The sensitive region determined by the small size of fibre diameter, which is typically a few microns, offers the prospect of providing acoustically small element sizes. Infrared (IR) thermography can be used to gain qualitative information about ultrasound fields

from the heating pattern within the absorbing material (Adam & John 2010). One of the drawbacks of IR thermography technique is that the ultrasound must be incident on an acoustically reflective air interface, because of the presence of the air interface between the IR camera and the heated surface.

2.3.3.2. Nonlinearity

For an ultrasound wave at intensity (order of 1000 W/cm^2) typically used in HIFU and at higher intensity used in newer HIFU devices (order of 10000 W/cm^2) (Canney *et al.* 2008), it increases local temperature and local speed of sound in a compressible material. As a harmonic sine wave propagates through a nonlinear homogeneous media, it provides compressive and tensile forces during the corresponding phases. The wave travels faster during the high pressure phase of the oscillation than during the lower pressure phase. The wave self-distorts as shown in Figure 2.4. These acoustic nonlinear effects lead to the appearance of additional higher harmonics in the initial wave spectrum, the formation of shock fronts in the wave profile, and correspondingly, the increase in the absorption of the ultrasound wave energy and in the efficiency of tissue heating (Filonenko & Khokhlova 2001). In this study, the characterisation of focused ultrasound beam profile was investigated using low power input in linear wave propagation conditions.

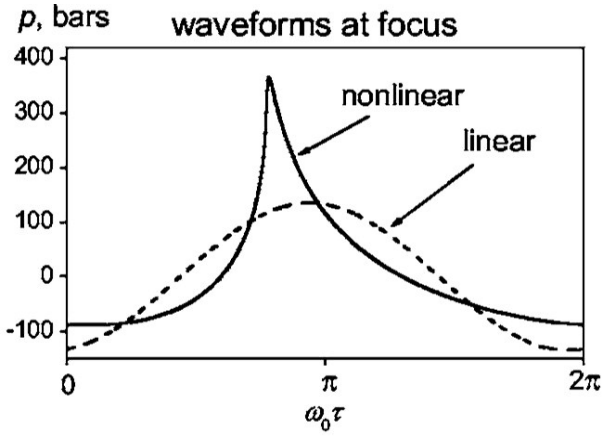

Figure 2.4 Numerical results of modelling HIFU in gel with (solid lines) and without (dash lines) accounting for the effects of nonlinear propagation: axial waveforms at the focus (Filonenko & Khokhlova 2001)

2.3.3.3. Acoustic power

The ultrasound output power of a HIFU system is a key parameter to estimate the efficiency of the system and describe the energy delivery at focal target during clinical treatment. It is typically characterised by measuring the radiation force on a target which intercepts the entire field. RFB has been widely used to measure ultrasound power as current primary standard method (Greenspan *et al.* 1978; Fick 1999; Beissner 2002). If the target is large enough to intercept the entire ultrasound beam and is connected to a force-measuring device, the change in force with the transducer power-on is proportional to the acoustic power contained in the ultrasound beam (Shaw & Hodnett 2008). If an absorbing target was used, the acoustic power can be obtained by equation (2.1):

$$P = cmg \tag{2.1}$$

where P is the acoustic power, m the change in mass, g the acceleration of gravity and c the temperature-dependent speed of ultrasound in the coupling medium (usually water). Some types of target have been designed for RFB, including acoustic absorbing material target, reflecting target and brush target made by placing long flag plastic fibres (Hynynen 1993; Maruvada *et al.* 2007). Another way to determine the acoustic power is the buoyancy method (Shaw 2006; Shaw 2008; Srinath & Adam 2012), which has been validated using a radiation force method at frequencies of 1 MHz and 3 MHz for acoustic powers in the range 1 W to 350 W, and the extended method is validated in the frequency range 3.151 MHz to 9.541 MHz using an improved target and applied powers in the range 100 mW to 1 W.

2.4. Tissue mimicking material phantoms

The characterisation of HIFU field requires phantoms to mimic the ultrasound propagation through tissues. The phantoms are made of tissue mimicking materials (TMMs), which possess similar properties to biological tissue and can provide a reproducible medium for the studies of ultrasound field under known propagation conditions. The TMMs mainly consist of water and can be shaped into arbitrary solid structures. Moreover, the TMM phantoms can be used as the focal target to evaluate the results of HIFU treatment. The desired HIFU phantom as a tissue substitute should possess similar density, acoustic properties thermal properties and elastic properties to

human tissues (King *et al.* 2011). This section reviews the applications and properties of TMMs.

2.4.1. Applications of TMM phantoms

TMM phantoms bridge the gap in translational research without the need of direct experimentation on humans or animals. The advantage of phantoms is that idealized tissue models can be constructed with well-defined acoustic properties, dimensions and internal features (Culjat *et al.* 2010). With these benefits, the propagation of ultrasound can be better understood or predicted. To develop diagnostic imaging technologies, the phantoms designed with TMMs are essential for assessing the imaging devices, and for training and research. To determine the safety and effectiveness of therapeutic HIFU devices, it is necessary to characterise the devices by developing TMM phantoms for visualizing the temperature change and coagulated necrosis caused by HIFU.

Various kinds of TMMs have already been used in ultrasound imaging research, HIFU dosimetry investigation, specific organ fabrication etc., such as gelatine, agar, silicone, polyvinyl alcohol (PVA) gel and polyacrylamide (PAA) gel (Alexei *et al.* 2003; Surry *et al.* 2004; Takegami *et al.* 2004; Zell *et al.* 2007). Agar and gelatine based phantoms are easily fabricated and can achieve a range of acoustic properties by adding scattering particles, but they can be easily damaged. Silicone is insensitive to rough handling compared with agar and gelatine phantom and can be stored for months or even years. PVA based phantom has high structural rigidity but its fabrication procedure is time consuming. PAA is highly carcinogenic and neurotoxic, which may limit PAA phantom being widely used.

The research of ultrasound phantoms has been started since the end of the 1970s (Madsen *et al.* 1978). TMMs for ultrasound imaging and for assessing ultrasonic imaging system performance have been investigated in the following years (Madsen *et al.* 1980; Madsen *et al.* 1982a; Madsen *et al.* 1982b, c). Agarose (Mitchell *et al.* 1986; Kraft *et al.* 1987; Howe 1988) and PVA gel material (Mano *et al.* 1986) has been used as a relaxation modifier in MRI phantom since the 1980s. Ni ions and Cu ions were doped into the agarose gel phantom to further affect their proton relaxation characteristics (Mitchell *et al.* 1986; Kraft *et al.* 1987; Howe 1988). T1 (spin-lattice relaxation time) depends more on copper ions than on agarose, and T2 (spin-spin relaxation time) depends more strongly

on agarose than on copper ions (Mitchell *et al.* 1986). MRI phantom equivalent to human tissues has been reported in 2005 (Kato *et al.* 2005). The ingredients of these phantoms are carrageenan as the gelling agent, $GdCl_3$ as a T1 modifier, agarose as a T2 modifier, NaCl as a conductivity modifier, NaN_3 as an antiseptic, and distilled water. Multi-imaging phantoms have been developed in the recent years, because three dimensional multi-modality images used in combination with one another might enhance the effectiveness of treatment planning (D'Souza *et al.* 2001; Madsen *et al.* 2003).

Another application of phantoms is for HIFU dosimetry studies, which allows the visualisation of temperature rise and lesion formation. Polyacrylamide hydrogel mixed with egg white protein was reported as an optically transparent HIFU TMM (Takegami *et al.* 2004). A thermally sensitive indicator protein Bovine Serum Albumin (BSA) with polyacrylamide hydrogel was introduced as a phantom for HIFU exposures (Lafon *et al.* 2001; Lafon *et al.* 2005). However, polyacrylamide with egg white material is toxic and non-reusable because of protein denaturation. For HIFU exposure experiment, it is important that the material should be repeatable and stable under HIFU environment. A nontoxic and reusable hydrogel with dispersed oxide particles and other chemicals has been developed for the acoustic and thermal characterisation of HIFU devices (King *et al.* 2011).

Manufactured organ phantoms are widely used because of their reduced cost, long-time stability, and non-existent ethical regulatory requirements (Opik *et al.* 2012). A wide range of organ phantoms have been reported, such as prostate phantom, liver phantom, kidney phantom and breast phantom. Prostate tissue mimicking materials for multi-imaging modality (D'Souza *et al.* 2001) and for the detection of prostate cancer using shear wave elastography (Cao *et al.* 2013) have been reported. High fidelity liver and kidney phantom organs have recently been used to validate robotic surgical system performance (Opik *et al.* 2012). A phantom consist of degassed water and an open cell sponge was created to simulate the echotexture of liver (Hopkins & Bradley 2001). Breast phantoms were fabricated using oil-in-gelatin dispersions for testing elastography systems (Madsen *et al.* 2006). To mimic internal structures such as tumour in the organs, simple or complex TMM targets were embedded within the phantoms (Skretting *et al.* 2010; Chmarra *et al.* 2013).

Apart from the manufactured phantoms, there are a number of commercial TMM phantoms available in the market which can provide more precise tissue simulation. Those phantoms include Zerdine (CIRS Inc., CT, USA), Gammex ultrasound phantom (GAMMEX Inc., WI, USA), ATS rubber-based phantom (ATS Laboratories Inc., Bridgeport, CT, USA), and Daily Quality Assurance (DQA) gel phantom (ATS Laboratories Inc., Bridgeport, CT, USA). The TMM phantoms are also available from other companies, such as Limb & Things (UK), Blue Phantom (WA, USA), The Phantom Laboratory (NY, USA), and Supertech (IN, USA).

2.4.2. Acoustic properties of TMMs

To mimic human tissue in ultrasound research, the substitute materials should possess acoustic properties similar to the tissues. This allows the ultrasound wave propagating in a tissue-like circumstance. The relevant parameters of acoustic properties mainly contain the acoustic impedance, the speed of sound, and acoustic attenuation.

TMMs with a broad range of acoustic parameters are needed and the TMMs could be mixed in order to achieve the desired properties similar to the different types of tissues, because the acoustic properties of real tissues are not constant among people, or even in different parts of tissues within a human body (Culjat *et al.* 2010).

A wide range of acoustic attenuation coefficient was found in the measurement results of normal (fatty) breast tissue (Bamber 1983). Approximately 3 dB/cm was the highest attenuation coefficient value at 1 MHz, while the lowest value was less than 1 dB/cm (No specific attenuation coefficient values were given in the original reference). This range became larger with the increase of the frequency of the ultrasound applied. Previously reported acoustic properties of mammalian tissues and human tissues (Goss *et al.* 1978; Culjat *et al.* 2010) are summarised in Table 2.2. The average acoustic velocity in soft tissue was reported as 1561 m/s in the range of 1478 m/s (fat) and 1595 m/s (liver).

Table 2.2 Acoustic properties of tissues (Culjat *et al.* 2010)

Material	Velocity (m/s)	Density (kg/m^3)	Attenuation (dB/cm MHz)	Acoustic Impedance (MRayl)
Air	330	1.2	-	0.0004
Blood	1584	1060	0.2	1.68
Bone, Cortical	3476	1975	6.9	7.38
Bone, Trabecular	1886	1055	9.94	1.45
Brain	1560	1040	0.6	1.62
Breast	1510	1020	0.75	1.54
Cardiac	1576	1060	0.52	1.67
Connective tissue	1613	1120	1.57	1.81
Cornea	1586	1076	-	1.71
Dentin	3800	2900	80	8.0
Enamel	5700	2100	120	16.5
Fat	1478	950	0.48	1.40
Liver	1595	1060	0.5	1.69
Marrow	1435	-	0.5	-
Muscle	1547	1050	1.09	1.62
Tendon	1670	1100	4.7	1.84
Soft tissue (average)	1561	1043	0.54	1.63
Water	1480	1000	0.0022	1.48

For bones, 3360 m/s and 20 dB/cm were reported for skull bone at 1 MHz (Hendee & Ritenour 2003). For trabecular (cancellous) bone specimens, the speed of sound was in the range 1500 m/s to 1650 m/s (Laugier *et al.* 1997). The mean value and standard deviation for the attenuation of calcaneus samples was 9.94 ± 5.74 dB/cm/MHz (Wear 1999). In a review of literatures (Goss *et al.* 1978), the highest value of acoustic attenuation of embalmed human skull reached as high as 214 dB/cm (approximate 3 to 4 MHz). It can be considered that the values of the results were in a slightly wide range. Bone is not uniform solid material, which contains compact (outer layer) and trabecular (interior) bone tissue. This may lead to different results in acoustic properties measurement at different location of the same type of bone. The cross-section area of rib cortex was found to be varied with age (Sedlin *et al.* 1963), which may indicate the

acoustic properties of bones changed with age. As a result, the speed of sound in bones was in the range of 1500 m/s to 3360 m/s. The attenuation coefficient was in the range of 9.94 dB/cm/MHz to 214 dB/cm at 3 to 4 MHz. The range of speed of sound and attenuation coefficient of soft tissues and bones from literatures is summarised in Table 2.3.

Table 2.3 Range of acoustic properties of soft tissues and bones

Parameters	Range of soft tissues	Range of bones
Speed of sound (m/s)	1478-1595	1500-3360
Acoustic attenuation coefficient (dB/cm/MHz)	0.2-4.7	9.94-214 (at 3 to 4 MHz)

To mimic the acoustic properties of those tissues, the acoustic properties of a large number of TMM phantoms have been reported (Alexei *et al.* 2003; Browne *et al.* 2003; Lafon *et al.* 2005; Zell *et al.* 2007; King *et al.* 2011), including agar, PAA, PVA, silicone, and some homemade phantoms (Lafon *et al.* 2005; King *et al.* 2011). Zell et al. (Zell *et al.* 2007) summarised tissue mimicking phantoms under different conditions for the development of phantoms used in photoacoustic and ultrasound imaging. In their study, PVA fits best to human breast tissue especially up to 10 MHz in photoacoustic and ultrasound imaging; agar is well for quick and easy preparation without the need for long-term stability; silicone is good for stable phantoms; PAA seems to be less appropriate for phantom production because of its toxicity (Zell *et al.* 2007).

The wide range of acoustic properties of biological tissues requires phantoms with adjustable acoustic properties. The acoustic properties can be adjusted by varying the concentration of specific compositions. Evaporated milk and powdered graphite was used to change attenuation and scattering properties in agarose-based material (Madsen *et al.* 1998). Al_2O_3 powder SiC can achieve the similar aims in agarsoed-based phantom (Ramnarine *et al.* 2001). Graphite or talcum powder was used as scattering agents to vary attenuation and n-propanol was used to control the speed of sound in the magnesium silicate gels manufacture (Sheppard & Duck 1982). The speed of sound in foam phantom can be varied by altering the concentration of NaCl (Lerski *et al.* 1982).

It is noted that the values of these acoustic properties are not constant in different environment. Temperature and frequency are considered as the main influential factors of the changes in acoustic properties. Acoustic properties of common TMMs, including commercial phantoms and customized designed phantoms, were assessed with variations with both frequency and temperature (Browne *et al.* 2003; Zell *et al.* 2007). Acoustic velocity remained constant (± 3 m/s) with increasing frequency, while attenuation was found to increase with increasing frequency. It was found that the acoustic velocity of the agar, Zerdine (CIRS Inc., CT, USA) and condensed milk increased with increasing temperature by a rate of approximately 1.5 $m \cdot s^{-1} \cdot °C^{-1}$. Whereas, the acoustic velocity of the urethane rubber TMM (GAMMEX Inc., WI, USA) decreased with ascending temperature, by a rate of 2.5 $m \cdot s^{-1} \cdot °C^{-1}$ (Browne *et al.* 2003). A wide range of acoustic attenuation coefficient was found in the measurement results of normal (fatty) breast tissue as shown in Figure 2.5 (Bamber 1983). This range was getting larger with the increase of the frequency of ultrasonic wave.

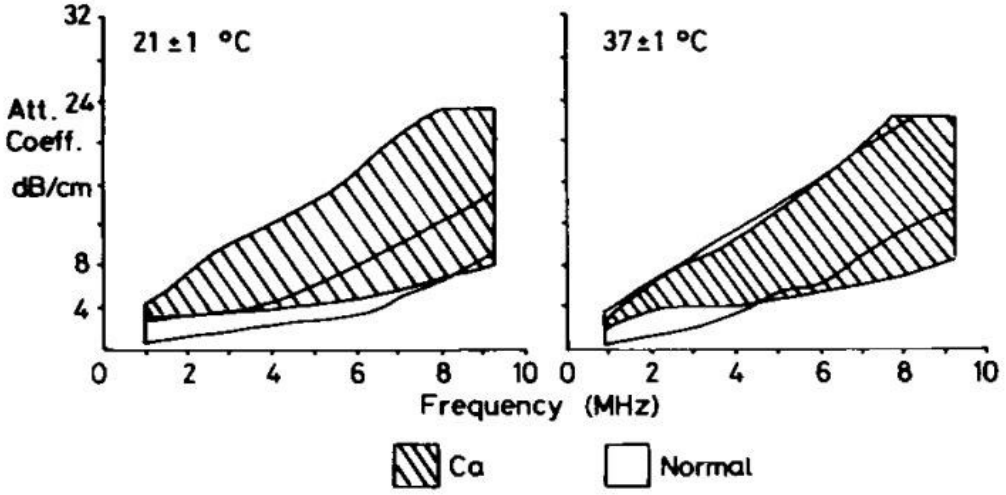

Figure 2.5 Range of mean attenuation coefficients of breast cancer and normal (fatty) breast in 7 specimens; 56 positions, 3 to 5 positions per average (Ca: breast cancer; Normal: normal breast) (Bamber 1983)

The acoustic properties of some phantoms also changed during the heating and coagulation process of HIFU sonication, such as PAA egg white phantom (Takegami *et al.* 2004; Lafon *et al.* 2005; Divkovic *et al.* 2007). Investigations revealed that the protein

denaturation in the phantom material has an impact on the acoustic attenuation. The coagulated phantom material showed an enhanced absorption and a threefold higher attenuation coefficient in comparison with the non-coagulated phantom at a 1 MHz frequency (Divkovic *et al.* 2007). For 7% BSA concentration, the attenuation coefficient was an approximately linear dependence in the frequency range between 1 to 5 MHz (Lafon *et al.* 2005).

The acoustic properties of some commonly used TMMs are summarised in Table 2.4.

Table 2.4 Acoustic properties of soft tissue substitutes (Culjat *et al.* 2010)

Material	Velocity (m/s)	Density (kg/m^3)	Attenuation (dB/cm MHz)	Acoustic Impedance (MRayl)
Agarose-based	1498-1600+	1016-1100	0.04-1.40	1.52-1.76+
Gelatin-based	1520-1650	1050	0.12-1.5	1.60-1.73
Magnesium Silicate-based	1458-1520	-	0.85	-
Oil Gel-based	1480-1580	1040-1060	0.4-1.8	1.54-1.67
Open Cell Foam-based	1540	-	0.46	-
Polyacrylamide Gel-based	1540	1103	0.7dB/cm @ 5MHz	1.7
Polyuerethane	1468	1130	0.13	1.66
Polyvinyl Alcohol-based	1520-1610	-	0.07-0.35	1.60-1.77
Water-based	1518-1574	1000+	-	1.48-1.60
Condensed Milk-based	1540	-	0.5	-
Urethane Rubber	1460	900	0.5-0.7	1.31
Zerdine	1540	-	0.5-0.7	-

2.4.3. Thermal properties of TMMs

In addition to the acoustic properties, thermal properties which determine the heat transmission through the materials are also important in fabricating and investigating TMM phantom. The thermal conductivity (k) is the quantity of heat transmitted due to a unit temperature gradient, in a direction normal to a surface of unit area in unit time under steady-state conditions and where heat transfer is dependent only on the temperature gradient. The thermal diffusivity (α) determines the relative time rate of temperature change, and is thus a measure of the ability of a thermally perturbed system to relax back to steady-state conditions. Another thermal quantity, the specific heat capacity (c) of a substance is the amount of heat per unit mass required to raise the temperature by one degree in temperature.

The heat effect induced by focused ultrasound is able to provide important information for the evaluation of HIFU field and allow the sonication results predictable via theoretic calculation. Furthermore, the phantoms possessed tissue mimicking thermal properties provide an environment similar to tissue for acoustic energy delivery and heat conduction and diffusion. Thus, to study the focal temperature in HIFU sonication, the phantom needs both tissue mimicking acoustic properties and thermal properties.

Similar to acoustic properties, the thermal properties varied in different part of tissues. The thermal properties of animal and human tissues and organs were summarised according to previous researches (Bowman *et al.* 1975). Bowman et al. summarised the thermal properties of a wide range of tissues and organs based on different investigators' studies. The thermal properties of tissues and organs of human were selected and listed in Table 2.5.

Table 2.5 Thermal properties of human and animal tissues and organs (Bowman *et al.* 1975)

Materials and conditions	Thermal conductivity ($W \cdot m^{-1} \cdot °C^{-1}$)	Thermal diffusivity ($m^2 \cdot s^{-1}$)
Human brain, white, 71% water	0.503	1.34 & 1.40×10^{-7}
Human brain, gray, 83% water	0.566	1.43×10^{-7}
Human brain, whole, 78% water	0.528	1.37 & 1.38×10^{-7}
Human fat	0.200	NA
Human heart, 81% water	0.587	1.48×10^{-7}
Human kidney, 84% water	0.545	1.32×10^{-7}
Human liver, 77% water	0.566	1.50×10^{-7}
Human muscle	0.385	NA
Human spleen	0.545	1.32 & 1.38×10^{-7}
Human blood	0.488	NA
Human blood	0.506	NA
Sheep kidney, corticomedyllary junction, anesthetized with anectine and nembutal	1.281	4.31×10^{-7}
Canine liver, 75% water	0.623-0.901	1.66-2.39×10^{-7}
Canine liver, 73% water	0.670-0.796	1.78-2.11×10^{-7}

A reference text (Duck 1990) includes a wide range of tissue thermal properties measured by different researchers under different conditions. Thermal diffusivity of soft tissue was reported in the range between 0.53×10^{-7} $m^2 \cdot s^{-1}$ for cow fat (7% water) to 2.03×10^{-7} $m^2 \cdot s^{-1}$ for rabbit liver. Thermal conductivity was between 0.23 $W \cdot m^{-1} \cdot °C^{-1}$ in human fat and 0.612 $W \cdot m^{-1} \cdot °C^{-1}$ in human aorta. For tissue specific heat capacity, the range was between 2250 $J \cdot kg^{-1} \cdot °C^{-1}$ for pig fat to 3930 $J \cdot kg^{-1} \cdot °C^{-1}$ for human blood plasma. Combined with the results in Table 2.5, the range of thermal properties of soft tissues can be summarised in Table 2.6.

Table 2.6 Range of thermal properties of soft tissues

Parameters	Range of soft tissues
Thermal conductivity ($W \cdot m^{-1} \cdot °C^{-1}$)	0.23-0.901
Thermal diffusivity ($m^2 \cdot s^{-1}$)	$0.53\text{-}4.31 \times 10^{-7}$
Specific heat capacity ($J \cdot kg^{-1} \cdot °C^{-1}$)	2250-3930

In 2005, a standard for contact transient methods of measurement of thermophysical properties was reported (Tye *et al.* 2005). This standard provided the basic requirements in the thermophysical properties measurement. PAA and BSA based phantom materials are more stable at high temperature in thermal therapy compared with those gel material, such as agar and gelatin, which have lower melting temperatures (Mark *et al.* 2004). As a result, these two kinds of materials are more widely used in the thermal properties research. The thermal response of a phantom consists of a mixture of PAA and 18% w/w BSA has been developed and tested in order to calibrate thermal therapy devices (Bouchard & Bronskill 2000). The research on the thermal properties of PAA egg white phantoms, which is used for visualisation of HIFU lesions, has been reported in 2007 (Divkovic *et al.* 2007). Thermal conductivity and specific heat capacity of a PAA phantom with 10% to 11% (w/w) dissolved egg white protein was measured using hot wire method and conventional calorimetry. The results for the thermal conductivity (0.59 ± 0.06 $W \cdot m^{-1} \cdot °C^{-1}$) and the specific heat capacity (4270 ± 365 $J \cdot kg^{-1} \cdot °C^{-1}$) capacity were similar to the values of water (0.6 $W \cdot m^{-1} \cdot °C^{-1}$ and 4182 $J \cdot kg^{-1} \cdot °C^{-1}$). The observed faster temperature rise in the coagulated focus compared to the normal phantom material indicates an increased absorption in this PAA material. This result was in good agreement with the changes in acoustic attenuation coefficient of canine liver tissue with and without coagulation (Techavipoo *et al.* 2004). The acoustic attenuation coefficient in canine liver tissue was proved to be dependent on both tissue coagulation effects and temperature elevation.

The thermophysical properties of PAA egg white phantoms with vaired egg white concentration for HIFU exposures were provided by the previous researchers in Dundee ultrasound group (Gao *et al.* 2012). Various egg white concentrations 0% to 40 % were used to fabricate the phantoms and step-wise transient plane source (TPS) method

(Kubicar & Bohac 2000) was utilized in the measurement. The results, including thermal conductivity, thermal diffusivity, specific heat capacity and R-squared values, are shown in Table 2.7.

Table 2.7 Measured thermophysical properties of egg white phantoms with different egg white concentrations (0% to 40%) (Gao *et al.* 2012)

Egg white concentration (v/v %)	Thermal conductivity ($W \cdot m^{-1} \cdot °C^{-1}$)	Thermal diffusivity ($m^2 \cdot s^{-1}$)	Specific heat capacity ($J \cdot kg^{-1} \cdot °C^{-1}$)
0	0.722	1.866×10^{-7}	4230.5
10	0.737	1.826×10^{-7}	4304.9
20	0.744	2.019×10^{-7}	3670.4
30	0.747	2.221×10^{-7}	3743.9
40	0.759	2.253×10^{-7}	3271.9
R^2	0.95	0.88	0.84

2.4.4. Elastic properties of TMMs and elastography

The elastic properties describe the resistance of an object or substance to being deformed elastically when a force is applied to it. The variations in elastic properties of tissues have been considered as diagnostic sign of diseases such as cancer. Imaging of elastic properties of normal and diseased tissues is carried out either by approaches that estimate displacement and strain or modulus reconstructions in response to a quasi-static deformation (O'Donnell *et al.* 1994; Bilgen & Insana 1996; Bamber 1999; Madsen *et al.* 2005) or dynamic approaches for reconstructing the mechanical properties of tissue using external vibration or methods that utilize localized acoustic radiation force to perturb small volumes of tissue (Fatemi & Greenleaf 1999; Nightingale *et al.* 2002; Urban *et al.* 2011).

ShearWave^{TM} elastography (SWE) (Bercoff *et al.* 2004; Bercoff *et al.* 2008) is a quantitative technique based on estimation of the shear wave speed or velocity, which is used to assess true tissue elasticity by displaying a colour coded image superimposed on

a B-mode image (Figure 2.6). The stiffness of tissue, quantified by the Young's modulus E (kPa), is related to the shear modulus (μ) by equation (2.2):

$$E = 2\times\mu\ (1+\upsilon) \approx 3\mu \tag{2.2}$$

where υ denotes the Poisson's ratio. Under the assumption of tissue incompressibility i.e. $\upsilon \approx 0.495$, $E \approx 3\mu$. The shear modulus is related to the density (ρ) and the shear wave propagation velocity (v_{sw}) through equation (2.3).

$$\mu = \rho \times v_{sw}^2 \tag{2.3}$$

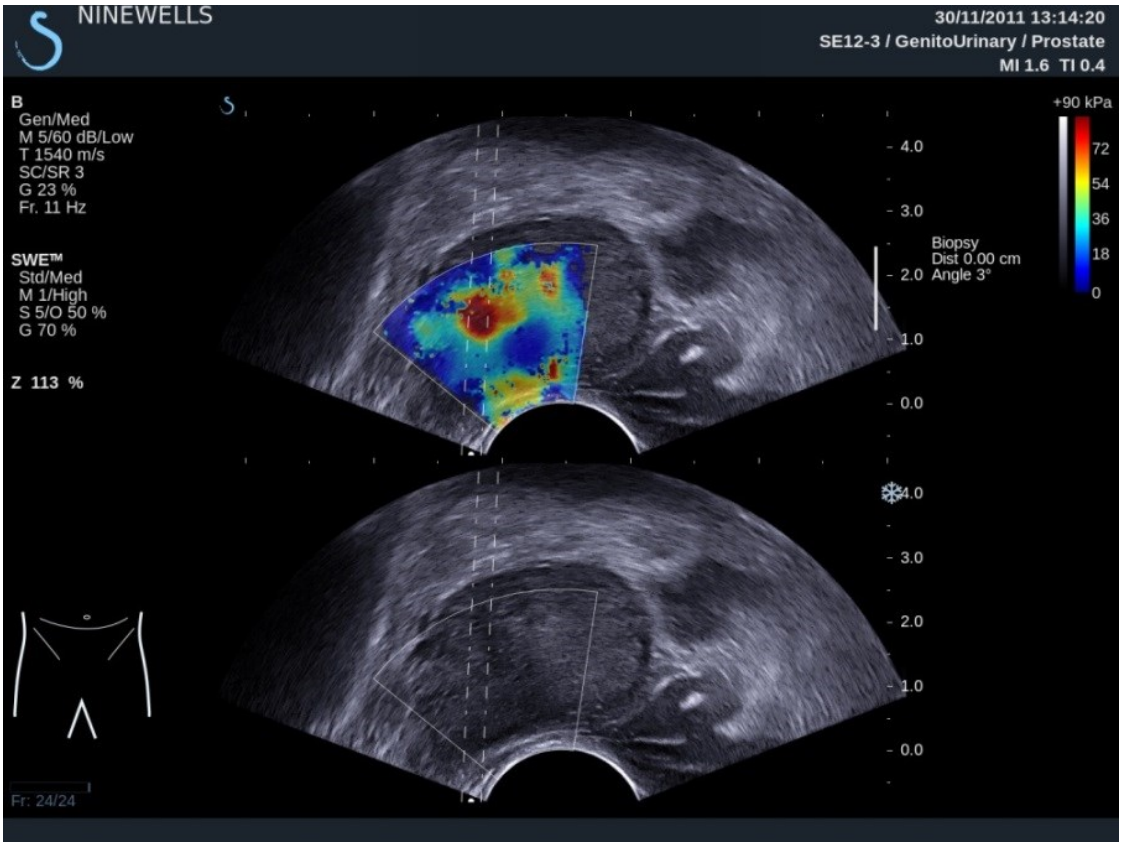

Figure 2.6 Ultrasound B-mode and Young's modulus image of a human patient's prostate obtained by tracking shear wave propagation based on supersonic shear imaging

By measuring the speed of the propagation of the shear wave at every point in the scanned region under the assumption of uniform and constant value of the tissue density, the stiffness of the tissue can be quantified in terms of the shear modulus. In SWE, the elasticity image measured in kilopascals (kPa) is refreshed in real time with the image

resolution around 1 mm (Bercoff *et al.* 2004). However, SWE is an evolving for the detection of prostate cancer and many parameters need to be standardised.

As the cancerous tissues were stiffer than normal tissues, they normally showed a larger Young's Modulus. The Young's Modulus of liver tumour was reported as 30.1 ± 10.7 kPa (n = 31), while it was 6.9 ± 0.9 kPa (n = 13) for normal liver tissue (Venkatesh *et al.* 2008). Prostate cancerous tissue is stiffer properties in the range of 58.0 kPa and 90.5 kPa based on patients data using shear wave elastography (Zhai *et al.* 2010; Barr *et al.* 2012). Zhang et al. (Zhang *et al.* 2008) have reported that the complex Young's modulus of normal and cancerous prostate of 15.9 ± 5.9 kPa (n = 8) and 40.4 ± 15.7 kPa (n = 9) at 150 Hz using stress relaxation tests.

Krouskop et al. (Krouskop *et al.* 1998) measured the Young's modulus of a larger number of prostate specimens using compression loading at two different pre-compression levels of 2% and 4% and for three different loading frequencies of 0.1, 1 and 4 Hz respectively. At a 1 Hz testing frequency and 2% pre-compression they reported Young's modulus values of 62 ± 17 kPa (n = 32) in the normal anterior and 69 ± 17 kPa (n = 32) in the normal posterior of the prostate. BPH was reported to be softer than the normal prostate at 36 ± 9 kPa (n = 21). Significant differences were observed in the Young's modulus of prostate cancers with an increase in the pre-compression from 2 to 4%, with values increasing by a factor of two from 100 ± 20 kPa (n = 28) to 221 ± 32 kPa respectively. These reports demonstrate that the Young's modulus values obtained by compression test can change with the testing frequency and pre-compression levels for different prostate tissue types. Therefore, the Young's Modulus of cancerous tissues was in a wide range of 30.1 kPa (liver tumour) to 221 kPa (prostate tumour).

Table 2.8 Range of Young's Modulus of tumours

Parameter	Range of tumours (kPa)
Young's Modulus	30.1-221

TMM phantoms play an important role in ultrasound and elastography research through simulating normal and diseased tissues for standardisation (D'Souza *et al.* 2001;

Alexei *et al.* 2003; Takegami *et al.* 2004; King *et al.* 2011). Various kinds of TMMs have already been used in ultrasound research, such as agar, silicone and PAA gel (D'Souza *et al.* 2001; Alexei *et al.* 2003; Takegami *et al.* 2004; King *et al.* 2011). The Young's modulus is an important parameter for elastography phantoms. Madsen et al. (Madsen *et al.* 1994) have demonstrated the use of TM phantoms for standardization of both ultrasound imaging of the prostate and elastographic imaging, using agar and gelatin materials. Anderson et al. (Anderson *et al.* 2011) have also presented the effect of graphite concentration on shear wave speed in the gelatin based phantoms. Aldehyde concentration was used to increase the stiffness of the gelatin by controlling the amount of collagen crossing-linking (Phantom materials for elastography).

Ultrasound elastography is a rapidly developing technology and several of the approaches discussed above have been implemented in commercial clinical diagnostic systems. This non-invasive technique has since then been reported in clinical trials in different anatomical areas using various perturbation techniques (Xu *et al.* 2010; Urban *et al.* 2011; Aboumarzouk *et al.* 2012; Barr *et al.* 2012; Brock *et al.* 2012; Evans *et al.* 2012; Zhai *et al.* 2012). Commercial systems include: VirtualTouch (Siemens Medical Solutions USA, Inc., Malvern, PA, USA), SonixTablet (ULTRASONIX, British Columbia, Canada), ElastoQ (Toshiba Medical Systems, Otawara, Japan), ShearWaveTM elastography (SuperSonic Imagine, Aix-en-Provence, France) etc.

2.5. Summary

Since there is a growing number of interests and clinical applications of HIFU, the efficacy and safety of the treatment has to be taken into consideration and the challenges of HIFU need to be overcome.

The ribcage of the patient, which blocked part of the beam path of the focused ultrasound wave and declines the efficacy of HIFU, was one of the challenges in the treatment of abdominal organs. To address this issue, a number of numerical analysis of HIFU procedures through ribcage have been reported, including wave propagation and its correction provided together with potential solutions. However, none has applied the physical experimental practice with the structure of human anatomy. Experimental data reporting on acoustic properties of ribs and surrounding soft tissues so far has been limited

to animal ribs, TMM phantoms or single piece of human rib without full anatomical structure (e.g. rib spacing). The reported experimental data may not be applicable to humans as anatomy and structure of ribs and surrounding structures have with little or no resemblance to real patients. Therefore, a physical model possesses human anatomical structures was necessary for assessing the role of the ribcage in HIFU treatment through ribs. In order to reconstruct human anatomical structures, it is the best way to use medical images of the patients. As the properties of human tissues have been known, a practical model could be created for pre-treatment planning based on image data from patients using proper TMMs.

Chapter 3 Patient-specific 3D Model Reconstruction, Fabrication and Characterisation

The ribcage is an obstacle in the ultrasound wave propagation in HIFU treatment of abdominal tumours and it is necessary to create a physical ribcage model to fully understand the effect on the focused ultrasound field. This chapter describes a rapid modelling technique for 3D reconstruction of the ribcage based on patient specific data, thus modelling human anatomical structures. The procedure of fabricating ribcage and surrounding tissue using selected tissue mimicking materials for imaging and HIFU applications is included.

To mimic human anatomical structures, a 3D modelling technique was utilised based on clinical images (e.g. CT and MRI). Digital Imaging and Communications in Medicine (DICOM) is the standardised data exchange format between medical systems. In this study, Simpleware (Simpleware Ltd, Exeter, UK) software was used to create the 3D models using the DICOM data from four patients CT scans with prior institutional approval (Caldicott/CSAppFY021211). The reconstruction procedure is described in section 3.1. The physical ribcage model was then produced from the profile of the computational model by rapid prototyping.

The fabrication of TMM phantoms is described followed by their characterised and comparison with the properties of human tissues. The TMMs for every part of the phantom in HIFU sonication must have approximate properties. Those properties included acoustic, thermal and elastic parameters. The lesion formed on different phantom caused by HIFU sonication was compared for selecting the phantom as sonication target in the following studies in section 4.4 of next chapter. The fabrication of several types of commonly used phantoms in ultrasound research is described in section 3.3. Measurement and result of TMMs properties are illustrated in section 3.4.

3.1. 3D reconstruction of patient's ribcage

Since mid-1990s, 3D modelling techniques have been used for reconstruction of the accurate details of the complex geometries not only of the surface but also of the internal tissue. They can provide the important information for surgical planning and computer aided simulation. There are many 3D modelling techniques available. For example, 3D Slicer (an open source software package, Surgical Planning Laboratory of Brigham and Women's Hospital, MA, USA) has been used in assisting planning of the surgical separation of conjoined twins (Norwitz *et al.* 2000). Analyze software (AnalyzeDirect Inc., KS, USA) can be used to create a virtual 3D models to design and manufacture a mould for correlating the images with histopathology (Shah *et al.* 2009).

Rapid prototyping (RP) techniques, which convert a computer reconstructed 3D model into a prototype, are widely used in manufacturing and in medical applications. RP can provide a realistic impression of complex structures and precise reproduction of objects, thus surgical planning and fabrication of prostheses have gained most benefits from RP technique in medical applications.

In the current study, 3D modelling and rapid prototyping were used for 3D reconstruction from patients' data. The procedure included creating a computer generated model from clinical images, prototyping a physical model and fabricating TMM phantoms based on the 3D models.

3.1.1. Patient data

Anatomical features and structures, for example, the width and spacing of ribs, vary greatly from patient to patient. The best way to obtain patient-specific anatomical structures is from clinical images, such as CT and MRI. Here image data from four patients was used for the ribcage reconstruction and the difference in ribcage dimensions is presented in this section.

Four patients, with different gender and age, were selected for the ribcage model reconstruction. Patient No.1 was an 80 years old male; No.2 was a 54 years old female; No.3 was male, 44 years old; and No.4 was female, 47 years old. The CT scan data obtained from Ninewells hospital was used with prior institutional ethical approval and patients consent (Caldicott/CSAppFY021211).

Spacing between the 9th and 10th ribs (Figure 3.1) was selected to investigate intercostal ultrasound propagation and the 9th ribs were used in the study of transcostal HIFU treatment (Chapter 4). To describe the difference in rib curvature, the height of the minor circular segment of the rib was measured. For an arc, different curvature results in different height of the circular segment if chord length is assumed to be constant. Figure 3.2 depicts a minor circular segment with chord length 80 mm on the 9th rib. H_{cs} indicates the height of this circular segment. The height on the 9th and 10th ribs of the four ribcages is shown in Table 3.1. The width of the ribs was measured at three different positions on the 9th and 10th ribs. These positions were determined by the chord length of 20 mm, 40 mm and 60 mm in the circular segment composed by the rib arch. For the 9th rib in Figure 3.3, w1 is the width at the end of the circular segment at 20 mm chord length. Likewise, w2 and w3 are at the end of the 40 mm and 60 mm chord, respectively. w4, w5 and w6 are at the end of the 20 mm, 40 mm and 60 mm chord on the 10th rib. Spacing between the 9th and 10th ribs was also measured at three positions at 20 mm, 40 mm and 60 mm chord length of the circular segment (s1-s3 in Figure 3.3).

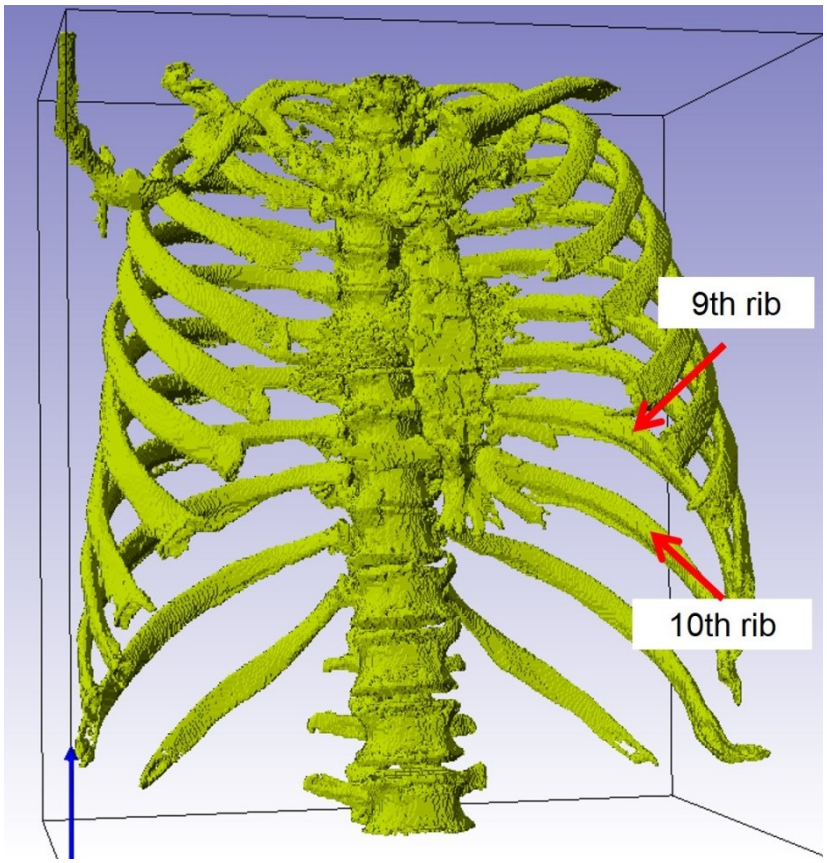

Figure 3.1 3D model of human ribcage (the 9th and 10th ribs were selected in the current study)

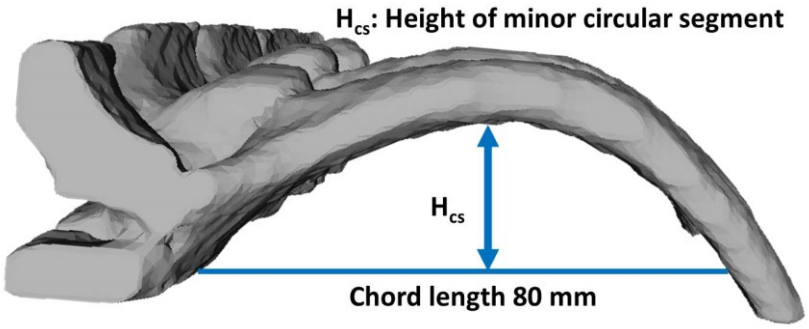

Figure 3.2 Top view of the ribcage model (Blue double headed arrow indicating height of minor circular segment of the 9th rib)

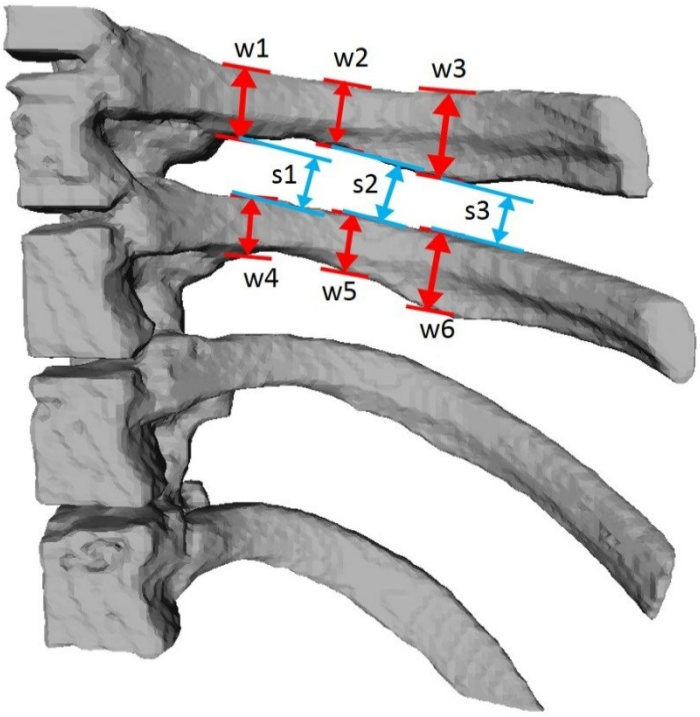

Figure 3.3 Dimensions of width and spacing of ribs. w1-w3 and w4-w6 indicate the widths of the 9th and 10th rib respectively. s1-s3 represent the spacing between 9th and 10th rib. w1, w4 and s1 are at the chord length of the rib 20 mm; w2, w5 and s2 are at 40 mm; w3, w6 and s3 are at 60 mm.

Measurement results of these dimensions are summarised in Table 3.1. Results show that ribcage of No.2 patient has the biggest spacing between the 9th and 10th ribs, while ribcage of No.3 patient has the smallest. Patient No.3 and No.4 have similar width in the 9th rib, which is obviously wider than that of the other two. Costal groove results in an increase in the width at w3 and w6, and a decrease in the spacing at s3 position.

Table 3.1 Dimensions of patients' ribs (mm, SD within ± 0.08 mm)

	Patient No.1	Patient No.2	Patient No.3	Patient No.4
w1	11.45	10.60	13.16	13.34
w2	11.28	11.91	12.71	11.43
w3	15.63	13.39	17.52	18.44
w4	11.22	10.76	11.45	11.06
w5	14.88	11.22	11.13	10.08
w6	18.52	15.15	14.77	15.01
s1	18.25	19.73	12.31	15.41
s2	18.58	21.52	13.82	17.06
s3	16.88	19.57	11.91	10.71
$H_{cs}(9^{th})$	16.03	15.94	23.47	17.20
$H_{cs}(10^{th})$	12.59	12.29	20.26	14.30

3.1.2. DICOM

DICOM , Digital Imaging and Communications in Medicine, is the international standard for medical images and related information (ISO 12052). It defines the formats for medical images that can be exchanged with the data and quality necessary for clinical use. DICOM is implemented in almost every radiology, cardiology imaging, and radiotherapy device (X-ray, CT, MRI, ultrasound, etc.), and increasingly in devices in other medical domains such as ophthalmology and dentistry.

Thanks to DICOM standard, the medical data processing can be simplified by the standardised data file format definition and network communications protocol. As the CT scan data from patients used in this study complied with DICOM standard, it can be directly imported into most of the imaging processing software for the 3D model reconstruction.

3.1.3. Image processing of DICOM data

In this section, the reconstruction from DICOM data to 3D computer generated model is described. The pixels of bones in CT images were brighter compared with soft tissues and this allowed better segmentation of the ribs from the raw image data. No.1 patient's data was used to describe the image processing. Before starting the reconstruction, in order to reduce the CPU and memory usage during the image processing, the CT images were cropped to contain only the whole ribcage area. Segmentation was performed to separate ribs and other tissues, so that a mask (representing the object of interest) of the ribcage can be extracted from the raw data. There could be over segmentation or cavities in the field of interest during the segmentation procedure limited by the image resolution and additional functions and filters, e.g. morphological filter and cavity fill filter, were applied to enhance the image quality. Finally, the 3D model was reconstructed based on this mask.

3.1.3.1. Segmentation

The segmentation on raw greyscale data (Figure 3.4(a)) was achieved through classification of pixels into appropriate groups by threshold values according to relative signal strength. The greyscale of pixels on raw CT images ranged from 0 to 4095. A lower threshold value of 1235 was selected to segment the ribcage area with 4095 as the upper threshold, because the rib parts possessed the highest grey value and all of these pixels should be included in the field of interest. The pixels that between the lower and upper threshold were segmented.

A few dispersive regions were selected with the ribcage area in this mask (red area in Figure 3.4(b)). It can be seen in Figure 3.4(b) that, the red area on the top left and in the middle of the figure did not represent ribs (most likely liver and heart). Additional functions were then applied, such as region growing. Region growing kept only the connected pixels as 'islands'. By using region growing, some of the unwanted parts in the segmented images were disconnected. It was also used to improve the lack of connectivity among the preservation area of the ribs. A better segmentation result was gained after further processing as shown in Figure 3.4(c).

3.1.3.2. Filter enhancement

After segmentation, there were some excess areas connected with the target ribs (green in Figure 3.4(c)). A morphological filter was applied, which got rid of small spurious features that cannot be removed by segmentation. Some small holes might be still in the field of interest and a cavity fill filter was used to fill them. The cavity fill filter automatically filled those cavities that were completely closed. These filters can be repeated to obtain an ideal result. In Figure 3.4(d), only ribcage was selected and coloured in the active yellow mask after image processing. The mask of the ribcage is presented in green in the 3D view on the raw data in Figure 3.5.

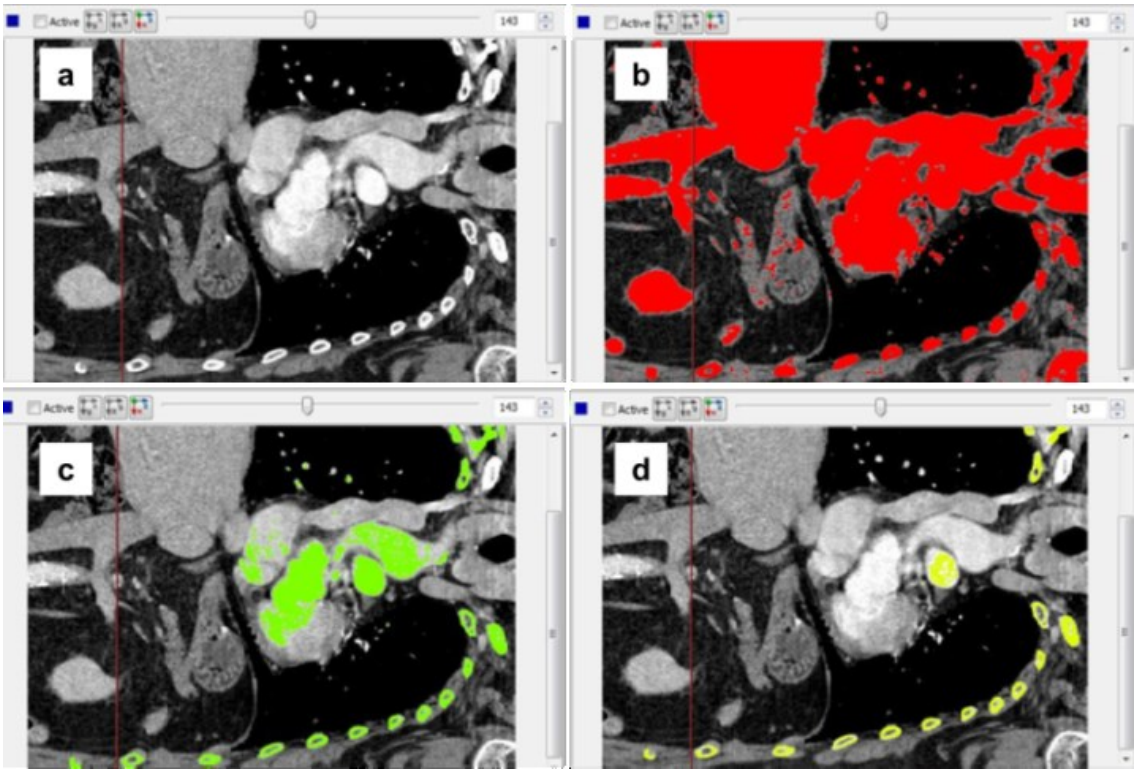

Figure 3.4 Image processing of CT data (a. Raw greyscale data; b. After basic segmentation; c. After region growing; d. After filter enhancement)

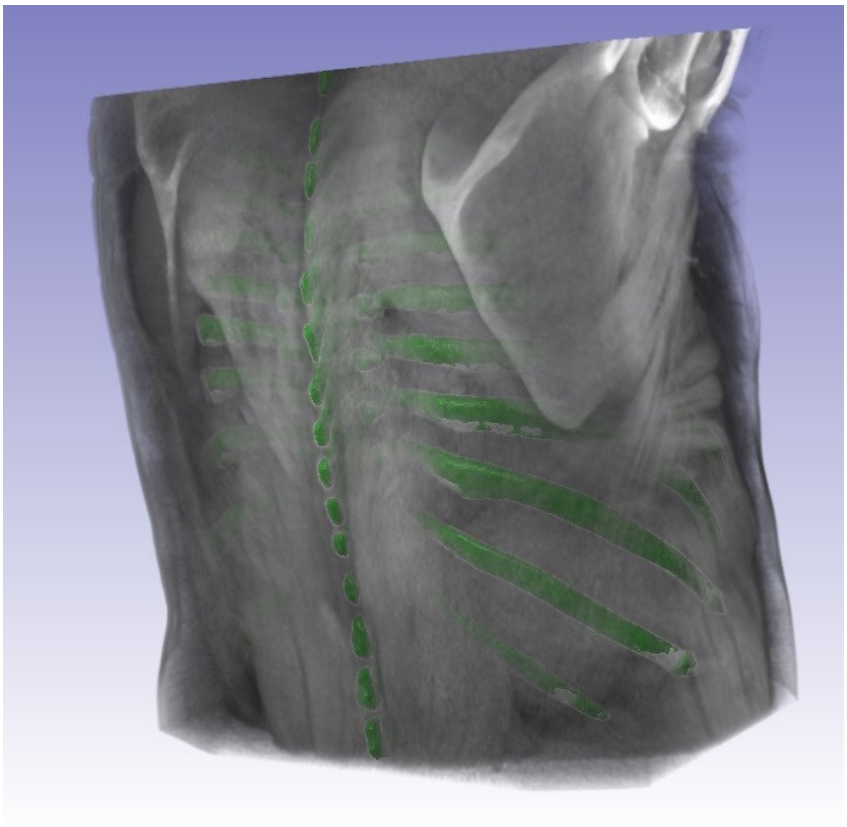

Figure 3.5 3D view of segmentation result of the ribcage from raw data

3.1.3.3. From images to 3D model

The segmented mask as shown in Figure 3.4(d) can be automatically converted into a 3D model (Figure 3.6(a)) by the software. The aim was to reconstruct the lower part of the ribcage, specifically from the 9^{th} to 12^{th} ribs, because the size of the whole ribcage was too large and thus expensive to produce and this lower part was the region in the beam path of the focused ultrasound wave in the treatment of abdominal organs. By reconstructing only the lower part, the processing time of the model was reduced. It was also much more convenient to use the smaller model in the experiments due to the limited size of MR scanner (allowing space for movement of phantom or for other devices). The region of interest (lower part of the ribcage) was selected from the whole ribcage using the editing tool in Simpleware. Because of the image resolution and slice thickness, as seen in Figure 3.6(b), the surface of this part was not smooth enough after modelling from 2D images without any processing. The surface was smoothed using a Recursive Gaussian algorithm. A model with smoothed surface is depicted in Figure 3.6(c). The meshing procedure then assigned material properties (e.g. Young's modulus and density)

and created surface or volume meshes. These were not used in this study but are very important for the models that would be utilised in finite element analysis. The meshed model is shown in Figure 3.6(d). Finally, the model was exported as 'STL' file format to be read by the prototyping machine.

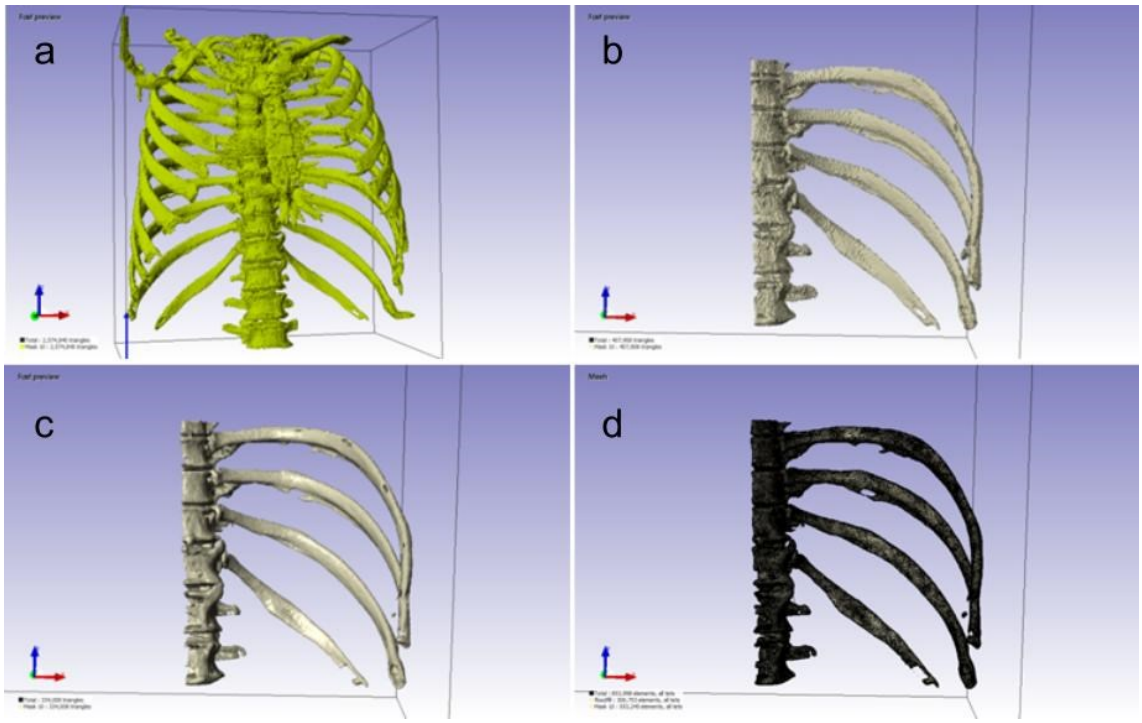

Figure 3.6 Reconstruction of lower part ribcage model (a. Whole ribcage model; b. Lower part of the ribcage model from 9th to 12th ribs; c. Model after surface smoothing; d. Model after meshing)

3.1.4. Prototyping of the physical model

Based on the computer reconstructed 3D ribcage model, the lower part of the ribcage was manufactured by a rapid prototyping machine uPrint SE (Stratasys Ltd., Eden Prairie, MN, USA) using Acrylonitrile Butadiene Styrene (ABS) thermoplastic material (ABSplus^{TM}-P430, Stratasys Ltd., Eden Prairie, MN, USA). After import of the model file in 'STL' format to uPrint SE, the software of the machine calculates the path to extrude thermoplastic material. The machine heats the thermoplastic material up to operating temperature and the material extrusion head that protrudes from the liquefier

(headed thermoplastic material) then lays down a ribbon of material along the extrusion path. After each layer is finished, the Z stage platform lowers slightly to prepare for building the next layer. Each layer of molten plastic is deposited on top of the previous one and flattened slightly by the extrusion head fusing the layers. The physical ribcage models of all of the four patients made by the rapid prototyping machine are shown in Figure 3.7.

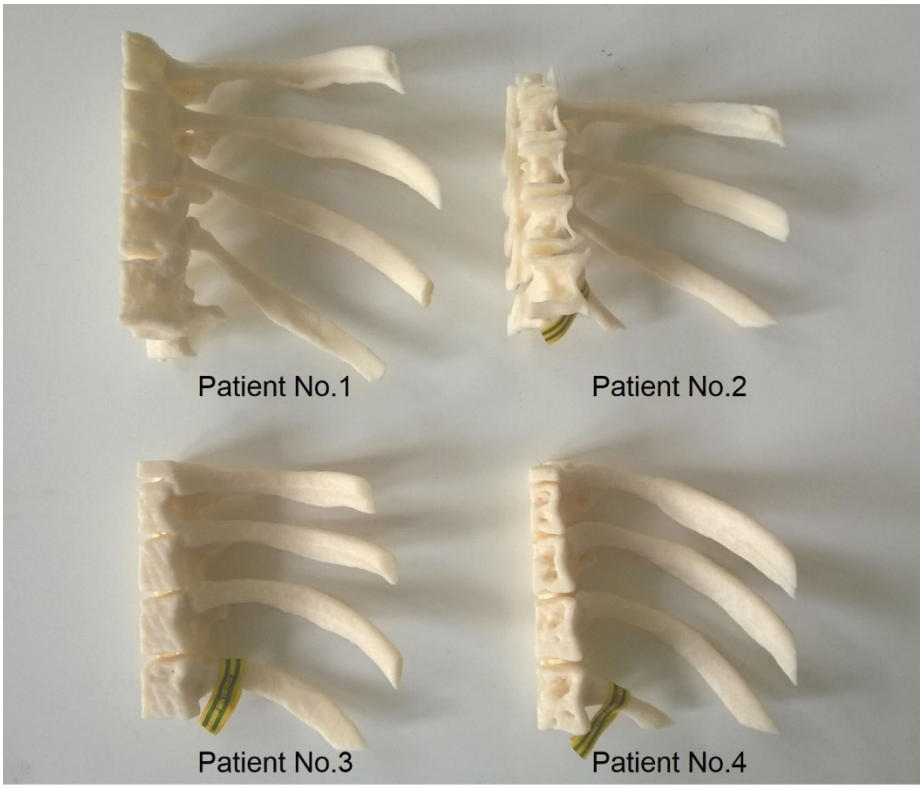

Figure 3.7 Patient specific ribcage models

To mimic the tissue around ribs, TMM was used to fabricate the surrounding tissue. As this phantom was to be used in a series of repeatability experiments to investigate the ribcage effect on HIFU treatment (in Chapter 4), it was not advisable to use a toxic material such as PAA phantom. The phantom needs to be preserved and used for a fortnight, 10% w/v polyvinyl alcohol (PVA) was selected, due to its long-term stability and non-toxicity. It is more elastic than agar. To fabricate the surrounding tissue, the solution of PVA powder (Sigma-Aldrich, Gillingham, Dorset, UK) was allowed to

rest for a few hours to allow air bubbles to rise to the surface. The solution was then processed through four freeze-thaw cycles. Figure 3.8(b) shows the lower part ribcage model embedded into PVA gel.

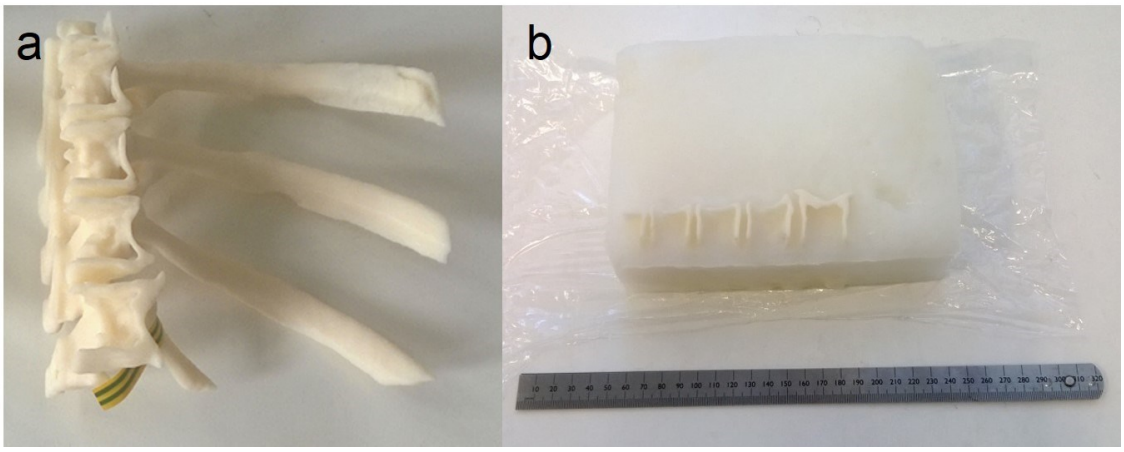

Figure 3.8 3D reconstructed model: (a) prototyped physical model of No.2 patient's lower part ribcage; (b) ribcage model embedded into PVA gel phantom

3.2. 3D modelling of other organs

The 3D modelling of human organs including kidney, liver, breast and prostate, are not included in the study on the ribcage effect, because as a phantom to mimic tissue for HIFU application, the shape of soft tissue is not as important as its properties. The priority of the present work is not to study the effect of the organ shape, but to investigate the effect of ribcage. The phantom is used as the substitute of tissue in the focused ultrasound propagation path. However, the 3D models of these organs can be used in finite element analysis and the phantom fabricated from these models can be used as tissue substitutes in other pre-clinical researches. This section reports the 3D modelling technique of other organs.

3.2.1. Kidney

The kidney model was created using Simpleware by a similar procedure to the reconstruction of ribcage. Based on the patient CT images, however, the reconstruction

of kidney model is more complicated due to different components of the anatomical structures of kidney. To simplify this model, it is assumed that the kidney contains two major regions, the cortex on the outside and the medulla on the inside. Guided by different brightness in pixels, these two parts were differentiated, Figure 3.9(a) for medulla and (b) for cortex.

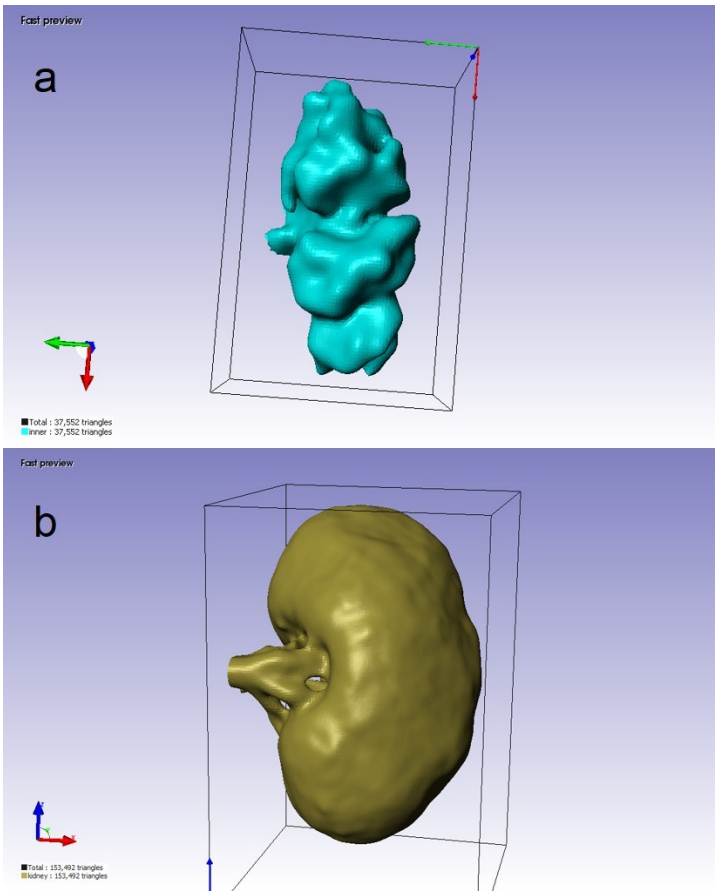

Figure 3.9 3D computer generated kidney model (a. medulla; b. cortex)

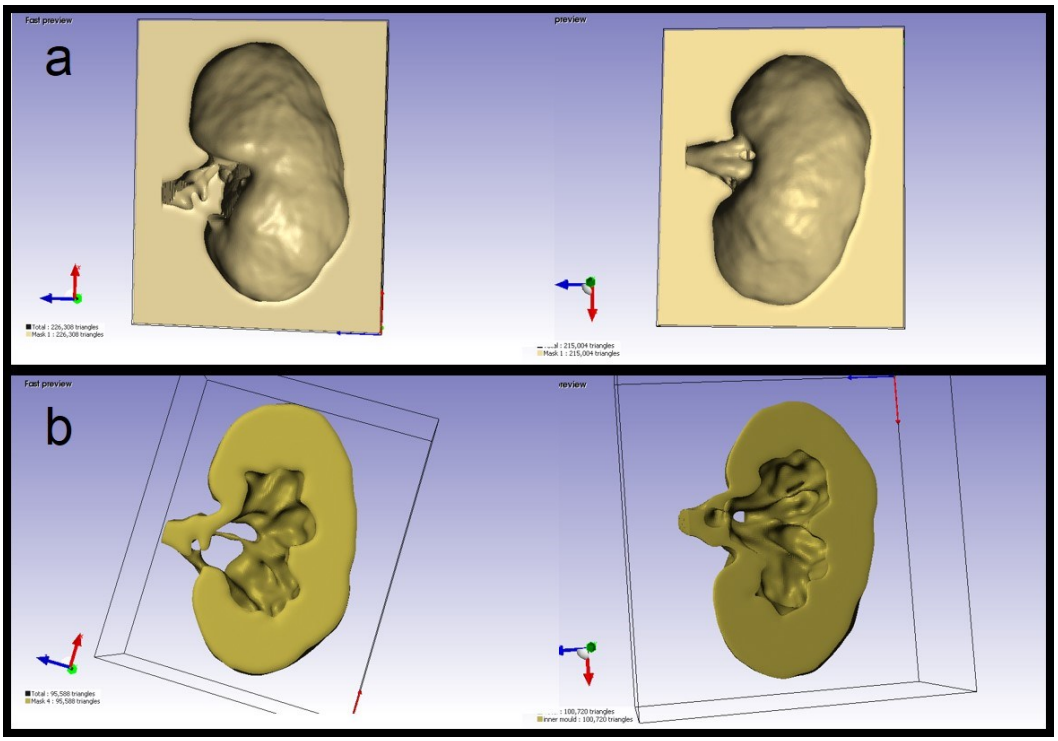

Figure 3.10 Computer generated kidney moulds (a. cortex mould; b. medulla mould)

The kidney moulds were created in accordance with the surface of cortex and medulla part. The medulla mould was achieved by separating the kidney cortex model from its central plane directly as shown in Figure 3.10(b). The cortex mould was produced by separating the medulla shape within a cuboid. Each cuboid possessed half of the kidney medulla model as seen in Figure 3.10(a). The computer generated moulds were then prototyped using uPrint SE machine (Figure 3.11).

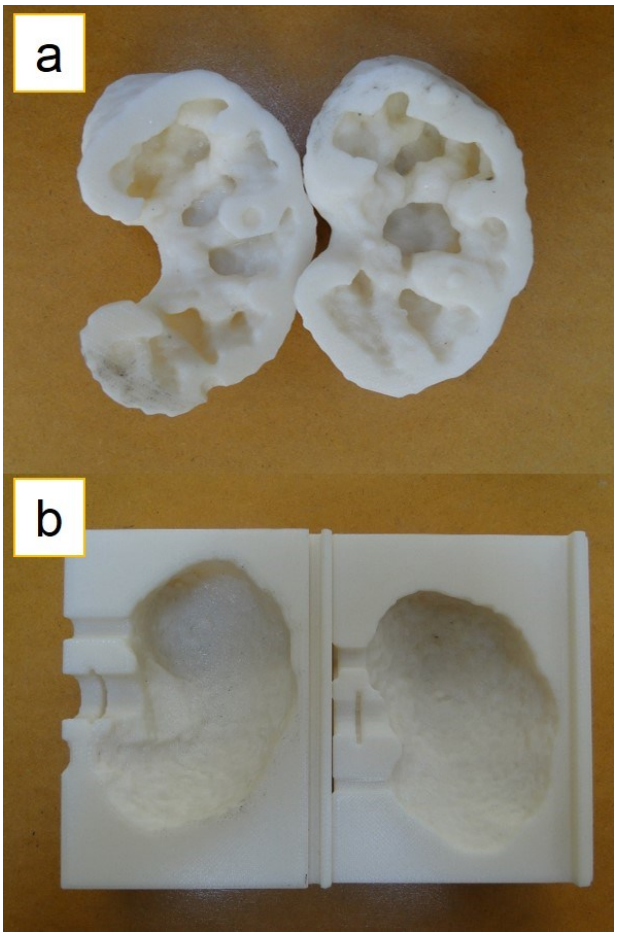

Figure 3.11 Rapid prototyped kidney moulds (a. medulla mould; b. cortex mould)

3.2.2. Liver

The liver model was reconstructed using a similar processing. Figure 3.12 depicts the computer generated model of the liver.

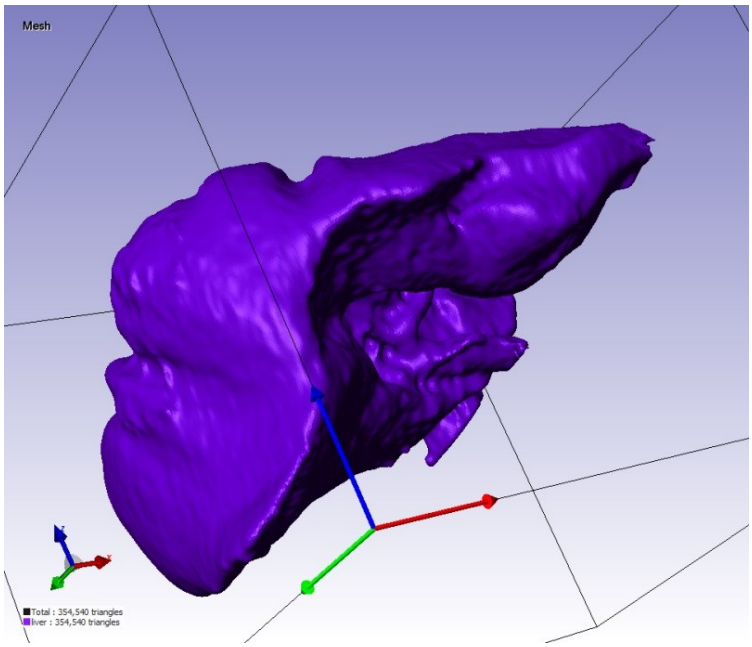

Figure 3.12 3D liver model

3.2.3. Breast

The breast phantom mould was created from MR images of a commercial breast phantom. To manufacture the breast phantom mould, a computer generated cuboid model was cut according to the outline of the breast model (Figure 3.13(a)). The physical mould of breast phantom was prototyped by uPrint SE using ABS material, as shown in Figure 3.13(b). To mimic the breast tissue, the phantom was made of refined lard and fresh egg white (Freed *et al.* 2011). Lard has a similar composition to human adipose tissue and is very stable and readily available. Egg white was used to simulate the glandular portion of the breast as a large part of the glandular tissue is made up of proteins. For this particular mould, the total volume is 240 ml. 223 ml lard and 17 ml egg white based on calculations of breast composition on MR images of volunteers (Cui 2014). The lard was melted and stirred in a beaker on the hot plate and poured into the mould. The egg white was then put into the mould. Finally, the mould with phantom was placed into a refrigerator for cooling down and solidification.

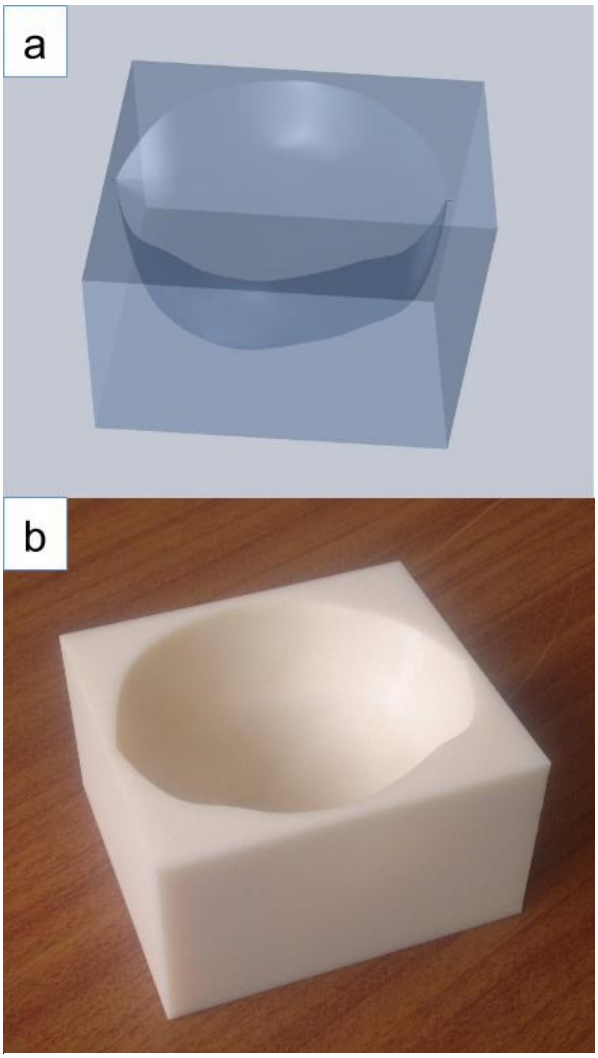

Figure 3.13 Breast phantom mould (a. computer generated model of breast phantom mould; b. prototyped breast phantom mould)

3.2.4. Prostate

The prostate model is shown in the flowchart in Figure 3.14. The fabrication of prostate phantom started from a 3D model reconstructed from MR images of a commercial prostate phantom. The two-part prostate mould was created by removing the prostate model from a cuboid model and separating the cuboid from the central plane. Outlets were prepared on the mould for placing a tube to mimic the ureter in the centre of the phantom. The two-part mould was then prototyped into physical mould for prostate phantom fabrication.

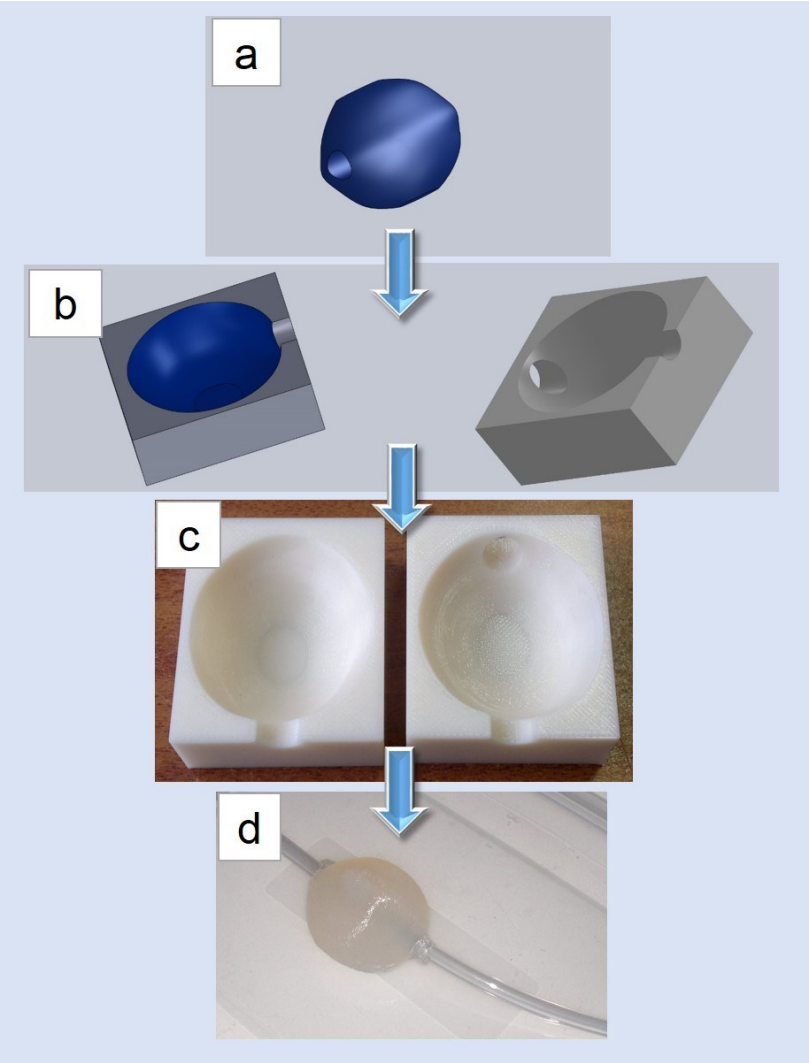

Figure 3.14 Fabrication of prostate phantom based on prostate model (a. prostate model; b. computer generated prostate mould; c. rapid prototyped prostate mould; d. prostate phantom)

3.3. TMM phantom fabrication

Tissue mimicking material (TMM) is used as an alternative to human tissue or animal tissue in medical training and research. It must possesse similar relevant properties to human or animal tissue. In this section, TMMs were characterised in order to determine the best materials for creating phantom for HIFU sonication experiments. The fabrication method of several commonly used TMMs, silicone, PAA, agar and PVA is described here. Samples were prepared for characterisation experiments, including acoustic, thermal and elastic properties.

3.3.1. Silicone

The silicone phantom was made of acetoxy cured silicone (Everbuild, Leeds, UK). It cures from a highly viscous liquid into an elastic solid at room temperature in approximate two hours (depending on temperature, i.e. the higher the temperature, the shorter the curing time). This material remains stable for months and is non-toxic. As the silicone polymer is anti-fungal, quick curing for fast application, it is suitable and easy to moulding into organ or tumour phantoms.

3.3.2. Polyacrylamide (PAA)

PAA based materials state in a liquid phase, after a chemical reaction it turns into a translucent solid. One of the advantages of polyacrylamide is that it can form rigid shapes within 15 minutes at room temperature. The PAA phantom was fabricated using degassed water, acrylamide, N, N'-Methylenebis (acrylamide), ammonium peroxodisulfate, N, N, N', N'-Tetramethylethylenediamine (Sigma-Aldrich, Gillingham, Dorset, UK). The concentration and procedure utilised in this study were based on the previously reported methods (Lafon *et al.* 2001; Takegami *et al.* 2004). It should be noted that if a beaker is used for mixing the chemicals to fabricate PAA phantom, it is best to pour the stirred solution into the mould as fast as possible to prevent the solution from part solidifying in the beaker. Considering its high toxicity, care should be taken when using the material. The protection measures of fabricating PAA phantom and Control of Substances Hazardous to Health (COSHH) risk assessment forms of relevant materials are illustrated in Appendix.

3.3.3. Agar

Agar powder (Sigma-Aldrich, Gillingham, Dorset, UK) added degassed distilled, water was heated and stirred at above 95 °C till it was dissolved completely. The agar solution was then poured into the desired mould for cooling down and forming solid shape. During the heating and stirring procedure, an erlenmeyer flask was applied as the container. There was a small opening on its conical body for air out when connected to a pump (Sam 12 Suction Unit, Aerosol Products Ltd., London, UK). The main opening on the top was sealed and a pump connected to the side opening, so that the air pressure in

the flask could be reduced. This reduced the chance of trapping air bubbles in the agar solution.

3.3.4. Polyvinyl alcohol (PVA)

Fabrication of PVA gel phantom was time consuming due to the freezing and thawing cycle. It was fabricated using 10% w/v PVA particles (Sigma-Aldrich, Gillingham, Dorset, UK) dissolved in degassed, distilled water. The water was heated and stirred until the solution became transparent without any PVA particles. After cooling down to room temperature to allow air bubbles rising to the surface and be removed, the PVA solution was sealed to avoid formation of a dry surface on the top of the phantom and put into a freezer. The phantom was frozen at -20 °C for 12 hours and then recovered to room temperature for thawing (Surry *et al.* 2004). A total of four cycles were applied in this study.

3.3.5. Specimen preparation

Phantoms were fabricated in different shapes for the characterisation of different properties. For acoustic properties, including speed of sound, acoustic impedance and attenuation coefficient, approximate 10 mm thickness cylindrical samples were prepared. Two smooth parallel surfaces were required, because the accurate ultrasound propagation path was used to calculate the relevant parameters. These cylindrical samples were also used in the mechanical compression test for elasticity measurement. For thermal properties measurement, samples were made into cylinder shape with 45 mm diameter and 50 mm height.

A phantom container was designed to characterise the elastic properties of TMMs using shear wave elastography. The phantom container (13.8 cm × 11.8 cm × 8.5 cm) was fabricated using perspex material. Inclusions that mimic the properties of tumours were placed into the phantom container at specific locations and embedded in agar gel background, and an opening was prepared for the ultrasound probe. In Figure 3.15, the blue circle indicates the probe opening. The inclusions in different sizes were made using the tumour mould, which consists of two halves with several cavities of different diameter as shown in Figure 3.16. In each isolated cavity of the mould, a tiny hole for exhausting air bubbles was drilled.

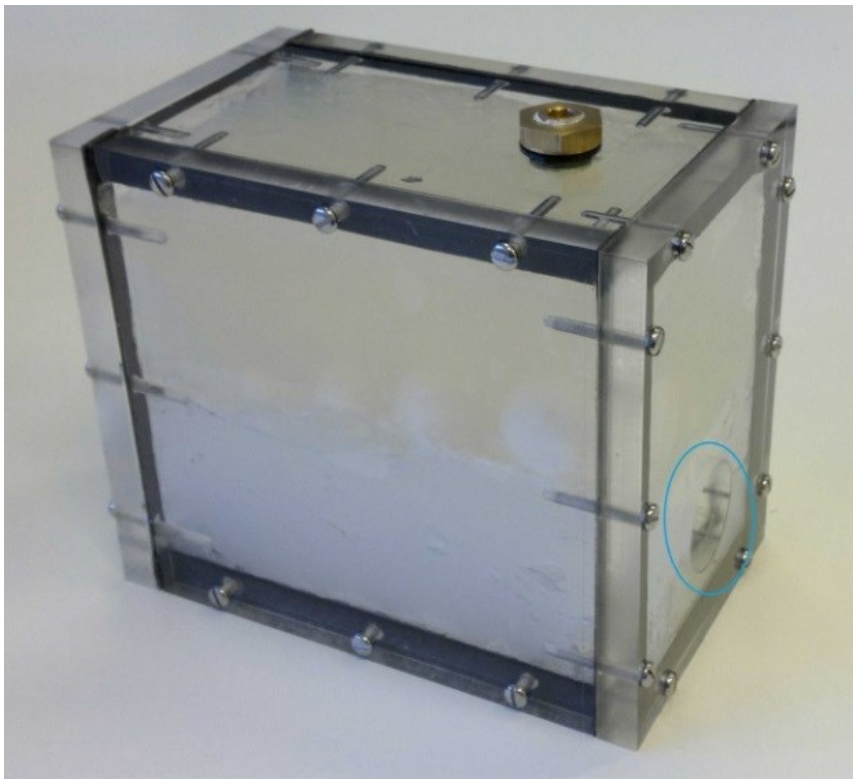

Figure 3.15 Tissue mimicking prostate phantom (the blue circle indicates the opening for ultrasound transrectal probe)

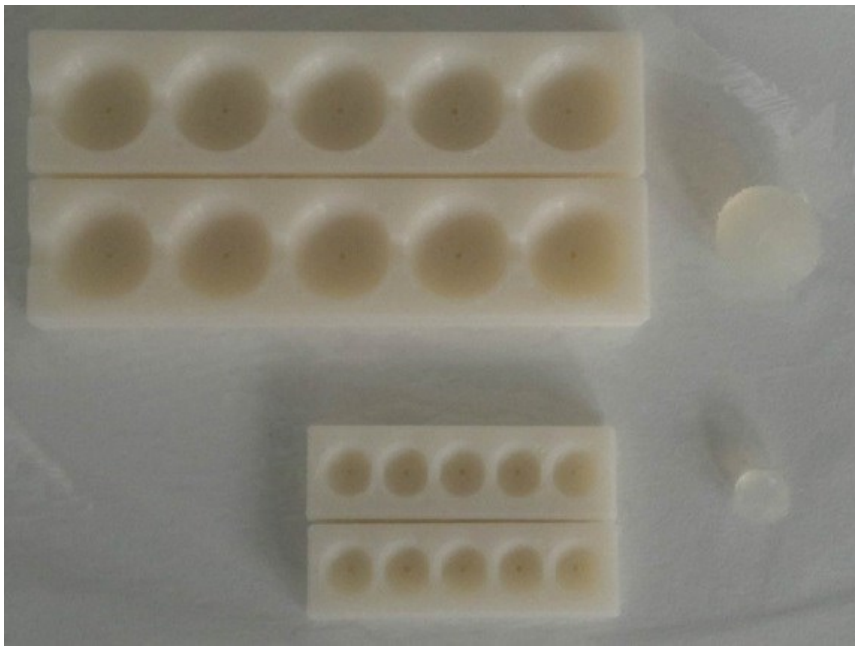

Figure 3.16 Tumour mould used to manufacture the spherical TMM inclusions that are embedded in the TM phantom shown in Figure 3.15

3.3.6. Specimen storage

Specimens were wrapped in cling film and stored in a refrigerator to reduce desiccation. Before the characterisation experiment, they were revered in room temperature for couple of hours.

3.4. Characterisation of Tissue Mimicking Materials for HIFU application

This section reports the characterisation of TMM properties. Material that has similar acoustic impedance and speed of sound to the tissue can provide an efficient path for ultrasonic propagation from the transducer to the target. If there is mismatch of impedance, there is significant reflection and refraction of the ultrasound beam at the interface. Thermal properties are the important factors to estimate the temperature rise in medical ultrasound field. Acoustic and thermal properties of TMMs were investigated to determine the suitable materials for the phantom used as the ultrasound beam path and focal target. Elastic properties of TMMs determined the best material for better imaging quality in the tumour mimicking tissue detection using elastography. Variations in elastic properties of tissues are considered as a good diagnostic sign of diseases such as cancer. Since elastography maps the stiffness of tissue, this medical imaging modality plays an important role in detecting diseased tissue. In order to determine the phantom used as the target in HIFU experiment (in Chapter 4), sonications were performed on DQA gel phantom (a commercial phantom used for HIFU sonication experiment, available from ATS Laboratories Inc., Bridgeport, CT, USA) and PAA egg white phantom to study the formation of the lesions induced by HIFU. Lesion size of each focus was measured after applying sonication on the phantom.

3.4.1. Acoustic properties test

The insertion/substitution technique described by Selfridge (Selfridge 1985) and Zell et al (Zell *et al.* 2007), was applied to measure the acoustic properties in this study. The ultrasound wave propagating from source to receiver with and without the sample in the beam path in a distilled degassed water environment was transmitted and detected

using a matched pair of SLIH transducers (Sonatest, Milton Keynes, UK). They can be used as ultrasound source and receiver respectively, as illustrated in Figure 3.17. The two transducers have to be coaxial to ensure the ultrasound wave completely detected by the receiver. As the frequency of HIFU device and imaging device was different, two pairs of transducers working at different frequencies were used. One pair of transducers have the peak frequency at 2 MHz the other at 4.8 MHz. The 2 MHz transducers were used for HIFU phantoms and the 4.8 MHz ones for imaging phantoms because higher frequency was used in imaging devices to provide a better spatial resolution. An arbitrary waveform/function generator (33220A, Agilent, Santa Clara, CA, USA) connected to the transmitter and was utilised to emit the sinusoidal wave in 5 bursts. A digital oscilloscope (DSOX2004A, Tektronix, Beaverton, OR, USA) was used to monitor the detected sound wave from the receiver transducer. The output of the generator was also connected to the oscilloscope as a reference signal. The sample of the phantom to be measured was inserted between the two transducers during the measurement with two parallel planes orthogonal to the coaxial line of the transducers.

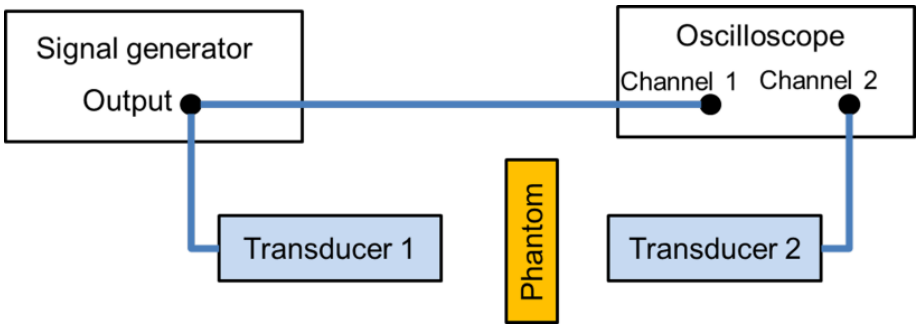

Figure 3.17 Schematic diagram used for the measurement of acoustic properties of tissue mimicking materials

Figure 3.18 shows the experimental setup of the acoustic properties measurement in a water tank. The two transducers were fastened coaxially on the adjustable holders of the tank in degassed water. The original holder for the measured sample can be lift out of the water for placing the sample (black part in Figure 3.18(b)). However, the slot of the original holder was only as narrow as 4 mm and not stable for placing a piece of thicker sample. Therefore, a new sample holder (white part in Figure 3.18(b) and Figure 3.18(c))

with an 8.4 mm width slot was designed and produced, which can be inserted into the original holder of the tank to hold the phantom sample more properly.

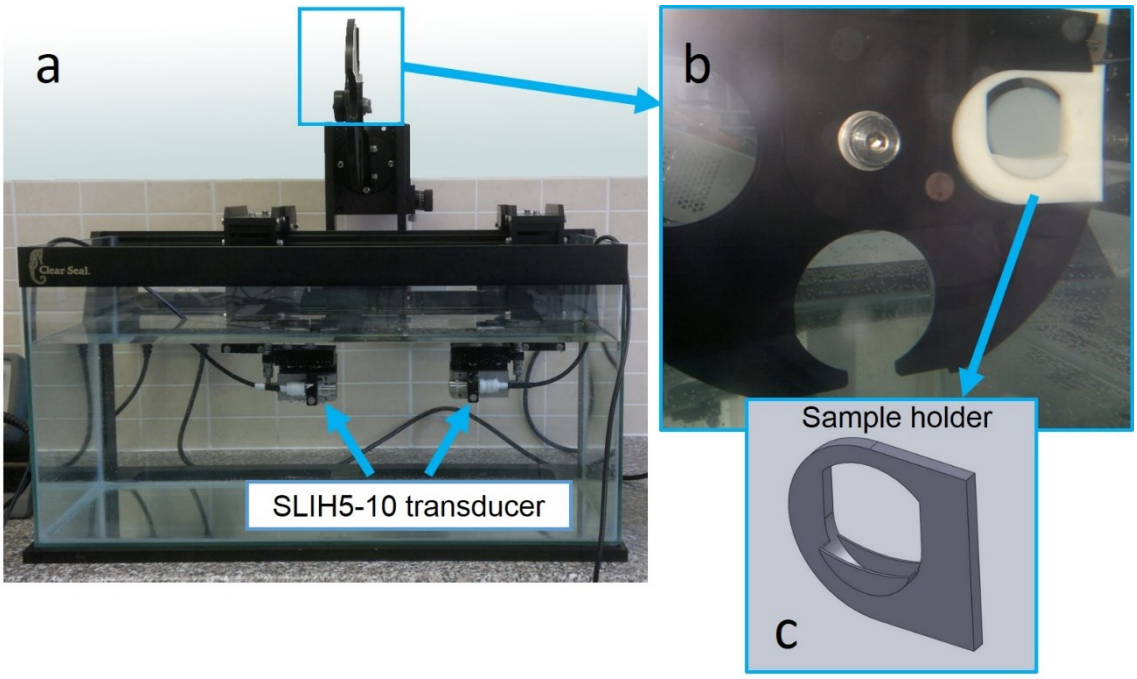

Figure 3.18 Experimental setup of measurement of acoustic properties

To calculate the longitudinal ultrasound velocity and acoustic attenuation coefficient, firstly the wave velocity in water is measured from the propagation time (t_0) of ultrasonic wave in water between the two transducers without the sample:

$$t_0 = \frac{D}{v_w} \tag{3.1}$$

where v_w is the acoustic velocity in water and D is the distance of ultrasound transmission path.

Difference in the transmission times (Δt) with and without the sample is measured. The acoustic sound speed in the sample is given by:

$$v_s = v_w/(1 - \frac{v_w \Delta t}{h}) \tag{3.2}$$

where v_s is the acoustic velocity in the sample and h is the thickness of the sample.

For the acoustic attenuation coefficient, the amplitude of the ultrasonic wave with the sample, and the amplitude of the wave without the sample in place are measured. The acoustic attenuation coefficient (α_s) is then given by:

$$\alpha_s(dB/cm) = \frac{1}{h(cm)} \times 20 \log_{10} \frac{A_w}{\frac{A_s}{T_r^2}} + \alpha_w \tag{3.3}$$

where A_w and A_s denote the amplitude of the received ultrasound pulse, indices w and s representing water and the sample, respectively. α_w is the acoustic attenuation coefficient in water. T_r denotes the transmission coefficient through the sample wall if present. T_r is given by:

$$T_r = \frac{4Z_1Z_2}{(Z_1 + Z_2)^2} \tag{3.4}$$

where Z_1 and Z_2 are the acoustic impedances of water and the sample respectively, depending on velocity (v) and density (ρ). Z is calculated by density multiplying acoustic velocity.

$$Z = v \cdot \rho \tag{3.5}$$

The density (ρ) is obtained by mass divided by volume. The mass of the sample is measured by electronic balance, while its volume is obtained through measuring the sample mould's volume.

The attenuation in water is $\alpha_w = 2.5 \times 10^{-4} f^2$, where the frequency f is given in MHz, and is ignored since it is small.

To measure the acoustic properties of ABS material, a square sheet of ABS material was produced by the prototyping machine (Figure 3.19). For more accurate measurement, four thicknesses were used (1.12 mm, 1.62 mm, 2.16 mm, and 2.66 mm). The procedure of the acoustic properties measurement was the same as the measurement of TMM using the insertion/substitution technique and result was calculated according to equations 3.1 to 3.5.

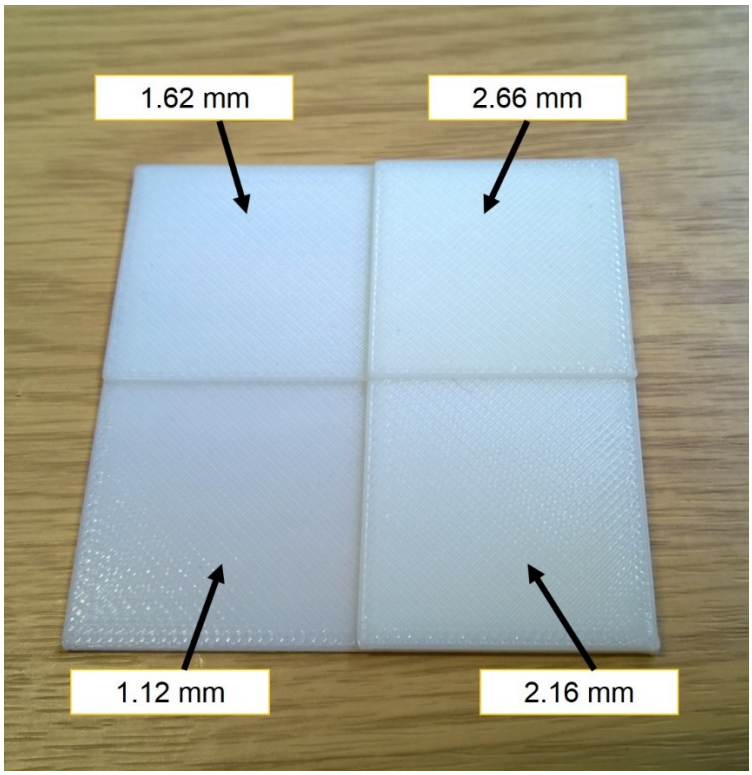

Figure 3.19 Sample of ABS material with different thickness

3.4.2. Thermal properties test

The step-wise transient plane source method (Kubicar & Bohac 2000; Gao *et al.* 2012) was applied to measure the thermal properties of TMM phantoms. Figure 3.20 depicts the setup including a block of phantom, a thermocouple and a heat source. The specimen to be measured is divided into three sections: A, B and C. A thin layer planar heat source (represented by red line in Figure 3.20) is located between layer A and B to provide heat from the inside of the specimen. A thermocouple (blue line in Figure 3.20) is placed between layer B and C parallel to the heat source plane to record the temperature change during the heating and cooling procedure. The temperature response $T(x, t)$ at a distance x from the heat source plane was recorded and used to calculate the thermal properties.

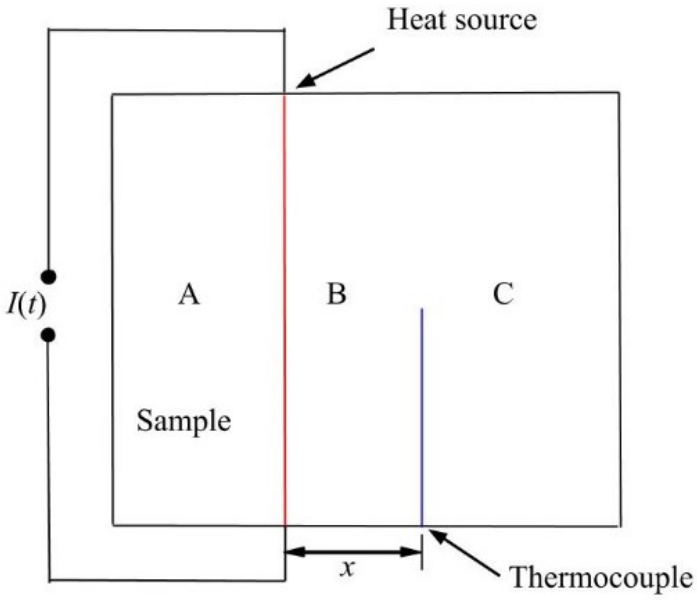

Figure 3.20 Principle of the step-wise method

In the experimental setup in Figure 3.21, the phantom specimen was prepared into cylinders with 45 mm diameter and 50 mm height. They were wrapped and fixed by specifically designed foam plastic shells to reduce heat loss. The white prototyped shell was used for holding the blue shells. A 53 mm diameter, 408 Ω heat source planar (Kapton heater, Omega Engineering, UK) was placed between the two pieces of specimens and fully contacted with each of them. Two thermocouples (Type K thermocouple, T.M. Electronics Ltd., Sussex, UK), the metal wires as seen in Figure 3.21, were inserted into the centre of one piece of specimen through the holes on the shell at distance x = 9 mm and 15 mm from the heat source plane. An 8-Channel Thermocouple Input USB Data Acquisition DAQ Device (USB-TC, Measurement Computing Corporation, Norton, MA, USA) was used to collect data from the two thermocouples. The heat source was driven at 6 Watts.

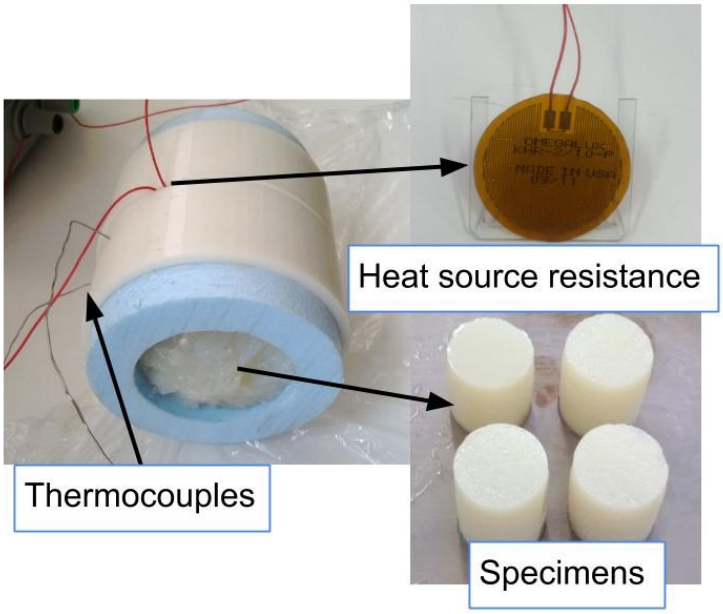

Figure 3.21 Experimental setup of thermal properties measurement

Theoretical calculation assuming the test specimens have no heat exchange with surrounding environment and the thickness of the heat source is zero, the measurement can be considered as the one-dimensional unsteady-state heat conduction problem in a semi-infinite solid (Carslaw & Jaeger 1959):

$$T(x,t) = \frac{q}{k}\left[2\sqrt{\frac{\alpha t}{\pi}}\exp\left(-\frac{x^2}{4\alpha t}\right) - x\,erfc\left(\frac{x}{\sqrt{4\alpha t}}\right)\right] \tag{3.6}$$

where $T = T(x,t)$ is the temperature change during time t, α denotes the thermal diffusivity, k represents the thermal conductivity, and q is the imposed constant heat flux. In the case of the step-wise method, q is given as:

$$q = \begin{cases} 0 (t = 0) \\ \dfrac{I^2 R}{2A} (t > 0) \end{cases} \tag{3.7}$$

where I is the electric current, R is the resistance of the heat source, and A is the area of the heat source. $erfc(x)$ is the complementary error function, defined as:

$$erfc(x) = 1 - \frac{2}{\sqrt{\pi}}\int_0^x e^{-t^2} dt \tag{3.8}$$

Therefore, for the following equation:

$$k = \rho \cdot \alpha \cdot c \tag{3.9}$$

where ρ is the density of the sample, the required thermal parameters in equation 3.6, α (thermal diffusivity) and c (specific heat capacity) can be estimated simultaneously using the curve fitting method by MATLAB (The MathWorks, Inc., Natick, MA, USA). The thermal conductivity (k) can then be calculated from equation 3.9.

3.4.3. Elasticity test

Phantoms manufactured from these TMMs provide tissue substitutes in ultrasound and elastography research by simulating normal and diseased tissues. Young's modulus is an important parameter for elastography phantoms. Two methods were used here, shear wave elastography machine and mechanical compression test to measure the elastic properties of samples made of TMMs.

3.4.3.1 Young's modulus measurement using the Aixplorer

ShearWave^{TM} elastography, is a quantitative method for imaging the elasticity of biological tissues. It is capable of providing quantitative result by displaying a colour coded image superimposed on a B-mode image (Bercoff *et al.* 2004; Bercoff *et al.* 2008). Supersonic Imagine Aixplorer® (SuperSonic Imagine, Aix-en-Provence, France) is the machine that uses shear wave velocity to estimate the stiffness of the TMMs in this study. To display the elasticity result on the screen of the system, transient shear waves are produced and captured using the Supersonic Shear Imaging method (Bercoff *et al.* 2004).

The measurement can be carried out in the phantom container described in Figure 3.15, as it includes the TMMs inside and provides a probe opening for the imaging transducer. In Figure 3.22 the side view of the phantom container, the imaging transducer can scan the tumour phantom (blue rectangular) via the probe opening at the bottom of the container.

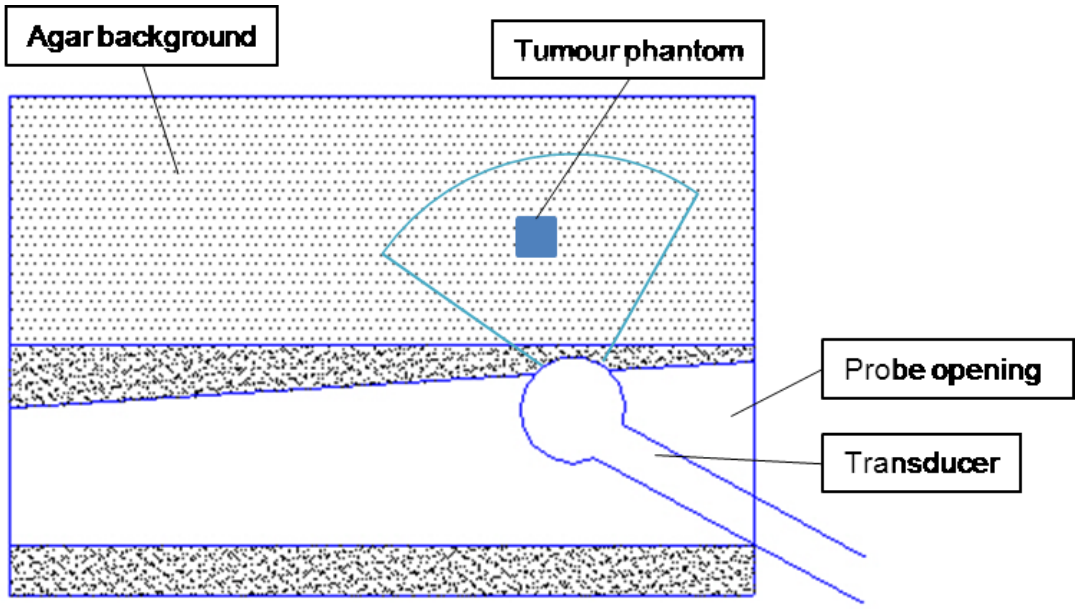

Figure 3.22 Schematic diagram showing placement of TMMs in agar background at different levels in relation to the imaging probe

For the measurement using the Aixplorer machine, TMMs were prepared in different shapes to indicate different materials of the tumour phantom. The samples to be measured were placed into the phantom container, as shown in Figure 3.15, with 2% agar gel as the background, as this low concentration of agar is clear enough to observe the inclusions by eye to guide the insertion of the imaging probe of the Aixplorer machine into the probe opening on the phantom container. Cancer mimicking inclusions were implanted into the background phantom at different depths to investigate the effect of distance on the shear wave velocity measurement.

Figure 3.23 is the elastography image of the tumour mimicking phantom acquired by the Aixplorer. The shear wave propagation speed in tissue or phantom was computed at each pixel and shown on the final speed map. The black and white B-scan image is on the bottom of this figure, while the shear wave elastography with a colour coded image superimposed on the B-mode image is displayed on the top. The colour bar on the top right indicates the elasticity value of the colour map.

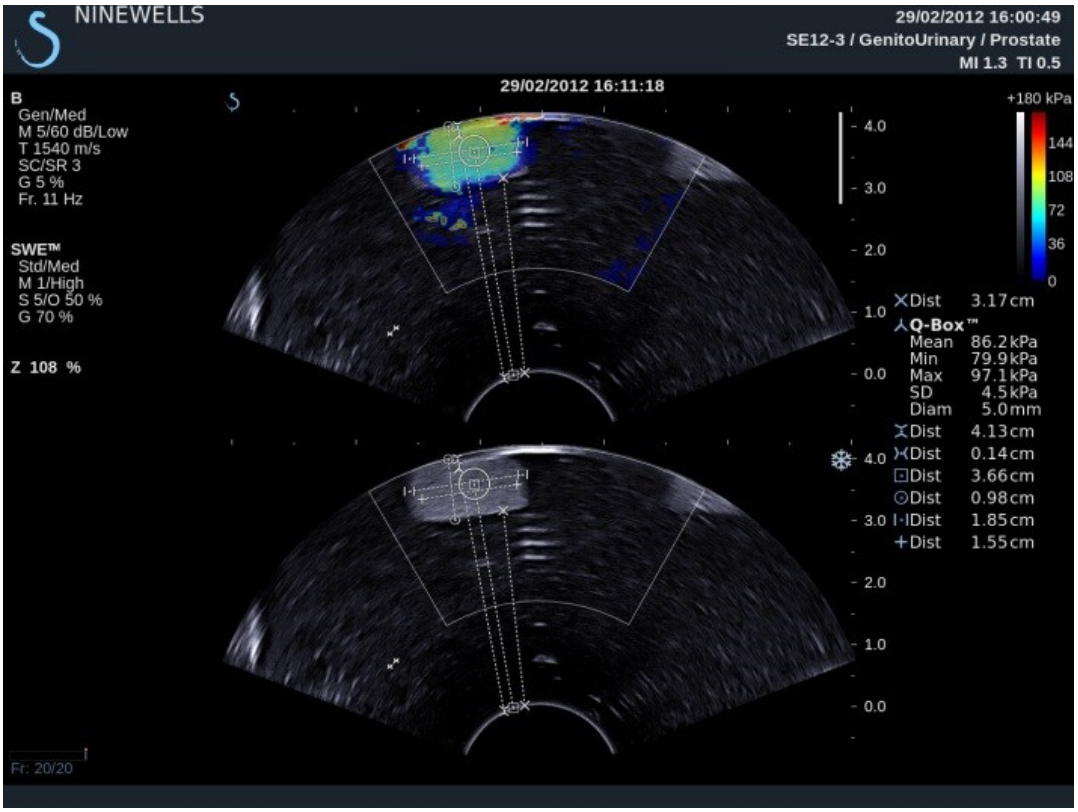

Figure 3.23 Quantitative estimation of Young's modulus in the TMM phantom using the Supersonic Imagine Aixplorer system

3.4.3.2 Young's modulus measurement by mechanical compression

A mechanical compression test was used to measure the Young's modulus using Tinius Olsen's line of Benchtop Materials Testing Machine (Tinius Olsen, Horsham, PA, USA) (Figure 3.24). The machine has two plates, one fixed on the base, the other on the column is connected to a force sensor and move up and down to stretch and compress the samples. The force change is measured by the force sensor in real time. The relation of stress-strain can be acquired and then applied to deduce the Young's modulus of the samples using a quasi-static measurement.

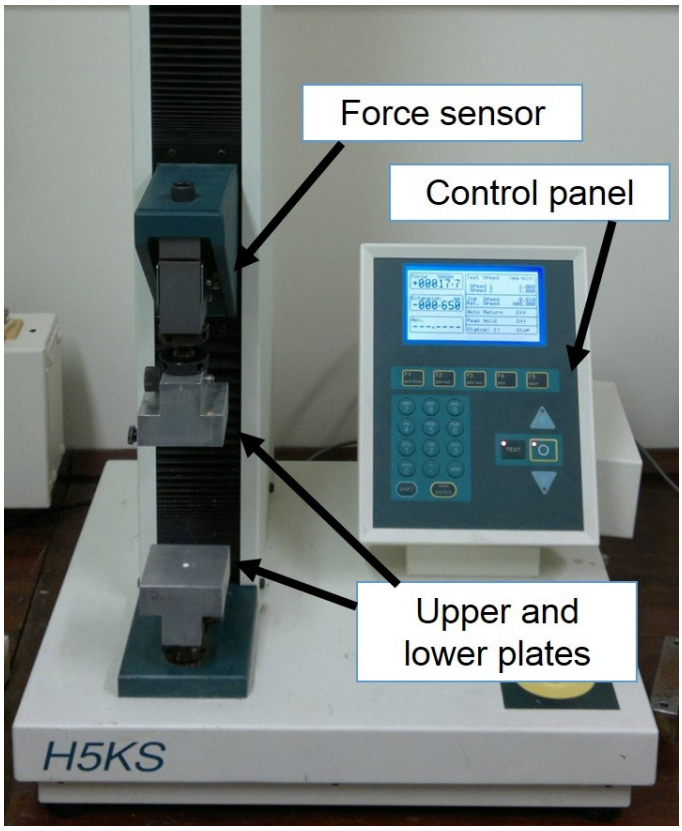

Figure 3.24 Benchtop Materials Testing Machine

A 5000 N load sensor (force accuracy: ± 0.5% of the indicated load) was applied to provide mechanical compression force to the sample. TMMs were fabricated in cylindrical samples with two parallel surfaces. To minimize the effects of the interface friction and the dehydration of the samples, the samples were dipped in water before the compression experiment. For the measurement, samples were placed onto the low plate of the testing machine. Full contact was needed between the top testing plate and the sample surface, and the compression was then applied after a 1 N to 2 N preload. The lower plate was fixed while the top one was moved downward at a rate of 0.5 mm/min (speed accuracy: ± 0.005% of set speed). A 2 mm quasi-static displacement was applied and a plot of force-displacement relationship was obtained using QMat Professional software (Tinius Olsen, Horsham, PA, USA), thus calculated a stress-strain relationship. With the known constant parameters of the area and the thickness of the samples, the Young's modulus was obtained by:

$$E = \frac{\sigma}{\varepsilon} = \frac{F/A_0}{\Delta L/L_0} \tag{3.10}$$

where:

E is the Young's modulus (modulus of elasticity);

σ is the stress;

ε is the strain;

F is the force exerted on an object under tension;

A_0 is the original cross-sectional area through which the force is applied;

ΔL is the amount by which the length of the object changes;

L_0 is the original length of the sample.

3.4.4. HIFU sonication test

Even if the TMMs possessed similar acoustic, thermal and elastic properties to the human or animal tissues, this does not prove that these materials are suitable as a focal target for HIFU sonication. In fact, agar and PVA both have low melting temperatures and could melt during the sonication. The PAA egg white phantom not only has similar acoustic properties to tissues, it can also provide visualisation of lesions of HIFU sonication due to protein denaturation. DQA gel as a commercial phantom has the capability of reuse as the target phantom for HIFU sonication.

The work in this section was designed to determine the best phantom as the target in the HIFU sonication through ribcage. For this purpose, HIFU sonications were performed on DQA gel phantom and PAA egg white phantom and the size of the lesions on these two phantoms caused by HIFU was investigated.

The PAA egg white phantom was fabricated following the procedures described in section 3.3. It was made into a 135 mm × 90 mm × 35 mm cuboid for better visualisation of the sonicated lesions. A transducer made in house using PZ26 (Ferroperm Piezoceramics A/S, Kvistgaard, Denmark) piezo-material, was used to perform the HIFU sonication on PAA egg white phantom. The parameters of the transducer is summarised in Table 3.2.

Table 3.2 Transducer parameters

Parameters	Value
Frequency	1.107 MHz
Diameter	64 mm
Focal length	63 mm

It was driven by the waveform/function generator (33220A, Agilent, Santa Clara, CA, USA) and the output was amplified by the power amplifier (1020L RF Amplifier, Electronics & Innovation, Ltd., Rochester, NY, USA). Continuous wave mode and pulse wave mode were applied to drive the transducer. The continuous wave cannot be used for long to prevent the transducer from damage by overheating. The pulse mode can extend the overall time by allowing some rest time during the HIFU application. For the pulse mode, the duty cycle determines the percentage of time of the sonication. The burst period indicated the overall time of one burst including the sonication time and the resting time. Different duty cycle (50% and 70%) and burst period (in the range of 90.90 μs and 129.86 μs) were applied in the sonication on PAA egg white phantom.

Another PAA egg white phantom was produced for the sonication using ExAblate 2000 system (InSightec, Tirat Carmel, Haifa, Israel) using 60 W acoustic power and 30 s sonication time. Nine sonications were applied on the phantom. The ExAblate system is compatible with MRI and the phantom was imaged in a GE Signa HDxt 1.5T scanner (GE Healthcare, Waukesha, WI, USA), which was also used for temperature measurement. The MRI thermometry applied proton resonance frequency (PRF) shift, which based on the fact that the water proton resonance frequency changes with temperature and such change can be calculated from the phase of the gradient echo image (Ishihara *et al.* 1995).

DQA gel phantom was sonicated by ExAblate 2000 system using 50 W acoustic power over different times ranged from 20 s to 60 s. At minimum of 3 sonications were applied at each duration time. Because the DQA gel phantom can re-solidify after an enough cooling time, the lesion resulted from HIFU can only be measured during the sonication. MRI thermometry provided monitoring of the focal temperature and was used

to depict the size of the focus on thermometry images according to the threshold of a selected temperature value.

3.4.5. Results and discussion

3.4.5.1 Acoustic properties test

In terms of TMMs for imaging, the acoustic properties measured using 4.8 MHz are summarised in Table 3.3, including agar of different concentrations along with Al_2O_3, polyacrylamide, polyacrylamide mixed with Al_2O_3 and silicone.

Table 3.3 Acoustic velocity, density, impedance and attenuation coefficient of TMMs at 4.8 MHz (at room temperature 20 °C)

Phantom	Acoustic velocity (m/s)	Density (10^3 kg/m^3)	Impedance (Mrayl)	Attenuation coefficient (dB/cm/MHz)
2% agar+1%Al_2O_3	1519±49	1.02±0.02	1.55±0.05	0.78±0.04
3% agar+1%Al_2O_3	1522±40	1.03±0.03	1.57±0.07	0.61±0.04
4% agar+1%Al_2O_3	1535±42	1.05±0.01	1.61±0.03	0.62±0.03
5% agar+1%Al_2O_3	1528±57	1.06±0.02	1.59±0.08	0.50±0.03
PAA	1469±20	0.96±0.05	1.42±0.06	0.26±0.04
PAA+2%Al_2O_3	1472±32	1.01±0.03	1.49±0.05	0.70±0.04
Silicone	1188±39	0.98±0.03	1.15±0.08	4.09±0.44

For the materials used in HIFU sonication experiment, including DQA gel phantom, PVA phantom and ABS material, a lower frequency was applied in the acoustic properties measurement, because the frequency of operating HIFU transducer was around 1 MHz. The lowest working frequency of ultrasonic transducers SLIH2-10 (Sonatest, Milton Keynes, UK) for properties measurement in our laboratory worked at 2 MHz. Its frequency can reach as low as 1.5 MHz. Thus, 1.5 MHz to 2.0 MHz was selected as the range of this measurement. The density of the DQA phantom was 1048.92 kg/m^3. Results

of acoustic properties of DQA gel phantom, including the speed of sound and acoustic attenuation coefficient, and their variation with frequency are depicted in Figure 3.25. The speed of sound ranged from 1495.2 ± 35.33 m/s to 1497.3 ± 46.83 m/s within the investigation frequency range of 1.5 MHz to 2.0 MHz. The acoustic attenuation increased when applying higher frequency in the measurement.

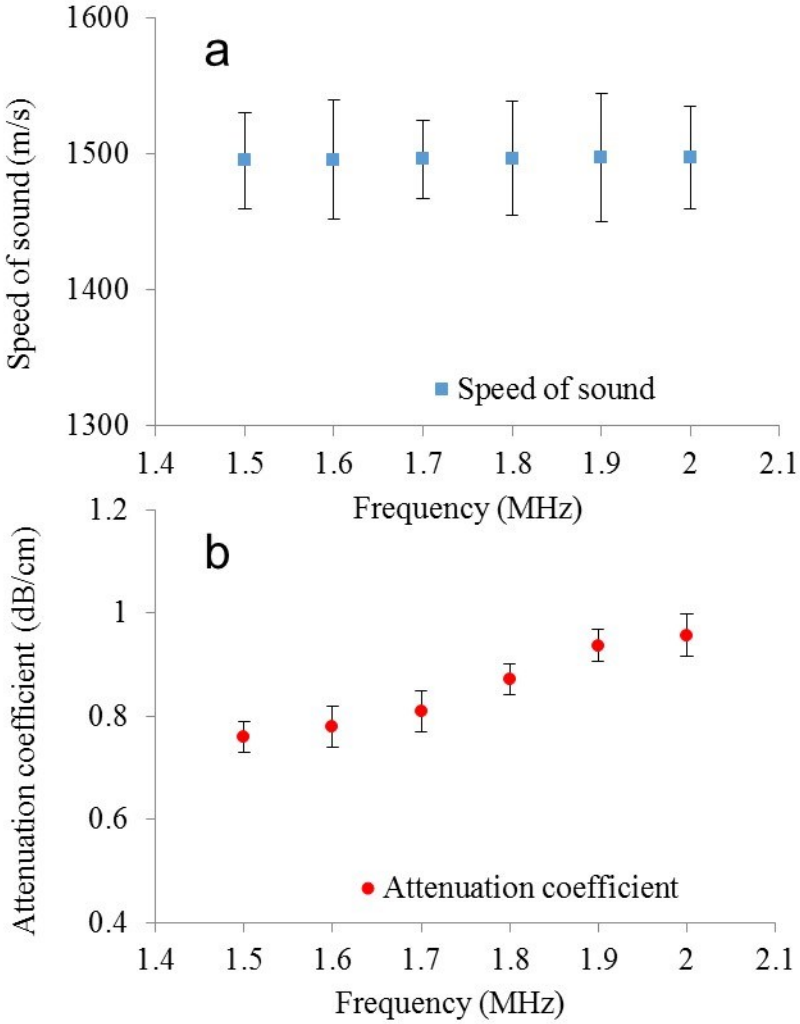

Figure 3.25 Acoustic properties of DQA gel phantom (a. Speed of sound; b. Attenuation coefficient)

In terms of the PVA gel phantom, the frequency range of 1.5 MHz to 2.0 MHz was applied in the measurement of its acoustic properties. The PVA phantom has the density of 1050.00 kg/m^3. Results of acoustic properties of PVA gel phantom, including

the speed of sound and acoustic attenuation coefficient, and their variation with frequency are displayed in Figure 3.26. The acoustic attenuation coefficient rose in general when increasing the measurement frequency.

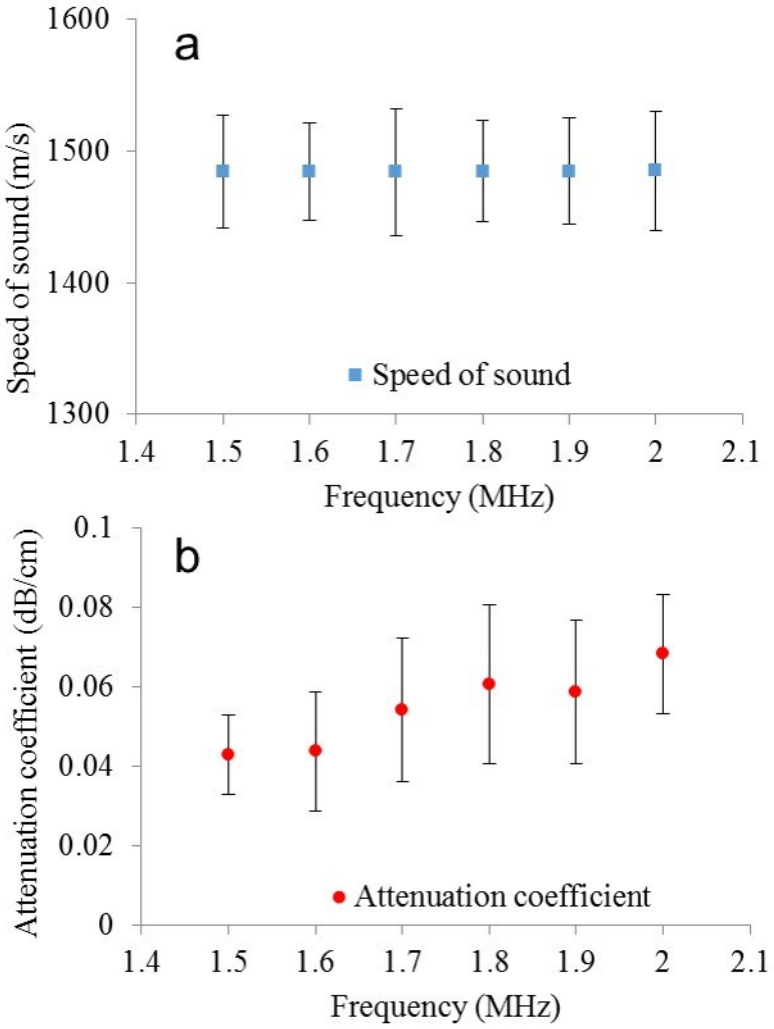

Figure 3.26 Acoustic properties of PVA gel phantom (a. Speed of sound; b. Attenuation coefficient)

As mentioned in section 2.4.2, a wide range of sound speed was found in the previous measurement results. The average value was 1576 m/s in the range of 1478 m/s in fat and 1595 m/s in liver (Table 2.3). PVA, PAA or agar materials are all capable of mimicking the soft tissues. The only disadvantage of PVA was that its attenuation coefficient was found lower than that in soft tissues.

In terms of the ABS material for the ribcage model, the density of it was 767.5 kg/m^3, and the speed of ultrasound in ABS was 1717 ± 63 m/s. The ultrasound attenuation coefficient of ABS was 46.2 ± 2.6 dB/cm/MHz measured at 2 MHz. According to acoustic properties in Table 2.3, the acoustic properties of ABS material were within the range of bone acoustic properties and ABS was able to be the substitute material of ribcage.

3.4.5.2 Thermal properties test

Figure 3.27 shows the temperature rise acquired in the experiment (blue dots) and by the curve fitting (red dots). The thermal properties of TMMs were summarised in Table 3.4. The thermal diffusivity and specific heat capacity of the TMMs were determined by curve fitting according to the experimental data. Both of the two parameters descend within the agar concentration ranged from 2% to 5%. The thermal conductivity, which was calculated from the previously measured parameters and the density of the material, also decreases with the agar concentration.

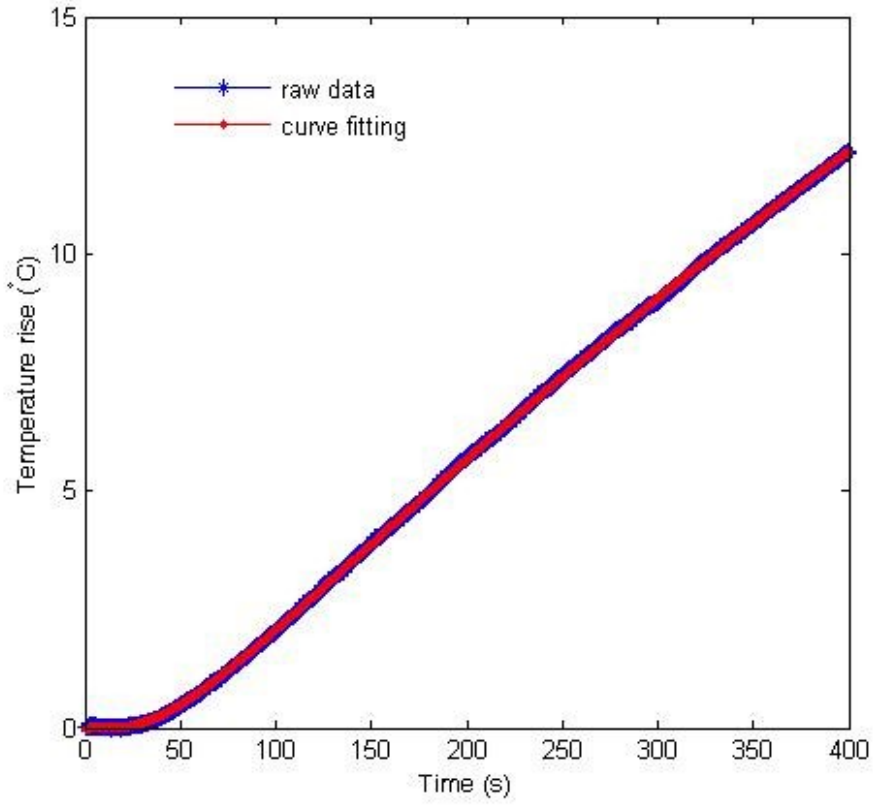

Figure 3.27 Temperature rise in heating period on 2% agar phantom (blue dots: raw data in the measurement; red dots: curve fitting results)

Table 3.4 Thermal properties of tissue mimicking materials

TMMs	Thermal conductivity k ($W \cdot m^{-1} \cdot °C^{-1}$)	Thermal diffusivity α ($m^2 \cdot s^{-1}$)	Specific heat capacity c ($J \cdot kg^{-1} \cdot °C^{-1}$)
2% agar	0.74±0.05	$(1.87\pm0.06)\times10^{-7}$	3883.5±99.8
3% agar	0.67±0.04	$(1.81\pm0.03)\times10^{-7}$	3627.3±83.9
4% agar	0.51±0.07	$(1.57\pm0.06)\times10^{-7}$	3096.3±132.5
5% agar	0.43±0.05	$(1.39\pm0.05)\times10^{-7}$	2999.0±109.2
DQA	0.62±0.03	$(1.51\pm0.05)\times10^{-7}$	3886.3±101.3

According to the range of thermal properties in soft tissues summarised in Table 2.6, all of the selected materials were qualified to mimic soft tissues in HIFU sonication experiment.

Errors do exist in the measurement reported here. The problems of the step-wise transient method mainly result from differences between the ideal model and the real experimental setup (Gao *et al.* 2012). The size of the sample was limited rather than geometrically non-limited size in the ideal model. The sample was assumed to have no heat exchange with the surrounding environment, but the experiment was performed in not vacuum. The thickness of the heat source, the heat capacity of the thermocouple and the mass of the thermocouple are negligible in the ideal model. Finally, in the ideal model, the heat source was considered to possess the equivalent thermal properties to the sample. This cannot be achieved in this experiment.

3.4.5.3 Elasticity test

3.4.5.3.1 Shear wave measurements

Stiffness quantification of the TMMs using shear wave imaging provided estimated Young's modulus values of 86.2 ± 4.5 kPa for PAA mixed with 2% Al_2O_3 particles and 271.5 ± 25.7 kPa for silicone respectively. The results for the different TMMs are listed in Table 3.5.

Table 3.5 Effect of depth on cancer mimicking phantom elasticity and width measurement

Phantom	Depth (±0.5 mm)	Young's modulus (kPa)	Measured width (±0.5 mm)
PAA+2%Al_2O_3	64.0	84.6±26.8	NA
	52.4	93.8±4.4	11.5
	43.8	78.9±5.8	14.6
	36.6	86.2±4.5	16.5
Silicone	30.6	271.5±25.7	NA

PAA with a 2% Al_2O_3 concentration in an 18.5 mm width cubic shape was utilised to merge into agar background to investigate the effect of depth on the target. Distance between pixels on the colour coded image (Figure 3.23) can be measured using 'Meas. Tools' of the Aixplorer system. No clear trend was observed in the mean values of the Young's modulus values obtained at different depths. However the standard deviation of Young's modulus demonstrated an increasing trend with depth. The measured width of the target phantom increased with a decrease of depth (Figure 3.28). At 64.0 mm depth, PAA with 2% Al_2O_3 phantom had higher standard deviation which reached ± 26.8 kPa but was similar to the standard deviation (SD) of silicone at 30.6 mm depth, ± 25.7 kPa. The standard deviations of the depth within 52.4 mm were all less than ± 5.8 kPa. The measured width of 16.5 mm at 36.6 mm distance approached to the real width value most compared with those at further depth.

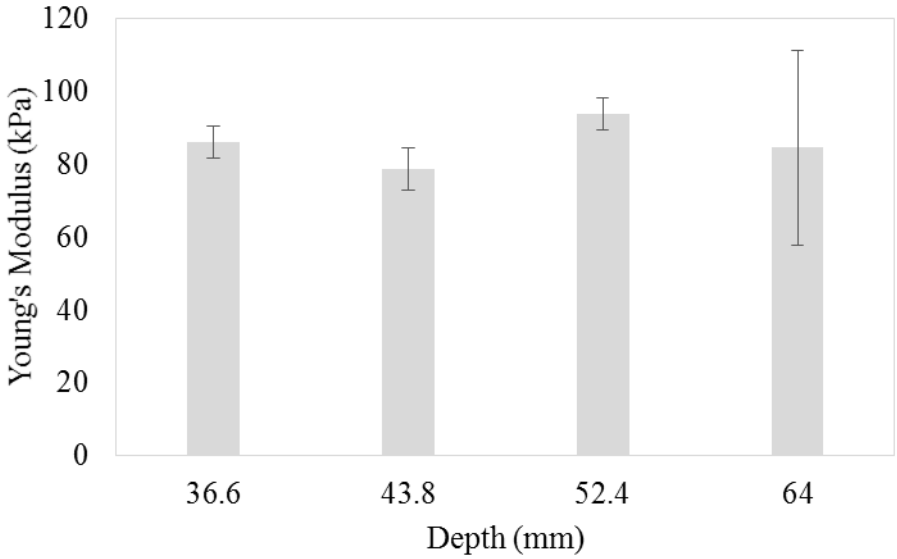

Figure 3.28 Young's Modulus and standard deviation of PAA with 2% Al_2O_3 measured by shear wave elastography at different depth

The standard deviation of Young's modulus measured using the Aixplorer was affected by the target depth. Measurements at larger depths about 64.0 mm showed low reliability with as large as ± 26.8 kPa standard deviation. The standard deviation was reduced for depths of 50 mm or less. The errors could be due to tissue attenuation at a higher depth. The cross section of the TM phantom inclusion interrogated by the system could also introduce some errors if surrounding background material is included in the measurements. However, the measurements up to a depth of 5 cm are fairly consistent with lower standard deviations. Measurements were performed using a transrectal transducer, where the ultrasound beams diverge with depth. This may also account for errors in the width measurements for shear wave images. Further research is needed to explore these factors in detail.

3.4.5.3.2 Elasticity of phantoms using mechanical compression testing

Using mechanical compression method, TMM phantoms showed a clear trend of higher Young's Modulus with an increased agar concentrations for the same 1% Al_2O_3 level as seen in Table 3.6. Silicone TMM had higher Young's modulus values when compared with PAA with 2% Al_2O_3. The Young's modulus of silicone compared favourably with the stiffness value obtained with the 3% agar and 1% Al_2O_3 TMM. PAA

with 2% Al_2O_3 TMM had the smallest Young's modulus value of 104.3 ± 5.6 kPa and can be utilised to mimic prostate cancer especially for quasi-static elastography at a 2% pre-compression level (Krouskop *et al.* 1998), while TMM utilizing an appropriate concentration between 2 - 3% can produce TMMs to mimic tumour at a 4% pre-compression level (Krouskop *et al.* 1998).

Table 3.6 Young's modulus results of TMM phantoms from Mechanical compression test

Phantom	Young's modulus (kPa)
2% agar + 1% Al_2O_3	157.8±9.2
3% agar + 1% Al_2O_3	299.4±7.1
4% agar + 1% Al_2O_3	331.8±8.8
5% agar + 1% Al_2O_3	443.0±11.3
PAA+2% Al_2O_3	104.3±5.6
Silicone	297.3±6.7

A comparison between the Young's modulus measurements obtained using shear wave elastography from the Aixplorer and using mechanical compression testing is summarised in Figure 3.29. In general, quasi-static mechanical testing provided higher values of Young's modulus for the same TMM.

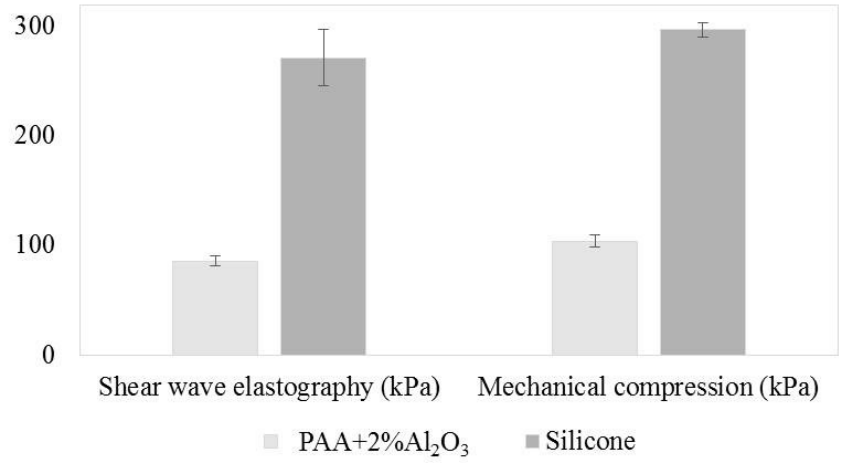

Figure 3.29 Comparison of the Young's modulus values obtained by tracking the shear waves using the Supersonic Imagine Aixplorer system and mechanical compression test

As stated in Table 2.8, the Young's Modulus range of tumour tissues was between 30.1 kPa to 221 kPa. Amongst the phantom materials, PAA with 2% Al_2O_3 possessed Young's modulus values closer to human prostate and liver tumours. Silicone used for tumour mimicking materials can be distinguished in elasticity images, but the stiffness of silicone was almost three times higher than Young's modulus of prostate cancer and much higher than that of liver cancerous tissue. What is more, the ultrasound velocity in silicone was lower than that in human tissues which could result in unrealistic refraction at the boundary of a simulated cancer phantom. Therefore, PAA with 2% Al_2O_3 provided the best fit to mimic tumour tissues.

A limitation of this study is related to the desiccation of the TMMs samples. The elastic properties of TMMs are time and moisture dependent. The samples were wrapped with cling film and stored in refrigerator to reduce desiccation and they were coated with water or gel to minimize the dehydration during the mechanical compression test.

3.4.5.4 HIFU sonication test

The HIFU has a cigar-shaped focal volume and creates elliptical lesions within the tissue or phantom. The size of the focal lesion can be represented by the length of the lesion and the diameter of its ellipsoid cross section. In Figure 3.30(a), lesions of the protein denaturation located within the phantom are obvious. The numbers on this figure indicate the sequence of the sonication as listed in the first column of Table 3.7. The

yellow circle in Figure 3.30(b) shows the longitudinal section of lesion 1 acquired by SonixTablet (ULTRASONIX, British Columbia, Canada). The diameter and length of the lesions on the PAA egg white phantom caused by single element HIFU transducer are reported in Table 3.7. The parameters of each sonication, input power, sonication time, and duty cycle, are included in the table.

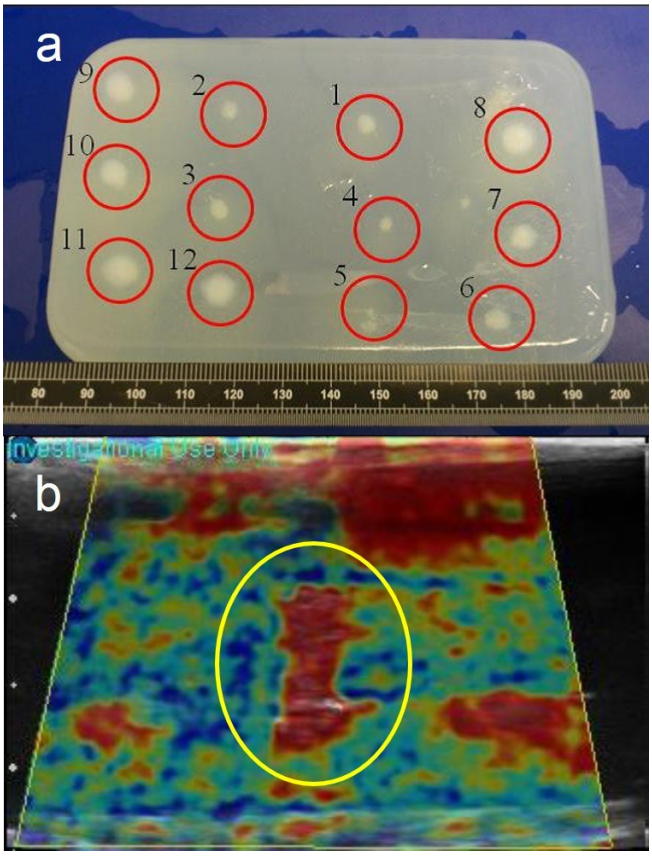

Figure 3.30 Lesions on PAA egg white phantom (a. 12 lesions on the phantom; b. longitudinal section of lesion 1 indicated by the yellow circle)

Table 3.7 Parameters of HIFU and size of lesions on PAA egg white phantom induced by HIFU (1 to 5 used continuous wave; 6 to 12 used pulse wave)

No.	Freq. (MHz)	Input electric power (W)	Duty cycle (%)	Burst period (μs)	Total time (min)	Diameter (mm)	Length (mm)
1	1.107	40	NA	NA	3	3.5	9
2	1.107	40	NA	NA	4	4	5.5
3	1.107	40	NA	NA	5	5	9
4	1.107	40	NA	NA	6	2.5	10
5	1.107	40	NA	NA	7	3	6
6	1.107	40	50	90.90	8	5	13
7	1.107	40	50	127.26	8	6	13
8	1.107	40	70	90.90	8	7	10
9	1.107	50	70	90.90	8	7	15
10	1.107	40	70	129.86	8	6	14
11	1.107	50	70	129.86	8	7	16
12	1.107	50	70	129.86	15	8	21

Dimensions were found not closely related to the energy applied. For lesion 1 to 5 using 40 W input power, the lesion size did not expand (either in diameter or length) related to the increase of sonication time. Using the same input power (40 W) and burst period (90.90 μs), lesion 8 generated by a higher duty cycle 70% was bigger in diameter but smaller in length than lesion 6 produced by 50% duty cycle. There was no obvious trend in the changes of lesion size from increasing the duty cycle or sonication time. These could be explained by the inhomogeneity of the PAA egg white phantom. The egg white was difficult homogeneous to be mixed with the polyacrylamide.

In the sonication on PAA egg white phantom using the ExAblate 2000, 60 W acoustic power and 30 s duration time was used in every sonication. The thermometry images were utilised to evaluate the lesion size by colouring the focal region above 50 °C

(baseline temperature of the system was body temperature 37 °C). These images were acquired after each single sonication. The red area within the blue rectangular on each subfigure of Figure 3.31 indicates the focal lesion. The blue rectangular was the planned focus location. There were only three lesions (sonication No. 1, 6, 8) producing obvious protein necrosis (lesion turned white). These three focal lesions appear a larger area compared with the other sonications as shown in Figure 3.31. Some sonications caused a very small lesion area that over 50 °C, such as lesion 4 and lesion 7. This also proved that the PAA egg white phantom could be inhomogeneous.

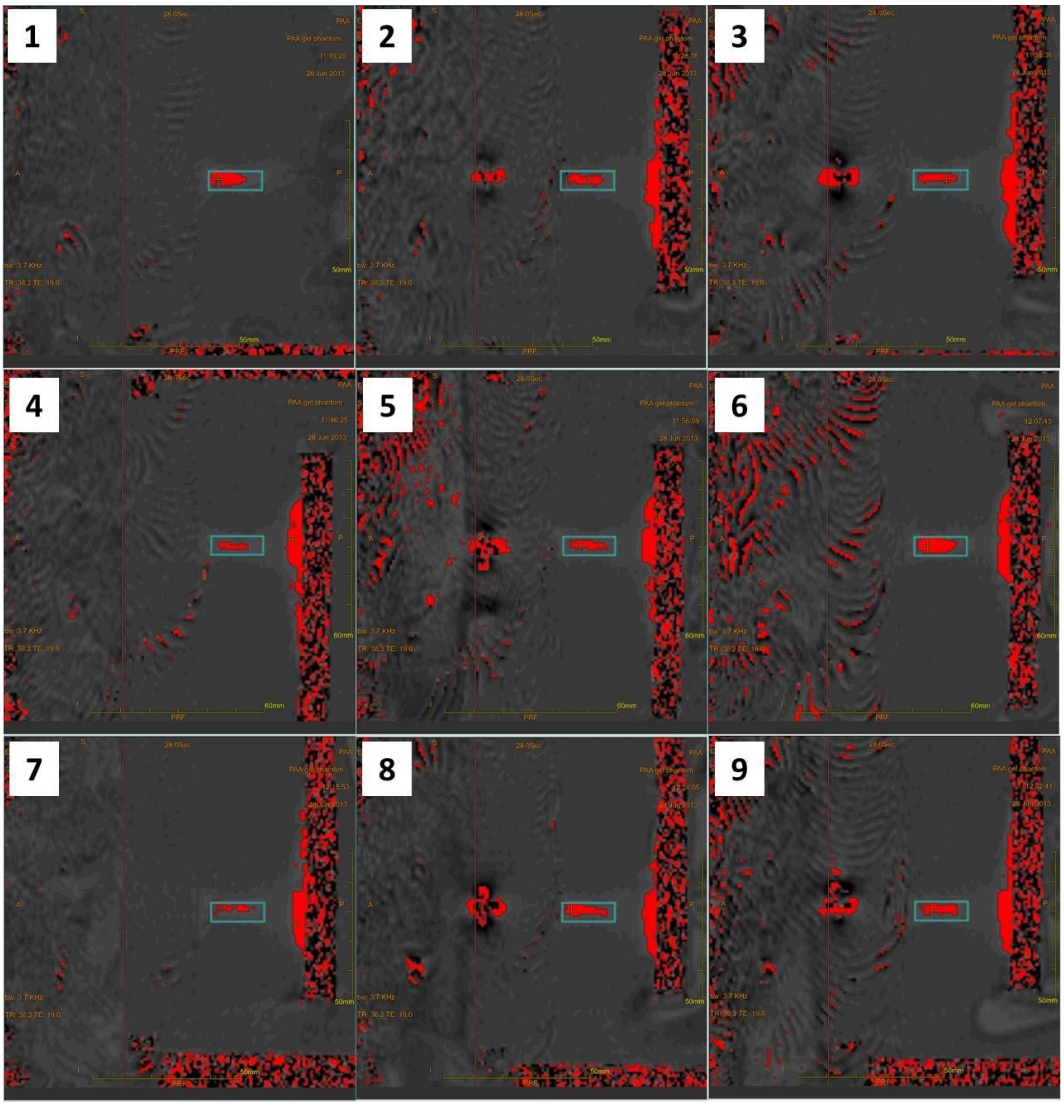

Figure 3.31 Focal lesion over 50 °C using 60 W acoustic power for 30 s on PAA egg white phantom acquired by MRI thermometry using ExAblate 2000 system (the number on each subfigure is the sonication number; red area indicates the focal region over 50 °C; blue rectangular represents the planned location of the focus)

For the sonications on DQA gel phantom using ExAblate 2000 system, the lesion size was also estimated by colouring the focal region over 50 °C (system baseline temperature was 37 °C). All the sonications applied constant a 50 W acoustic power but over different times in the range of 20 s to 60 s. Longer sonication times resulted in a larger lesion as shown in Figure 3.32. Lengths and diameters of the lesions are listed in Table 3.8. It is noticeable that the dimension of the focal lesion increased with the time of sonication, which suggests that the DQA gel phantom is more suitable as a target phantom in HIFU sonication.

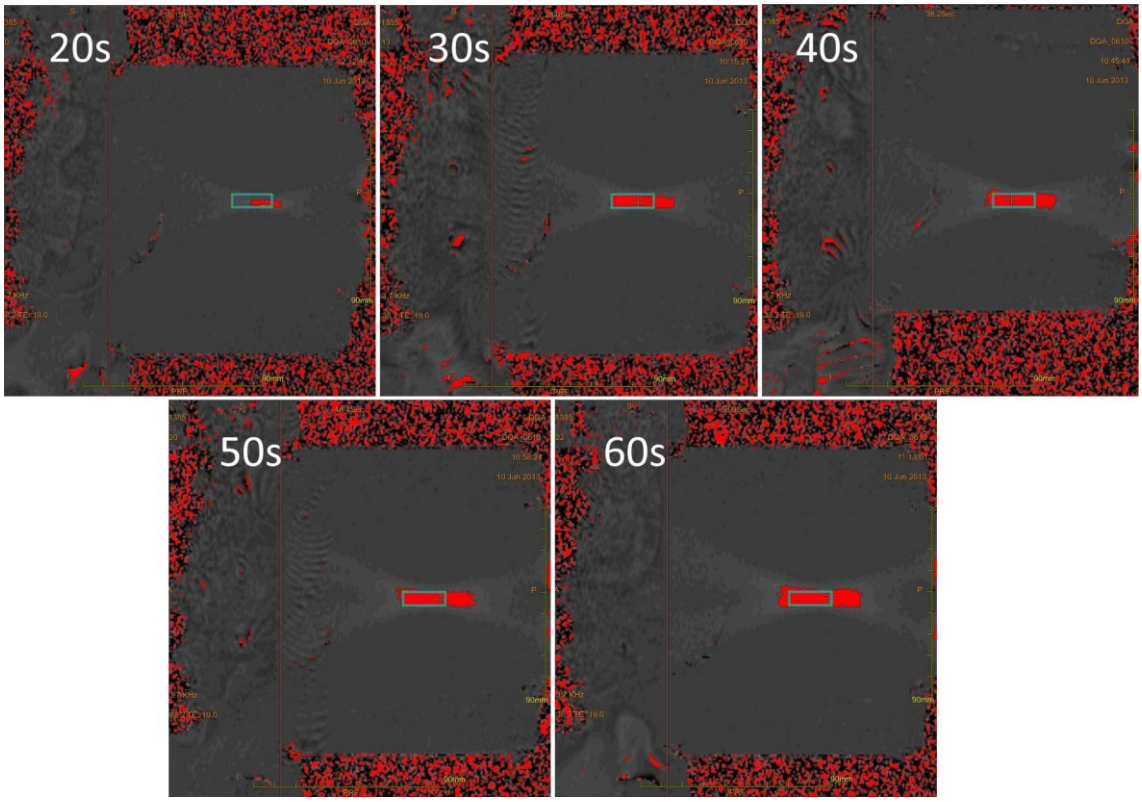

Figure 3.32 Focal lesion over 50 °C using 50 W acoustic power over different times ranged from 20 s to 60 s on DQA gel phantom acquired by MRI thermometry using ExAblate 2000 system (red area indicates the focal region over 50 °C; blue rectangular represents the planned location of the focus)

Table 3.8 Length and diameter of focal lesion on DQA gel phantom using 50 W acoustic power sonicated by ExAblate 2000 (lesion pattern over 50 °C)

Time (s)	Length (±0.05mm)	Diameter (±0.05mm)
20	14.3	2.6
	15.9	2.8
	16.7	2.9
30	29.5	4.9
	30.1	4.8
	28.6	5.1
40	33.4	5.6
	32.5	5.5
	33.0	5.6
50	40.1	6.5
	34.4	6.4
	35.2	5.8
60	44.3	7.0
	40.1	6.9
	37.6	6.3

3.4.5.5 Determination of the best materials

The measurements of acoustic and thermal properties of optional TMMs showed similar results to soft tissues. The acoustic attenuation coefficient of PVA is a disadvantage for this material as ribcage surrounding tissues, but this did not affect the

accuracy of imaging or location of HIFU focus. For a phantom block with a ribcage model inside, PAA gel is highly toxic and expensive to make phantom in this size for long-term usage. Agar gel is more easily broken because of the segmentation by the ribcage model. PVA is non-toxic during the fabrication and the utilization, has long-term stability, and is elastic and strong enough to include the ribcage inside. Considering its benefits, PVA is determined as the best material for fabricating the surrounding tissue of ribcage. ABS was selected be the substitute material of ribcage. To mimic tumour for elastography, PAA with 2% Al_2O_3 was chosen, as it possessed Young's Modulus close to tumour tissues and was easily identified by elastography. DQA phantom was the best material for target phantom in HIFU sonication experiment, because it matched the acoustic and thermal properties and showed a proportional dimension change of lesion to acoustic energy. Table 3.9 shows the applications and main advantages of the selected TMMs.

Table 3.9 Applications and advantages of selected TMMs

TMMs	Applications	Advantages
PVA	Ribcage surrounding tissue	Non-toxic, long-term stability, capable of embedding ribcage model inside
ABS	Ribcage	Strong and stable over time
PAA+2%Al_2O_3	Tumour	Easily identified by elastography
DQA	HIFU sonication target	Lesion dimension closely related to acoustic energy

3.5. Summary

A physical ribcage model was proposed in this study to investigate the effect of ribcage on HIFU treatment and help to determine the sonication parameters and optimise the treatment protocols. To mimic the human anatomical features and structures, the 3D modelling and rapid prototyping technique have been developed based on patient images. This is a fast, accurate and reproducible technique, and the reconstructed models could be used for pre-treatment planning. In this technique, image processing was used to extract the contour of the region of interest from raw image data. A computer generated

3D model was reconstructed base on this contour using Simpleware. Finally, a physical 3D ribcage model was produced on the prototyping machine. This may take up to one day.

The fabrication and characterisation of different tissue mimicking materials have been performed in order to determine the best materials for phantoms used in the HIFU sonication or diagnostic imaging. The acoustic properties, elastic properties and thermal properties have been investigated. PVA was found the best suitable material for surrounding tissue and ABS was used for the ribcage. The optimal TMM to mimic the tumour for elastography was PAA with 2% Al_2O_3. This provided useful information to create TMM phantom in the diagnostic stage and pre-surgical planning stage for mimicking the anatomical structures and features of the patients. HIFU sonications can be performed in the planning stage using the TMM phantom and sonication parameters that would be used in the treatment can be verified and further optimised.

In terms of the TMMs used for HIFU sonication, PVA and agar both possess low melting temperatures, and agar gel with low concentration is easily damaged. PAA material is highly toxic and not suitable for routine use. Lesions created by HIFU on PAA egg white phantom appear no obvious trend in the changes of lesion size by increasing the duty cycle or sonication time. However, results of the sonication on DQA gel phantom show a proportional size change in the lesion induced by HIFU sonication. The DQA phantom is non-toxic and can be reusable. Therefore, the DQA gel phantom was determined to be the target phantom in the HIFU sonication through ribcage in the following study.

It should be noted that the physical model of any abdominal organs, such as liver and kidney, are not used in the further studies on HIFU sonication experiments. The propagation of ultrasound is determined more by the properties of the medium than by the shape of it. The priority of the present work is not to study the effect of the organ shape, but to investigate the effect of ribcage on HIFU treatment. Therefore, a DQA gel phantom with similar properties to human tissues in a simple cone shape is used as the target phantom in the following experiment. However, details of the reconstruction of human organs were still described in section 3.2 for future applications.

Chapter 4 Effect of Ribcage on Focused Ultrasound Field

As a non-invasive treatment, it is necessary to ensure the acoustic energy being delivered at the correct level and deposited to the accurate location in tissue ablation using HIFU. However, considering the differences in the anatomical structures among patients, a constant protocol of HIFU treatment could not be applicable to different wave propagation circumstances. Applying the same acoustic energy on varied patient may cause insufficient heat deposition at focus or potential risk of overheating. Ribcage, as one of the barriers in the focused ultrasound beam path in the treatment of liver and kidney diseases, decreased the focal temperature elevation by affecting the ultrasound wave propagation. Patient-specific treatment plan of HIFU through ribs is yet to be investigated. To study the influence of the ribcage in focused ultrasound field, it is more efficient to use an alternative model that possesses human anatomical structures in the planning and verifying stage of HIFU treatment. In this study, it has used four different ribcage models based on CT scan image data from four patients to find out how they affected the delivery of HIFU energy.

This chapter describes the characterisation of HIFU device and the quantification of the effect of ribcage on focused ultrasound field. Before placing the ribcage in focused ultrasound beam path, the features of focused ultrasound field were characterised in free field, including acoustic pressure distribution, acoustic power and focal temperature (on TMM phantom). Subsequently, the experiments with the ribcage in the ultrasound beam path are presented. Basic effects on the ultrasound field are described in section 4.1 to 4.3, including the acoustic pressure distribution, acoustic power delivery and heat deposition at focal region. To study the complicated situations in the HIFU treatment, further details of HIFU sonication with the ribcage model are illustrated in section 4.4, including varying acoustic power and sonication time, applying sonication at different focal distance, and changing the location of the ribcage model. Image guidance and temperature measurement have been taken into consideration during the sonication. It should be noted that the ablation of each focal volume of the tissue or phantom is described as a sonication in this study.

4.1. Effect on acoustic pressure distribution

Acoustic pressure is the local pressure deviation from the ambient atmospheric pressure caused by a sound wave. A map of the acoustic pressure distribution of a focused ultrasound field can provide a visualised profile of the ultrasound beam. Region of the damaged tissue induced by focused ultrasound therefore could be predicted according to the ultrasound beam profile. Changes in focal area affected by ribcage in the beam path can also be visualised by comparing with the focused beam in free field.

Acoustic pressure distribution mapping was acquired using a needle hydrophone based scanning system. A high resolution 3D scanning system (Cao *et al.* 2012) was used to drive the hydrophone in the acoustic field. The entire setup consisted of a motor controller and automated 3D stages capable of moving in three orthogonal directions with 3.8 μm resolution as the positioning unit (Figure 4.1).

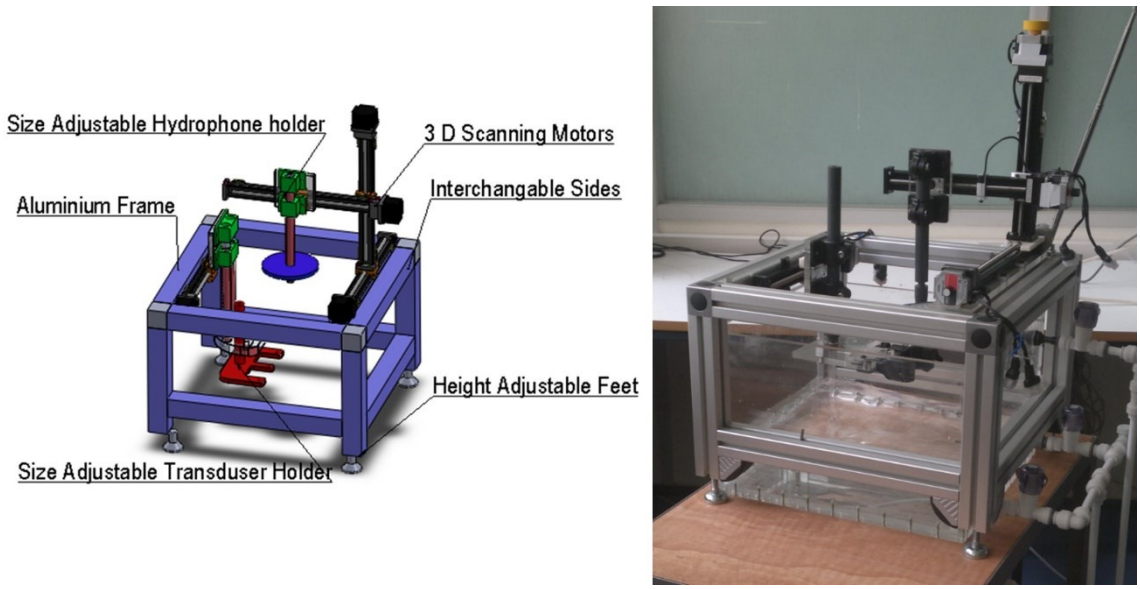

Figure 4.1 Scanning tank for acoustic field mapping

A homemade single element HIFU transducer (parameters are listed in Table 3.2) was used to generate the acoustic field with continuous sine wave using 5 V_{pp} input from a waveform/function generator (33220A, Agilent, Santa Clara, CA, USA). To maximize the range of the scanning field, the transducer was located and fixed at the central bottom of a water tank (47 cm × 41 cm × 30 cm) with piezoelectric material facing up. Output

signal of the transducer was recorded by a needle hydrophone (0.5 mm diameter probe with 9 μm thick gold electroded polyvinylidene fluoride (PVdF) film, Precision Acoustics, Dorchester, Dorset, UK), which was faced to the transducer and mounted on and moved by the 3D stages. A piece of acoustic absorber material (approximate 10 mm) was placed about 20 mm behind the needle hydrophone to reduce the multipath artefact. Figure 4.2 depicts the schematic diagram of the acoustic pressure field scanning.

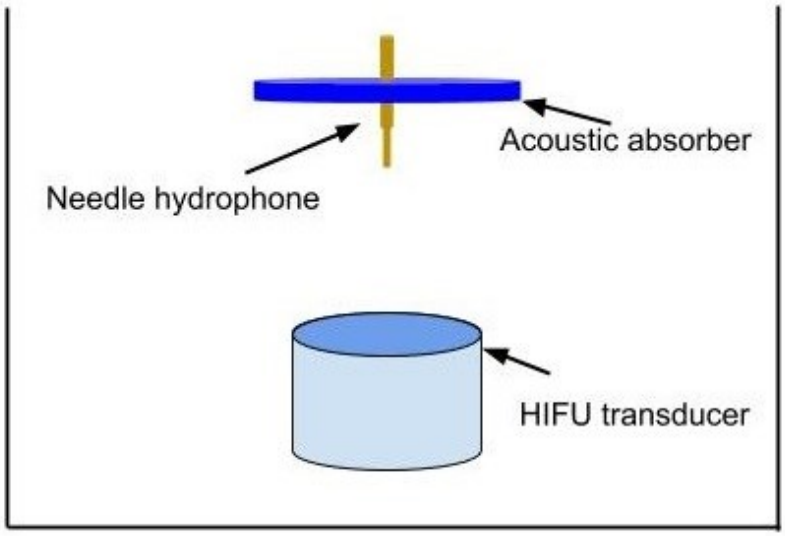

Figure 4.2 Schematic diagram of acoustic field scanning setup in the water tank

PicoScope 4262 (Pico Technology, St Neots, Cambridgeshire, UK) was connected to the needle hydrophone through the signal output of a DC coupler (DCPS160, Precision Acoustics, Dorchester, Dorset, UK) for data acquisition. A computer with LabVIEW program (National Instruments, Austin, TX, USA) controlled the motion of the 3D stages and data acquisition unit. The 3D acoustic scanning was carried out in degassed water environment. As water possesses similar acoustic properties to tissue and TMMs, it can be used to characterise the acoustic properties when the measurement in a phantom is difficult to approach. Measurement was performed at lower output level than that used for clinical therapy to avoid damaging the hydrophone. The scanning resolution was set to 0.2 mm for accurate acoustic field mapping.

To investigate the acoustic pressure field with the presence of ribcage model, a model was placed in the focused ultrasound beam path, orthogonal to the acoustic

propagation axis. The ribcage model was fixed on the same holder for the transducer to keep a constant distance between transducer and ribcage (approximate 20 mm). Transcostal and intercostal propagation was studied respectively. A piece of ribs was placed in the central front position of the transducer (with the rib on the axis of the ultrasound beam) (Figure 4.3(a)) for transcostal position. Ultrasound wave propagated through both sides of the central rib in this setup. Figure 4.3(b) depicts the ribcage model placing with two pieces of ribs above the transducer leaving the axis of the transducer off the ribs.

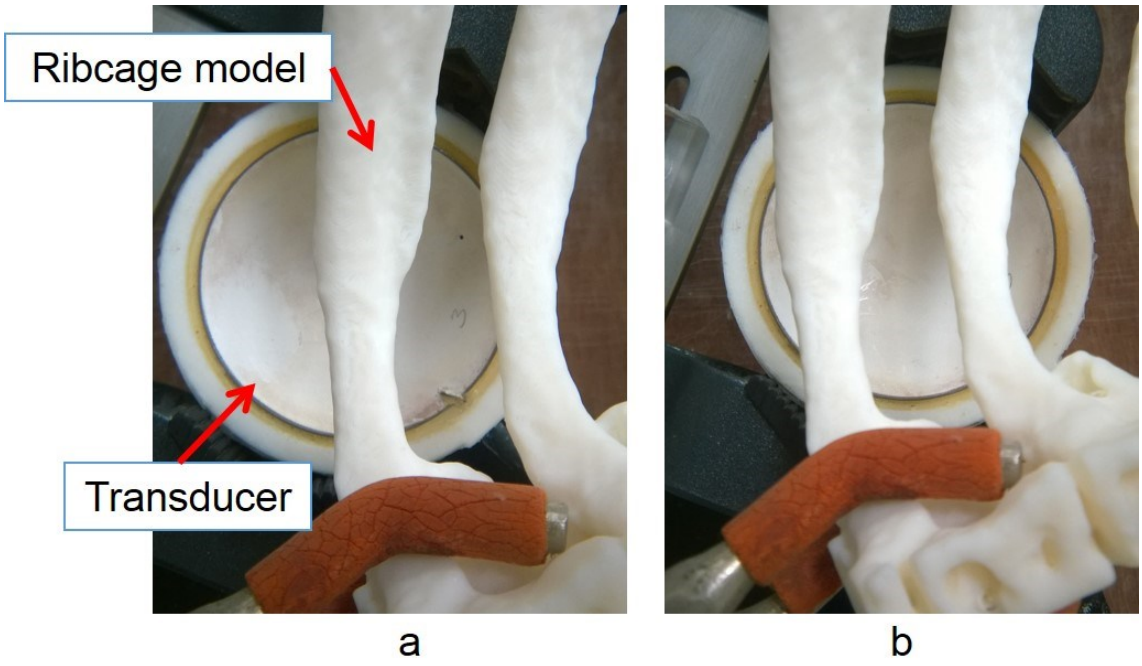

Figure 4.3 Setup of acoustic field mapping. (a) transcostal position; (b) intercostal position (pictures were captured without needle hydrophone in the field)

4.2. Effect on acoustic power delivery

Acoustic power has a direct relation to the dose applied to patients in HIFU treatment. The input electric power of the focused ultrasound transducer is converted to output acoustic power and then be delivered to diseased target tissue to create local heating and tissue damaging.

To achieve an effective and safe HIFU ablation, acoustic power was required to be determined in the planning stage of a customized treatment. This section reports the experimental methods for measurement of the acoustic power generated by a homemade HIFU transducer. The power conversion ratio of acoustic power and electric power of this HIFU transducer is also included.

Radiation force balance (RFB) is the most commonly used measurement method to determine the acoustic power. The acoustic power is acquired by measuring the radiation force experienced by a target, normally a piece of acoustic absorber. For an ultrasound wave perpendicular to the target, the momentum of the ultrasound is transferred to the target, resulting in a force. This force is measured by a change in mass using an analytical balance. The total acoustic power P_{vert} corresponding to the vertical component of radiation force is related to the mass reading on the balance, m_{rad}, and calculated by equation 4.1.

$$P_{vert} = m_{rad} \cdot v_w \cdot g \cdot F_a \tag{4.1}$$

where:
v_w: speed of sound in water
g: gravitational acceleration
F_a: calibration factor for absorbing target (0.99 for this device according to the calibration certificate provided by Precision Acoustics)

In the current study, the homemade HIFU transducer (parameters are listed in Table 3.2) was driven by waveform/function generator (33220A, Agilent, Santa Clara, CA, USA) and amplified by a power amplifier (1020L RF Amplifier, Electronics & Innovation, Ltd., Rochester, NY, USA). The RFB (Precision Acoustics, Dorchester, Dorset, UK) used in this measurement is able to determine total ultrasonic power radiated in the forward direction from transducers operating in the frequency range 1 to 10 MHz.

Figure 4.4 describes the schematic diagram of the acoustic power measurement. The RFB measurement system included a force balance with a serial interface placed on the plexiglass plinth, an anechoic absorber target placing into a water container, and four supporting wires for connecting the balance and the absorber target. The transducer to be measured was held by a clamp to ensure that the piezoelectric material surface of the transducer was fully immersed into the water and positioned centrally above and parallel

to the absorber. To eliminate the possibility of cavitation, measurements were performed in freshly degassed and distilled water. Because the force balance is extremely sensitive, the RFB setup was placed on the optical table and a draught shield was used to cover the whole setup to reduce the effect of vibration and air flow in the lab. The measurement data was transferred to a computer via serial communication for calculating the results according to equation 4.1.

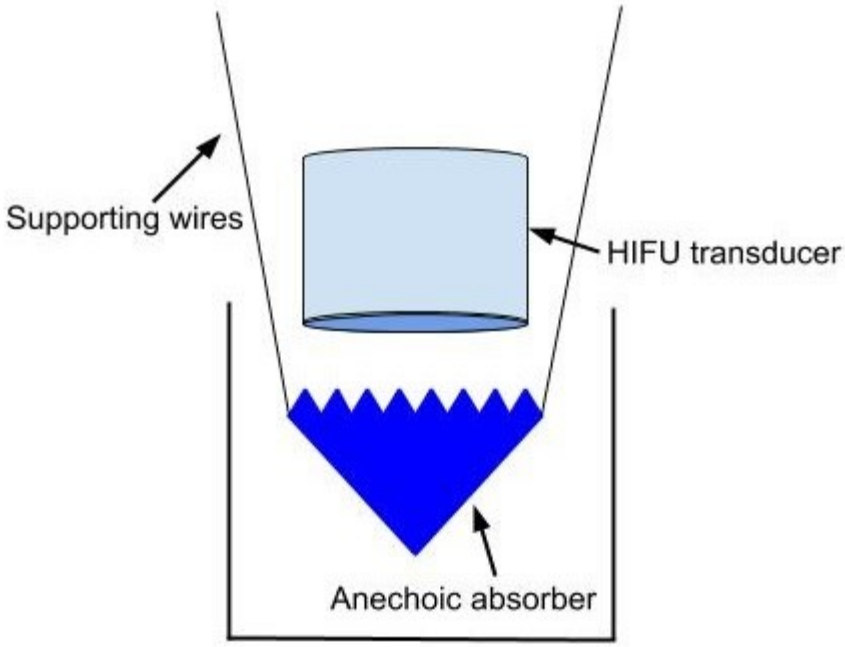

Figure 4.4 Schematic diagram of acoustic power measurement

Input electric power of the HIFU transducer ranged from 10 W to 50 W (10 W per step). The power conversion ratio of acoustic power and electric power was calculated at each power level using the detected acoustic power divided by the input electric power. Cooling time was required between two power-on times to avoid damaging the acoustic absorber or giving rise to transducer overheating during the measurement.

After measuring the acoustic power in free field, effect of ribcage on acoustic power delivery was investigated. Power conversion ratio was used to describe the acoustic power converted from the electric power by the transducer. The acoustic power produced by the transducer did not change even if the ribcage in place. In order to evaluate the effect of ribcage model on energy delivery in the acoustic field, the RFB was used to

measure the force experienced by the absorber target in the HIFU field with the presence of ribcage model. As this result was related to the acoustic energy affected by the ribcage model, the measured force was used to calculate the power conversion ratio. The ratio was calculated using the measured acoustic power by the RFB with the ribcage models in ultrasound field divided by the input electric power of the transducer.

To study the effect of ribcage, the ribcage model was placed in the beam path of the transducer and above the absorber target (Figure 4.5). Distance from transducer to the surface of the absorber target was set to 25 mm which allowed placing the ribcage model in the beam path. Both transcostal and intercostal propagation was investigated using all of the four ribcage models. For the transcostal position, the model was placed above the absorber target approximately 10 mm away to the transducer, with the axis of the HIFU transducer on a rib. In terms of the intercostal propagation, two ribs placing in the beam path allowing the axis of the transducer in the intercostal space. The acoustic power calculated from the measured force was considered to be related to the energy deposition at focus affected by the ribcage model. Different input electric powers ranged from 10 W to 50 W were applied to drive the transducer.

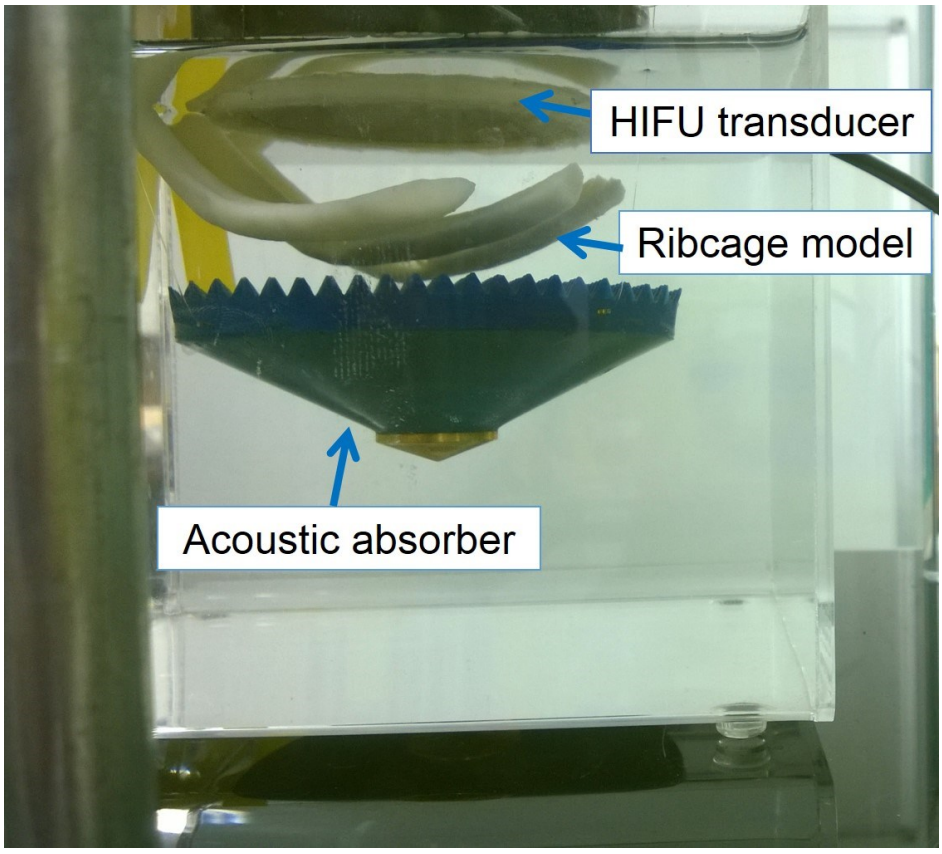

Figure 4.5 Acoustic power measurement with ribcage model in the beam path using RFB

4.3. Effect on heat deposition at focus

Heat deposition in ultrasound field provides the temperature information at focal region and may be used to determine the therapeutic parameters. The most commonly used method to acquire the temperature map is to use thermal camera by non-contact measurement without affecting the temperature field. In order to obtain the heat deposition at focal region of a focused ultrasound field, the temperature field of the transverse focal plane was captured by focusing the beam on the surface of an object.

Figure 4.6 depicts the schematic diagram of the temperature distribution mapping. The aim was to focus the beam on a smooth surface of a piece of agar phantom and capture the temperature field from the phantom surface. A 3D scanning system (Figure 4.1) with a water tank and a thermal camera (thermoIMAGER TIM 160, Micro-Epsilon, Ortenburg, Germany) was used in this measurement. The thermal camera was fixed on the 3D stages above the water tank with image sensor facing down. A homemade HIFU

transducer (parameters are listed in Table 3.2) was positioned in the water tank with piezoelectric surface upwards to the water surface aligned with the thermal camera. The depth of the transducer in the water was 5 mm shorter than the focal length. The phantom was placed in the tank with its top surface 5 mm out of the water to avoid focal heat diffusion by the water. This position ensured that the focus of the transducer was exactly located on the phantom upper surface.

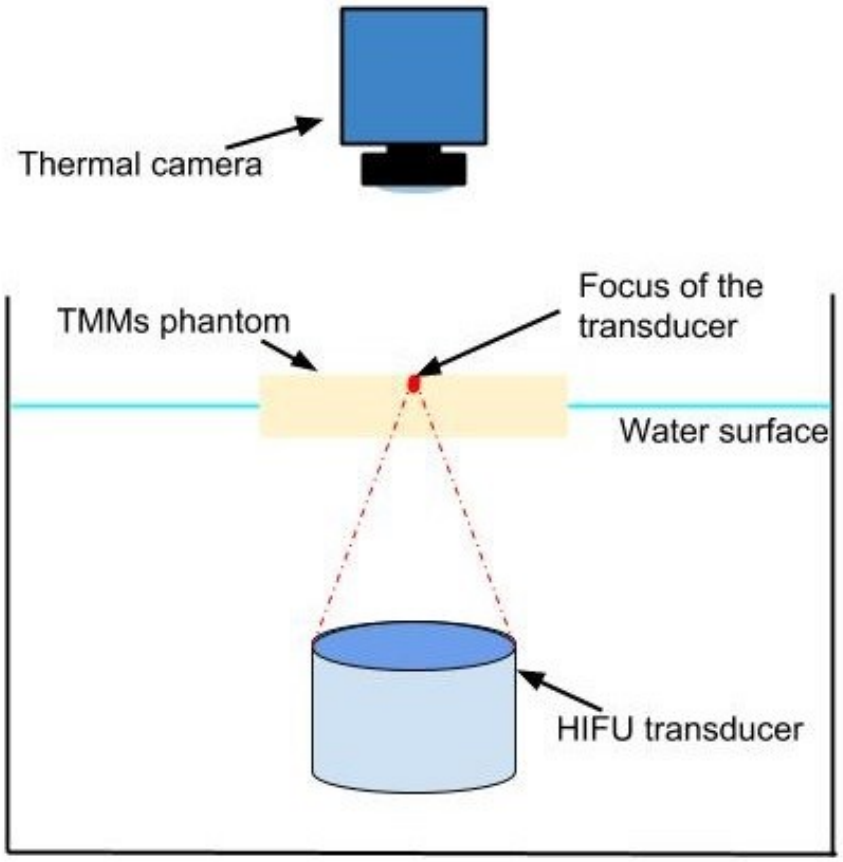

Figure 4.6 Schematic diagram of heat deposition measurement setup in a water tank

Experiment was performed with and without the ribcage model using 24 W electric power over 10 s duration time at room temperature 20 °C. The temperature field map was captured by the thermal camera and recorded using TIM Connect software (Micro-Epsilon, Ortenburg, Germany) in real time.

4.4. Effect on focal temperature elevation

The aim of the experiments in this section was to study the effect of ribcage model on focal temperature by performing HIFU sonication on TMM phantom with the model in ultrasound beam path. For this purpose, the experiments required image guidance to locate the focus, temperature measurement to monitor the focal temperature change, and mechanical device to accurately move the target or ribcage position. MRI is able to provide the image guidance and temperature measurement simultaneously. In order to implement the HIFU sonication experiments in MRI environment, both HIFU system (for sonication) and mechanical device (for moving target or ribcage) have to be MRI compatible.

The experimental systems are described in section 4.4.1. In the rest of section 4.4, considering various situations in the HIFU treatment through ribcage, sonication experiments on phantom using various parameters at different locations were conducted to study the influence of the ribcage. The ribcage model of No.2 patient was selected in this experiment placing in the beam path, because the difference in ultrasound propagation between transcostal and intercostal position was found maximum using this model in all of the four models (results are stated in section 4.5.1 and 4.5.2). To study the ribcage effect at different positions, the phantom or ribcage model was moved accurately along axial or radial direction of the transducer by a robotic arm in MRI suite. Transcostal and intercostal propagation were both investigated and compared with the shadow area of the ribcage projected on the transducer.

4.4.1. HIFU system and robotic assistance system

HIFU platform used for providing sonication and robotic assistance system used for controlling the movement of phantom or ribcage locations are described in this section.

4.4.1.1. HIFU system: ExAblate 2000

ExAblate 2000 (InSightec, Tirat Carmel, Haifa, Israel) focused ultrasound system operates with 1.5 Tesla MR scanner (Signa HDxt 1.5T, GE Healthcare, Waukesha, WI, USA). This magnetic resonance-guided focused ultrasound surgery (MRgFUS) system integrates two well established technologies, focused ultrasound and MRI, to non-invasively ablate targeted tissue lying within the body while sparing the surrounding

tissue. The MRI provides patient's anatomy in the planning stage of the treatment and measures the temperature change inside the body/phantom during the HIFU treatment. With the temperature maps, physicians are aware of the extent of thermal ablation and will ensure safety and efficacy of the treatment.

Figure 4.7 depicts the patient table of ExAblate 2000 which contains the focused ultrasound transducer embedded into the patient table along with the mechanical positioning unit that moves the transducer. The water circulation system is also included in the patient table for the transducer. Focused ultrasound propagates through a membrane located on top of the transducer. With MRgFUS, HIFU beam can be simulated and displayed on MR images before the treatment to ensure that the ultrasound wave travels through a safe pathway to the focus.

ExAblate 2000 system possesses a phased array transducer and the phase of the sinusoidal signal produced by each element on this transducer can be adjusted independently with respect to the target position. This can benefit the HIFU sonication experiments at different focal distances and locations. Sonication parameters can be adjusted in planning stage according to the result of continuously temperature monitoring inside the tissue or phantom.

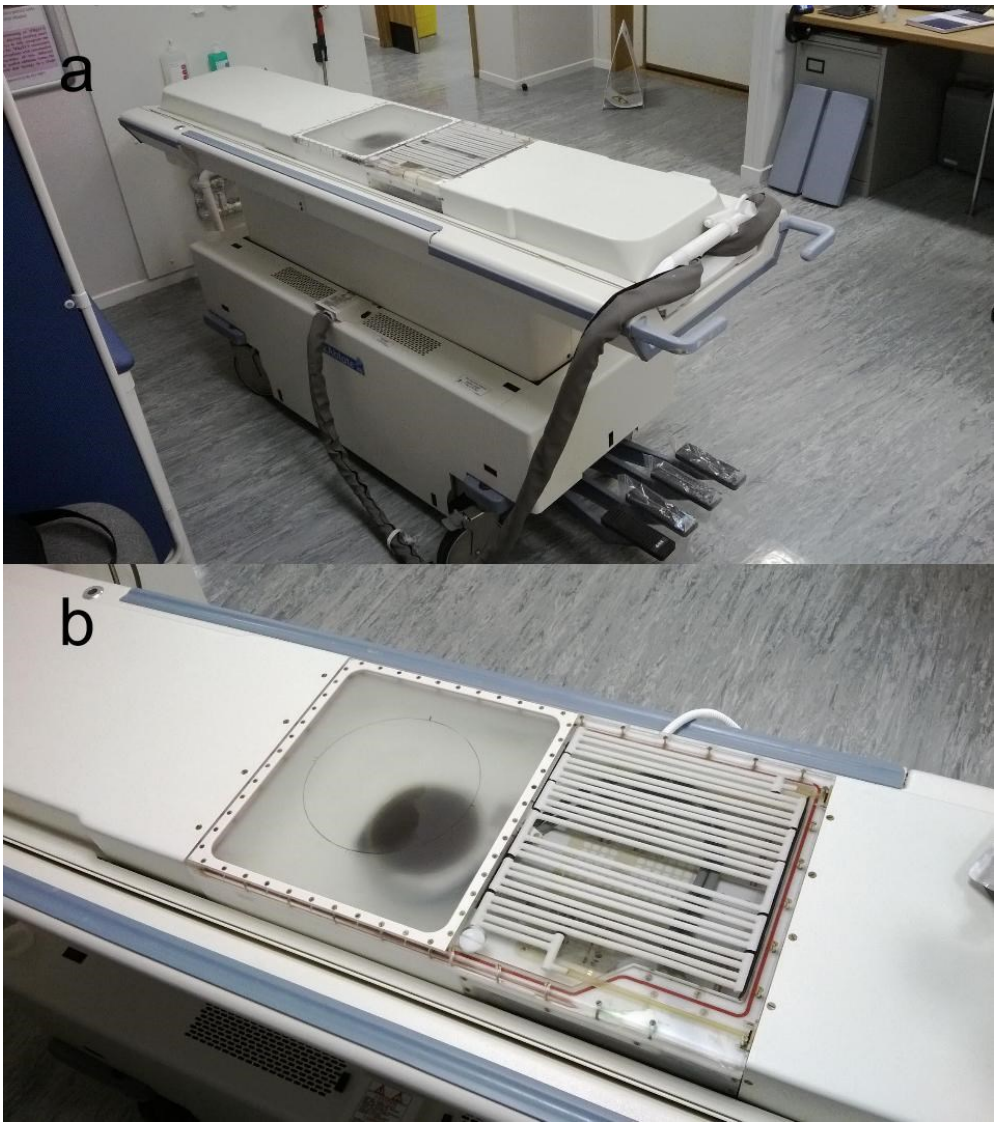

Figure 4.7 ExAblate 2000 system (a. Patient table; b. Focused ultrasound transducer and positioning and cooling system)

ExAblate system provides a graphic user interface to perform the panning and the treatment. InSightec MR protocols, which have been pre-loaded into the GE Signa prorocol database, are used for the scanning before and during the treatment. Pelvic coil (InSightec, Tirat Carmel, Haifa, Israel) is used with ExAblate 2000 system in the following experiments in this chapter. After positioning the phantom and coil, an MRI 3D localizer is scanned firstly to ensure that the phantom is properly positioned and there are no trapped air bubbles in the potential beam path. The MR images of the 3D localizer, meantime, provide the system with the position information of the transducer to determine its home position and orientation. A spin echo scan (TE 120.0, TR 2000.0) is

then automatically performed to obtain images to determine the region of treatment (ROT), skin line, beam path and etc. The ROT is defined via drawing it on the MR images. The system calculates the beam path according to its position and may deny a ROT if it is too close to the skin line.

In Figure 4.8, the MR image shows a phantom placed on patient table of ExAblate 2000 system with a HIFU transducer in the patient table underneath the phantom. The blue area indicates the ultrasonic beam path from the transducer to the target, which can be visualised in every slice of MR images within the beam path zone. Adjustment has to be made if there is unacceptable medium in the energy pass zone (e.g. air bubbles) for the selected ROT. Sonication parameters including acoustic power, sonication duration time, frequency and cooling duration time are determined afterwards. The frequency is selected as 1.15 MHz, which is the default working frequency of ExAblate 2000 system (The transducer can work at frequency in the range of 0.95 MHz to 1.35 MHz).

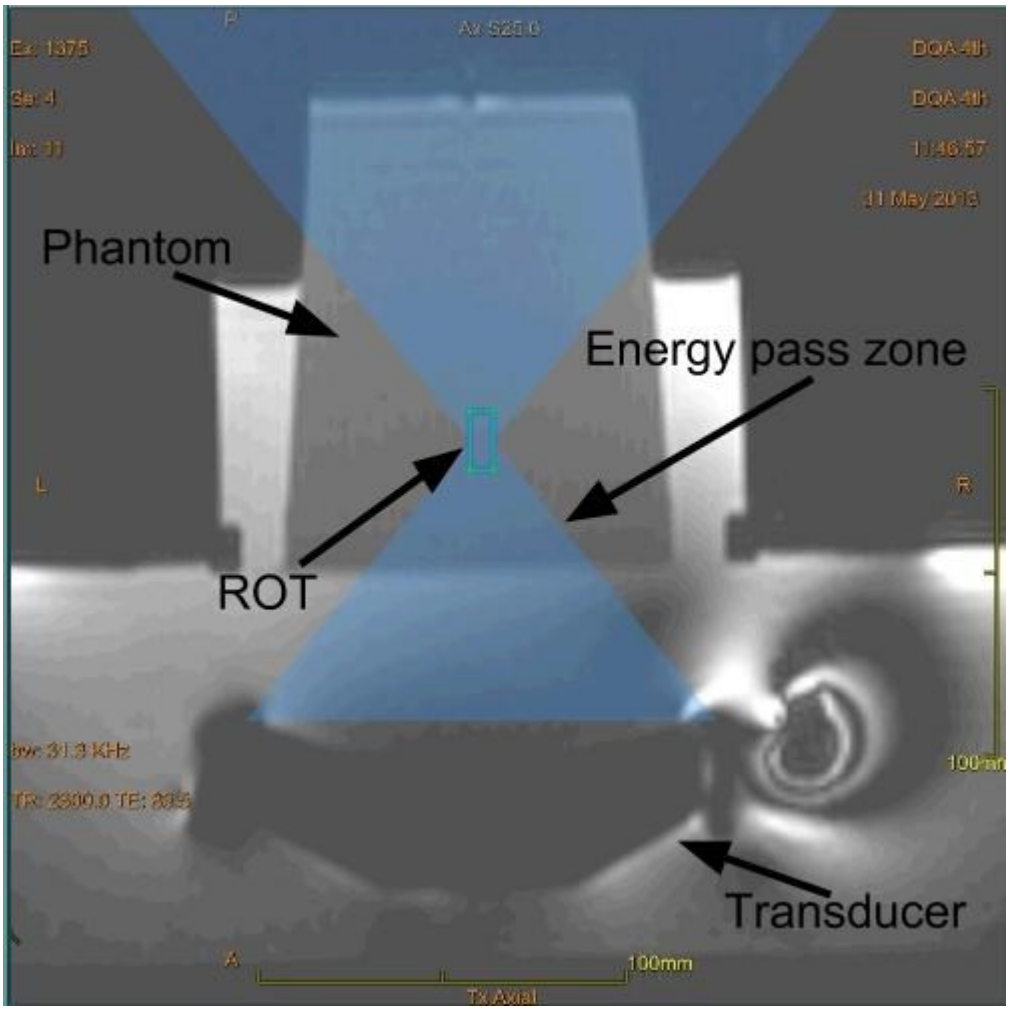

Figure 4.8 Planning stage on ExAblate system (blue area indicates the energy pass zone, which was generated from the transducer according to the ROT on the phantom)

4.4.1.2. HIFU system: ExAblate 2100

ExAblate 2100 system (also called CBS, Conformal Bone System, InSightec, Tirat Carmel, Haifa, Israel) is MRI compatible. Its patient table (Figure 4.9(a)) incorporates the focused ultrasound transducer (Figure 4.9(b)) along with the transducer's water interface unit, including a water balloon created by a porous membrane that ensures sufficient acoustic coupling and straps that secure the transducer in place. The transducer has watermarks at entry and exit points of water hoses, which are used in the 3D localizer scan. The markers in the MR images help the system to calibrate the transducer's home position and orientation.

The system provides a graphic user interface and MR protocols. An 8 channel body coil (GE Healthcare, Waukesha, WI, USA) is used with ExAblate 2100 system in the experiments in this chapter. A spin echo scan (TE 85.0, TR 1306.8) is used to obtain images and determine the ROT, beam path and etc. after a 3D localizer scan. The ROT is defined on the MR images and the beam pass zone is validated by the system according to the calibrated transducer location. It is necessary to check the beam path on every slice to ensure a safe ultrasound propagation.

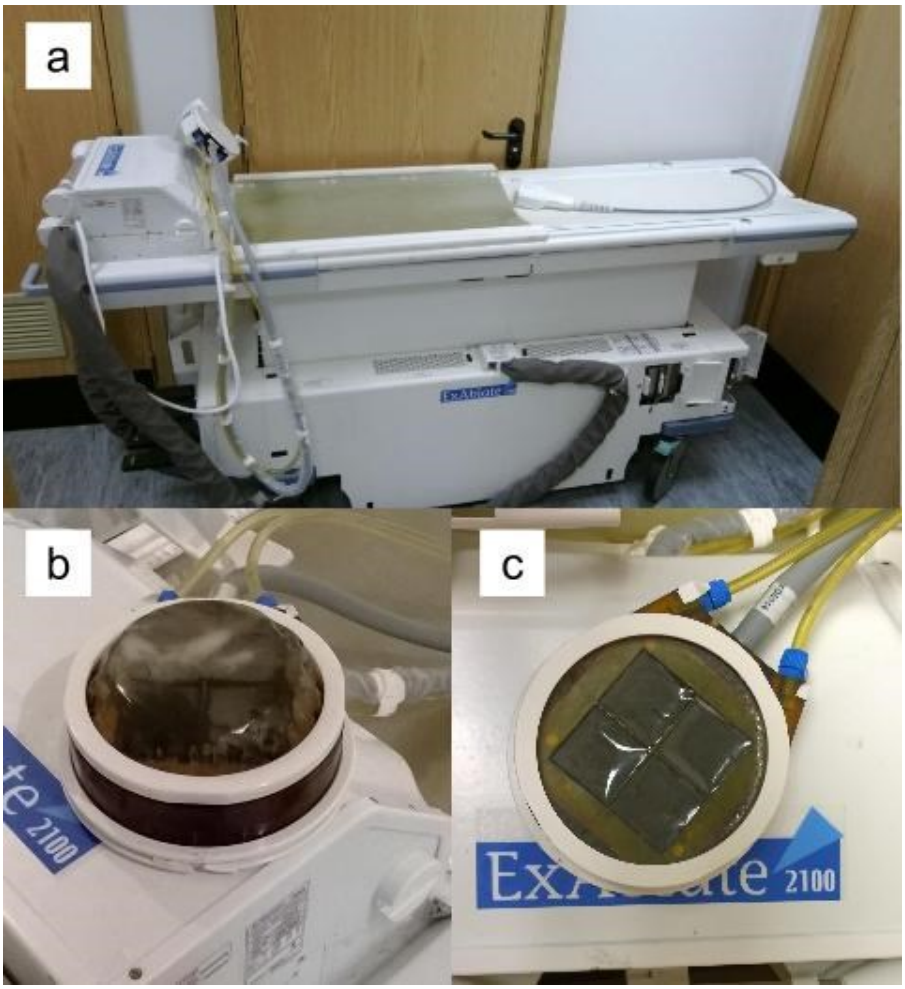

Figure 4.9 ExAblate 2100 system (a. Patient table; b. CBS transducer with the water balloon; c. Transducer before filling the balloon with water)

Compared with ExAblate 2000, the ExAblate 2100 has a flexible transducer and enables more options to place the transducer in the experimental setup. The elements of the transducer is in 80 mm × 80 mm square and also has the capability to vary the location

of the focus by adjusting the phase of the sinusoidal signal of each element on the phased array transducer. This transducer operates at a lower frequency (0.55 MHz) than ExAblate 2000 system does, because it is originally designed for bone treatment.

4.4.1.3. INNOMOTION robotic assistance system

INNOMOTION robotic assistance system (IBSMM Engineering, spol. s. r.o., Brno, South Moravian Region, Czech Republic) can be assembled onto the patient table of ExAblate 2100 system working in MR environment. In Figure 4.10, the patient table of ExAblate 2100 with the robotic assistance system assembled is docked to the MR scanner. Front end of the robotic arm can be moved into the MR scanner by the patient table. This MRI-compatible robotic system is a pneumatically driven system with 5 degrees of freedom. Its positioning accuracy is ± 1 mm in translational direction and ± 1° in angular direction. The front end of the robotic arm can hold the biopsy needle, as it was designed for needle biopsy research. In the current study, holder for phantom and ribcage model was produced, which can be mounted on to the robotic arm. The motion of phantom and ribcage model in MRI suite was driven by this robotic assistance system.

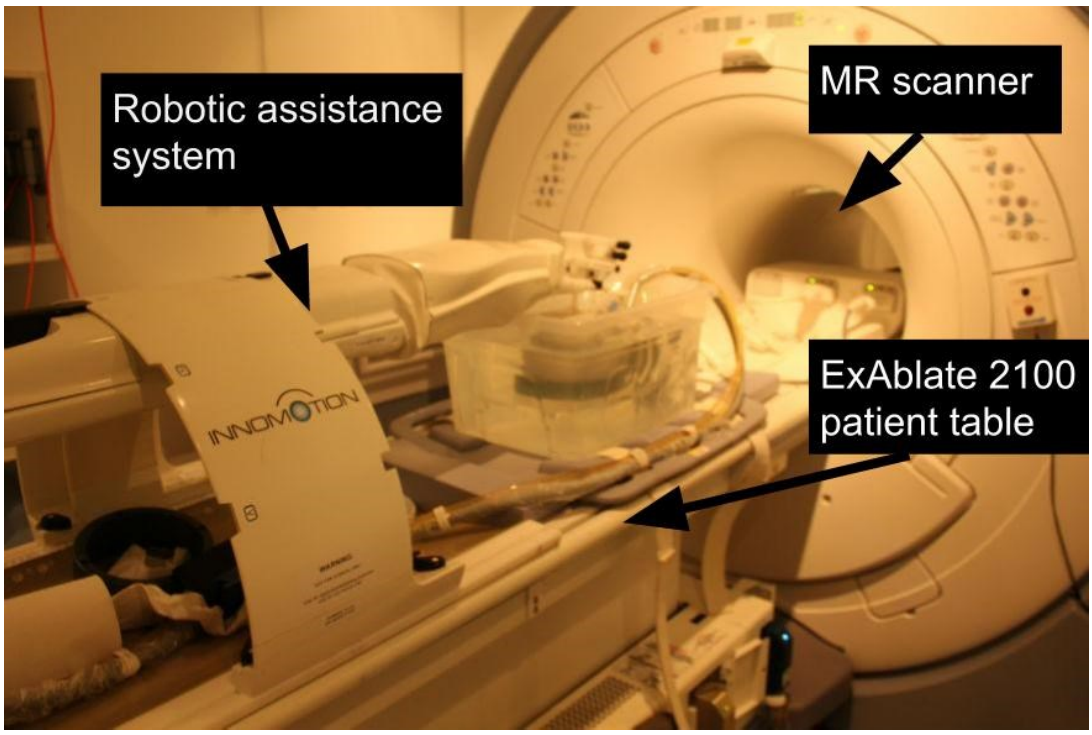

Figure 4.10 Robotic assistance system assembled on ExAblate 2100 system patient table in front of the 1.5T MR scanner

4.4.2. Sonication on TMM phantom

DQA phantom (ATS Laboratories, Bridgeport, CT, USA) was selected as the target to obtain the information of focal temperature elevation. A number of sonications were performed on DQA gel phantom to analyse its performance at focus in HIFU sonication using ExAblate 2000 system before applying the ribcage in the focused ultrasound beam path. As the DQA gel phantom can maintain steady acoustic properties after cooling down from heating effect by HIFU, results of the repetition experiment on this phantom are reliable.

The DQA phantom, in a simple truncated cone shape (Figure 4.11, short diameter 90 mm, long diameter 108 mm, height 130 mm), was located in a small water container positioned on the patient table of ExAblate 2000 system above the focused ultrasound transducer. The container was filled with distilled and degassed water for acoustic coupling and to minimize reflection at the surface of the phantom. The sonications lasted for 10 s, 20 s, 30 s, 40 s, 50 s and 60 s using a constant acoustic power 50 W at near, medium and far focal distance. Figure 4.11(b) indicates the location of the sonication spots on the DQA phantom. Six spots were selected with three different depth: spot 1 at focal distance 80 mm, spot 2 - 4 at 120 mm and spot 5 and 6 at 150 mm. A time interval of at least five minutes was allowed for cooling time of the phantom after each sonication.

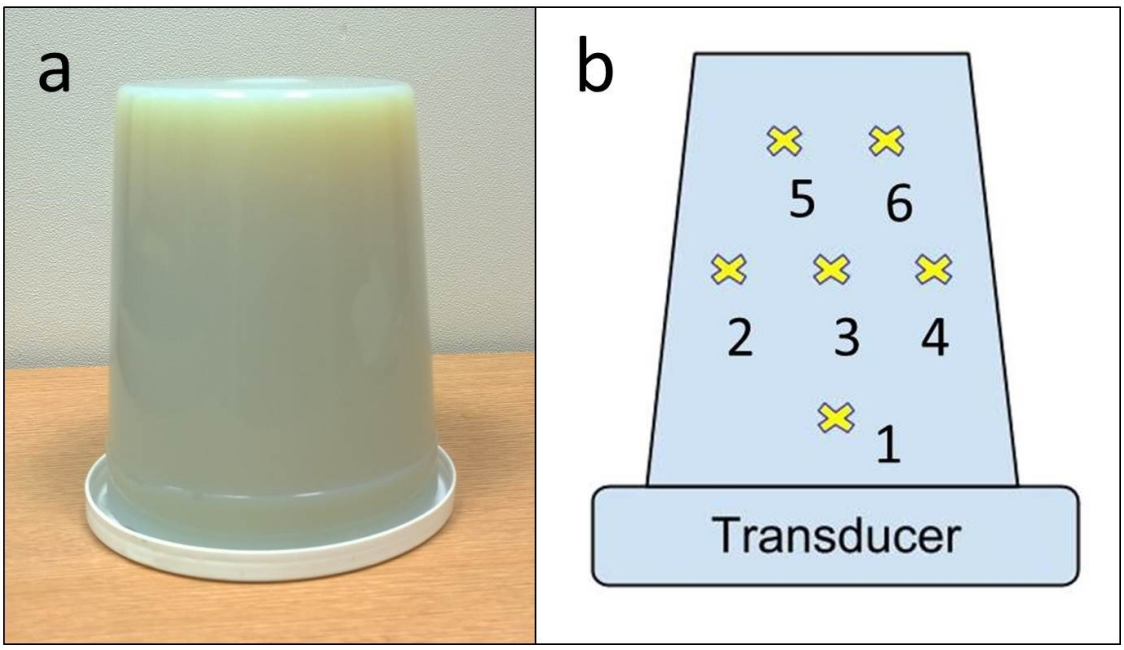

Figure 4.11 Sonication spots located on DQA gel phantom (a. DQA gel phantom; b. Location of the focal spots)

4.4.3. Varying parameters in HIFU sonication through ribcage

This experiment was to investigate the effect of the ribcage in case of varying the sonication parameters, such as acoustic power and sonication time. For this purpose, a two-layer phantom was produced containing the ribcage model. The first layer was the ribcage model embedded into a cuboid PVA gel phantom (Figure 3.8(b)). The PVA gel mimicked the surrounding tissue of the ribcage. DQA gel phantom as the second layer was carefully placed onto the PVA phantom without any bubbles at interface to ensure continuous ultrasound coupling. The phantom in a container with degassed water was placed on to the patient table of ExAblate 2000 system above the HIFU transducer, as shown in the sagittal view of MR image Figure 4.12. Ultrasound wave propagated from the transducer passed through the first layer phantom and focused on the DQA phantom. A time interval of at least five minutes was allowed for the cooling time of the phantom after each sonication. Focal length was fixed in this experiment using varied acoustic power and sonication time. This experimental setup was used in every experiment section 4.4.3.

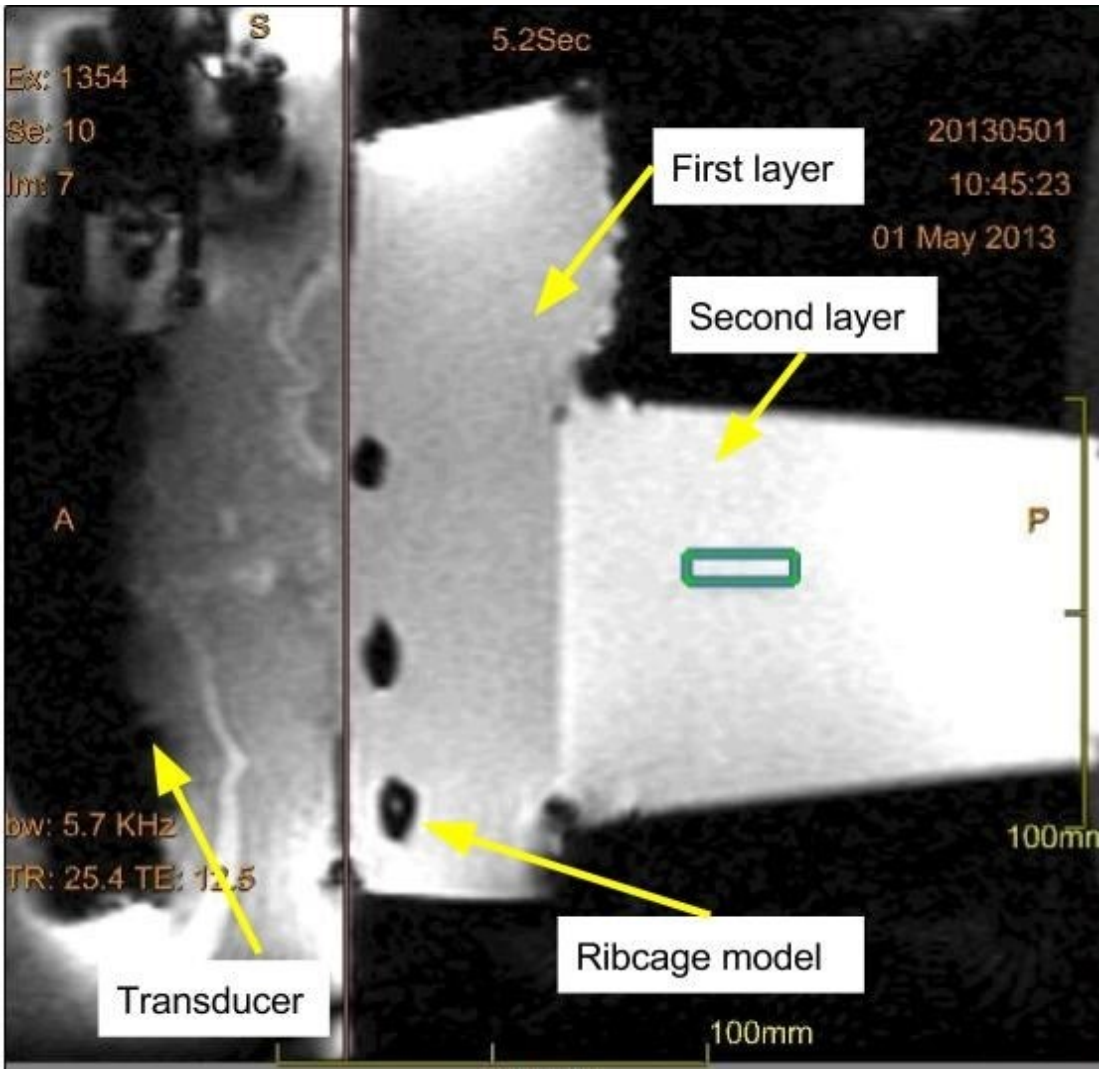

Figure 4.12 Sagittal view of MR image of the two-layer phantom containing ribcage model on patient table of ExAblate 2000 system

Using varied acoustic power

This experiment was designed to investigate the ribcage effect on focal temperature elevation using different acoustic powers at a transcostal position. ExAblate 2000 system combined with 1.5 Tesla MR scanner was applied to perform the sonications on the two-layer phantom and temperature measurement. Sonications applied a constant 20 s duration time, but different acoustic powers (ranged from 25 W to 150 W, 25 W per step).

Using varied sonication duration time

In order to estimate the influence of ribcage model using different sonication times, a constant 50 W acoustic power over varied sonication times (in the range of 10 s to 60 s, 10 s per step) was used.

Using constant acoustic energy

This was to study the difference in focal temperature change between extending sonication time and increasing acoustic power when applying the same total acoustic energy in transcostal HIFU. Sonications were performed using totally six acoustic energy levels ranged from 500 J to 3000 J (500 J per step). At each energy level, a lower acoustic power over longer sonication time and a higher acoustic power over shorter sonication time was performed respectively.

Control experiment

Control experiment was designed to investigate the focal temperature elevation without the effect of ribcage model. A piece of pure PVA gel phantom was fabricated in the same thickness as the first layer of the two-layer phantom used in the previous experiments in section 4.4.3. The DQA gel phantom was placed on top of the pure PVA gel layer. This setup was to provide a similar wave propagation circumstance as the experiments with the ribcage model. Sonications also applied the same parameters to those experiments with ribcage model.

4.4.4. Varying target phantom locations

This section was to study the effect of ribcage model at different focal lengths. By fixing transducer and ribcage model, sonications were performed on DQA phantom whose position can be moved along the axis direction of the transducer.

ExAblate 2100 system was used, as it has a flexible transducer. Compared with ExAblate 2000 system with a transducer embedded within the patient table, the flexible transducer provides more positioning options in the experimental setup.

In Figure 4.13, the computer generated models depict the HIFU sonication using different focal distances. Both of the transducer and the ribcage model were at a fixed position and the phantom was moved by the MRI compatible INNOMOTION robotic assistance arm. The ultrasound wave produced by the transducer focused on the phantom

through the ribcage model. For a fixed transducer, focusing at different positions can be achieved by adjusting the phase of each element on the transducer. The double headed arrow in Figure 4.13 indicates the phantom was moved along the axial direction of the transducer.

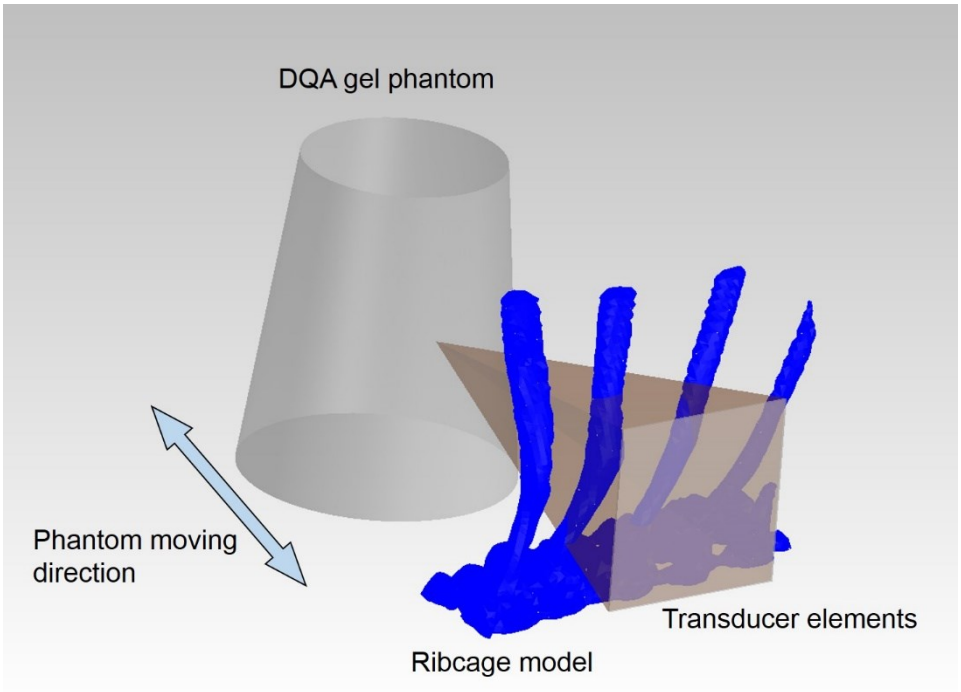

Figure 4.13 Schematic diagram of varying focal length in transcostal HIFU experiment

Figure 4.14 describes the experimental setup: by setting the transducer and the ribcage phantom at fixed position in a water tank full of degassed water, the truncated DQA phantom was placed in the same tank underneath the robotic arm. The transducer was sealed into a water proof bag facing to the phantom to avoid immersing into water. The ribcage model was placed at transcostal position with the axis of the transducer on a piece of ribs. The phantom was placed onto the smooth surface of a gel pad to minimize the moving resistance in the tank. A specially designed plastic clamp, which can be mounted onto the front end of the robotic arm, was used to hold the phantom from its top. The robotic arm can move the DQA phantom to different focal distance using this clamp. The target phantom was moved to a new position 15 mm away from its previous one along the axis of the transducer with at least three sonications at each position. The focal distances achieved in this experiment was in the range of 130 mm to 190 mm. 1000 J

acoustic energy was applied in each sonication. Sonications without ribcage model were then performed for control experiment using the same parameters.

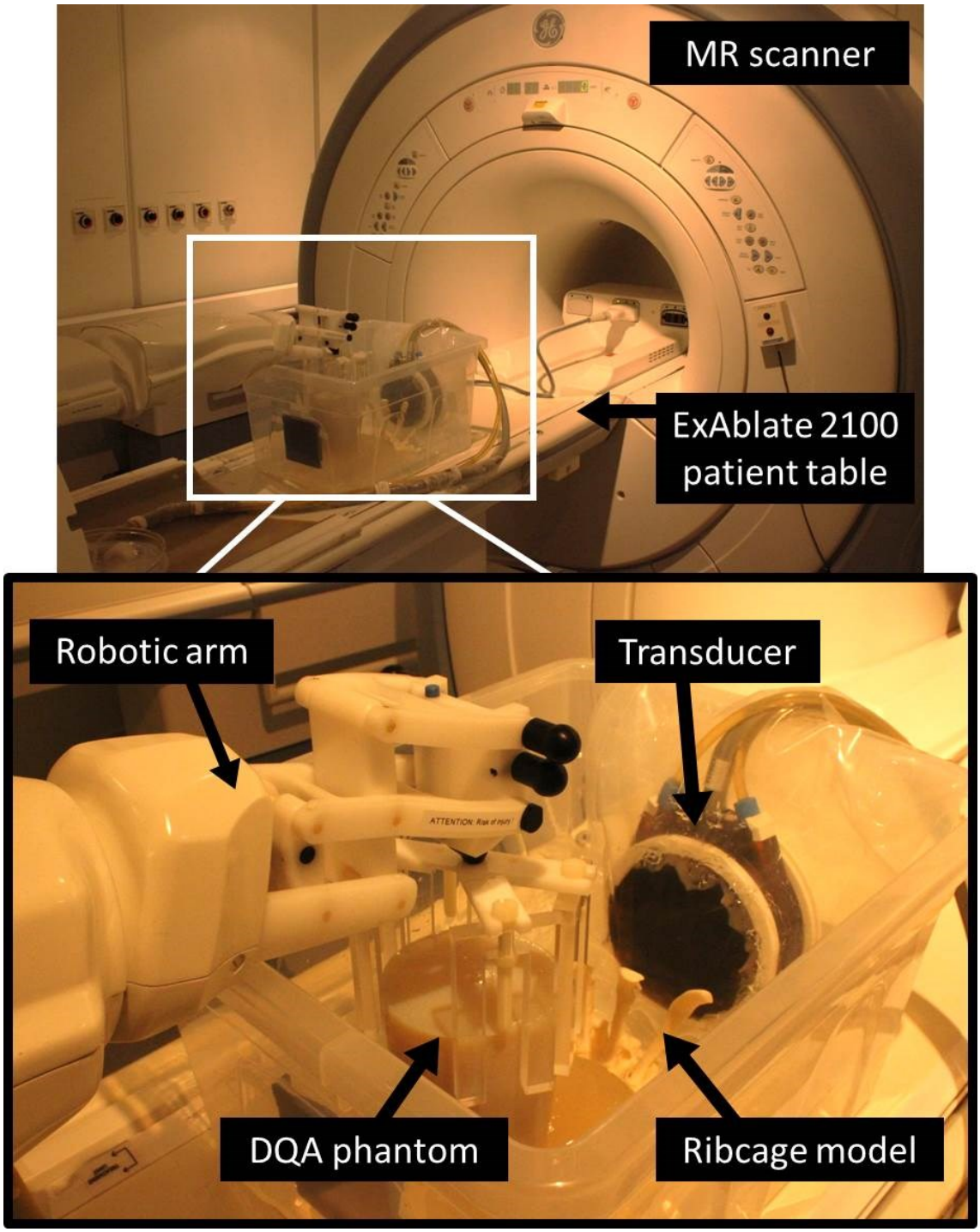

Figure 4.14 Experimental setup of sonication with different focal distance in transcostal HIFU

4.4.5. Varying ribcage model locations

This section reports the effect of ribcage model with varied ribcage model locations. By fixing transducer and target phantom, sonications were performed through ribcage with varied ribcage positions along the radial direction of the transducer. To understand the difference between transcostal and intercostal propagation, both transcostal and intercostal positions are included.

In Figure 4.15, transducer and target phantom were fixed in position, while the ribcage model was moved by the robotic arm along the radial direction of the transducer (indicated by double headed arrow).

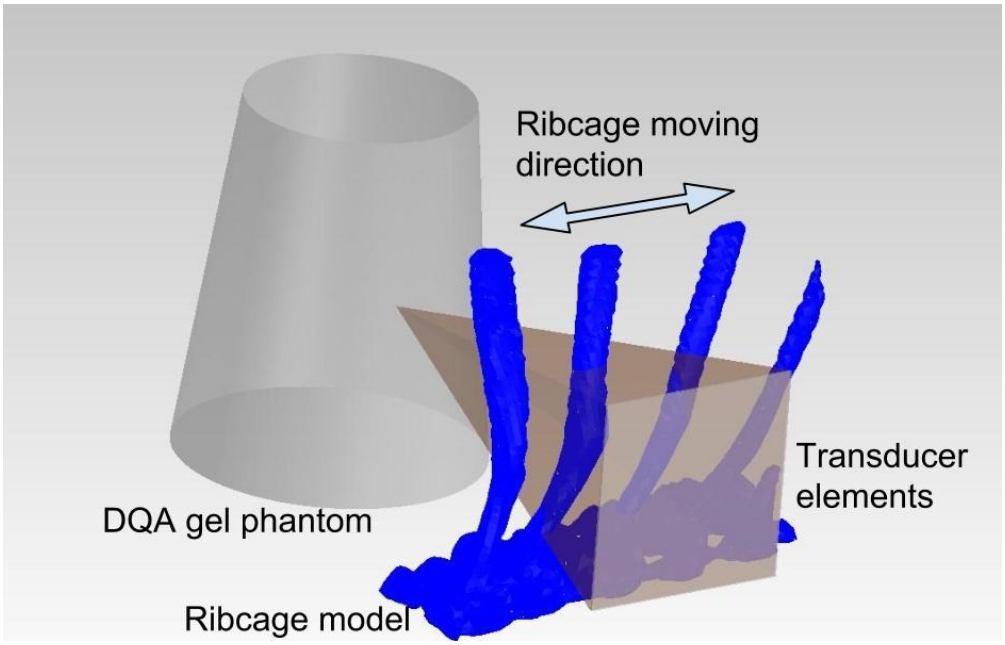

Figure 4.15 Schematic diagram of varying ribcage location along the radial direction of the transducer elements plane

In Figure 4.16, the experiment was set up on ExAblate 2100 patient table. The ribcage model was held by the plastic clamp connecting to the front end of the robotic arm, while the phantom and transducer were fixed in the water tank. The ribcage model was moved by the robotic arm with 5 mm per step in ± 20 mm motion range in radial direction of the transducer (same to sagittal direction of the MR scanner). At least three sonications were used at each position. 1000 J acoustic energy was applied in each

sonication. The sonication started at transcostal position with axis of the transducer on a piece of ribs.

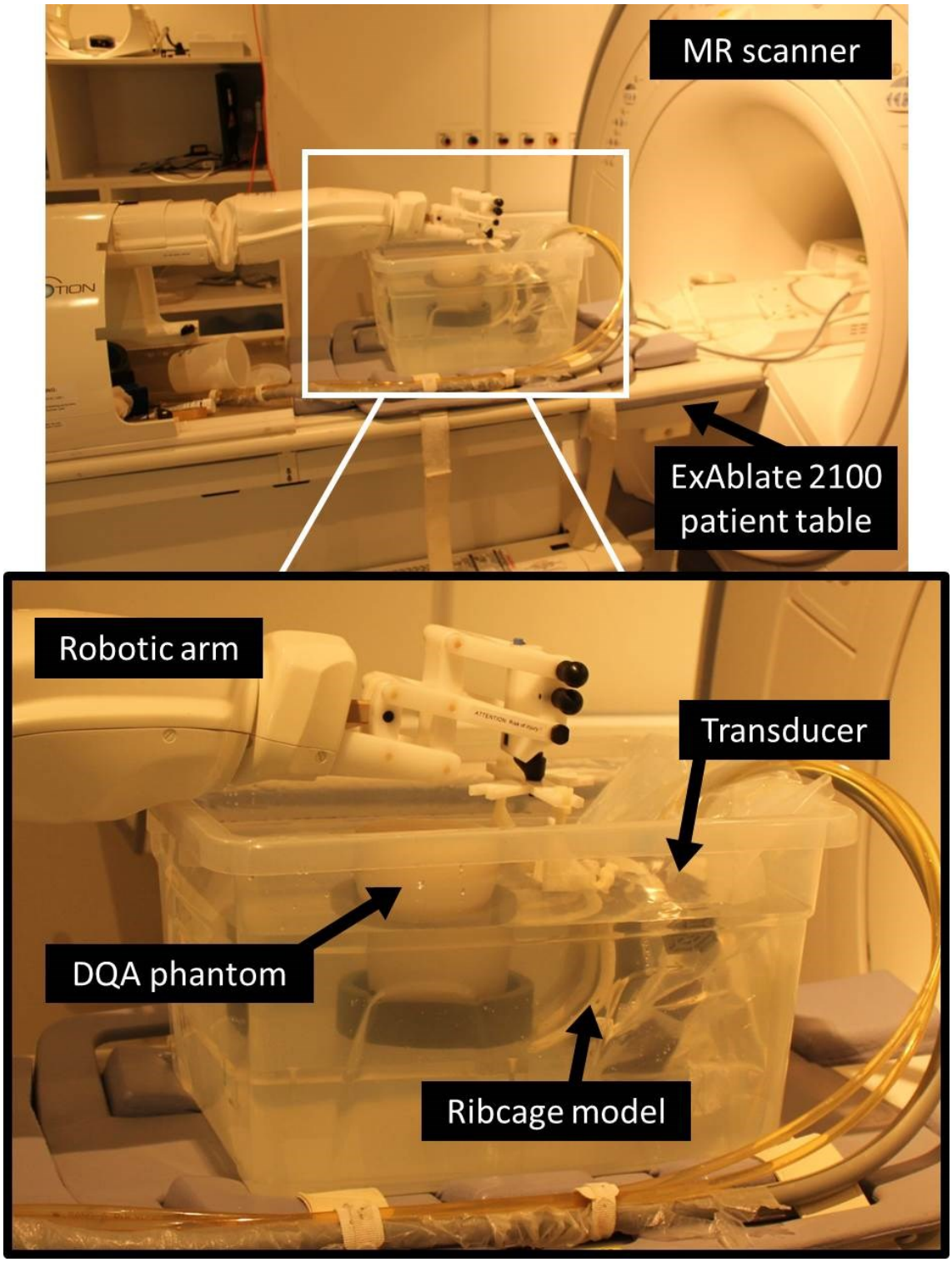

Figure 4.16 Experimental setup of sonication with different ribcage location

4.4.6. Validation of focal temperature change

In order to investigate the relation between temperature change and shadow area on transducer plane caused by the ribcage model, the total occluded area was estimated using a computer generated ribcage model placing between a transducer and phantom with the same dimensions as the real ones. The location of the phantom and ribcage models was varied in both axis and radial direction of the transducer.

The blocked area in the beam path was projected onto the transducer plane according to the spatial positions. Considering the focused ultrasound beam as a radiation from the focus to the transducer, as seen in Figure 4.17(a), the actual shadow area on the transducer was larger than that in the beam path. Therefore, this projection used the ray tracing from the focal point to the transducer plane.

In the sonications with varied focal distances (section 4.4.4), transducer and phantom were in fixed position. Different target phantom positions were according to the same relative position in the experiment. For different ribcage locations with a fixed focal length (section 4.4.5), the ribcage model was placed at varied locations the same to that in the experiment. Results were then be compared with the focal temperature changes.

This projection can be better understood by the ray tracing from focus to transducer in Figure 4.17(b), coronal view of MR image. It is the top view of the experimental setup of sonication with ribcage in the beam path. The field of view includes a phantom, a transducer and a ribcage model within a water tank. Focus (yellow point) of the sonication was determined within the phantom. The elements of the transducer appeared to be a straight line from this view and were marked by a yellow solid line. The cross section of the ribs in this view was represented by green circles. The shadow area was projected by oblique ray tracing (red dashed line) from the focus passing the edge of the green circles onto the transducer plane. The shadow area on transducer in this image slice was drawn by cyan blue lines.

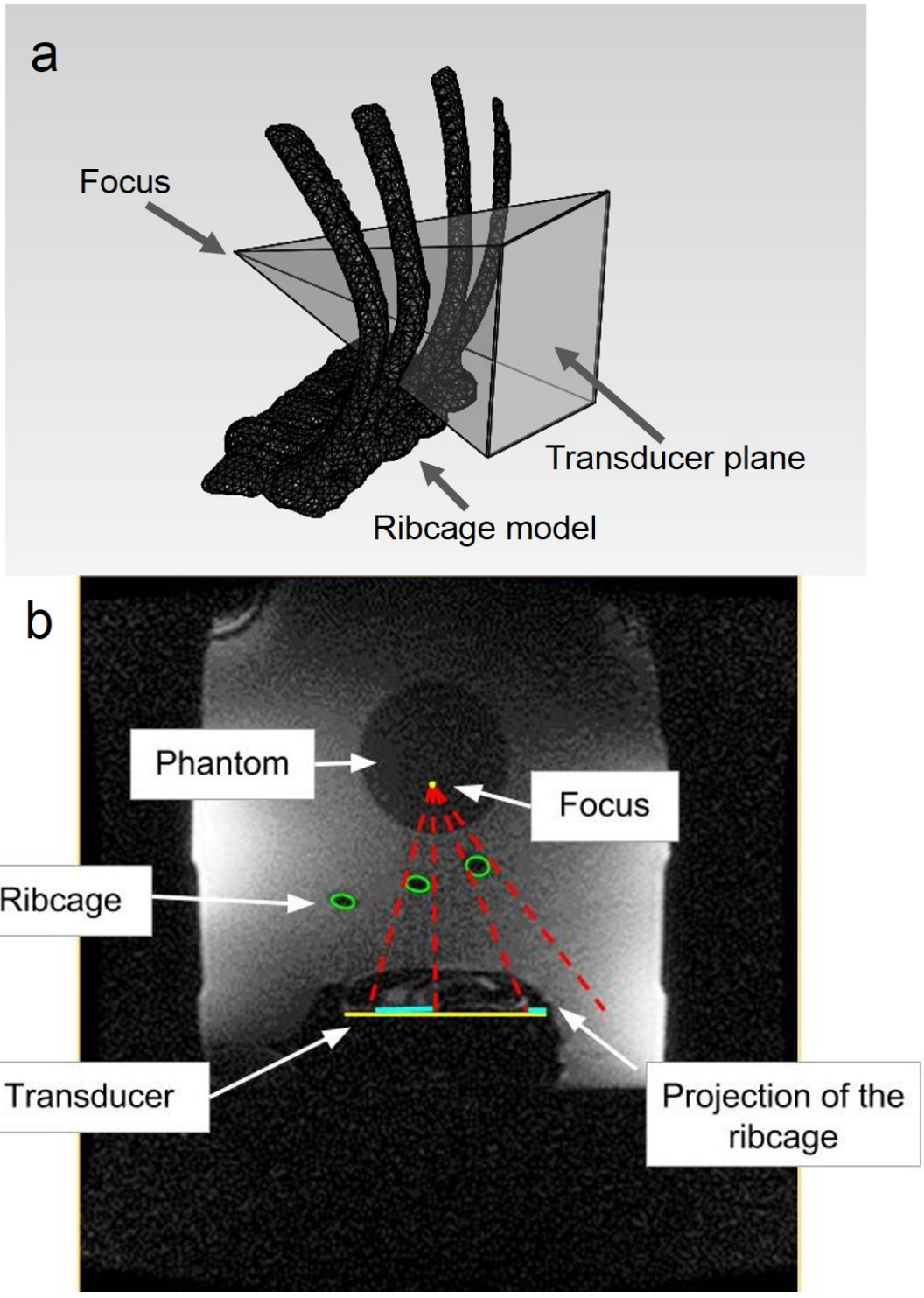

Figure 4.17 Propagation of ultrasound beam through ribcage: (a) 3D model of the ultrasound propagation through ribcage; (b) Projection of ribcage on transducer surface (Spin Echo, TE 85.0, TR 1306.8)

4.5. Results and discussion

The results of acoustic pressure distribution and acoustic power were normalised because different power levels were used in the two different types of measurement. They were compared with the dimensions of the four ribcage models. Results of the effect of ribcage on focal temperature elevation are described and discussed subsequently.

4.5.1. Effect of ribcage on acoustic pressure distribution

4.5.1.1. Changes in peak acoustic pressure of acoustic field

Acoustic field distribution was visualised by acoustic pressure mapping in three orthogonal views. In Figure 4.18, the three images in each row indicate the three orthogonal views of acoustic pressure at focal region in free field (a, b, c), with the effect of the ribcage model of patient No.1 in transcostal position (d, e, f), and with the presence of the same ribcage model in intercostal position (g, h, i) respectively. Within the transverse plane of the focal region, the focal shape was round in free field as shown in Figure 4.18(a) and it distorted with the presence of ribcage. Focus splitting occurred in transcostal propagation (Figure 4.18(d)), while the radius of the focus expanded in y axis direction at intercostal position (Figure 4.18(g)). Details of focus distortion will be presented in section 4.5.1.2.

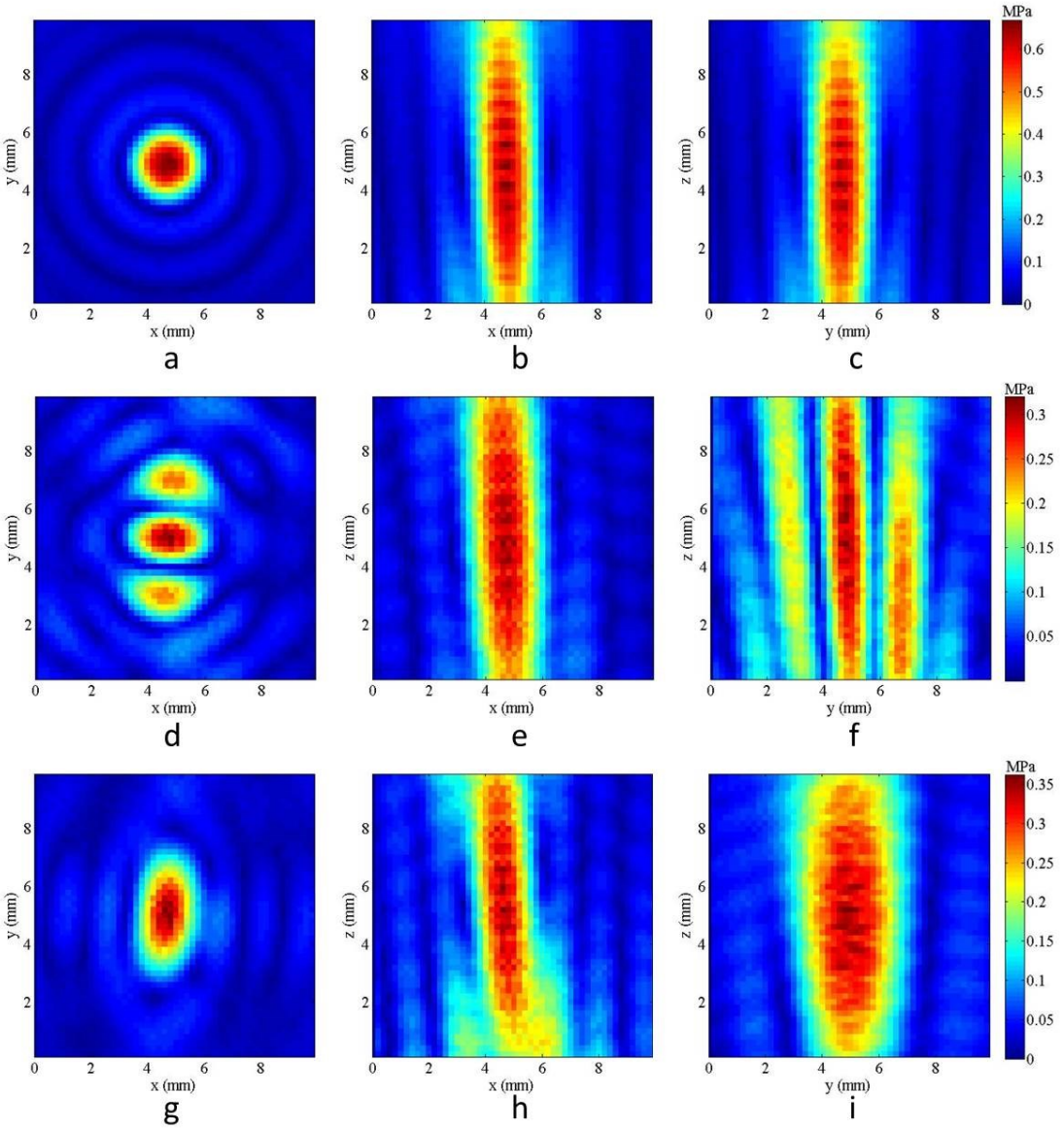

Figure 4.18 Acoustic pressure distribution in three orthogonal focal planes in free field (a, b and c); with the ribcage in transcostal position (d, e and f); and with the ribcage in intercostal position (g, h and i) using No.1 patient's ribcage model

Peak value of the acoustic pressure at focus varied according to the width or spacing dimension of the ribs. Peak acoustic pressure at focus was 0.669 MPa in free field, and it decreased significantly owing to both transcostal and intercostal wave propagation. Results were normalised using peak acoustic pressure in transcostal and intercostal propagation divided by the peak value obtained in free field. In three (patient No.1, 2 and 4) out of four models, the peak pressure of acoustic filed using intercostal setup was apparently higher than that using transcostal setup (Table 4.1). Considering the ultrasound wave generated from piezo-material concentrating to a focus, most of the energy

propagated via the sides of the single rib at transcostal position and through the spacing of two ribs at intercostal position (Figure 4.3). Compared with intercostal propagation, more acoustic energy was blocked by the ribcage model in the pathway in transcostal position and resulted in a lower focal peak pressure.

Table 4.1 Ratio of peak acoustic pressure in transcostal (and intercostal) propagation and free field propagation

Patient No.	Transcostal propagation	Intercostal propagation
1	0.482	0.542
2	0.445	0.680
3	0.417	0.411
4	0.360	0.557

In the measurement result of the width and spacing dimensions of the ribcage models (section 3.1.1), the spacing between 9^{th} and 10^{th} ribs of No.3 patient's ribcage model is the smallest in all of the four models. This resulted in minimal ultrasound wave propagating through intercostal space using No.3 patient's ribcage model. Peak acoustic pressure at focus using this model showed the lowest intercostal value. On the other hand, a larger spacing implies more energy could be delivered to the focus through the intercostal spaces. The highest peak acoustic pressure was found in the measurement using No.2 patient's ribcage model, as this model has the largest spacing between 9^{th} and 10^{th} ribs.

In HIFU treatment with the ribcage in the beam path, the intercostal setup can provide a wider acoustic window through the ribcage to reduce the energy loss in most of the cases. In terms of transcostal setup, the width of the ribs affected the wave propagation. Because the width is varied at different position of a rib and it is not easy to compare two ribs considering the difference in curvature. An effective method was needed to determine the effect of ribcage. The shadow area on the transducer resulted from the ribcage was selected to study the relation between ribs occlusion and focal temperature change. The

validation study of the focal temperature change related to the shadow area is illustrated in section 4.5.4.5.

4.5.1.2. Distortion at focal region

Results of acoustic field mapping with the presence of all of the four ribcage models in the focused ultrasound beam path showed similar focal pressure distribution pattern to Figure 4.18. By placing different ribcage models in the ultrasound beam path, the focus splitting occurred at transcostal wave propagation and focal radius expanded in y axis direction using intercostal propagation. The location of the peak acoustic pressure at focal region shifted within 0.1 mm to 0.3 mm in different propagation circumstances. Considering the extent of HIFU should include the tumour lesion and its marginal tissue about 1.5 cm to 2.0 cm around the tumour (Wu *et al.* 2003b), shift within this scale could be negligible when treating large tumours.

In the acoustic pressure field mapping at transcostal position, the focus was splitted into three main parts in transverse focal plane, which has been investigated using numerical modelling and tissue ablation *in vitro* (Khokhlova *et al.* 2010). The rib model on ultrasound beam axis was parallel to the x axis of the 3D stages as shown in Figure 4.19. The ultrasound wave was interfered by the rib and concentrated to form a main focus with another two secondary foci located on both sides of the main one. To better understand the acoustic pressure distribution of the focal region, the transverse view of the acoustic field was superposed on the transcostal propagation setup in Figure 4.19(a).

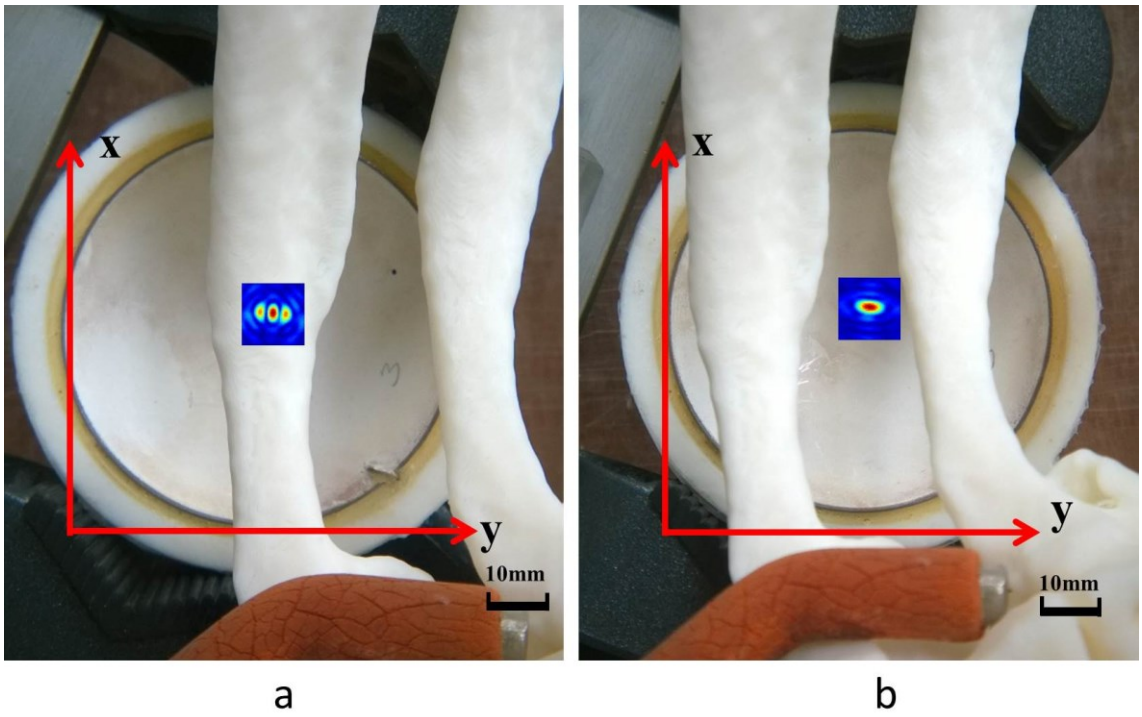

Figure 4.19 (a) Transcostal acoustic field and (b) intercostal acoustic field superposed on the two setups respectively using No.1 patient's ribcage model (x, y in the figure indicate the x and y axis of the scanning system)

Figure 4.20 indicate that the focused ultrasound wave provided similar acoustic pressure distribution at focus with the four ribcage models. In each subfigure, two secondary foci located next to the main focus along y axis direction within 2 mm. The peak acoustic pressures of the secondary foci were different and all in the range between 70% (patient No.1) and 85% (patient No.4) of the peak acoustic pressure of the main focus. The two secondary foci may be not in the same transverse plane (xy plane) with the main focus. In Figure 4.18(f), the left secondary focus stayed in the same focal distance with the main one, but the right secondary focus was approximately 2 mm closer to the transducer.

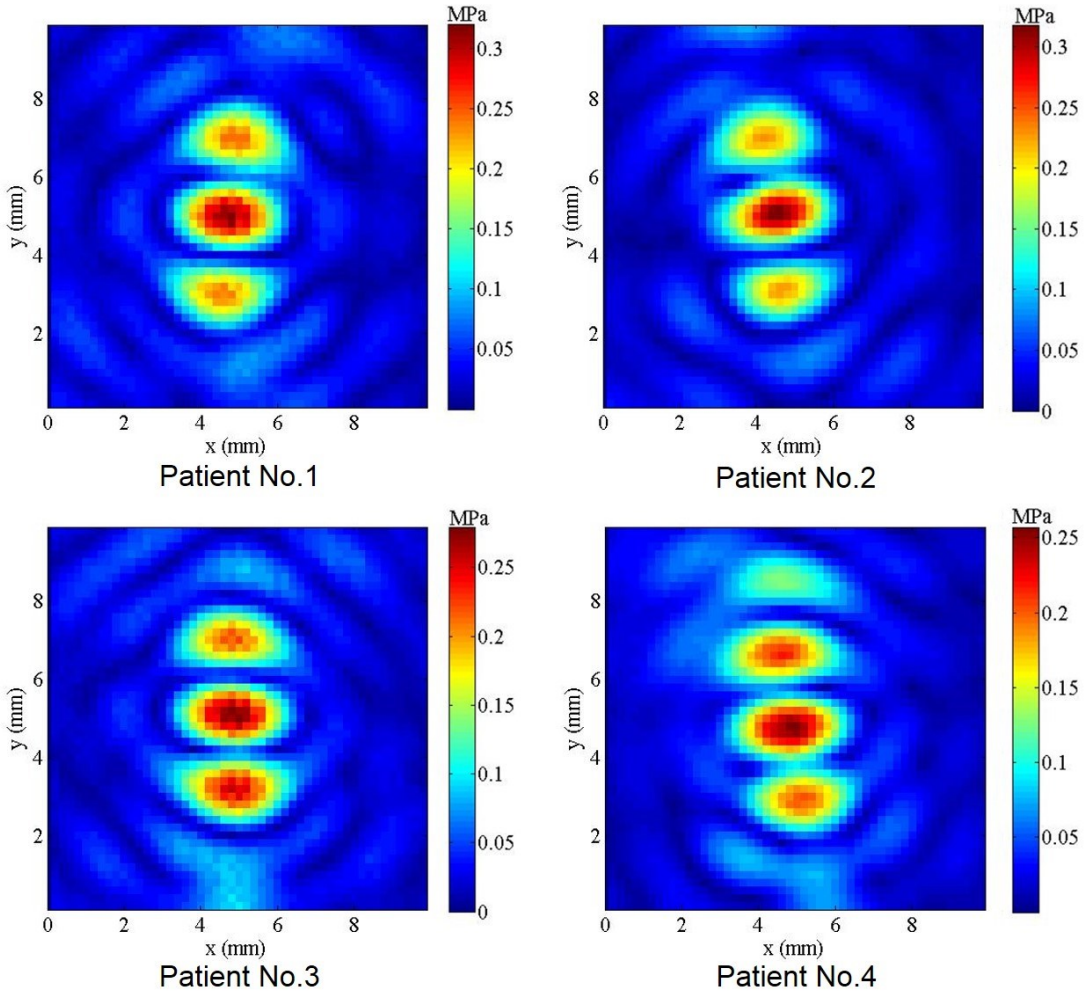

Figure 4.20 Focus splitting in transverse focal plane

In terms of propagating through intercostal space, the focal shape in transverse plane turned into elliptical shape (Figure 4.18(g)), which was completely different compared with the focus in free field (round shape, Figure 4.18(a)) or at transcostal position (focus splitting, Figure 4.18(d)). The ultrasonic wave deflected by the ribs distributed surrounding the original focus and formed a wider focal pattern in y axis direction in the transverse plane. This distortion was superposed onto the experimental intercostal propagation setup, as displayed in Figure 4.19(b).

Since a decrease has been observed in the peak acoustic pressure at focus with the presence of ribcage model, the focal temperature rise could be affected if more than one single focus appears or the focal area becomes larger. Effect on focal temperature change were be verified in the following experiments.

4.5.2. Effect of ribcage on acoustic power delivery

For the single element transducer, power conversion ratio of acoustic power and electric power in free field was 0.622 ± 0.016 using input electric power in the range of 10 W to 50 W. This ratio was reduced owing to the ribcage by absorption, scattering and reflection to ultrasound wave. The power conversion ratio through intercostal propagation was found to be higher than that via transcostal propagation with all of the four ribcage models in the beam path, as depicted in Figure 4.21.

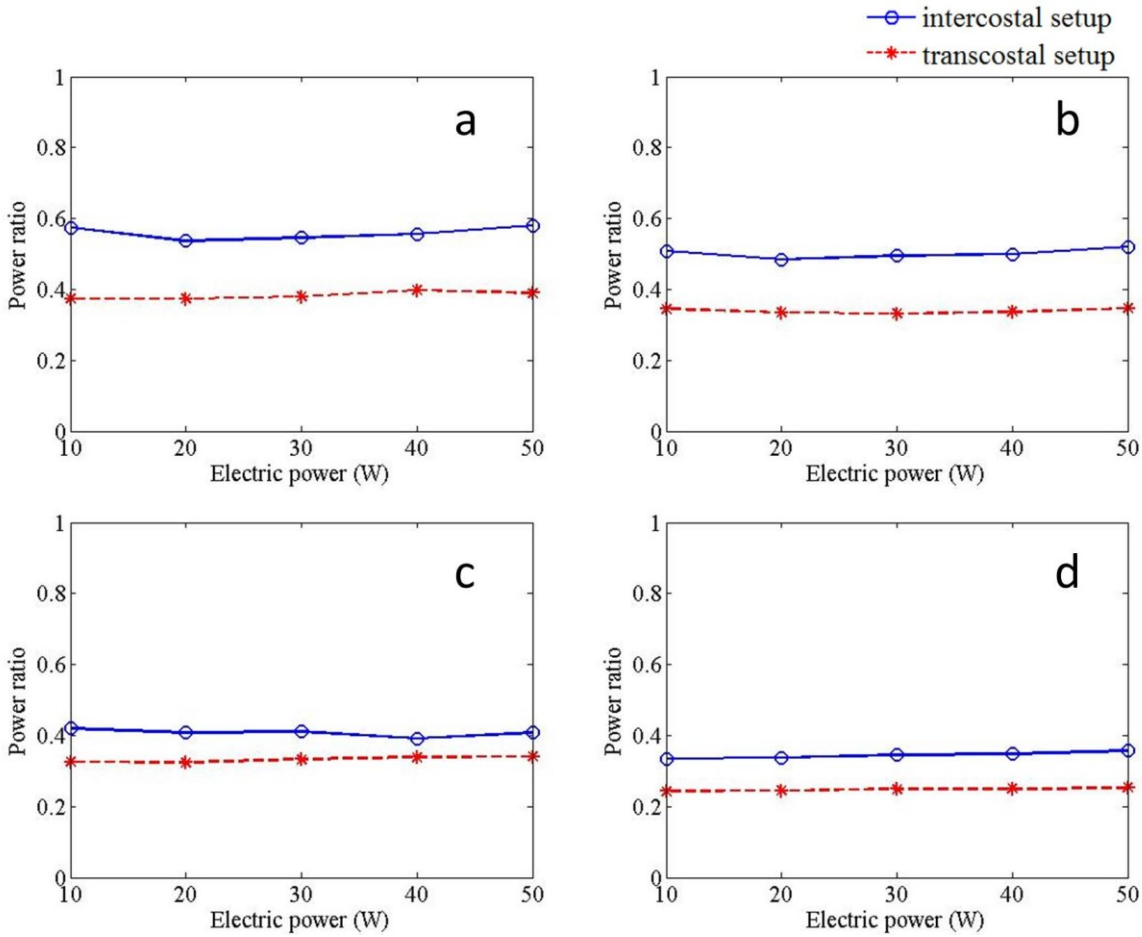

Figure 4.21 Power conversion ratio of acoustic power (output) and electric power (input). a: patient No.1; b: patient No.2; c: patient No.3; d: patient No.4

This ratio at intercostal position was just slightly higher than that at transcostal position regarding the model of No.3 patient (Figure 4.21(c)). The difference in power delivery between intercostal and transcostal position was the smallest using No.3 patient's

ribcage in all of the four models, which is in good agreement with the result in acoustic pressure mapping. The peak acoustic pressure using intercostal and transcostal setup provided highly close result.

Ribcage model of patient No.1 and No.2 at intercostal position showed higher power conversion ratio compared with the results that using transcostal setup or the other models. Likewise, the maximum peak acoustic pressure of the focal region was also acquired at intercostal position when using No.2 patient's ribcage model (Table 4.1). This can be verified using the dimensions of the ribs. In Table 3.1, No.2 patient's ribcage model has the biggest spacing of 9^{th} and 10^{th} ribs in all of the four models.

The lowest power conversion ratio was obtained in transcostal setup with No.4 patient's ribcage model in place. Similarly, the minimum peak acoustic pressure also occurred in transcostal setup using No.4 patient's ribcage model. According to the widths at three positions (w1-w3 in Table 3.1) on a rib, the model of patient No.4 has the widest 9^{th} rib compared with the other three models. Therefore, least energy was delivered to the focus with the influence of No.4 patient's ribcage model placing at transcostal position.

However, differences still existed between the effect of ribcage models on acoustic pressure and acoustic power, because different setups were used in the measurement of these two parameters. It should be noted that acoustic pressure and acoustic power cannot be measured simultaneously or measured in the same environment. The measurement of acoustic power required a water environment as small as possible to ensure the stability of the radiation force balance and the acoustic absorber target, but this will definitely limit the range of the acoustic pressure field scanning. The supporting wires for connecting the force balance and the absorber target could narrow down the space for the movement of the needle hydrophone driven by the 3D stages. The variation in curvature of the four ribcage models could be another reason that caused different results in acoustic pressure and power measurement, even if no obvious trend related to rib curvature was found.

This study was not to find out the relation between the acoustic pressure and acoustic power of HIFU transducer, as the input for the transducer in the two measurements was in different levels considering the safety of needle hydrophone in

acoustic field mapping. However, the relative position of the ribcage model placing in the two setups was ensured as similar as possible.

Because of the remarkable difference in peak focal pressure and acoustic power delivery between transcostal and intercostal setup using No.2 patient's ribcage model, this model was selected as the obstacle in HIFU sonication experiment to investigate the focal temperature change.

4.5.3. Effect of ribcage on heat deposition at focus

Temperature field was captured on a smooth surface of the TMM phantom. 29 °C temperature rise was observed at focus without any barriers in the acoustic field, while 25 °C increase with the effect of ribcage model. The temperature field mapping at transverse plane of the focus was shown in Figure 4.22. The two subfigures were cropped from the original temperature field mapping of the whole field of view of the thermal camera for a larger display. More energy was delivered to the focus in free field and obvious distortion can be seen from the temperature contours due to the effect of ribcage model. It was a nearly round focus in Figure 4.22(a) even there was a little spread at 5 mm away from the focal centre. It may be resulted from the inhomogeneous heat diffusion of the phantom at that area. The focus appeared as an ellipse shape with the presence of the ribcage (Figure 4.22(b)). No focus splitting was observed because this was not a steady thermal field during the HIFU sonication. As the thermal image was captured at the end of each sonication, heat deposited at focus may have been exchanged with surrounding area. This could cause the whole focal region a high temperature and result in secondary foci not significant.

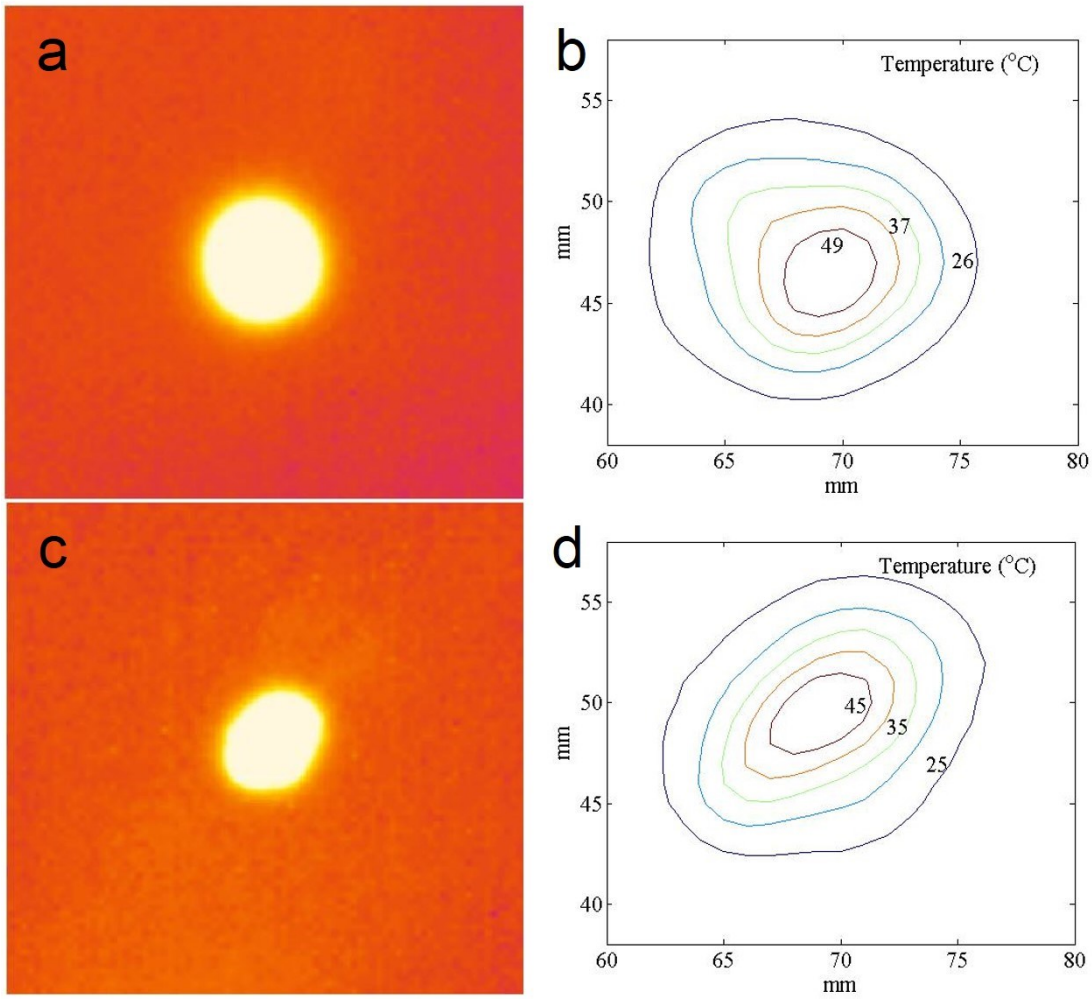

Figure 4.22 Heat deposition at focus using transcostal propagation (a and c are IR images; b and d are contour maps of temperatures; a and b: in free field; c and d: with the presence of ribcage model)

Atomization and fountain formation (Simon *et al.* 2012) at focal area on the phantom surface was occasionally observed at the end of the sonication. The water based phantom could be boiled at focus and produce vapour bubble. As part of the energy at focus was consumed for atomization, less heat deposited at focus along with the atomization and fountain formation. As a result, the temperature field mapping on a phantom exposed in the air may not provide accurate temperature distribution at focal region, even if the thermal field captured by the thermal camera showed obviously different focal shape with and without the ribcage model in the beam path. The temperature measurement at focus of HIFU needs to be carried out within the tissue or phantom with less heat loss to ensure a more reliable result.

4.5.4. Effect of ribcage on focal temperature elevation

The ribcage model of patient No.2 was selected to place into the HIFU beam path to study the ribcage effect by HIFU sonication using varied sonication parameters and locations of target phantom and ribcage model. As the experiments have covered as many as the circumstances, including both transcostal and intercostal propagation and different focal distance, it was reasonable to use only one ribcage model for the sonication experiment and presumably a waste of resources to apply all of the ribcage models to repeat these sonications.

The initial temperature of the phantom was determined by the room temperature, which was 20.0 °C and the room temperature was controlled by the air conditioner in MRI suite. It was different from the commonly accepted average core body temperature (taken internally) 37.0 °C. However, acoustic energy applied in this study was high enough to provide a maximum temperature rise over 40 °C on the TMM phantom, which would be definitely enough to result in protein necrosis and damage the diseased tissue.

4.5.4.1. Sonications on TMM phantom

Sonications were performed at different locations on DQA phantom without any barriers in the focused ultrasound field. The temperature rise of six sonication spots on the phantom using 50 W acoustic power over varied duration time was shown in Figure 4.23. According to the spot location number marked in Figure 4.11(b), higher temperature rise was obtained at a closer focal distance (spot 1, 2, 3 and 4), while the temperature rise at spot 5 and 6 was obviously lower than that at the other 4 spots. Longer focal distance resulted in more acoustic attenuation during ultrasound wave propagating in the phantom. Therefore, to study the temperature change at different focal distance, it is necessary to locate the focus at a fixed depth in the target phantom.

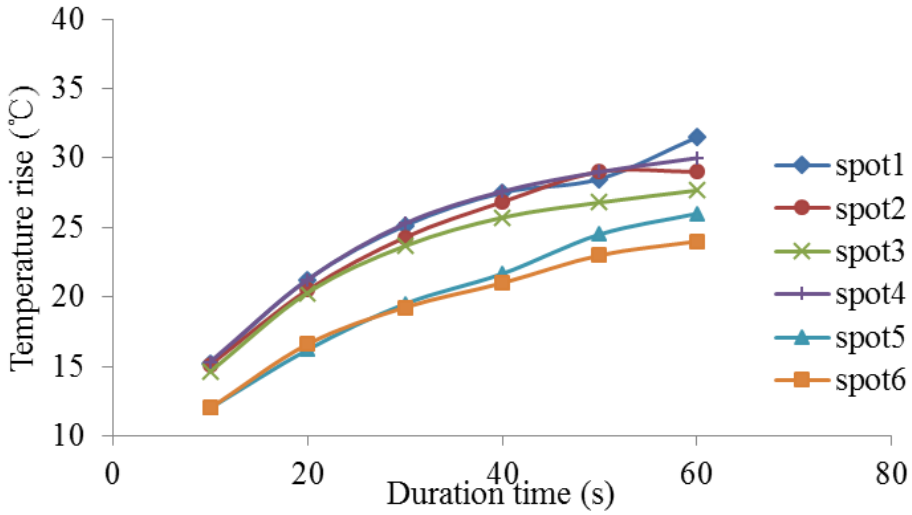

Figure 4.23 Focal temperature at different locations

4.5.4.2. Varying sonication parameters

Acoustic power was varied in the sonications over a constant time of 20 s. In Figure 4.24(a), difference between temperature rise with and without the ribcage effect was gradually getting larger when a higher acoustic power was applied. The presence of the ribcage model caused a 5.5 °C decrease in focal temperature change at 25 W and 9 °C at 150 W.

Then the sonication time was varied (from 10 s to 60 s, 10 s per step) in the sonications using a constant acoustic power of 50 W. The similar trend was observed in the temperature difference with and without ribcage model. Figure 4.24(b) shows the temperature difference induced by ribcage model was 3.2 °C using 10 s exposure time, while it was 7.3 °C over 60 s.

The effect of ribcage on focal temperature was varied by increasing acoustic power or extending sonication time. The thermal diffusion in the phantom may varied at different temperature, which could result in the different effect in Figure 4.24.

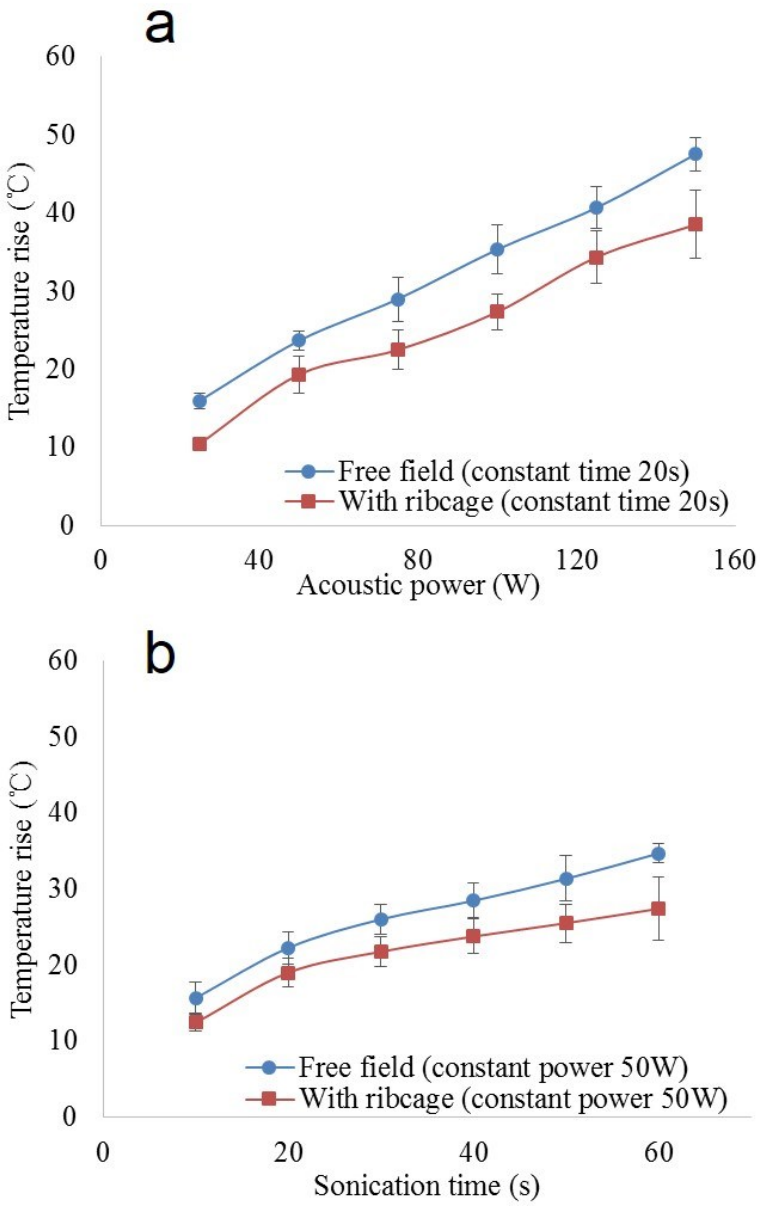

Figure 4.24 Temperature change using (a) a constant sonication time and (b) a constant acoustic power (a. Temperature rise at focus using 25 W – 150 W acoustic power over 20 s; b. Temperature rise at focus using 50 W acoustic power over 10 s – 60 s sonication time)

To compare and analyse the difference in efficacy between increasing acoustic power and extending sonication time, sonications were performed using the same total acoustic energy. Figure 4.25 shows the focal temperature rise on phantom using acoustic energy in the range of 500 J to 3000 J (500 J per step). Increasing acoustic power (red square markers) over constant sonication time and extending sonication time (blue dot markers) using constant acoustic power was compared. Figure 4.25(a) is the result

without the presence of ribcage model. The red line denotes the results using 25 W to 150 W acoustic power over constant 20 s and blue line indicates sonication results using constant 50 W over 10 s to 60 s. The focal temperature change reveal that in the use of 25 W to 150 W over constant 20 s, temperature rose more rapidly than using 50 W over 10 s to 60 s.

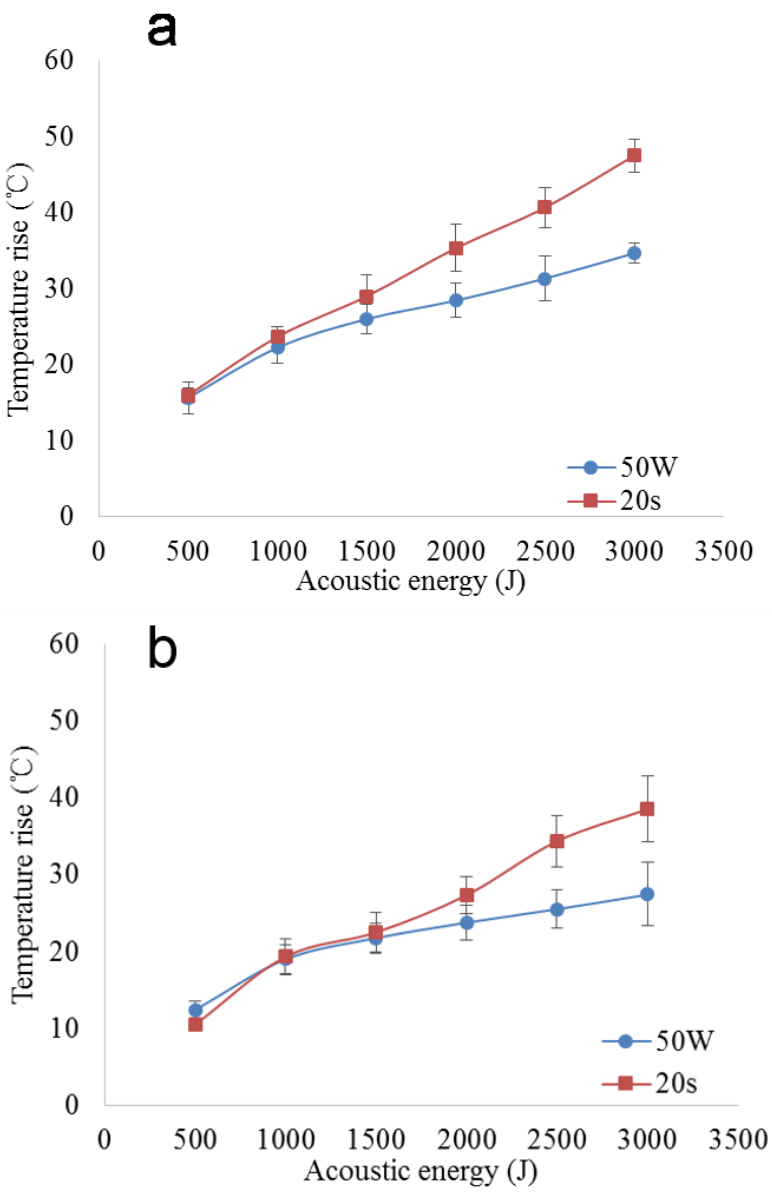

Figure 4.25 Comparison of using constant power and constant duration time (a. Free field; b. With the presence of ribcage model)

Results with the presence of ribcage phantom (Figure 4.25(b)) indicate the similar trend. Temperature rise with increasing acoustic power or extending sonication time agreed well below 1500 J. When the total acoustic energy exceeded 2000 J, focal temperature rise of sonications using growing acoustic power (red line in Figure 4.25(b)) was dramatically higher than sonications using extending sonication time (blue line in Figure 4.25(b)). The most significant difference in temperature elevation occurred when highest acoustic energy 3000 J was applied.

Therefore, in the case of using the same total energy (within the range of 500 J to 3000 J), high acoustic power over short sonication time can provide a higher efficiency in the acoustic energy delivery and lead to a higher temperature rise at focus than using low acoustic power over long sonication time. This was due to more energy attenuated in the beam path during a longer sonication time. It suggested that to improve the efficacy of HIFU treatment, it is best to apply higher acoustic power over a short time period with the power below the tolerability of the patients. When comes to the treatment on patients, the complicated structures of the tissues and different characteristics of humans should be considered. There may not be a strictly safety value for all the cases in HIFU treatment and more research is needed to determine the individual safe thermal dose. The TMM phantom presented in Chapter 3 could pave the way for this thermal dose study.

It should be note that the measurement of ribcage effect on acoustic power delivery (section 4.5.2) and on focal temperature elevation (section 4.5.4) used different HIFU transducer and experimental setup, which resulted in different circumstances for focused ultrasound wave propagation. The RFB device cannot work with MR scanner and the acoustic power of multi-element transducer of ExAblate patient table works only with the MR scanner. It is impossible to evaluate the acoustic pressure distribution or focal acoustic energy in MRI environment using needle hydrophone or RFB device. Therefore, the homemade single element transducer was selected to determine the ribcage effect on acoustic pressure and acoustic power out of MRI environment. The multi-element transducer of ExAblate 2100 system was used to investigate the influence of the ribcage on focal temperature using MRI thermometry.

RFB setup (section 4.2) for acoustic power measurement applied water as the medium and used acoustic absorber as a target to experience the radiation force. Ultrasound wave propagated through the water with less energy loss compared with the

propagation in tissue or phantom. The phantom was used in the sonication experiment and the acoustic attenuation of the phantom cannot be neglected. Therefore, some of the energy lost during the ultrasound wave propagation in the phantom before approaching to the focus. The loss of energy may be absorbed by the phantom in the pathway, produce mechanical effect, be reflected at the interface of two different materials (water and phantom) and etc.

4.5.4.3. Varying target phantom locations

Focal length of HIFU sonication was varied with and without the presence of ribcage model. The results of focal temperature change at various focal lengths within 130 mm to 190 mm were reported in Figure 4.26. By extending the focal length, focal temperatures with and without the effect of ribcage model were both decreased. This was because more energy was lost during longer pathway of the ultrasound wave propagation. It can be seen that the ribcage model resulted in a reduction in focal temperature rise and this reduction was dependent on the focal distance. When beam focusing at a closer location, the ribcage model affected slightly more on the focal temperature than that with a longer focal distance, because the shadow area on transducer blocked by the ribcage model was generally becoming smaller with longer focal length (it is verified in section 4.5.4.5). Specifically, 3.33 °C decreased owing to the ribcage model at 130 mm focal distance and 2.67 °C at 190 mm.

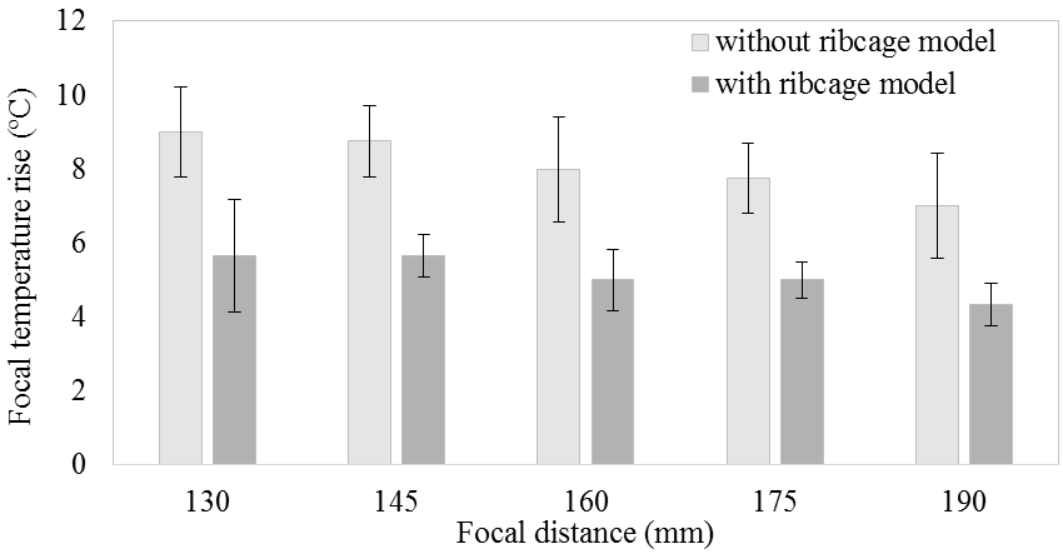

Figure 4.26 Focal temperature rise at different focal distance

4.5.4.4. Varying ribcage model locations

By changing the position of ribcage model along radial direction of the transducer, the wave propagation at both transcostal and intercostal space were studied. This variation did not provide much difference in focal temperature rise. The focal temperature increased 5.72 ± 0.67 °C when moving the ribcage model along the radial direction of the transducer. Ribcage model at different radial positions had almost the same influence on the focal temperature rise and no trend in temperature change was found. This could be explained by similar blocked area by the ribcage at different locations. The validation of the relation between shadow area and temperature difference will be presented in section 4.5.4.5.

By varying the position of the phantom and the ribcage model in the HIFU beam path, different focal length and both transcostal and intercostal propagation can be investigated. Other ribcage models were not applied to repeat the same sonication experiments.

4.5.4.5. Validation calculation of focal temperature change

In this validation study, projection of the blocked area on transducer elements was calculated at varied focal distance and varied ribcage radial locations.

For sonication at varied focal length, Figure 4.27 shows the occluded area owing to the ribcage at different focal length. The five subfigures indicate the shadow area at varied focal distance ranged from 130 mm to 190 mm. The blocked area on transducer decreased with longer focal length, which is listed in Table 4.2.

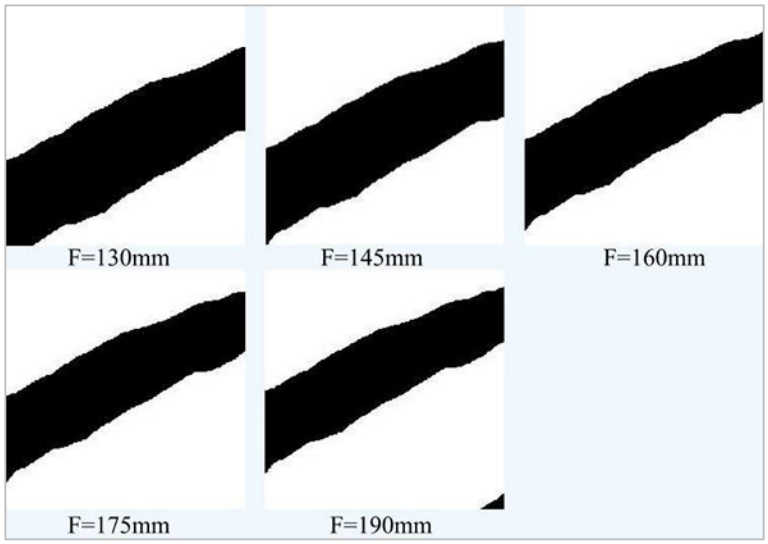

Figure 4.27 Shadow area on the transducer owing to the ribcage at varied focal length

Table 4.2 Blocked area on the transducer at different focal length

Focal length (mm)	Blocked area (mm^2)
130	2515.20
145	2328.96
160	2150.40
175	2022.40
190	1937.28

Compared with temperature differences in Figure 4.26, effect of ribcage model was becoming slightly smaller by extending the focal distance. This indicates that the effect of ribcage on focal temperature elevation related to ribcage induced shadow area on HIFU transducer.

In terms of different ribcage location in radial direction of the transducer plane, the total blocked areas on transducer were similar when moving the ribcage within ± 20 mm. Figure 4.28 denotes ribcage projection on the transducer plane at different radial locations. The calculated results of the each shadow area are listed in Table 4.3. The elements area of the transducer is 80 mm × 80 mm, which is bigger than the projection of the interval space of the ribs. Therefore, when a piece of ribs moved out of the transducer elements area another piece moved into it, which resulted in the total blocked area to be almost constant (Table 4.3) if varying the ribcage location along the radial direction of the transducer.

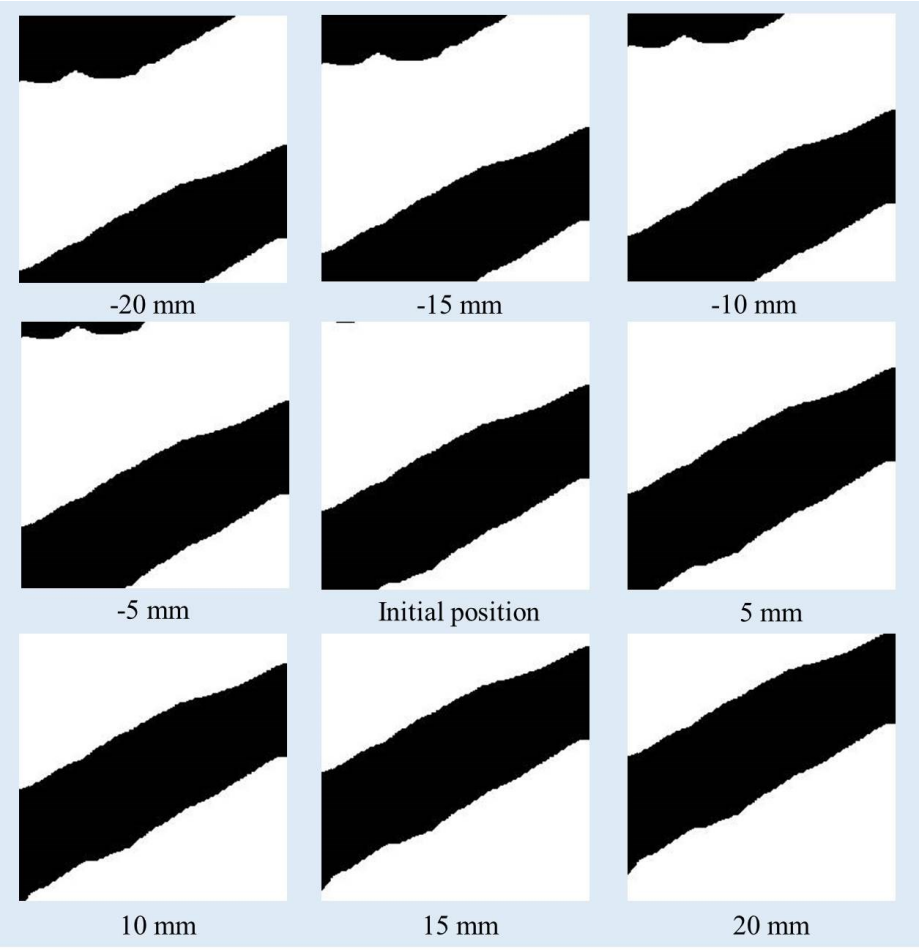

Figure 4.28 Shadow area on HIFU transducer owing to the ribcage model at varied ribcage location in radial direction of the transducer in the range of ± 20 mm

Table 4.3 Blocked area on the transducer at different radial position

Position	Blocked area (mm^2)
-20	2563.20
-15	2518.40
-10	2473.60
-5	2451.84
0	2515.20
+5	2536.96
+10	2538.88
+15	2536.32
+20	2493.44

Movement range of the ribcage was within ± 20 mm, which was large enough to reach both transcostal position and intercostal position. Effect of the ribcage model did not show much difference on focal temperature at transcostal and intercostal positions by using a transducer with elements area in an 80 mm × 80 mm square. By comparing the temperature rise and the shadow area on transducer elements for validation, the temperature change in the transcostal and intercostal sonication can be related to the coverage area on the transducer elements owing to the ribcage. This enables the prediction of the focal temperature change with the ribcage at different locations.

Slice thickness of MRI during the sonications was 3 mm with 1 mm spacing. If estimating the projection using the combination of the discrete projection parts on every single image slice, the interval between two slices may not as accurate as the direct projection from a 3D model. Estimation of the shadow area was not to calculate the exact value of this area, but to validate the trend of the temperature change at focus. Therefore, the computer generated model was use to acquire and estimate the accurate shadow area for better agreement with the structure profile of the ribcage.

4.6. Summary

Using the reconstructed physical ribcage models based on image data from patients, influence of this model on acoustic pressure, acoustic power and focal temperature rise was investigated. Both transcostal and intercostal propagation were studied. Results reveal that three in four ribcage models delivered more energy to focus when ultrasound beam focusing through intercostal space. The results also suggest that the acoustic pressure and acoustic power delivered to focus was closely related to the width and spacing of the ribcage, while the curvature did not affect as significantly as the width and spacing of the ribcage.

For HIFU sonication on TMM phantom through ribcage model, effect on focal temperature rise was related to the energy applied as well as the focal distance. By using a constant sonication time, the ribcage affected more on the focal temperature change when increasing the acoustic power. Similarly, extending sonication time enhanced the effect of ribcage on focal temperature rise using a constant acoustic power. In the case of using the same total acoustic energy in the sonication, high power applied over a short time (e.g. 150 W for 20 s) provided more temperature rise at the focus than low power applied over a long time (e.g. 50 W for 60 s). The temperature change at focus was found to be related to the shadow area on the transducer blocked by the ribcage. The beam path should be determined for a minimal shadow area on transducer occluded by the ribcage.

Patients-specific models based on patients' clinical image data was successfully used to investigate the parameters of HIFU treatment in simulated experiments, in particular, the effect of the ribcage. The patient-specific model presented in this study can be used for the further research in abdominal HIFU treatment for mimicking the real situation and could act as a potential step towards stratification of treatment protocols.

Chapter 5 Feasibility Studies

To achieve the human anatomy structure as realistic as possible, Thiel embalmed cadaver was used to test HIFU sonication process. The cadaver sonication experiments helped to verify the results from the experiments using ribcage models. This study was to investigate the feasibility of the application of HIFU on Thiel embalmed cadaver in MRgFUS treatment through ribcage. HIFU effects rely on rapid rise in focal tissue temperature which in turn causes damage of the target tissues. The cooling effect of blood flow through vessels in target area may lead to substantially different HIFU treatment outcomes compared with focusing on tissues with slow or without flow. In this chapter, the blood flow effect was taken into consideration and tested during HIFU application. The influence of blood flow on focal temperature change was tested on phantom and *ex-vivo* tissue before experiments on the Thiel cadaver for the sonication test. Firstly, a TMM phantom was designed and fabricated with tubing inside mimicking blood vessels. This TMM phantom was perfused using dynamic flow and used to study the flow effect on HIFU sonication. Further sonication study on perfused *ex-vivo* organ was then performed with static perfusion and dynamic flow perfusion respectively. The static perfusion indicates the perfusion material (gel or fluid) within the vessels is static, while the dynamic perfusion is with a flowing fluid in the vessels. Finally, sonications on the liver of a Thiel embalming cadaver are performed using ExAblate system.

5.1. Sonications on dynamic perfused gel phantom

Blood flow near the sonication focus absorbed heat from the focal region resulting in less energy accumulation at the target and this affected the efficacy of the sonication. To investigate the blood flow effect on focal temperature in HIFU sonication, a flow circulation system was established and phantom study was conducted before tests on *ex-vivo* animal tissue. This was to validate the performance of dynamic flow perfusion in MRI environment.

5.1.1. TMM phantom for dynamic perfusion

For dynamic flow perfused phantom, a proper soft tube to mimic the vessel in the phantom was used. The typical vessel walls (Burton 1954) of human main arteries have 2000 μm inner radius and 3000 μm outer radius. Veins have 2500 μm inner radius and 3000 μm outer radius. A selection of vessels parameters (Crezee & Lagendijk 1992) for human circulation was summarised by Crezee et al. They reported that the diameter of large arteries was in the range of 2 to 6 mm with blood velocity 20 to 50 cm/s, large veins had diameters 5 to 10 mm with 15 to 20 cm/s blood flow velocity and renal artery had 4 mm diameter with 50 cm/s blood velocity. To enhance the flow effect on focal temperature in the sonication, the vessel mimicking material C-Flex tubing (6424-71, Cole-Parmer Instrument Co. Ltd., London, UK) with 6.350 mm inner diameter and 1.588 mm wall thickness was applied to mimic the vessel. The acoustic properties of C-Flex have been reported by Hoskins' group previously (Hoskins 2008).

For HIFU sonication, the DQA phantom was found unsuitable as tube implantation to produce a blood vessels containing phantom could have caused rapped air bubbles in the phantom when inserting the tubes. Polyacrylamide (PAA) material was selected to fabricate the phantom with C-Flex tubes inside. Its fabrication procedure has been presented in section 3.3. Two C-Flex tubes were placed into the PAA solution before the PAA curded. The tubes can be smoothly embedded within the phantom and no air bubbles trapping could have been possible.

5.1.2. Flow circulation system on the phantom

Maquet Jostra HL30 Heart-Lung Perfusionist Machine (Moquet, Rastatt, Germany), as shown in Figure 5.1, provided the dynamic flow perfusion with a constant flow rate. It can provide up to four channels of flow circulation simultaneously using roller pumps. The flow rate of all the channels is adjustable during the circulation.

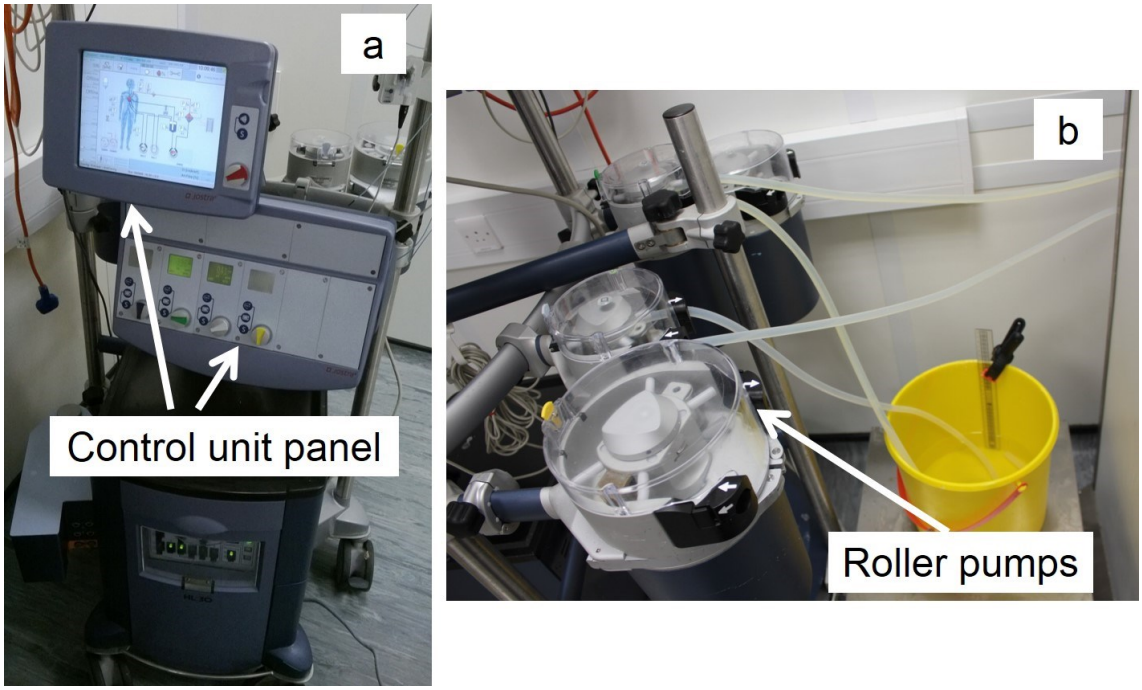

Figure 5.1 Maquet Jostra HL30 Heart-Lung Perfusionist Machine (a. Control unit panel to manage flow rate and channel selection; b. Roller pumps to provide the flow circulation)

The Hear-Lung Perfusionist Machine was located out of the MRI suite because it is not MRI compatible. For one circulation using a single channel, a flexible silicone tube was required, which must be long enough to connect the C-Flex tube (in MR suite) and the perfusionist machine (out of MRI suite). This flexible tube was placed into a roller pump of the machine for the circulation by squeezing the tube periodically. Both ends of this long tube were extended into MRI suite through a small hole on the wall of the lab. As shown in Figure 5.2, the roller pump sends the flow circulation to the C-Flex tube through the silicone tube. Both of the other ends of the C-Flex tube and the silicone tube were extended into a water bucket filled with degassed distilled water. This was to allow the air bubbles in the tubes getting out of the circulation. The two C-Flex tubes in the phantom applied the same flow rate via two channels. When the setup was ready, the circulation system needed to be turned on to working status to remove the air within the tubes before applying the sonication on the phantom, because the tubes were initially full of air and the trapped air bubbles affect the ultrasound propagation. The removal of air in C-Flex tube within the phantom was verified by MR images.

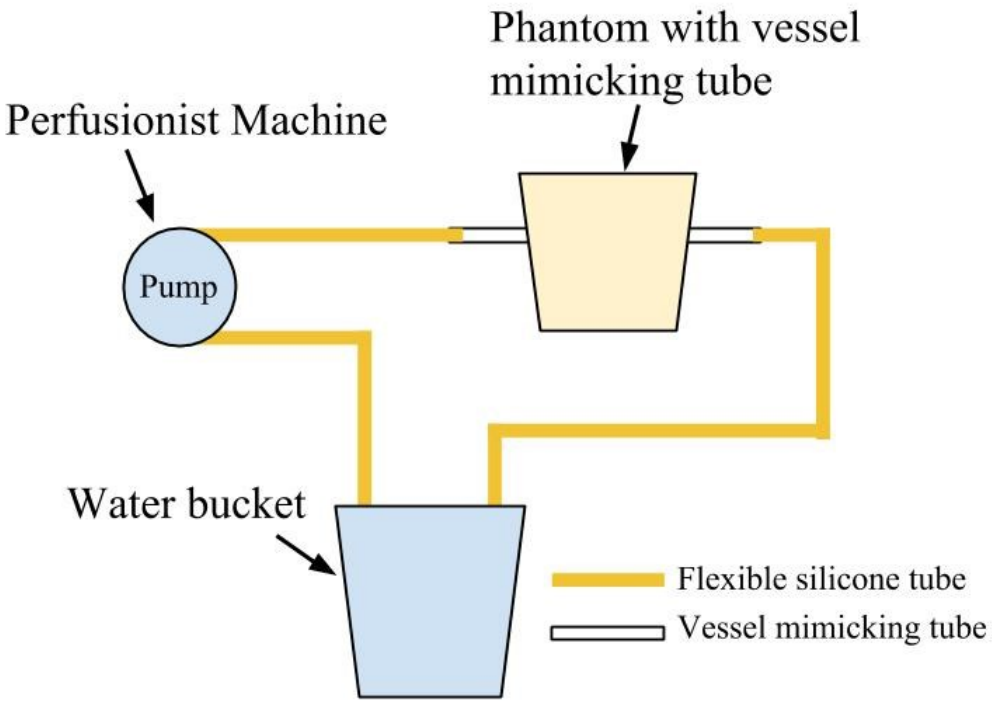

Figure 5.2 One channel circulation on phantom with vessel mimicking tube

5.1.3. Sonications on dynamic perfused phantom

Sonications were performed using ExAblate 2100 system. Figure 5.3 depicts the sagittal view of MR image of the setup for sonication on the dynamic perfused phantom. The PAA gel phantom with vessel mimicking tubing was put into a container full of degassed distilled water. This container was for better acoustic coupling and prevented water leakage from the tubing in MR scanner. It was carefully placed on the top of the HIFU transducer without air bubbles at interface. An acoustic window was cut at the central bottom of the container and sealed using a piece of thin polymer film for the pathway of the focused ultrasound beam. A gel pad was placed underneath the phantom in the container, because a larger phantom can provide a better contact with the polymer film and the transducer for a better acoustic coupling. DuoFLEX 24 cm × 24 cm coil set (MR Instruments Incorporated, Minneapolis, MN, USA) was placed on both sides of the container with phantom for MR imaging.

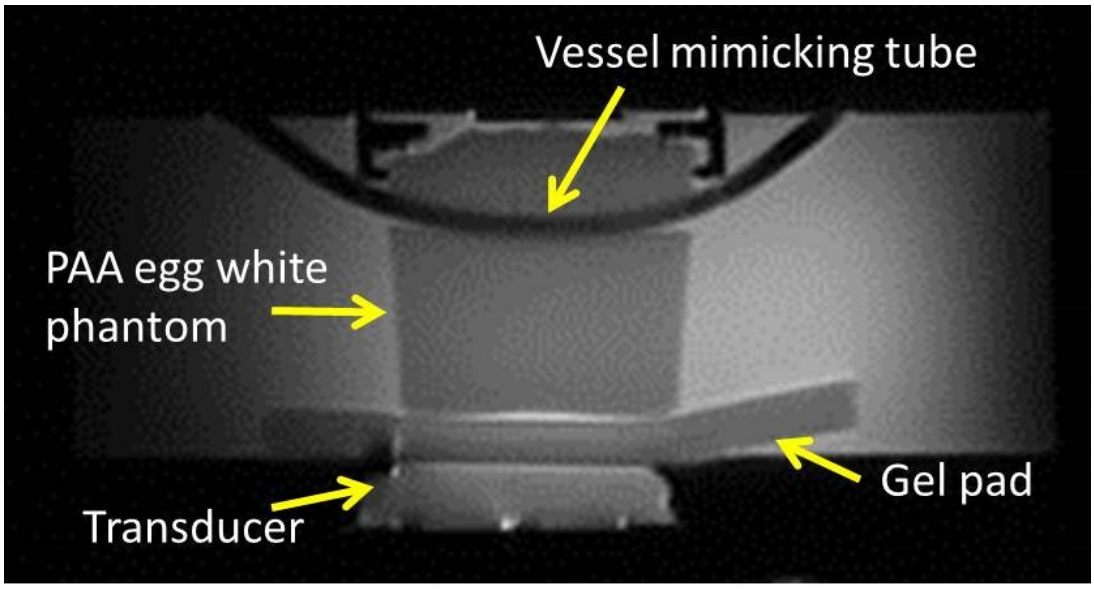

Figure 5.3 Perfusion in vessel mimicking tubing phantom (Spin Echo, TE 85.0, TR 1306.8)

Considering the operation of the flow in the C-Flex tubes within the phantom was on the patient table inside the MR scanner, the flow velocity in the C-Flex tubes cannot reach as high as the realistic value. For the safety reason, flow perfusion established in the PAA phantom through the vessel mimicking tubing was set to a flow rate of 398 ml/min. 800 J acoustic energy was applied to each sonication. The focal temperature was measured by MRI thermometry. Sonications were located surrounding the C-Flex tube with flow circulation as shown in Figure 5.4. Position No. 1 and 3 were at the back of the tube with the dynamic perfusion. Position No.2 was performed without the tube in the beam path. Position No.4 located in front of the tube with flow. The distance between the focus and the C-Flex tube is indicated in Figure 5.4.

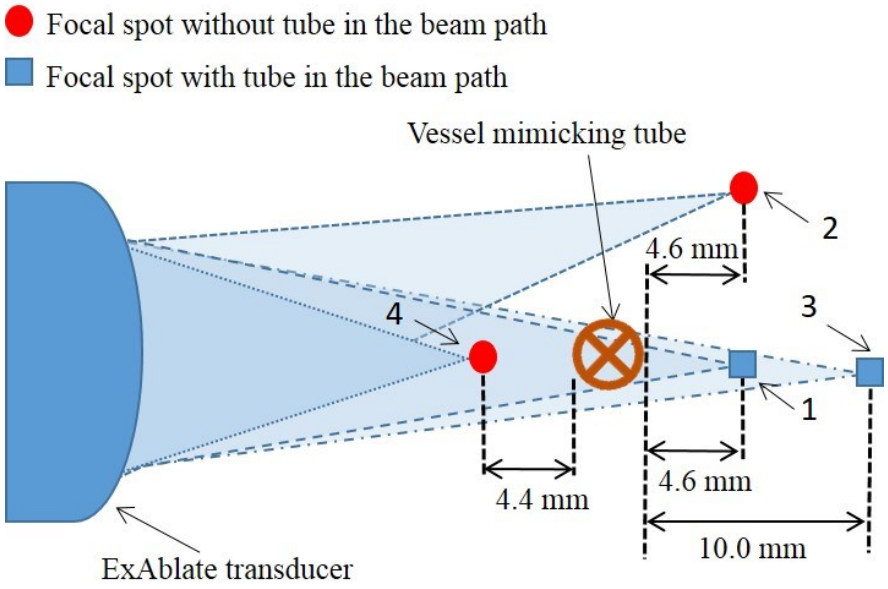

Figure 5.4 Focal positions on flow perfused phantom (1. 4.6 mm at the back of the tube; 2. 4.6 mm at the back without tube; 3. 10.0 mm at the back; 4. 4.4 mm at the front)

5.2. Sonications on static and dynamic perfused *ex-vivo* organs

After performing the flow circulation in the phantom, a sheep liver was applied as the sonication target with static and dynamic perfusion. The sheep liver used in this experiment was preserved using Thiel embalming technique (Thiel 1992). For static perfusion, tissue mimicking material was injected into the liver vessels. In terms of dynamic perfusion, a bag for the flow circulation on liver was produced to perform the perfusion with the perfusionist machine.

5.2.1. Sonications on *ex-vivo* organs with static perfusion

2% agar mixed with MRI contrast agent was used to fill in the vessels of the liver. The agar solution was injected through the portal vein of the liver and then solidified into gel status when cooling down within the vessels. The vessels were full of agar gel and air in the vessels was removed. During the sonication, the liver was placed into a well-sealed polymer bag filled with degassed and distilled water. This bag was put onto the patient table of ExAblate 2000 system. HD single channel surface coil (GE Healthcare, Waukesha, WI, USA) was placed on top of the liver bag for MR imaging. 1000 J acoustic

energy was applied for each sonication on this static perfused liver and the sonication spots were selected surrounding the vessels.

5.2.2. Sonications on *ex-vivo* organs with dynamic perfusion

5.2.2.1. Preparation of liver bag for dynamic perfusion

A dynamic flow perfused liver model was established to study the effect of the vessels with flow on focal temperature change in HIFU sonication. The tissue has to be within a water environment during the sonication for flow circulation in the vessels, thereby a bag (Figure 5.5) for dynamic perfusion in liver was created using polymer film. Firstly, three edges of the polymer plastic bag were sealed and three small holes were cut on the top side of the bag. Three plastic tube connectors were then fixed through the small holes. Two connectors were in the centre for water inlet (port 1 in Figure 5.5) and air outlet (port 3) and the other one was located near the edge for water outlet (port 2). After placing the liver in the centre of the bag, the water inlet connector was inserted into the liver from the hepatic portal vein and fastened using a cable tie. Finally, the last opening edge of the bag was sealed. It is important to prevent leakage of liquid during the experiment on ExAblate patient table in MR scanner. The sealing of the perfusion bag has to be tested for water tightness before using it in MR scanner. What is more, the bag was placed into an empty water tank during the perfusion and sonication to ensure extra safety. The central bottom of the tank was cut and sealed by a thin polymer film for the acoustic window.

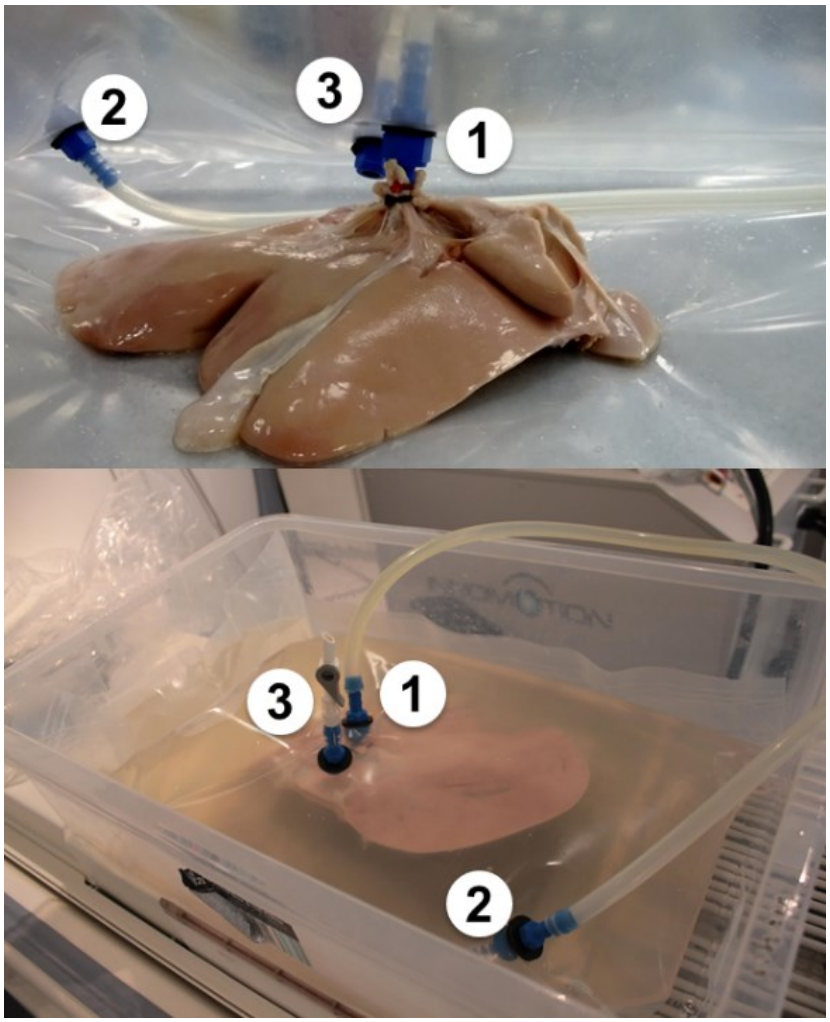

Figure 5.5 Perfused liver bag with saline solution (1. water inlet; 2. water outlet; 3. air outlet)

5.2.2.2. Dynamic flow circulation system on the liver

HIFU sonication procedures were applied on *ex-vivo* Thiel liver with dynamic flow perfusion in the vessels. The flow circulation was provided by Maquet Jostra HL30 Heart-Lung Perfusionist Machine. Two pumps of the machine were used in this setup to separate water inlet and outlet circulation. In Figure 5.6, pump 1 was connected to the water outlet and pump 2 was connected to the water inlet by long flexible tubes. Both the other ends of the long tubes were put into a bucket filled with degassed and distilled water. The purpose of using two pumps in the liver perfusion was to maintain a steady state fluid level within the bag. This can prevent bubbles from being sucked into the water outlet, because each end of inlet and outlet used an individual roller pump. To keep the balance of the water pressure in the bag, the water line in the water bucket can be monitored and

adjusted the flow rate according to increasing or decreasing level of the line. Flow was established in the liver through the hepatic portal vein at a flow rate 400 ml/min.

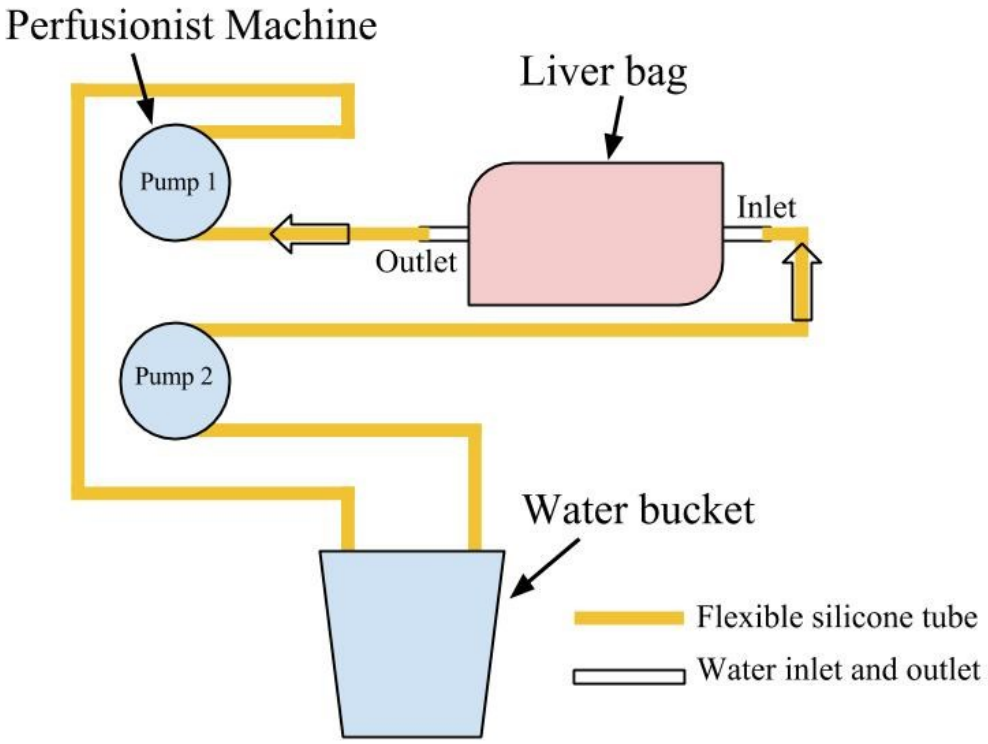

Figure 5.6 Flow circulation in the sheep liver

5.2.2.3. Sonications on dynamic perfused liver

ExAblate 2000 system combined with 1.5 Tesla MR scanner was applied to perform the sonication and monitoring of the temperature. HD single channel surface coil (GE Healthcare, Waukesha, WI, USA) was placed on top of the liver bag for MR imaging. Total acoustic energy 800 J was applied on the liver tissue both in front of and back of the vessels, and directly on the vessels. All sonications located around two different vessels. One diameter was 3.57 mm and another one was 1.56 mm. A total number of 9 sonications were performed, including 4 on the tissue at the back of the vessels, 3 on the tissue in front of the vessels and 2 on the vessels.

5.3. Sonications on Thiel cadaver: a feasibility study

5.3.1. Thiel embalmed cadaver

The Thiel cadaver was provided by Centre of Anatomy & Human Identification (University of Dundee, UK), which is one of the few departments in the UK to embalm bodies using the Thiel soft-fix method. This method can preserve the cadavers with life-like flexibility and tissue quality. Thiel embalming technique (Thiel 1992) has been reported as an alternative preservation method that keeps the tissues life-like colour, odourless, native articular joint mobility and relative long-time preservation. The research on the cadaver in this study was in accordance to UK Anatomy Act (2006).

5.3.2. Sonications on Thiel cadaver

Before moving the cadaver from the Thiel room to the MRI lab, the Thiel embalming liquid in the cadaver bag must be pumped out, because any leakage of the liquid inside the MR scanner could lead to damage the ExAblate system or MR scanner. To enable the use of CBS transducer of ExAblate 2100 system on Thiel cadaver, the transducer except the membrane area was wrapped using cling film to prevent contacting with the Thiel embalming liquid on the cadaver. As the location of the sonication target was on the liver, the transducer was positioned at upper abdomen facing to anatomical location of the liver.

The cadaver in the bag was placed on the patient table of ExAblate 2100 system docked with MR scanner. An 8 channel cardiac coil (GE Healthcare, Waukesha, WI, USA) was used for imaging. MRI was used not only to provide images of the cadaver anatomy and prepare the appropriate treatment plan, but also to measure the temperature maps to ensure the safety and efficacy of the sonication. Totally 10 sonications were applied on the cadaver using 800 J or 1000 J acoustic energy.

5.4. Results and discussion

5.4.1. Sonications on dynamic perfused gel phantom

The vessel mimicking tube showed significant effect on the temperature rise at focus. For position No.1 (Figure 5.4) at focus 4.6 mm behind the vessel mimicking tube

with flow, temperature rise was only for 2.0 °C. Sonications at the same focal distance without the tube in the beam path provided 9.5 °C rise in the temperature on an average. The temperature rise at the positions 4.4 mm in front of the vessel mimicking tube was 11.0 °C. There was a 2.2 °C temperature rise when the focus located 10.0 mm behind the tube. All the results are summarised in Table 5.1. The results indicate that vessels with a 6.4 mm inner diameter conducted heat from the focal region and affected the efficacy significantly when the target located behind the tube.

Table 5.1 The effect of vessel mimicking tube with flow on focal temperature rise

Position No.	Distance to tube (mm)	Temperature rise at focus (°C)
1	4.6 (back)	2.0
2	4.6 (without tube)	9.5
3	10.0 (back)	2.2
4	4.4 (front)	11.0

The focal position without the tube in the ultrasound beam path or 4.4 mm in front of the tube can both be heated up approximate 10 °C, which means that there was not much effect when the flow was out of the ultrasound beam path. This could be explained by the insufficient flow rate. For safety reason, up to approximate 400ml/min flow rate was used. All the setup was based on the ExAblate patient table within the MR scanner, therefore the flow has to be limited at a safe value to ensure no splash or leakage during the experiments.

5.4.2. Sonications on static and dynamic perfused *ex-vivo* organs

The results of sonications on static perfused liver showed that the effect of blood vessel with agar gel can almost be negligible. The temperature rise with and without the vessel were very close. This could be explained that the static agar gel in the vessels possessed similar acoustic properties to the liver tissue and this static perfusion in the vessels cannot lead to substantial heat loss during the HIFU sonication.

In terms of the dynamic flow perfused liver, 400 ml/min flow was perfused from the portal vein. The complex vascular system of the liver was clearly observed in the coronal MR images (Figure 5.7). For the sonication with focus on the vessel, focal temperature rise was over 10 °C lower than focusing on the liver tissue. There was not evident temperature change at focal spot at the front or back of the flow vessel. On the other hand, no visualised lesion was found by using elastography ultrasound imaging or observed by eye. The protein denaturation in liver tissue caused by the embalming material could result in no necrosis formed at foal region. However, the protein denaturation did not significantly affect the temperature rise. The *ex-vivo* Thiel liver tissue in HIFU sonication experiments showed a logical temperature rise and can be used as the focal target.

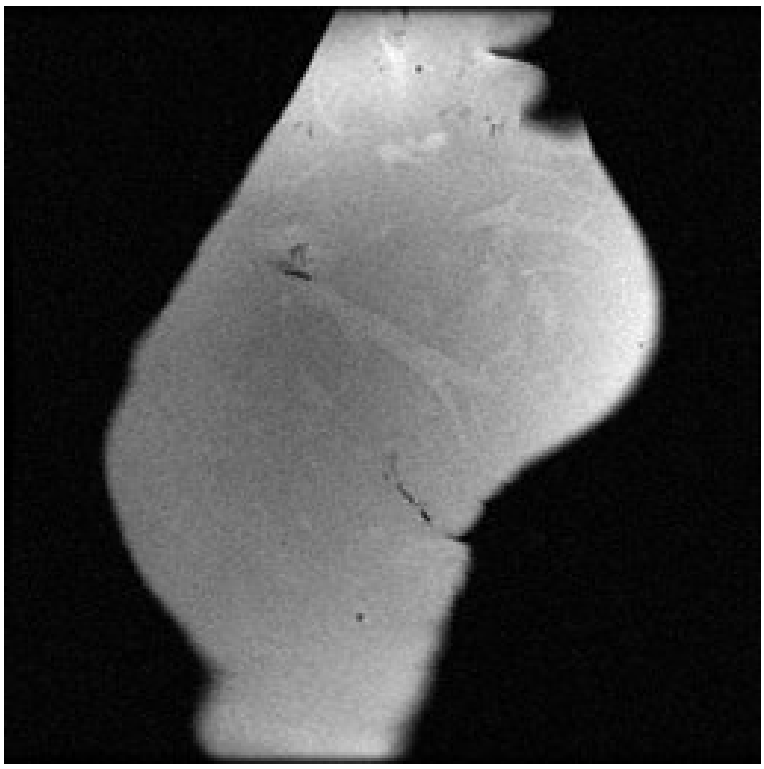

Figure 5.7 Coronal MR image of perfused Thiel sheep liver (Fast spin echo, TE 88.9, TR 3340.0)

The flow effect was not apparent mostly because the vessels near the sonication focus had smaller diameters than the C-Flex tube used in the phantom study. This may lead to less heat loss at focal region which was not enough to significantly affect focal

temperature change. As discussed in section 5.4.1, the flow rate has to be limited at 400 ml/min level for safety reasons in the MRI lab.

5.4.3. Sonications on Thiel cadaver

This cadaver model was not ideal for HIFU sonication on the liver through ribcage. As seen in the MR images of the cadaver in Figure 5.8, the thoracic cavity of the cadaver was full of air. The cadaver was lying on the patient table and the viscera in the body were shrunk to the bottom. This resulted in an empty chamber on the top of the chest. To prevent ultrasound wave propagation through air chamber in the chest, lower part of the liver was selected as the sonication target in the experiment. In Figure 5.8(b), the red area was the region of treatment pointed out by a green arrow.

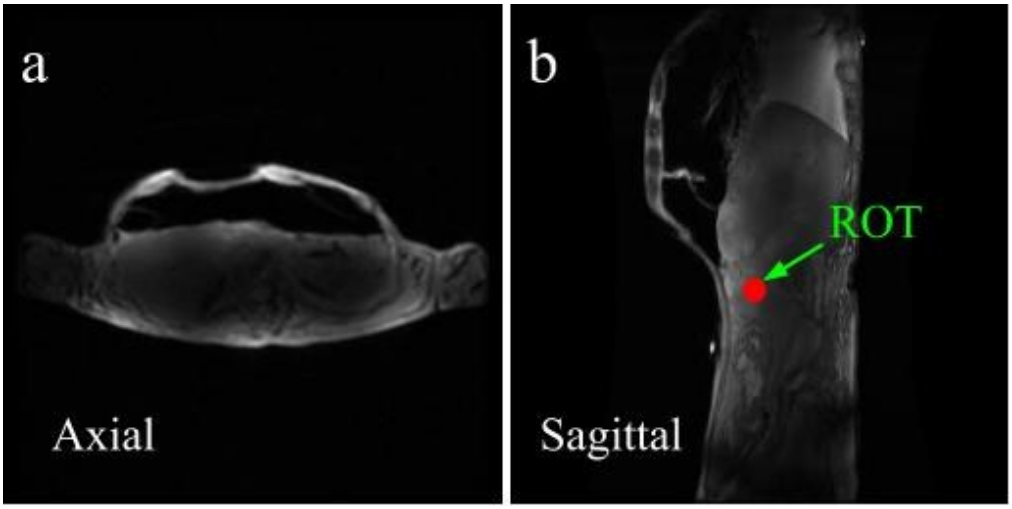

Figure 5.8 (a) Axial and (b) sagittal view of MR images of the Thiel cadaver. The red circular area in b indicates the region of treatment (ROT). (FIESTA: fast imaging employing steady state acquisition, TE 1.3, TR 3.2)

In the cadaver applied in this experiment, the air chamber in the chest affected the sonication pathway significantly. This cadaver was not fresh enough when used in this experiment, which resulted in vacancy in the thoracic cavity. It would be a better model with compact viscera in the body for liver sonication test.

Because of the vacancy chamber in the thoracic cavity, it was not easy to find a proper path for ultrasound wave propagation. Some sonications show artefact in the

temperature field mapping. Ten sonications were applied but only three of them provided reliable profile in thermometry result. Focal temperature changes in the three sonications were summarised in Table 5.2. Potential ways may change this situation, such as to perfuse the organs of the cadaver to expand the volume and make a better pathway for the ultrasound beam. However, it is best to apply a fresh cadaver model without losing much water. It should be noted that MRI thermometry of Thiel embalmed tissue has higher temperature differences compared with the fresh organs (Karakitsios *et al.* 2013). This indicated that calibration for the MRI thermometry on Thiel embalmed tissue is necessary in the future work.

Table 5.2 Focal temperature rise on the liver of Thiel cadaver

Acoustic power (W)	Acoustic energy (J)	Temperature rise (°C)
40	800	11
50	1000	35
50	1000	34

Despite these difficulties in cadaver experiment, the temperature change on cadaver tissue caused by HIFU sonication still showed positive outcomes. Considering the human anatomy and the good agreement with tissue properties, the Thiel cadaver should be explored in HIFU test for further studies.

5.5. Summary

The feasibility of performing HIFU sonication test on Thiel embalming cadaver model has been studied. The blood flow was taken into consideration and investigated on a TMM phantom and *ex-vivo* organs with static and dynamic perfusion. Thiel sheep liver was selected as the *ex-vivo* sonication target tissue to study the static or dynamic perfusion effect on animal tissue. The effect of the flow in vessel mimicking tubing on focal temperature change was evident in phantom study, while the focal temperature on liver tissue was not affected apparently by static or dynamic perfusion in the vessels. The application of HIFU on Thiel tissue has been validated. However, the viscera shrunk and

left a vacancy chamber filled with air in the chest of the cadaver used in this experiment. Because of this situation, it was impossible to locate the focus of HIFU onto the liver tissue through the ribs. A Thiel cadaver with a vacancy chamber in the body was not an ideal cadaver model for HIFU test on the liver through ribcage, however, HIFU sonication on cadaver still showed positive outcomes.

Thiel cadaver provided anatomical structures and tissue properties of human, which made it possible to be a substitute in the HIFU test. This study provided validation results and exposed the potential issues of its application to test HIFU procedure. For a cadaver with compact organs in the body, it can be considered as a valuable model for HIFU test in pre-clinical stage.

Chapter 6 Conclusions and Future Work

This study was to investigate the influence of the ribcage on HIFU applications using the reconstructed ribcage model that possessed patient's anatomical structures, which could help translate HIFU technology into more widespread clinical applications. This chapter gives summary of the work reported in the above chapters and indicate the possible work to be furthered in the future.

6.1. Conclusions

HIFU therapy has been approved for cancer diseases treatment in many countries and a number of clinical applications proved HIFU a promising non-invasive treatment. A review of literatures showed that the ribs located in the focused ultrasound beam path affected the therapeutic process and a lot of work has been done to overcome this challenge. It was noted that there was not an investigation provided full effect of the ribcage on HIFU treatment due to the lack of physical practice with human anatomical structures. Therefore this study conducted HIFU experiment through ribcage with human anatomical structures and tissue mimicking properties in order to bridge the gap between HIFU and abdominal non-invasive treatment. The physical model with the structures of human anatomy based on medical images provided a way to evaluate the effect of the ribcage and help to develop patient-specific treatment plan. To predict the sonication effect of HIFU treatment through ribcage accurately, a specialised model was required for individual patient. The investigation on the reconstructed ribcage model should serve as an illustration of its effect on focused ultrasound field. With the benefit of 3D reconstruction, the HIFU sonication experiments using realistic phantoms based on patient's data would be a step towards translation of HIFU technology into widespread clinical practice.

6.1.1. Reconstruction of ribcage model

A rapid 3D modelling technique was developed to prototype models with original human anatomical structures. The 3D modelling of patient-specific ribcage models

applied DICOM data from totally four patients. Physical ribcage models were manufactured using rapid prototyping technique based on the computer generated 3D models. These ribcage models therefore possessed the anatomical structures and features of the patients, which made it possible to fully investigate the ribcage effect on HIFU treatment of each individual patient. This 3D modelling technique could bring broader implication into the surgery by providing reliable tissue mimicking models with human anatomical structures and assisting to physically simulate the surgical circumstance.

The TMMs were characterised to determine the best material for the phantom used in HIFU sonication through the ribcage. The acoustic, thermal and elastic properties of most commonly used TMMs have been measured, which may also provide reference results for other researches. According to Table 3.9, ABS thermoplastic material and PVA phantom was used for ribcage model and surrounding tissue respectively. PAA with 2% Al_2O_3 was the best tumour mimicking material for elastography. DQA phantom was the best to be the sonication target because it possessed tissue mimicking acoustic properties and thermal properties, and was suitable to apply repeatable high power sonication when allowing enough cooling time. The materials and methodology used in the present study could bridge the gap from tissue and organ substitutes used in research to anatomical structures of human and form the basis for designing future TMM phantoms and associated researches.

6.1.2. Investigation of the effect of ribcage on focused ultrasound field

To evaluate ribcage effect, HIFU experiments were implemented using the patient-specific models with focused ultrasound covering both transcostal and intercostal propagation. The effects were investigated on acoustic pressure distribution, acoustic power and focal temperature rise.

Acoustic pressure distribution and acoustic power in focused ultrasound field by both intercostal and transcostal propagation was investigated and then compared with ribcage dimensions. The width and spacing of the ribs were found to be closely related to the effect of ribcage on acoustic pressure distribution and acoustic power. Results also revealed that the intercostal position allowed more energy deposition at focus and transcostal position caused significant focus distortion, specifically, focus splitting into three main parts. For the HIFU sonication on phantom at varied focal locations,

temperature change at focal region was proved to be highly associated with the shadow area of the ribcage projected from the focus onto the transducer.

To enhance the efficacy of HIFU treatment, the intercostal position should be the best option for the treatment if the HIFU beam is possible to be focused to the target through the intercostal spaces. In this case, the ultrasound wave has a minimal energy loss and the focal temperature elevation can reach the maximum. When the cancerous tissue located exactly behind the rib, the first option could be shifting the beam path to intercostal space by physically moving the transducer or adjusting the phase of each element on the transducer. This technique has been already available in some of the existing HIFU systems. However, if the beam cannot be adjusted to the ideal path or this adjustment is not technically feasible, it is best to locate the transducer to achieve a minimal shadow area on the elements by the ribcage in transcostal propagation. This would ensure the most energy delivered through the ribs in the current circumstance.

6.1.3. Feasibility studies on Thiel cadaver model

HIFU sonication test has been conducted on liver tissue of a cadaver, which showed that the cadaver can be a good model for the investigation of HIFU because of the tissue properties and anatomical structures. However, the sonication through the ribs was not available on this cadaver model. The potential wave propagation path was full of air if locating the focus on the liver tissue, because the loss of water resulted in viscera shrunk during the long-term storage. A possible way to address this is to perform the perfusion in the abdominal organs of the cadaver to expand their volume and recover to normal size. Apart from this complicated potential solution, it would be the best to apply an ideal cadaver model, which should be as fresh as possible and without any air in the chest, for the sonication through the ribs.

6.2. Suggestions for future work

The work reported in this thesis was the first stage investigation into the effect of patient-specific ribcage on HIFU application. This research contributed to establish a unique HIFU treatment plan for each individual patient based on the models with patient's anatomical structures and human tissue properties. Some improvements and suggestions

for the future work are presented in this section based on the summary and analysis of the completed research.

One practical issue of this work is that the characterisation of TMMs was carried out in constant room temperature (20 °C), but as a matter of fact the acoustic and thermal properties are temperature dependent. What is more, the stiffness of the tissue varied after protein denaturation. Taking these factors into consideration, the evaluation result of focal temperature change using phantom would be slight different compared with that using human tissue. Therefore it is best to measure these properties at various temperature conditions to provide more comprehensive analysis. By using the proper temperature dependent TMM material, the temperature change at focus would be more accurate to determine the treatment plan.

MRI thermometry was used to monitor the focal temperature in the current study. As the focal lesion became stiffer after HIFU sonication and elastography can measure stiffness the lesion formation, elastography could be used to evaluate the result of HIFU sonication by providing the dimension of the lesion. This will be helpful when MRI thermometry is not feasible or not available in the HIFU treatment.

Apart from the challenge of ribcage in abdominal HIFU treatment, the research on overcoming organ motion is underway. The 3D modelling technique could assist the study of tracking the organ movement. By using the reconstructed target organs, a patient-specific model can be created with a simulated movement for image tracking. The Thiel cadaver could be used as the model for organ tracking and HIFU sonication to verify the tracking results.

References

Aboumarzouk, O. M., Ogston, S., Huang, Z. H., Evans, A., Melzer, A., Stolzenberg, J. U. & Nabi, G. 2012: Diagnostic accuracy of transrectal elastosonography (TRES) imaging for the diagnosis of prostate cancer: a systematic review and meta-analysis. *Bju International 110*, 1414-1423.

Abrams, E., Mohr, M., Engel, C. & Bottlang, M. 2003: Cross-sectional geometry of human ribs. *American Society of Biomechanics*, pp., Toledo, OH.

Adam, S. & John, N. 2010: The feasibility of an infrared system for real-time visualization and mapping of ultrasound fields. *Physics in Medicine and Biology 55*, N321.

Adams, J. B., Moore, R. G., Anderson, J. H., Strandberg, J. D., Marshall, F. F. & Davoussi, L. R. 1996: High-intensity focused ultrasound ablation of rabbit kidney tumors. *Journal of endourology / Endourological Society 10*, 71-75.

Al-Bataineh, O., Jenne, J. & Huber, P. 2012: Clinical and future applications of high intensity focused ultrasound in cancer. *Cancer Treatment Reviews 38*, 346-353.

Alexei, K., Srirang, M., Rosalyn, S., Roy, G. M. K., René, A. B., Wiendelt, S. & Frits, F. M. d. M. 2003: Poly(vinyl alcohol) gels for use as tissue phantoms in photoacoustic mammography. *Physics in Medicine and Biology 48*, 357.

Anderson, P. G., Rouze, N. C. & Palmeri, M. L. 2011: Effect of Graphite Concentration on Shear-Wave Speed in Gelatin-Based Tissue-Mimicking Phantoms. *Ultrasonic Imaging 33*, 134-142.

Association, W. M. 2008: *World Medical Association Declaration of Helsinki: ethical principles for medical research involving human subjects*. pp. World Medical Association.

Aubry, J. F., Pernot, M., Marquet, F., Tanter, M. & Fink, M. 2008: Transcostal high-intensity-focused ultrasound: ex vivo adaptive focusing feasibility study. *Physics in Medicine and Biology 53*, 2937-2951.

Aubry, J. F., Tanter, M., Pernot, M., Thomas, J. L. & Fink, M. 2003: Experimental demonstration of noninvasive transskull adaptive focusing based on prior computed tomography scans. *The Journal of the Acoustical Society of America 113*, 84-93.

Azzouz, H. & de la Rosette, J. J. M. C. H. 2006: HIFU: Local Treatment of Prostate Cancer. *EAU-EBU Update Series 4*, 62-70.

Ballantine, H. T., Jr., Bell, E. & Manlapaz, J. 1960: Progress and problems in the neurological applications of focused ultrasound. *Journal of neurosurgery 17*, 858-876.

Bamber, J. C. 1983: Ultrasonic propagation properties of the breast. *Ultrasonic Examination of the breast*, 37-44.

Bamber, J. C. 1999: Ultrasound elasticity imaging: definition and technology. *European Radiology 9*, S327-S330.

Barr, R. G., Memo, R. & Schaub, C. R. 2012: Shear Wave Ultrasound Elastography of the Prostate Initial Results. *Ultrasound Quarterly 28*, 13-20.

Beissner, K. 2002: Report on key comparison CCAUV.U-K1 (ultrasonic power). *Metrologia 39*, 09001.

Bellemare, F., Jeanneret, A. & Couture, J. 2003: Sex differences in thoracic dimensions and configuration. *American Journal of Respiratory and Critical Care Medicine 168*, 305-312.

Bercoff, J., Criton, A., Cohen-Bacrie, C., Souquet, J., Tanter, M., Deffieux, T., Gennisson, J. L., Fink, M., Juhan, V., Colavolpe, A., Amy, D., Athanasiou, A. & Ieee 2008: ShearWave (TM) Elastography A new real time imaging mode for assessing quantitatively soft tissue viscoelasticity. *2008 Ieee Ultrasonics Symposium, Vols 1-4 and Appendix*, 321-324 pp.

Bercoff, J., Tanter, M. & Fink, M. 2004: Supersonic shear imaging: A new technique for soft tissue elasticity mapping. *Ieee Transactions on Ultrasonics Ferroelectrics and Frequency Control 51*, 396-409.

Bilgen, M. & Insana, M. F. 1996: Deformation models and correlation analysis in elastography. *Journal of the Acoustical Society of America 99*, 3212-3224.

Bobkova, S., Gavrilov, L., Khokhlova, V., Shaw, A. & Hand, J. 2010: Focusing of High-Intensity Ultrasound Through the Rib Cage Using a Therapeutic Random Phased Array. *Ultrasound in Medicine & Biology 36*, 888-906.

Bouchard, L. S. & Bronskill, M. J. 2000: Magnetic resonance imaging of thermal coagulation effects in a phantom for calibrating thermal therapy devices. *Medical Physics 27*, 1141-1145.

Bowman, H. F., Cravalho, E. G. & Woods, M. 1975: Theory, measurement, and application of thermal properties of biomaterials. *Annual Review of Biophysics and Bioengineering 4*, 43-80.

Brock, M., von Bodman, C., Palisaar, R. J., Loeppenberg, B., Sommerer, F., Deix, T., Noldus, J. & Eggert, T. 2012: The Impact of Real-Time Elastography Guiding a Systematic Prostate Biopsy to Improve Cancer Detection Rate: A Prospective Study of 353 Patients. *Journal of Urology 187*, 2039-2043.

Browne, J. E., Ramnarine, K. V., Watson, A. J. & Hoskins, P. R. 2003: Assessment of the acoustic properties of common tissue-mimicking test phantoms. *Ultrasound in Medicine & Biology 29*, 1053-1060.

Bryan, P. J., Custar, S., Haaga, J. R. & Balsara, V. 1984: Respiratory movement of the pancreas - an ultrasonic study. *Journal of Ultrasound in Medicine 3*, 317-320.

Bu, R., Yin, L., Yang, H., Wang, Q., Wu, F. & Zou, J. Z. 2013: Tissue Ablation Accelerated by Peripheral Scanning Mode with High-Intensity Focused Ultrasound: A Study on Isolated Porcine Liver Perfusion. *Ultrasound in Medicine & Biology 39*, 1410-1419.

Burton, A. C. 1954: Relation of structure to function of the tissues of the wall of blood vessels. *Physiological Reviews 34*, 619-642.

Canney, M. S., Bailey, M. R., Crum, L. A., Khokhlova, V. A. & Sapozhnikov, O. A. 2008: Acoustic characterization of high intensity focused ultrasound fields: A combined measurement and modeling approach. *Journal of the Acoustical Society of America 124*, 2406-2420.

Cao, R., Gao, J., Melzer, A., Nabi, G. & Huang, Z. H. 2012: Rapid 3D Human Ribcage And Kidney Modeling For Transcostal HIFU Surgery. *In* Meairs, S. (ed.): *12th International Symposium on Therapeutic Ultrasound*, 95-100 pp. Amer Inst Physics, Melville.

Cao, R., Huang, Z. H., Varghese, T. & Nabi, G. 2013: Tissue mimicking materials for the detection of prostate cancer using shear wave elastography: A validation study. *Medical Physics 40*.

Carslaw, H. H. S. & Jaeger, J. C. 1959: *Conduction of heat in solids*. pp. Oxford University Press, London.

Chapelon, J. Y., Margonari, J., Theillère, Y., Gorry, F., Vernier, F., Blanc, E. & Gelet, A. 1992: Effects of high-energy focused ultrasound on kidney tissue in the rat and the dog. *European Urology 22*, 147-152.

Chaussy, C. & Thüroff, S. 2000: High-intensity focused ultrasound in prostate cancer: results after 3 years. *Molecular urology 4*, 179-182.

Chen, L., Haar, G. t., Hill, C. R., Dworkin, M., Carnochan, P., Young, H. & Bensted, J. P. M. 1993a: Effect of blood perfusion on the ablation of liver parenchyma with high-intensity focused ultrasound. *Physics in Medicine and Biology 38*, 1661.

Chen, L., Rivens, I., Ter Haar, G., Riddler, S., Hill, C. R. & Bensted, J. P. M. 1993b: Histological changes in rat liver tumours treated with high-intensity focused ultrasound. *Ultrasound in Medicine & Biology 19*, 67-74.

Cheung, T., Chu, F. K., Jenkins, C., Tsang, D. F., Chok, K. H., Chan, A. Y., Yau, T. C., Chan, S., Poon, R. P., Lo, C. & Fan, S. 2012: Tolerance of High-Intensity Focused Ultrasound Ablation in Patients with Hepatocellular Carcinoma. *World Journal of Surgery 36*, 2420-2427.

Chmarra, M. K., Hansen, R., Marvik, R. & Lango, T. 2013: Multimodal Phantom of Liver Tissue. *Plos One 8*.

Clarke, R. L., Bush, N. L. & Ter Haar, G. R. 2003: The changes in acoustic attenuation due to in vitro heating. *Ultrasound in Medicine & Biology 29*, 127-135.

Clement, G. T. & Hynynen, K. 2002: A non-invasive method for focusing ultrasound through the human skull. *Physics in Medicine and Biology 47*, 1219.

Cochard, E., Prada, C., Aubry, J. F. & Fink, M. 2009: Ultrasonic focusing through the ribs using the DORT method. *Medical Physics 36*, 3495-3503.

Coleman, D. J., Lizzi, F. L., Driller, J., Rosado, A. L., Burgess, S. E., Torpey, J. H., Smith, M. E., Silverman, R. H., Yablonski, M. E. & Chang, S. 1985a: Therapeutic ultrasound in the treatment of glaucoma. II. Clinical applications. *Ophthalmology 92*, 347-353.

Coleman, D. J., Lizzi, F. L., Torpey, J. H., Burgess, S. E. P., Driller, J., Rosado, A. & Nguyen, H. T. 1985b: Treatment of experimental lens capsular tears with intense focused ultrasound. *British Journal of Ophthalmology 69*, 645-649.

Crezee, J. & Lagendijk, J. J. W. 1992: Temperature uniformity during hyperthermia - the impact of large vessels. *Physics in Medicine and Biology 37*, 1321-1337.

Cui, L. 2014: Comparison of different methods of assessing the fibro-glandular volume of the breast using magnetic resonance imaging (MRI). *School of Engineering, Physics and Mathematics*. University of Dundee, Dundee, UK.

Culjat, M. O., Goldenberg, D., Tewari, P. & Singh, R. S. 2010: A Review of Tissue Substitutes for Ultrasound Imaging. *Ultrasound in Medicine & Biology 36*, 861-873.

Curie, J. & Curie, P. 1880: Développement par compression de l'électricité polaire dans les cristaux hémièdres à faces inclinées. *Bulletin de la Société minérologique de France 3*, 90-93.

D'Souza, W. D., Madsen, E. L., Unal, O., Vigen, K. K., Frank, G. R. & Thomadsen, B. R. 2001: Tissue mimicking materials for a multi-imaging modality prostate phantom. *Medical Physics 28*, 688-700.

Dansereau, J. & Stokes, I. A. F. 1988: Measurements of the three-dimensional shape of the rib cage. *Journal of Biomechanics 21*, 893-901.

Dasgupta, S., Hariharan, P., Myers, M. R., Banerjee, R. K. & Asme 2009: *Effect of rate of blood flow through large blood vessels on HIFU temperature rise*. 469-470 pp.

Davies, S. C., Hill, A. L., Holmes, R. B., Halliwell, M. & Jackson, P. C. 1994: Ultrasound quantitation of respiratory organ motion in the upper abdomen. *British Journal of Radiology 67*, 1096-1102.

Divkovic, G. W., Liebler, M., Braun, K., Dreyer, T., Huber, P. E. & Jenne, J. W. 2007: Thermal properties and changes of acoustic parameters in an egg white phantom

during heating and coagulation by high intensity focused ultrasound. *Ultrasound in Medicine and Biology 33*, 981-986.

Duck, F. A. 1990: *Physical properties of tissue: a comprehensive reference book*. pp. Academic Press.

Esnault, O., Franc, B., Menegaux, F., Rouxel, A., De Kerviler, E., Bourrier, P., Lacoste, F., Chapelon, J. Y. & Leenhardt, L. 2011: High-Intensity Focused Ultrasound Ablation of Thyroid Nodules: First Human Feasibility Study. *Thyroid 21*, 965-973.

Evans, A., Whelehan, P., Thomson, K., McLean, D., Brauer, K., Purdie, C., Baker, L., Jordan, L., Rauchhaus, P. & Thompson, A. 2012: Invasive Breast Cancer: Relationship between Shear-wave Elastographic Findings and Histologic Prognostic Factors. *Radiology 263*, 673-677.

Fatemi, M. & Greenleaf, J. F. 1999: Application of radiation force in noncontact measurement of the elastic parameters. *Ultrasonic Imaging 21*, 147-154.

Fennessy, F. M., Tempany, C. M., McDannold, N. J., So, M. J., Hesley, G., Gostout, B., Kim, H. S., Holland, G. A., Sarti, D. A., Hynynen, K., Jolesz, F. A. & Stewart, E. A. 2007: Uterine leiomyomas: MR imaging-guided focused ultrasound surgery - Results of different treatment protocols. *Radiology 243*, 885-893.

Fick, S. E. 1999: Ultrasound power measurement by pulsed radiation pressure. *Metrologia 36*, 351.

Filonenko, E. A. & Khokhlova, V. A. 2001: Effect of acoustic nonlinearity on heating of biological tissue by high-intensity focused ultrasound. *Acoustical Physics 47*, 468-475.

Fleury, G., Berriet, W., Chapelon, J. Y., ter Haar, G., Lafon, C., Le Baron, O., Chupin, L., Pichonnat, F. & Lenormand, J. 2005: Safety issues for HIFU transducer design. *In* TerHaar, G. R. & Rivens, I. (eds.): *4th International Symposium on Therapeutic Ultrasound*, 233-241 pp.

Foster, R. S., Bihrle, R., Sanghvi, N. T., Fry, F. J. & Donohue, J. P. 1993: High-Intensity Focused Ultrasound in the Treatment of Prostatic Disease. *European Urology 23*, 29-33.

Freed, M., de Zwart, J. A., Loud, J. T., El Khouli, R. H., Myers, K. J., Greene, M. H., Duyn, J. H. & Badano, A. 2011: An anthropomorphic phantom for quantitative evaluation of breast MRI. *Medical Physics 38*, 743-753.

Frizzell, L. A. 1988: Threshold dosages for damage to mammalian liver by high intensity focused ultrasound. *Ultrasonics, Ferroelectrics and Frequency Control, IEEE Transactions on 35*, 578-581.

Frizzell, L. A., Linke, C. A., Carstensen, E. L. & Fridd, C. W. 1977: Thresholds for Focal Ultrasonic Lesions in Rabbit Kidney, Liver, and Testicle. *Biomedical Engineering, IEEE Transactions on BME-24*, 393-396.

Fry, F. J. 1958: Precision high intensity focusing ultrasonic machines for surgery. *American journal of physical medicine 37*, 152-156.

Fry, W. J. 1955: Ultrasonic lesions in the mammalian central nervous system. *Science 122*, 517-518.

Fry, W. J. & Fry, F. J. 1960: Fundamental Neurological Research and Human Neurosurgery Using Intense Ultrasound. *Medical Electronics, IRE Transactions on ME-7*, 166-181.

Fry, W. J., Mosberg, W. H., Barnard, J. W. & Fry, F. J. 1954: Production of Focal Destructive Lesions in the Central Nervous System With Ultrasound*. *Journal of Neurosurgery 11*, 471-478.

Gao, J., Cochran, S. & Huang, Z. 2014: Ultrasound beam distortion and pressure reduction in transcostal focused ultrasound surgery. *Applied Acoustics 76*, 337-345.

Gao, J., You, J., Huang, Z. H., Cochran, S. & Corner, G. 2012: Simultaneous Measurement of Thermophysical Properties of Tissue-Mimicking Phantoms for High Intensity Focused Ultrasound (HIFU) Exposures. *International Journal of Thermophysics 33*, 495-504.

Gelat, P., ter Haar, G. & Saffari, N. 2011: Modelling of the acoustic field of a multi-element HIFU array scattered by human ribs. *Physics in Medicine and Biology 56*, 5553-5581.

Gelat, P., ter Haar, G. & Saffari, N. 2012a: The optimization of acoustic fields for ablative therapies of tumours in the upper abdomen. *Physics in Medicine and Biology 57*.

Gelat, P., ter Haar, G., Saffari, N. & Iop 2012b: Scattering of the field of a multi-element phased array by human ribs. *10th Anglo-French Physical Acoustics Conference (Afpac 2011) 353*.

Gelet, A., Chapelon, J. Y., Margonari, J., Theillère, Y., Gorry, F., Souchon, R. & Bouvier, R. 1993: High-intensity focused ultrasound experimentation on human benign prostatic hypertrophy. *European Urology 23 Suppl 1*, 44-47.

Gianfelice, D., Gupta, C., Kucharczyk, W., Bret, P., Havill, D. & Clemons, M. 2008: Palliative treatment of painful bone metastases with MR imaging--guided focused ultrasound. *Radiology 249*, 355-363.

Goss, S. A., Johnston, R. L. & Dunn, F. 1978: Comprehensive compilation of empirical ultrasonic properties of mammalian tissues. *The Journal of the Acoustical Society of America 64*, 423-457.

Greenspan, M., Breckenridge, F. R. & Tschiegg, C. E. 1978: Ultrasonic transducer power output by modulated radiation pressure. *Journal of the Acoustical Society of America 63*, 1031-1038.

Hariharan, P., Myers, M. R. & Banerjee, R. K. 2007: HIFU procedures at moderate intensities - effect of large blood vessels. *Physics in Medicine and Biology 52*, 3493-3513.

Hendee, W. R. & Ritenour, E. R. 2003: Ultrasound Waves. *Medical Imaging Physics*, 303-316 pp. John Wiley & Sons, Inc.

Hill, C., Bamber, J. & Haar, G. T. 2004: *Physical Principles of Medical Ultrasonics. 2nd ed*. pp. Wiley.

Hill, C. R., Rivens, I., Vaughan, M. G. & Ter Haar, G. R. 1994: Lesion development in focused ultrasound surgery: A general model. *Ultrasound in Medicine & Biology 20*, 259-269.

Hopkins, R. E. & Bradley, M. 2001: In-vitro Visualization of Biopsy Needles with Ultrasound: A Comparative Study of Standard and Echogenic Needles Using an Ultrasound Phantom. *Clinical Radiology 56*, 499-502.

Hoskins, P. R. 2008: Simulation and Validation of Arterial Ultrasound Imaging and Blood Flow. *Ultrasound in Medicine & Biology 34*, 693-717.

Howe, F. A. 1988: Relaxation times in paramagnetically doped agarose gels as a function of temperature and ion concentration. *Magnetic Resonance Imaging 6*, 263-270.

Hynynen, K. 1993: Acoustic power calibrations of cylindrical intracavitary ultrasound hyperthermia applicators. *Medical Physics 20*, 129-134.

Hynynen, K., Chung, A., Fjield, T., Buchanan, M., Daum, D., Colucci, V., Lopath, P. & Jolesz, F. 1996: Feasibility of using ultrasound phased arrays for MRI monitored noninvasive surgery. *Ieee Transactions on Ultrasonics Ferroelectrics and Frequency Control 43*, 1043-1053.

Illing, R. O., Kennedy, J. E., Wu, F., ter Haar, G. R., Protheroe, A. S., Friend, P. J., Gleeson, F. V., Cranston, D. W., Phillips, R. R. & Middleton, M. R. 2005: The safety and feasibility of extracorporeal high-intensity focused ultrasound (HIFU) for the treatment of liver and kidney tumours in a Western population. *British journal of cancer 93*, 890-895.

Ishihara, Y., Calderon, A., Watanabe, H., Okamoto, K., Suzuki, Y., Kuroda, K. & Suzuki, Y. 1995: A precise and fast temperature mapping using water proton chemical shift. *Magnetic Resonance in Medicine 34*, 814-823.

Jenne, J. W., Preusser, T. & Günther, M. 2012: High-intensity focused ultrasound: Principles, therapy guidance, simulations and applications. *Zeitschrift für Medizinische Physik 22*, 311-322.

Karakitsios, I., Bobeica, M., Saliev, T., Rube, M. & Melzer, A. 2013: Thermometry during MR-guided focused ultrasound in a preclinical model based on Thiel embalmed tissue. *Minimally invasive therapy & allied technologies : MITAT : official journal of the Society for Minimally Invasive Therapy*.

Kato, H., Kuroda, M., Yoshimura, K., Yoshida, A., Hanamoto, K., Kawasaki, S., Shibuya, K. & Kanazawa, S. 2005: Composition of MRI phantom equivalent to human tissues. *Medical Physics 32*, 3199-3208.

Kennedy, J. E., Clarke, R. I. & ter Haar, G. R. 2003: The effects of absorbers such as ribs in the HIFUS beam-path on the focal profile. *Proceedings of the 2nd International Symposium on Therapeutic Ultrasound. Seattle: University of Washington*, 185-192.

Kennedy, J. E., Wu, F., ter Haar, G. R., Gleeson, F. V., Phillips, R. R., Middleton, M. R. & Cranston, D. 2004: High-intensity focused ultrasound for the treatment of liver tumours. *Ultrasonics 42*, 931-935.

Khokhlova, T. D. & Hwang, J. H. 2011: HIFU for palliative treatment of pancreatic cancer. *Journal of gastrointestinal oncology 2*, 175-184.

Khokhlova, V. A., Bobkova, S. M. & Gavrilov, L. R. 2010: Focus splitting associated with propagation of focused ultrasound through the rib cage. *Acoustical Physics 56*, 665-674.

King, R. L., Yunbo, L., Maruvada, S., Herman, B. A., Wear, K. A. & Harris, G. R. 2011: Development and characterization of a tissue-mimicking material for high-intensity focused ultrasound. *Ultrasonics, Ferroelectrics and Frequency Control, IEEE Transactions on 58*, 1397-1405.

Kohrmann, K. U., Michel, M. S., Gaa, J., Marlinghaus, E. & Alken, P. 2002: High intensity focused ultrasound as noninvasive therapy for multilocal renal cell carcinoma: Case study and review of the literature. *Journal of Urology 167*, 2397-2403.

Kraft, K. A., Fatouros, P. P., Clarke, G. D. & Kishore, P. R. S. 1987: An MRI phantom material for quantitative relaxometry. *Magnetic Resonance in Medicine 5*, 555-562.

Kratzik, C., Schatzl, G., Lackner, J. & Marberger, M. 2006: Transcutaneous high-intensity focused ultrasonography can cure testicular cancer in solitary testis. *Urology 67*, 1269-1273.

Krouskop, T. A., Wheeler, T. M., Kallel, F., Garra, B. S. & Hall, T. 1998: Elastic moduli of breast and prostate tissues under compression. *Ultrasonic Imaging 20*, 260-274.

Kubicar, L. & Bohac, V. 2000: A step-wise method for measuring thermophysical parameters of materials. *Measurement Science & Technology 11*, 252-258.

Kun, G. & Wan, M. X. 2004: Effects of fascia lata on HIFU lesioning in vitro. *Ultrasound in Medicine and Biology 30*, 991-998.

Lafon, C., Kaczkowski, P. J., Vaezy, S., Noble, M. & Sapozhnikov, O. A. 2001: Development and characterization of an innovative synthetic tissue-mimicking material for High Intensity Focused Ultrasound (HIFU) exposures. *In* Yuhas, D. E. & Schneider, S. C. (eds.): *2001 Ieee Ultrasonics Symposium Proceedings, Vols 1 and 2*, 1295-1298 pp.

Lafon, C., Zderic, V., Noble, M. L., Yuen, J. C., Kaczkowski, P. J., Sapozhnikov, O. A., Chavrier, F., Crum, L. A. & Vaezy, S. 2005: Gel phantom for use in high-intensity focused ultrasound dosimetry. *Ultrasound in Medicine & Biology 31*, 1383-1389.

Laugier, P., Droin, P., LavalJeantet, A. M. & Berger, G. 1997: In vitro assessment of the relationship between acoustic properties and bone mass density of the calcaneus by comparison of ultrasound parametric imaging and quantitative computed tomography. *Bone 20*, 157-165.

Lavine O, L. K. B. C. F. F. G. V. T. W. 1952: Effects of ultrasonic waves on the refractive media of the eye. *A.M.A. Archives of Ophthalmology 47*, 204-219.

Lerski, R. A., Duggan, T. C. & Christie, J. 1982: A simple tissue-like ultrasound phantom material. *British Journal of Radiology 55*, 156-157.

Li, F. Q., Gong, X. B., Hu, K., Li, C. Y. & Wang, Z. B. 2006: Effect of ribs in HIFU beam path on formation of coagulative necrosis in goat liver. *In* Clement, G. T., McDannold, N. J. & Hynynen, K. (eds.): *Therapeutic Ultrasound*, 477-480 pp. Amer Inst Physics, Melville.

Li, J. J., Xu, G. L., Gu, M. F., Luo, G. Y., Rong, Z., Wu, P. H. & Xia, J. C. 2007: Complications of high intensity focused ultrasound in patients with recurrent and metastatic abdominal tumors. *World Journal of Gastroenterology 13*, 2747-2751.

Liberman, B., Gianfelice, D., Inbar, Y., Beck, A., Rabin, T., Shabshin, N., Chander, G., Hengst, S., Pfeffer, R., Chechick, A., Hanannel, A., Dogadkin, O. & Catane, R. 2009: Pain Palliation in Patients with Bone Metastases Using MR-Guided Focused Ultrasound Surgery: A Multicenter Study. *Annals of Surgical Oncology 16*, 140-146.

Lin, J. X., Liu, X. Z. & Gong, X. F. 2013: Computational study on the propagation of strongly focused nonlinear ultrasound in tissue with rib-like structures. *Journal of the Acoustical Society of America 134*, 1702-1714.

Linke, C., Carstensen, E. L., Frizzell, L. A., Elbadawi, A. & Fridd, C. W. 1973: Localized tissue destruction by high-intensity focused ultrasound. *Archives of Surgery 107*, 887-891.

Liu, H.-L., Chang, H., Chen, W.-S., Shih, T.-C., Hsiao, J.-K. & Lin, W.-L. 2007: Feasibility of transrib focused ultrasound thermal ablation for liver tumors using a spherically curved 2D array: A numerical study. *Medical Physics 34*, 3436-3448.

Liu, H. L., Hsu, C. L., Huang, S. M. & Hsi, Y. W. 2010: Focal beam distortion and treatment planning for transrib focused ultrasound thermal therapy: A feasibility study using a two-dimensional ultrasound phased array. *Medical Physics 37*, 848-860.

Lizzi, F. L., Coleman, D. J., Driller, J., Franzen, L. A. & Jakobiec, F. A. 1978: Experimental, ultrasonically induced lesions in retina, choroid, and sclera. *Investigative Ophthalmology & Visual Science 17*, 350-360.

Lynn, J. G., Zwemer, R. L., Chick, A. J. & Miller, A. E. 1942: A new method for the generation and use of focused ultrasound in experimental biology. *The Journal of general physiology 26*, 179-193.

Madersbacher, S., Kratzik, C., Susani, M. & Marberger, M. 1994: Tissue ablation in benign prostatic hyperplasia with high intensity focused ultrasound. *The Journal of Urology 152*, 1956-1960; discussion 1960-1951.

Madersbacher, S., Schatzl, G., Djavan, B., Stulnig, T. & Marberger, M. 2000: Long-term outcome of transrectal high-intensity focused ultrasound therapy for benign prostatic hyperplasia. *European Urology 37*, 687-694.

Madsen, E. L., D'Souza, W. D. & Frank, G. R. 2003: Multi-imaging modality tissue mimicking materials for imaging phantoms. Wisconsin Alumni Research Foundation.

Madsen, E. L., Frank, G. R. & Dong, F. 1998: Liquid or Solid Ultrasonically Tissue-Mimicking Materials with Very Low Scatter. *Ultrasound in Medicine & Biology 24*, 535-542.

Madsen, E. L., Hobson, M. A., Frank, G. R., Shi, H., Jiang, J., Hall, T. J., Varghese, T., Doyley, M. M. & Weaver, J. B. 2006: Anthropomorphic breast phantoms for testing elastography systems. *Ultrasound in Medicine & Biology 32*, 857-874.

Madsen, E. L., Hobson, M. A., Shi, H. R., Varghese, T. & Frank, G. R. 2005: Tissue-mimicking agar/gelatin materials for use in heterogeneous elastography phantoms. *Physics in Medicine and Biology 50*, 5597-5618.

Madsen, E. L., Zagzebski, J. A., Banjavie, R. A. & Jutila, R. E. 1978: Tissue mimicking materials for ultrasound phantoms. *Medical Physics (Woodbury) 5*, 391-394.

Madsen, E. L., Zagzebski, J. A. & Frank, G. R. 1982a: Oil-in-gelatin dispersions for use as ultrasonically tissue-mimicking materials. *Ultrasound in Medicine & Biology 8*, 277-287.

Madsen, E. L., Zagzebski, J. A., Frank, G. R., Greenleaf, J. F. & Carson, P. L. 1982b: Anthropomorphic breast phantoms for assessing ultrasonic imaging system performance and for training ultrasonographers: Part I. *Journal of Clinical Ultrasound 10*, 67-75.

Madsen, E. L., Zagzebski, J. A., Frank, G. R., Greenleaf, J. F. & Carson, P. L. 1982c: Anthropomorphic breast phantoms for assessing ultrasonic imaging system performance and for training ultrasonographers: Part II. *Journal of Clinical Ultrasound 10*, 91-100.

Madsen, E. L., Zagzebski, J. A. & Ghilardi-Netto, T. 1980: An anthropomorphic torso section phantom for ultrasonic imaging. *Medical Physics 7*, 43-50.

Madsen, E. L., Zagzebski, J. A., Medina, I. R. & Frank, G. R. 1994: Performance testing of transrectal US scanners. *Radiology 190*, 77-80.

Mano, I., Goshima, H., Nambu, M. & Iio, M. 1986: New polyvinyl alcohol gel material for MRI phantoms. *Magnetic Resonance in Medicine 3*, 921-926.

Mark, M., Shanna, L., Rajiv, C. & Michael, J. B. 2004: Multi-modality tissue-mimicking phantom for thermal therapy. *Physics in Medicine and Biology 49*, 2767.

Marquet, F., Aubry, J. F., Pernot, M., Fink, M. & Tanter, M. 2011: Optimal transcostal high-intensity focused ultrasound with combined real-time 3D movement tracking and correction. *Physics in Medicine and Biology 56*, 7061-7080.

Martin, E., Jeanmonod, D., Morel, A., Zadicario, E. & Werner, B. 2009: High-intensity focused ultrasound for noninvasive functional neurosurgery. *Annals of Neurology 66*, 858-861.

Maruvada, S., Harris, G. R., Herman, B. A. & King, R. L. 2007: Acoustic power calibration of high-intensity focused ultrasound transducers using a radiation force technique. *Journal of the Acoustical Society of America 121*, 1434-1439.

Mitchell, M. D., Kundel, H. L., Axel, L. & Joseph, P. M. 1986: Agarose as a tissue equivalent phantom material for NMR imaging. *Magnetic Resonance Imaging 4*, 263-266.

Mulligan, E. D., Lynch, T. H., Mulvin, D., Greene, D., Smith, J. M. & Fitzpatrick, J. M. 1997: High-intensity focused ultrasound in the treatment of benign prostatic hyperplasia. *British Journal of Urology 79*, 177-180.

Nakamura, K., Baba, S., Saito, S., Tachibana, M. & Murai, M. 1997: High-intensity focused ultrasound energy for benign prostatic hyperplasia: Clinical response at 6 months to treatment using Sonablate 200(TM). *Journal of Endourology 11*, 197-201.

Nightingale, K., Soo, M. S., Nightingale, R. & Trahey, G. 2002: Acoustic radiation force impulse imaging: In vivo demonstration of clinical feasibility. *Ultrasound in Medicine and Biology 28*, 227-235.

Norwitz, E. R., Hoyte, L. P. J., Jenkins, K. J., van der Velde, M. E., Ratiu, P., Rodriguez-Thompson, D., Wilkins-Haug, L., Tempany, C. M. C. & Fishman, S. J. 2000: Separation of conjoined twins with the twin reversed-arterial-perfusion sequence after prenatal planning with three-dimensional modeling. *New England Journal of Medicine 343*, 399-402.

O'Donnell, M., Skovoroda, A. R., Shapo, B. M. & Emelianov, S. Y. 1994: Internal displacement and strain imaging using ultrasonic speckle tracking. *Ultrasonics, Ferroelectrics and Frequency Control, IEEE Transactions on 41*, 314-325.

Opik, R., Hunt, A., Ristolainen, A., Aubin, P. M. & Kruusmaa, M. 2012: Development of high fidelity liver and kidney phantom organs for use with robotic surgical systems. *Biomedical Robotics and Biomechatronics (BioRob), 2012 4th IEEE RAS & EMBS International Conference on*, 425-430 pp.

Paterson, R. F., Barret, E., Siqueira Jr, T. M., Gardner, T. A., Tavakkoli, J., Rao, V. V., Sanghvi, N. T., Cheng, L. & Shalhav, A. L. 2003: Laparoscopic Partial Kidney

Ablation With High Intensity Focused Ultrasound. *The Journal of Urology 169*, 347-351.

Poissonnier, L., Gelet, A., Chapelon, J. Y., Bouvier, R., Rouviere, O., Pangaud, C., Lyonnet, D. & Dubernard, J. M. 2003: Results of transrectal focussed ultrasound for the treatment of localized prostate cancer (120 patients with PSA <= 10 ng/ml). *Progres En Urologie 13*, 60-72.

Purnell, E. W., Sokollu, A., Torchia, R. & Taner, N. 1964: Focal chorioretinitis produced by ultrasound. *Investigative ophthalmology 3*, 657-664.

Qiao, S., Shen, G. F., Bai, J. F. & Chen, Y. Z. 2013: Transcostal high-intensity focused ultrasound treatment using phased array with geometric correction. *Journal of the Acoustical Society of America 134*, 1503-1514.

Quesson, B., Merle, M., Kohler, M. O., Mougenot, C., Roujol, S., de Senneville, B. D. & Moonen, C. T. 2010: A method for MRI guidance of intercostal high intensity focused ultrasound ablation in the liver. *Medical Physics 37*, 2533-2540.

Ramnarine, K. V., Anderson, T. & Hoskins, P. R. 2001: Construction and geometric stability of physiological flow rate wall-less stenosis phantoms. *Ultrasound in Medicine & Biology 27*, 245-250.

Ren, X.-L., Zhou, X.-D., Zhang, J., He, G.-B., Han, Z.-H., Zheng, M.-J., Li, L., Yu, M. & Wang, L. 2007: Extracorporeal ablation of uterine fibroids with high-intensity focused ultrasound - Imaging and histopathologic evaluation. *Journal of Ultrasound in Medicine 26*, 201-212.

Ross, C. S., Hussey, D. H., Pennington, E. C., Stanford, W. & Doornbos, J. F. 1990: Analysis of movement of intrathoracic neoplasms using ultrafast computerized tomography. *International journal of radiation oncology, biology, physics 18*, 671-677.

Sedlin, E. D., Frost, H. M. & Villanueva, A. R. 1963: Variations in Cross-section Area of Rib Cortex with Age. *Journals of Gerontology 18*, 9-13.

Selfridge, A. R. 1985: Approximate Material Properties in Isotropic Materials. *Sonics and Ultrasonics, IEEE Transactions on 32*, 381-394.

Shah, V., Pohida, T., Turkbey, B., Mani, H., Merino, M., Pinto, P. A., Choyke, P. & Bernardo, M. 2009: A method for correlating in vivo prostate magnetic resonance imaging and histopathology using individualized magnetic resonance -based molds. *Review of Scientific Instruments 80*.

Shalom, A., Wiser, I., Brawer, S. & Azhari, H. 2013: Safety and Tolerability of a Focused Ultrasound Device for Treatment of Adipose Tissue in Subjects Undergoing Abdominoplasty: A Placebo-Control Pilot Study. *Dermatologic Surgery 39*, 744-751.

Shaw, A. 2006: How to measure HIFU output power properly. *In* Clement, G. T., McDannold, N. J. & Hynynen, K. (eds.): *Therapeutic Ultrasound*, 628-632 pp. Amer Inst Physics, Melville.

Shaw, A. 2008: A Buoyancy Method for the Measurement of Total Ultrasound Power Generated by HIFU Transducers. *Ultrasound in Medicine & Biology 34*, 1327-1342.

Shaw, A. & Hodnett, M. 2008: Calibration and measurement issues for therapeutic ultrasound. *Ultrasonics 48*, 234-252.

Sheppard, J. & Duck, F. A. 1982: Ultrasonic tissue-equivalent materials using inorganic gel mixtures. *British Journal of Radiology 55*, 667-669.

Simon, J. C., Sapozhnikov, O. A., Khokhlova, V. A., Wang, Y. N., Crum, L. A. & Bailey, M. R. 2012: Ultrasonic atomization of tissue and its role in tissue fractionation by high intensity focused ultrasound. *Physics in Medicine and Biology 57*, 8061-8078.

Skretting, A., Glomset, O. & Bogsrud, T. V. 2010: A phantom for investigation of tumour signal and noise in PET reconstruction with various smoothing filters: experiments and comparisons with simulated intensity diffusion. *Radiation Protection Dosimetry 139*, 191-194.

Srinath, R. & Adam, S. 2012: The buoyancy method—a potential new primary ultrasound power standard. *Metrologia 49*, 327.

Staudenraus, J. & Eisenmenger, W. 1993: Fibre-optic probe hydrophone for ultrasonic and shock-wave measurements in water. *Ultrasonics 31*, 267-273.

Stewart, E. A., Gedroyc, W. M. W., Tempany, C. M. C., Quade, B. J., Inbar, Y., Ehrenstein, T., Shushan, A., Hindley, J. T., Goldin, R. D., David, M., Sklair, M. & Rabinovici, J. 2003: Focused ultrasound treatment of uterine fibroid tumors: Safety and feasibility of a noninvasive thermoablative technique. *American Journal of Obstetrics and Gynecology 189*, 48-54.

Surry, K. J. M., Austin, H. J. B., Fenster, A. & Peters, T. M. 2004: Poly(vinyl alcohol) cryogel phantoms for use in ultrasound and MR imaging. *Physics in Medicine and Biology 49*, 5529-5546.

Takegami, K., Kaneko, Y., Watanabe, T., Maruyama, T., Matsumoto, Y. & Nagawa, H. 2004: Polyacrylamide gel containing egg white as new model for irradiation experiments using focused ultrasound. *Ultrasound in Medicine & Biology 30*, 1419-1422.

Techavipoo, U., Varghese, T., Chen, Q., Stiles, T. A., Zagzebski, J. A. & Frank, G. R. 2004: Temperature dependence of ultrasonic propagation speed and attenuation in excised canine liver tissue measured using transmitted and reflected pulses. *Journal of the Acoustical Society of America 115*, 2859-2865.

Tempany, C. M. C., Stewart, E. A., McDannold, N., Quade, B. J., Jolesz, F. A. & Hynynen, K. 2003: MR Imaging–guided Focused Ultrasound Surgery of Uterine Leiomyomas: A Feasibility Study1. *Radiology 226*, 897-905.

Terhaar, G., Sinnett, D. & Rivens, I. 1989: High intensity focused ultrasound-a surgical technique for the treatment of discrete liver tumours. *Physics in Medicine and Biology 34*, 1743-1750.

Thiel, W. 1992: The preservation of the whole corpse with natural color. *Annals of anatomy = Anatomischer Anzeiger : official organ of the Anatomische Gesellschaft 174*, 185-195.

Tye, R. P., Kubičár, L. & Lockmuller, N. 2005: The Development of a Standard for Contact Transient Methods of Measurement of Thermophysical Properties. *International Journal of Thermophysics 26*, 1917-1938.

Urban, M. W., Chalek, C., Kinnick, R. R., Kinter, T. M., Haider, B., Greenleaf, J. F., Thomenius, K. E. & Fatemi, M. 2011: Implementation of Vibro-Acoustography on a Clinical Ultrasound System. *Ieee Transactions on Ultrasonics Ferroelectrics and Frequency Control 58*, 1169-1181.

Vallancien, G., Harouni, M., Guillonneau, B., Veillon, B. & Bougaran, J. 1996: Ablation of superficial bladder tumors with focused extracorporeal pyrotherapy. *Urology 47*, 204-207.

Venkatesh, S. K., Yin, M., Glockner, J. F., Takahashi, N., Araoz, P. A., Talwalkar, J. A. & Ehman, R. L. 2008: MR elastography of liver tumors: Preliminary results. *American Journal of Roentgenology 190*, 1534-1540.

Visioli, A. G., Rivens, I. H., ter Haar, G. R., Horwich, A., Huddart, R. A., Moskovic, E., Padhani, A. & Glees, J. 1999: Preliminary results of a phase I dose escalation clinical trial using focused ultrasound in the treatment of localised tumours. *European Journal of Ultrasound 9*, 11-18.

Wan, H., VanBaren, P., Ebbini, E. S. & Cain, C. A. 1996: Ultrasound surgery: Comparison of strategies using phased array systems. *Ieee Transactions on Ultrasonics Ferroelectrics and Frequency Control 43*, 1085-1098.

Warwick, R. & Pond, J. 1968: Trackless lesions in nervous tissues produced by high intensity focused ultrasound (high-frequency mechanical waves). *Journal of Anatomy 102*, 387-&.

Watkin, N. A., Morris, S. B., Rivens, I. H. & ter Haar, G. R. 1997: High-intensity focused ultrasound ablation of the kidney in a large animal model. *Journal of endourology / Endourological Society 11*, 191-196.

Wear, K. A. 1999: Frequency dependence of ultrasonic backscatter from human trabecular bone: Theory and experiment. *Journal of the Acoustical Society of America 106*, 3659-3664.

Wu, F. 2006: Extracorporeal high intensity focused ultrasound in the treatment of patients with solid malignancy. *Minimally Invasive Therapy & Allied Technologies 15*, 26-35.

Wu, F., Chen, W.-Z., Bai, J., Zou, J.-Z., Wang, Z.-L., Zhu, H. & Wang, Z.-B. 2001a: Pathological changes in human malignant carcinoma treated with high-intensity focused ultrasound. *Ultrasound in Medicine & Biology 27*, 1099-1106.

Wu, F., Wang, Z.-B., Chen, W.-Z., Bai, J. I. N., Zhu, H. U. I. & Qiao, T.-Y. 2003a: Preliminary Experience Using High Intensity Focused Ultrasound for the

Treatment of Patients With Advanced Stage Renal Malignancy. *The Journal of Urology 170*, 2237-2240.

Wu, F., Wang, Z.-B., Chen, W.-Z., Wang, W., Gui, Y., Zhang, M., Zheng, G., Zhou, Y., Xu, G., Li, M., Zhang, C., Ye, H. & Feng, R. 2004a: Extracorporeal high intensity focused ultrasound ablation in the treatment of 1038 patients with solid carcinomas in China: an overview. *Ultrasonics Sonochemistry 11*, 149-154.

Wu, F., Wang, Z.-B., Chen, W.-Z., Zhu, H., Bai, J., Zou, J.-Z., Li, K.-Q., Jin, C.-B., Xie, F.-L. & Su, H.-B. 2004b: Extracorporeal high intensity focused ultrasound ablation in the treatment of patients with large hepatocellular carcinoma. *Annals of Surgical Oncology 11*, 1061-1069.

Wu, F., Wang, Z.-B., Chen, W.-Z., Zou, J.-Z., Bai, J., Zhu, H., Li, K.-Q., Xie, F.-L., Jin, C.-B., Su, H.-B. & Gao, G.-W. 2004c: Extracorporeal focused ultrasound surgery for treatment of human solid carcinomas: early Chinese clinical experience. *Ultrasound in Medicine & Biology 30*, 245-260.

Wu, F., Wang, Z., Chen, W. & et al. 2001b: Pathological study of extracorporeally ablated hepatocellular carcinoma with high-intensity focused ultrasound. *Zhonghua Zhongliu Zazhi 23*, 237-239.

Wu, F., Wang, Z. B., Cao, Y. D., Chen, W. Z., Bai, J., Zou, J. Z. & Zhu, H. 2003b: A randomised clinical trial of high-intensity focused ultrasound ablation for the treatment of patients with localised breast cancer. *British journal of cancer 89*, 2227-2233.

Wurster, C., Staudenraus, J. & Eisenmenger, W. 1994: The fiber optic probe hydrophone. *Ultrasonics Symposium, 1994. Proceedings., 1994 IEEE*, 941-944 vol.942 pp.

Xu, H., Rao, M., Varghese, T., Sommer, A., Baker, S., Hall, T. J., Sisney, G. A. & Burnside, E. S. 2010: Axial-Shear Strain Imaging for Differentiating Benign and Malignant Breast Masses. *Ultrasound in Medicine & Biology 36*, 1813-1824.

Zderic, V., Keshavarzi, A., Andrew, M. A., Vaezy, S. & Martin, R. W. 2004: Attenuation of porcine tissues in vivo after high-intensity ultrasound treatment. *Ultrasound in Medicine & Biology 30*, 61-66.

Zell, K., Sperl, J. I., Vogel, M. W., Niessner, R. & Haisch, C. 2007: Acoustical properties of selected tissue phantom materials for ultrasound imaging. *Physics in Medicine and Biology 52*, N475.

Zhai, L., Madden, J., Foo, W.-C., Mouraviev, V., Polascik, T. J., Palmeri, M. L. & Nightingale, K. R. 2010: Characterizing Stiffness of Human Prostates Using Acoustic Radiation Force. *Ultrasonic Imaging 32*, 201-213.

Zhai, L., Polascik, T. J., Foo, W.-C., Rosenzweig, S., Palmeri, M. L., Madden, J. & Nightingale, K. R. 2012: Acoustic Radiation Force Impulse Imaging of Human Prostates: Initial In Vivo Demonstration. *Ultrasound in Medicine & Biology 38*, 50-61.

Zhang, M., Nigwekar, P., Castaneda, B., Hoyt, K., Joseph, J. V., Agnese, A. d. S., Messing, E. M., Strang, J. G., Rubens, D. J. & Parker, K. J. 2008: Quantitative characterization of viscoelastic properties of human prostate correlated with histology. *Ultrasound in Medicine and Biology 34*, 1033-1042.

Zhou, Y.-F. 2011: High intensity focused ultrasound in clinical tumor ablation. *World journal of clinical oncology 2*, 8-27.

Zhu, H., Zhou, K., Zhang, L., Jin, C. B., Peng, S., Yang, W., Li, K. Q., Su, H. B., Chen, W. Z., Bai, J., Wu, F. & Wang, Z. B. A. 2009: High intensity focused ultrasound (HIFU) therapy for local treatment of hepatocellular carcinoma: Role of partial rib resection. *European Journal of Radiology 72*, 160-166.

Appendix I: Protection measures for PAA phantom fabrication

Due to the strong toxicity of parts of the components to fabricate the PAA phantom, personal protection of acrylamide and N, N, N', N'-Tetramethylethylenediamine is listed to provide useful information for potential users. All the contact with skin, eyes and clothing should be avoided. Hands must be washed before breaks and immediately after handling the materials.

Personal protection:

Eye/face protection

Face shield and safety glassed. Use equipment for eye protection tested and approved under appropriate government standards such as NIOSH (US) or EN 166 (EU).

Skin protection

Handle with gloves. Gloves must be inspected prior to use. Use proper glove removal technique (without touching glove's outer surface) to avoid skin contact with this product. Dispose of contaminated gloves after use in accordance with applicable laws and good laboratory practices.

Body protection

Complete suit protecting against chemicals. The type of protective equipment must be selected according to the concentration and amount of the dangerous substance at the specific workplace.

Respiratory protection

Where risk assessment shows air-purifying respirators are appropriate use a full-face particle respirator type N100 (US) or type P3 (EN143) respirator cartridges as a backup to engineering controls. If the respirator is the sole means of protection, use a full-face supplied air respirator. Use respirators and components tested and approved under appropriate government standards such as NIOSH (US) or CEN (EU).

Control of environmental exposure

Prevent further leakage or spillage if safe to do so. Do not let product enter drains. Discharge into the environment must be avoided.

First aid measures

For general advice, consult a physician. If breathed in, move person into fresh air. If not breathing, give artificial respiration. In case of skin contact, wash off with soap and plenty of water. Take victim immediately to hospital. In case of eye contact, rinse thoroughly with plenty of water for at least 15 minutes. If swallowed, never give anything by mouth to an unconscious person. Rinse mouth with water.

All the above information of personal protection is from the safety data sheet of the materials provided by the supplier (Sigma-Aldrich, Gillingham, Dorset, UK).

Appendix II: COSHH Special Risk Assessment Form of Acrylamide/Bis-acrylamide

1. Name and brief description of procedure

Acrylamide/Bis-acrylamide Laboratory chemicals, manufacture of substances

2. Name, amount and form of hazardous substances used or created in procedure

Acute toxicity, oral; acute toxicity, inhalation; acute toxicity, dermal; skin irritation; eye irritation; skin sensitisation; germ cell mutagenicity; carcinogenicity; reproductive toxicity; specific target organ toxicity-repeated exposure

3. Human health effects identified

Toxic if swallowed. Harmful in contact with skin. Causes skin irritation. May cause an allergic skin reaction. Causes serious eye irritation. Harmful if inhaled. May cause genetic defects. May cause cancer. Suspected of damaging fertility. Causes damage to organs through prolonged or repeated exposure.

4. Information sources used

Safety data sheet from SIGMA-ALDRICH

5. Can the procedure be modified to reduce risk of ill health? If so, why not

No data available

6. Control measures

Avoid exposure. Avoid contact with skin and eyes. Avoid formation of dust and aerosols. Provide appropriate exhaust ventilation at places where dust is formed. Store in cool place. Keep container tightly closed in a dry and well-ventilated place. Light sensitive.

7. Level of supervision required

Approval will be needed.

8. Level of training required

PhD student lab training.

9. Lone working permissible

Yes.

10. Testing and maintenance of control measures

No.

11. Is environmental monitoring required

No data available

12. Is health surveillance required

No data available

13. Disposal procedures

Offer surplus and non-recyclable solutions to a licensed disposal company. Dissolve or mix the material with a combustible solvent and burn in a chemical incinerator equipped with an afterburner and scrubber.

14. Emergency procedures

a. First aid measures

Consult a physician. Show safety data sheet to the doctor in attendance. If breathed in, move person into fresh aire. If not breathing, give artificial respiration. Consult a physician. Wash off with soap and plenty of water. Take victim immediately to hospital. Consult a physician. Rinse thoroughly with plenty of water for at least 15 minutes and consult a physician. Never give anything by mouth to an unconscious person. Rinse mouth with water. Consult a physician.

b. Firefighting measures

Use water spray, alcohol-resistant foam, dry chemical or carbon dioxide. Special hazards arising from the substance or mixture: carbon oxides, nitrogen oxides (NO_x). Wear self-contained breathing apparatus for firefighting if necessary.

c. Accidental release measures

Wear protective gloves/clothing and eye/face protection. Prevent further leakage or spillage if safe to do so. Do not let product enter drains. Discharge into the environment must be avoided. Pick up and arrange disposal without creating dust. Sweep up and shovel. Keep in suitable, closed containers for disposal.

15. Monitoring procedures

Standard

16. Special risk factors and additional control measures

As described in emergency procedures.

Appendix III: COSHH Special Risk Assessment Form of N,N,N'N'-Tetramethylethylenediamine

1. Name and brief description of procedure

N,N,N'N'-Tetramethylethylenediamine Laboratory chemicals, manufacture of substances

2. Name, amount and form of hazardous substances used or created in procedure

N,N,N'N'-Tetramethylethylenediamine Flammable liquids; skin corrosion; acute toxicity, inhalation; acute toxicity, oral

3. Human health effects identified

Highly flammable liquid and vapour. Harmful if swallowed. Causes severe skin burns and eye damage. Harmful if inhaled.

4. Information sources used

Safety data sheet from SIGMA-ALDRICH.

5. Can the procedure be modified to reduce risk of ill health? If so, why not

No data available.

6. Control measures

a. Precautions for safe handling Avoid contact with skin and eyes. Avoid inhalation of vapour or mist. Keep away from sources of ignition. Take measure to prevent the build up of electrostatic charge. b. Conditions for safe storage, including any incompatibilities Store in cool place. Keep container tightly closed in a dry and well-ventilated place. Containers which are opened must be carefully resealed and kept upright to prevent leakage. Handle and store under inert gas. Air and moisture sensitive.

7. Level of supervision required

Approval is needed.

8. Level of training required

PhD student lab training.

9. Lone working permissible

Yes.

10. Testing and maintenance of control measures

No.

11. Is environmental monitoring required

No data available

12. Is health surveillance required

No data available

13. Disposal procedures

Offer surplus and non-recyclable solutions to a licensed disposal company. Dissolve or mix the material with a combustible solvent and burn in a chemical incinerator equipped with an afterburner and scrubber.

14. Emergency procedures

a. First aid measures

If breathed in, move person into fresh air. If not breathing, give artificial respiration. Consult a physician. In case of skin contact, take off contaminated clothing and shoes immediately. Wash off with soap and plenty of water. Take victim immediately to hospital. Consult a physician. In case of eye contact, rinse thoroughly with plenty of water for at least 15 minutes and consult a physician. If swallowed, do not induce vomiting. Never give anything by mouth to an unconscious person. Rinse mouth with water. Consult a physician.

b. Firefighting measures

Use water spray, alcohol-resistant foam, dry chemical or carbon dioxide. Special hazards arising from the substance or mixture: carbon oxides, nitrogen oxides (NO_x). Wear self contained breathing apparatus for fire fighting if necessary. Use water spray to cool unopened containers.

c. Accidental release measures

Wear respiratory protection. Avoid breathing vapours, mist or gas. Ensure adequate ventilation. Remove all sources of ignition. Evacuate personnel to safe areas. Beware of vapours accumulating to form explosive concentrations. Vapours can accumulate in low areas. Prevent further leakage or spillage if safe to do so. Do not let product enter drains. Contain spillage, and then collect with an electrically protected vacuum cleaner or by wet-brushing and place in container for disposal according to local regulations.

15. Monitoring procedures

Standard

16. Special risk factors and additional control measures

As described in emergency procedures.